

**Vibrational spectroscopy and
density functional theory calculations,
a powerful approach for the characterization of
pharmaceuticals and new organometallic
complexes**

Dissertation

zur Erlangung des

Naturwissenschaftlichen Doktorgrades

der Bayerischen Julius-Maximilians-Universität Würzburg

vorgelegt von

Ioana-Emilia Pavel

aus

Cluj-Napoca

Würzburg 2003

Eingereicht am:

bei der Fakultät für Chemie und Pharmazie

1. Gutachter:

2. Gutachter:

der Dissertation

1. Prüfer:

2. Prüfer:

3. Prüfer:

des öffentlichen Promotionskollquiums

Tag des öffentlichen Promotionskollquiums:

Doktorurkunde ausgehändigt am:

Dedication

To my wonderful parents

CONTENTS

| | | |
|------------|--|-----------|
| 1 | Introduction | 1 |
| 2 | Theoretical background | 3 |
| 2.1 | Vibrational spectroscopy | 3 |
| 2.1.1 | Infrared and Raman spectroscopy | 3 |
| 2.1.2 | Surface enhanced Raman spectroscopy | 12 |
| 2.1.2.1 | Electromagnetic enhancement mechanism | 15 |
| 2.1.2.2 | Charge transfer enhancement mechanism | 18 |
| 2.1.2.3 | Surface enhanced Raman scattering substrates | 20 |
| 2.2 | Density functional theory | 25 |
| 2.2.1 | The Kohn-Sham approach | 25 |
| 2.2.2 | Exchange and correlation energy functionals | 27 |
| 2.2.3 | Basis set effects | 30 |
| 2.2.3.1 | Slater and Gaussian type orbitals | 30 |
| 2.2.3.2 | Pople style basis sets | 32 |
| 2.2.4 | Population analysis and electron densities | 34 |
| 3 | Experimental section | 37 |
| 3.1 | Chemicals and procedures | 37 |
| 3.1.1 | Syntheses | 37 |
| 3.1.2 | Substrates and solutions preparation | 37 |
| 3.2 | Instrumentation | 39 |
| 3.3 | Computational details | 41 |
| 4 | Why SERS and DFT? A combination that can certainly help in analyzing pharmaceutical materials and their behavior near a biological artificial model | 43 |
| 4.1 | 1,4-Dihydrazinophthalazine | 45 |
| 4.1.1 | Molecule presentation | 45 |

| | | |
|------------|---|-----|
| 4.1.2 | Results and discussion | 45 |
| 4.1.2.1 | Geometry optimization | 45 |
| 4.1.2.1 | Vibrational spectroscopy | 50 |
| 4.1.3 | Conclusions | 61 |
| 4.2 | Caffeine (1,3,7-trimethyl-2,6-purinedione) | 62 |
| 4.2.1 | Molecule presentation | 62 |
| 4.2.2 | Results and discussion | 62 |
| 4.2.2.1 | Geometry optimization | 62 |
| 4.2.2.2 | Vibrational spectroscopy | 65 |
| 4.2.3 | Conclusions | 80 |
| 4.3 | Papaverine hydrochloride | 81 |
| 4.3.1 | Molecule presentation | 81 |
| 4.3.2 | Results and discussion | 82 |
| 4.3.2.1 | Geometry optimization | 82 |
| 4.3.2.2 | Vibrational spectroscopy | 84 |
| 4.3.3 | Conclusions | 94 |
| 4.4 | Nickel(II) cupferronato complexes | 95 |
| 4.4.1 | Molecules presentation | 95 |
| 4.4.2 | Results and discussion | 97 |
| 4.4.2.1 | Geometry optimization | 97 |
| 4.4.2.2 | Vibrational spectroscopy | 99 |
| 4.4.3 | Conclusions | 107 |
| 5 | Why Raman and DFT? An already well-known method of studying new organometallic compounds | 108 |
| 5.1 | Silylene-bridged dinuclear iron complexes | 109 |
| 5.1.1 | Molecules presentation | 109 |
| 5.1.2 | Results and discussion | 110 |
| 5.1.2.1 | Geometry optimization | 110 |
| 5.1.2.2 | Vibrational spectroscopy | 117 |
| 5.1.3 | Conclusions | 127 |
| 5.2 | 3-Silaoxetane and 3-silathietane | 128 |
| 5.2.1 | Molecules presentation | 128 |

VII

| | | |
|----------|----------------------------------|------------|
| 5.2.2 | Results and discussion | 129 |
| 5.2.2.1 | Geometry optimization | 129 |
| 5.2.2.2 | Vibrational spectroscopy | 135 |
| 5.2.3 | Conclusions | 141 |
| 6 | Summary | 142 |
| | References | 151 |
| | Abbreviations and Symbols | 165 |
| | Curriculum Vitae | 169 |
| | Word of gratitude | 171 |

Chapter 1

INTRODUCTION

Spectroscopy in the pharmaceutical and chemical industry is dominated by techniques such as nuclear magnetic resonance, X-ray and mass spectroscopy, which serve for the elucidation of a chemical structure. Despite this, the versatility of infrared spectroscopy ensures it still remains a key technique in quality control laboratories, and in applications where solid form characterization or minimal sample preparation is a necessity. Due to the advances in technology and the appropriate use in some specific applications, Raman spectroscopy becomes widely used now in pharmaceutical and chemical research. Consequently, it is the vibrational spectroscopy (a collective term of infrared and Raman) that is regularly used in identification, characterization, and investigation of new chemical or pharmaceutically active compounds.

However, the Raman process is associated with a low photon scattering efficiency because of its two-photon nature, although multichannel photon detectors enhance Raman sensitivities. Due to the low scattering cross-section and the possibility of high background-fluorescence interference, the application of Raman spectroscopy to trace analysis is limited. Therefore, there was a great need for techniques that can overcome this limitation. The surface enhanced Raman (SER) scattering is a process in which adsorbed molecules at or near a certain rough metal surface (e.g., Ag, Au, Cu) can enhance the Raman scattering signal by up to 11 orders of magnitude compared to the intensity expected for nonadsorbed species at the same concentration. Such enormous enhancement overcomes the disadvantages associated with the low detection sensitivity of normal Raman scattering process at interfaces and allows a monolayer or less of a coverage to be observed in a Raman experiment. Moreover, SERS active surfaces display a weak continuum inelastic background scattering and are very effective at quenching fluorescence. This type of spectroscopy allows monitoring the kinetic behavior of adsorbates and determining adsorbate properties such as identity, bonding, and orientation.

Although the theories explaining SERS are not definite and still evolving, the experimental research and development in recent years has demonstrated SERS to be a

2 *Introduction*

potential technique for trace analysis of pharmaceuticals and biological active organometallic complexes, enabling in some cases the detection of even single molecules. The enhancement calculated from these observations (approximately 10^{14}), reinvigorated the field and offers new perspectives.

But the direct assignment of infrared or Raman bands of relatively complex molecules, as biological or organometallic compounds, is rather complicated. Theoretical calculations can certainly assist to obtain a deeper understanding of the vibrational spectra of such molecules. In the last twenty years, quantum chemical methods have so successfully been developed that now they are almost an indispensable complement of experimental studies in chemistry. In particular, recent developments in Density Functional Theory (DFT) have shown that this method is a powerful computational alternative to the conventional quantum chemical methods, since they are much less computationally demanding and take account of the effects of electron correlations. Because DFT includes corrections to Hartree-Fock (HF) energies for the correlation energy, the structures and relative energies become much more reliable, while computations using Kohn-Sham orbitals become simpler.

In the present work, several new metal complexes, which have successfully been characterized by using DFT calculations and the infrared and Raman spectroscopy techniques, are presented.

The promising results obtained by these two complementary methods, determined us to try a new approach and use DFT for interpreting the rich SERS spectra of well-known pharmaceuticals or new potentially biological active organometallic complexes obtained near a biological artificial model (Ag substrate), taking into account that information about the species present under particular conditions could be of great importance in the interpretation of biochemical processes.

THEORETICAL BACKGROUND

2.1 *Vibrational spectroscopy*

Vibrational spectroscopy is one of the most widely used tools for the analysis of organic and inorganic substances, whether of biological, geological or synthetic origin. The two very important techniques, which allow studying the interaction of the electromagnetic radiation with matter, are the infrared (IR) and Raman spectroscopy. They require very small quantities and can be used in the examination of samples in all phases of matter.¹⁻⁹

2.1.1 *Infrared and Raman spectroscopy*

IR and Raman spectra result from transitions between quantized vibrational energy states. Molecular vibrations can range from the simple coupled motion of the two atoms of a diatomic molecule to the much more complex motion of every atom in a large polyfunctional molecule. The $3N-6$ degrees of freedom of a molecule with N atoms ($3N-5$ for a linear molecule) give the number of ways that the atoms in the molecule can vibrate, i.e. the number of *vibrational modes*.¹⁻⁹

Each mode i involves approximately harmonic displacements of the atoms from their equilibrium positions (v_i). The potential energy, $V(r)$, of a harmonic oscillator is shown as a function of the distance between the atoms, r , as the broken line in Figure 2.1.¹ For any mode in which the atoms vibrate with simple harmonic motions, i.e. obeying Hooke's law, the vibrational energy states, V_{iv} , can be described by equation (2.1)¹:

$$V_{iv} = h\nu_i \left(v_i + \frac{1}{2} \right), \quad (2.1)$$

where h is the Planck's constant, ν_i is the *fundamental frequency* of the particular mode and v_i is the *vibrational quantum number* of the i^{th} mode ($v_i = 0, 1, 2, \dots$). The energy difference for transitions between the ground ($v_i = 0$) and the first excited state ($v_i = 1$) of most vibrational modes corresponds to the energy of radiation in the MIR spectrum ($4000-400 \text{ cm}^{-1}$).

For small displacements of the atoms from their equilibrium positions, the forces on the nuclei are linearly proportional to the displacement r , and for displacements from

4 Theoretical Background

equilibrium these must be towards the rest position, i.e. negative. Since force equals mass times acceleration we have¹:

$$\text{Force} = -fr = -\frac{\partial V^2}{\partial r^2} \cdot r = \mu \frac{\partial^2 r}{\partial t^2}, \quad (2.2)$$

where $m_1 m_2 / (m_1 + m_2)$ is the reduced mass and t represents time. The solution of this equation is¹:

$$r = r_0 \cos(2\pi\nu t + \theta) \quad (2.3)$$

$$\frac{\nu}{c} = \tilde{\nu} = \frac{1}{2\pi c} \sqrt{\frac{f}{\mu}}, \quad (2.4)$$

where θ is an arbitrary phase angle, ν is the frequency of the vibration and $\tilde{\nu}$ is the wavenumber. It transpires that for first-row elements and hydrogen the force constant, $f = \partial^2 V / \partial r^2$, is reasonably proportional to the bond order, and we can suppose that for single bonds ν is inversely proportional, to a first approximation, to the inverse square root of the reduced mass. One should be aware that they are dimensionally different and are strictly proportional only as long as the wavelength is measured in vacuum or in constant atmospheric conditions, so that the velocity of light is constant. On this basis we can rationalize the relative positions of many of the bands arising in the spectra of complex molecules.

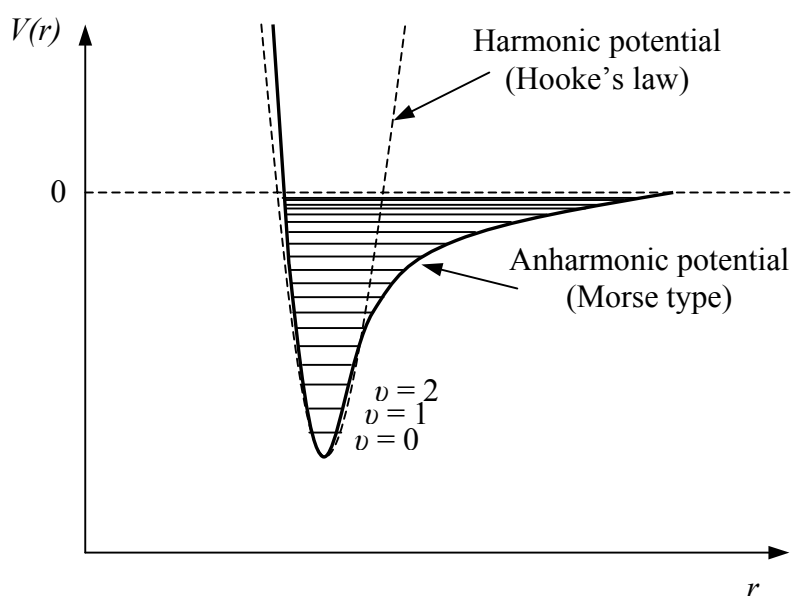


Figure 2.1. Potential energy of a diatomic molecule as a function of the atomic displacement during a vibration for a harmonic oscillator (broken line) and an anharmonic oscillator (solid line).

5 Theoretical Background

The motion of atoms during a vibration is usually described in terms of the *normal coordinate*, Q . The molecule is only promoted to the excited state if its dipole moment, μ , changes during the vibration, i.e. provided that $(\partial\mu/\partial Q) \neq 0$.¹⁻⁷ For molecules with certain elements of symmetry, some vibrational modes may be degenerate, so that more than one mode has a given vibrational frequency while the others may be completely forbidden. Thus, because of the degeneracy, the number of observable fundamental absorption bands is often less than $3N-6$.¹⁻⁷

The actual variation of the potential energy as a function of the displacement of the atoms from their equilibrium positions is shown as the solid line in Figure 2.1. From this curve it can be seen that equation (2.1) is valid only for low values of the vibrational quantum number, and is not valid when ν_i is large. In practice, V_{iv} must be described using an *anharmonic* potential function. This behavior is illustrated in Figure 2.1 as the solid line, and the potential energy is given to a first approximation by equation (2.5)¹:

$$V_{iv} = h\nu_i\left(\nu_i + \frac{1}{2}\right) + h\nu_i x_i\left(\nu_i + \frac{1}{2}\right)^2, \quad (2.5)$$

where x_i is the anharmonicity constant. x_i is dimensionless and typically has values between -0.001 and -0.02 depending on the mode.

If all vibrational modes were strictly harmonic, no transitions involving changes in ν_i by more than ± 1 would be allowed. The effect of anharmonicity is to relax this selection rule, i.e. to allow bands caused by $|\Delta\nu_i| > 1$ to become allowed. Thus overtone ($\Delta\nu_i = 2, 3, \dots$) and combination bands ($\Delta\nu_i = 1, 2, \dots; \Delta\nu_j = 1, 2, \dots$), where j represents a different mode, commonly appear as being weak in the IR spectrum of organic compounds along with the bands due to fundamental transitions ($\Delta\nu_i = 1$).¹⁻⁷

The dipole can be expanded as a Taylor series in the molecular distortion¹:

$$\mu = \mu_0 + \frac{\partial\mu}{\partial Q}Q + \frac{1}{2}\frac{\partial^2\mu}{\partial Q^2}Q^2 + \text{higher terms.} \quad (2.6)$$

The term containing Q^2 arises due to a change in the vibrational quantum number of 2, and therefore, overtones will occur if the second derivative of the dipole moment is non-zero. Since the total molecular wavefunction can be written as a product over all states, then the condition for combination bands to occur (simultaneous changes in two different quantum numbers) is that $\partial^2\mu/\partial Q_i\partial Q_j \neq 0$. Occasionally combination bands appear with considerable strength due to the mixing with a nearby fundamental transition of the same symmetry (Fermi resonance).

6 Theoretical Background

The intensity of fundamental bands in IR spectra is proportional to $(\partial\mu/\partial Q)^2$:¹

$$\Gamma_i = \frac{N\pi}{3c\nu_i \epsilon_0} \left(\frac{\partial\mu}{\partial Q_i} \right)^2, \quad (2.7)$$

where Γ_i is the integrated absorption intensity of mode i (for an ensemble of randomly oriented molecules) and ϵ_0 is the permittivity of the free space.

Every molecule has slightly different vibrational modes from all other molecules, but the enantiomers. Thus the IR spectrum of a given molecule is unique and can be used to identify that molecule. But not all vibrations may give rise to absorption bands in the IR spectrum. The interaction of matter with electromagnetic radiation is subject to selection rules.¹⁻⁷ That is, the stretching vibrations of homonuclear diatomic molecules (such as H₂, O₂, etc.) or the totally symmetric vibrations of larger molecules having a centre of symmetry, as well as any other vibrations which do not generate a vibrating electric dipole, are IR inactive. In order to detect such vibrations, it is necessary to consider the inelastic scattering of light, a phenomenon that is referred as Raman scattering. This is governed by different selection rules compared to the absorption of light.¹⁻⁹

In Raman spectrometry, the sample is illuminated with a monochromatic beam of radiation of wavenumber $\tilde{\nu}_0$. All photons that interact with the sample cause the potential energy of a molecule to be raised to a virtual state, $h\nu_0$ above the ground state. Almost immediately most molecules return to the ground state through the emission of a photon of the same wavelength as that of the incident photon (*the Rayleigh scattering*) (Figure 2.2).¹⁻⁹ A small fraction of the incident photons drops back to the first excited vibrational state of the k^{th} vibrational mode of the molecule, so that the energy of the scattered photon is $h(\nu_0 - \nu_k)$, i.e., it will be observed at a wavenumber of $(\tilde{\nu}_0 - \tilde{\nu}_k)$, where $\tilde{\nu}_k$ is the wavenumber of the k^{th} vibrational mode. Since the energies of the incident and scattered photons are different, the scattering is inelastic. This process is known as *Stokes Raman scattering* (Figure 2.2).¹⁻⁹ Since a given molecule has many different vibrational modes, measurement of the spectrum from $\tilde{\nu}_0$ to $(\tilde{\nu}_0 - 4000) \text{ cm}^{-1}$ allows all Raman-active bands to be measured.

Molecules that are in an excited vibrational state will undergo analogous effects when irradiated by a laser. Again, most of these molecules will bear Rayleigh scattering, but a small number will return from the virtual state to the ground vibrational state. In this case, which is known as *anti-Stokes Raman scattering* (Figure 2.2), radiation will be observed at a wavenumber of $(\tilde{\nu}_0 + \tilde{\nu}_k)$.¹⁻⁹ In practice, anti-Stokes-shifted Raman bands are seen only for

bands where $\tilde{\nu}_k$ is low, usually below 1000 cm^{-1} , because only for these bands the Boltzmann population of the excited vibrational state is populated to greater than 1% at ambient temperature.

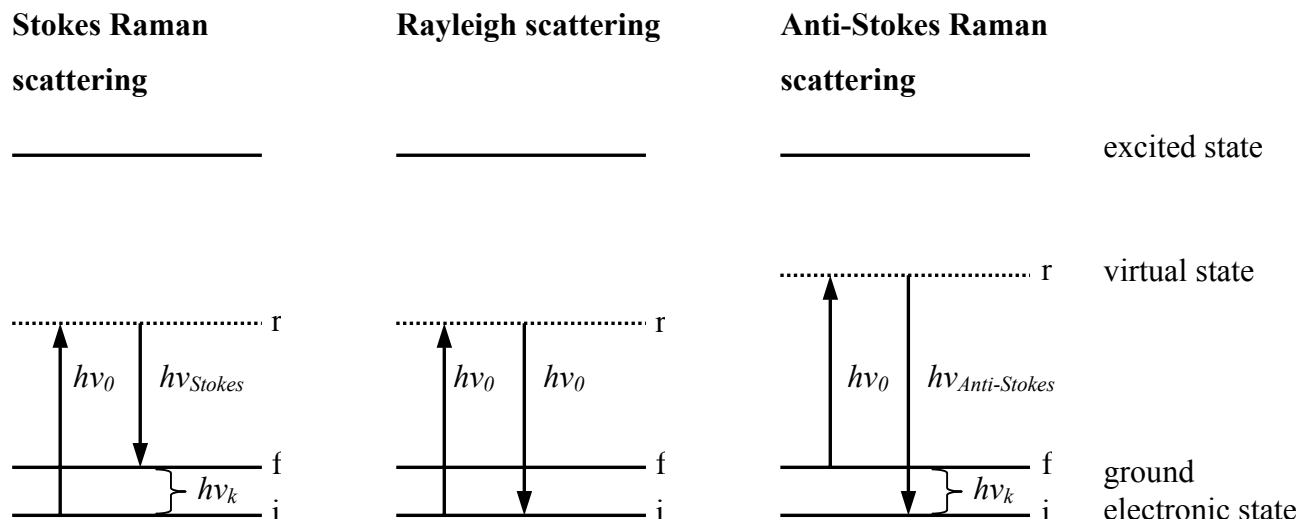


Figure 2.2. Principle of Raman scattering.

The classical theory of Rayleigh and Raman scattering is based on the concept that scattered light is generated by oscillating electric dipoles induced by the electric field of incident radiation. The relation between the induced dipole moment vector μ and the electric field vector E can be written in the form of the following power series^{1, 8}:

$$\mu = \alpha E + \frac{1}{2} \beta E E + \frac{1}{6} \gamma E E E + \dots, \quad (2.8)$$

where α is the polarizability, β the hyperpolarizability, and γ the second hyperpolarizability of the molecule. Polarizabilities α , β , γ are tensors of rank 2, 3, and 4, respectively. The polarizabilities can be regarded as the measure of the flexibility of the electron cloud: the ease with which the electron cloud of a molecule can be deformed or displaced to produce an electric dipole under the influence of an external electric field. The nonlinear terms in equation (2.8) are usually so small compared to the linear one that they do not play a role in the normal, linear Raman scattering. If we restrict the discussion to the linear term in equation (2.8), i.e., $\mu = \alpha E$, then it can be written in the form of three linear equations,^{1, 8}

$$\left. \begin{aligned} \mu_x &= \alpha_{xx} E_x + \alpha_{xy} E_y + \alpha_{xz} E_z \\ \mu_y &= \alpha_{yx} E_x + \alpha_{yy} E_y + \alpha_{yz} E_z \\ \mu_z &= \alpha_{zx} E_x + \alpha_{zy} E_y + \alpha_{zz} E_z \end{aligned} \right\}, \quad (2.9)$$

8 Theoretical Background

corresponding to the matrix multiplication^{1, 8}

$$\begin{bmatrix} \mu_x \\ \mu_y \\ \mu_z \end{bmatrix} = \begin{bmatrix} \alpha_{xx} & \alpha_{xy} & \alpha_{xz} \\ \alpha_{yx} & \alpha_{yy} & \alpha_{yz} \\ \alpha_{zx} & \alpha_{zy} & \alpha_{zz} \end{bmatrix} \begin{bmatrix} E_x \\ E_y \\ E_z \end{bmatrix} \quad (2.10),$$

where the nine coefficients α_{ij} are the components of the polarizability tensor α .

The polarizability tensor can be described in most cases by a real, symmetric matrix, where $\alpha_{ij} = \alpha_{ji}$. Thus it has at most 6 independent components: 3 diagonal and 3 off-diagonal. This matrix is necessarily symmetric only in the case of nonresonant Raman scattering.

The dependence of the molecular polarizability on the normal coordinates can be expressed in the form of the Taylor series^{1, 8}:

$$\alpha_{ij} = (\alpha_{ij})_0 + \sum_k \left(\frac{\partial \alpha_{ij}}{\partial Q_k} \right)_0 Q_k + \frac{1}{2} \sum_{k,l} \left(\frac{\partial^2 \alpha_{ij}}{\partial Q_k \partial Q_l} \right)_0 Q_k Q_l + \dots, \quad (2.11)$$

where α_{ij} is a component of the polarizability tensor, with $(\alpha_{ij})_0$ being its value at the equilibrium configuration; Q_k is the k^{th} normal coordinate associated with vibration of wavenumber $\tilde{\nu}_k$; the subscripts 0 refer to derivatives taken at the equilibrium configuration.

In order to further simplify the treatment, the double harmonic approximation is adopted, which neglects both mechanical and electrical anharmonicities. That is, on one hand, instead of equation (2.11), a linear dependence of the polarizability on each vibrational coordinate (for small amplitude motions near the equilibrium) is assumed, i.e.,^{1, 8}

$$\alpha_k = \alpha_0 + \left(\frac{\partial \alpha}{\partial Q_k} \right)_0 Q_k. \quad (2.12)$$

On the other hand, the normal vibrations are treated as being harmonic, i.e.,^{1, 8}

$$Q_k = Q_{k0} \cos 2\pi c \tilde{\nu}_k t. \quad (2.13)$$

Let us consider now the time dependence of the induced electric dipole moment μ , generated under the influence of the electric field of the incident radiation of wavenumber $\tilde{\nu}_0$ in a vibrating molecule. The variation of the electric field strength with time is given by^{1, 8}:

$$E = E_0 \cos 2\pi c \tilde{\nu}_0 t. \quad (2.14)$$

Plugging equations (2.12)-(2.14) into equation $\mu = \alpha E$ yields for the k^{th} vibration^{1, 8}:

$$\mu = \alpha_0 E_0 \cos 2\pi c \tilde{\nu}_0 t + \left(\frac{\partial \alpha}{\partial Q_k} \right)_0 \times Q_{k0} E_0 \cos 2\pi c \tilde{\nu}_0 t \times \cos 2\pi c \tilde{\nu}_k t. \quad (2.15)$$

Trigonometric transformation yields^{1, 8}:

9 Theoretical Background

$$\mu = \alpha_0 E_0 \cos 2\pi c \tilde{\nu}_0 t + \frac{1}{2} \left(\frac{\partial \alpha}{\partial Q_k} \right)_0 Q_{k0} E_0 \times [\cos 2\pi c (\tilde{\nu}_0 - \tilde{\nu}_k) t + \cos 2\pi c (\tilde{\nu}_0 + \tilde{\nu}_k) t]. \quad (2.16)$$

The three cosine functions having three different arguments in this equation mean that the induced dipole oscillates with three distinct frequencies simultaneously. Therefore it generates radiation at $\tilde{\nu}_0$ (the Rayleigh scattering) and also at wavenumbers shifted by $\pm \tilde{\nu}_k$ (the Stokes and anti-Stokes Raman scattering). These so-called beat frequencies are produced when the dipole oscillating at $\tilde{\nu}_0$ is modulated by the molecular vibration at wavenumber $\tilde{\nu}_k$.

It is now clear from equation (2.16) that derived polarizability tensor serves as the measure of the Raman activity: those vibrations for which $\alpha'_k = 0$ (meaning that all tensor components are zero) are inactive in Raman scattering, and those normal vibrations for which at least one component of α'_k differs from zero, i.e.,^{1,8}

$$(\alpha'_{ij})_k = \left(\frac{\partial \alpha_{ij}}{\partial Q_k} \right)_0 \neq 0 \quad (2.17)$$

are Raman active.¹⁻⁹

The intensity of bands in Raman spectrum of a compound is governed by the change in *polarizability*, α , that occurs during the vibration.¹⁻⁹ The intensity of any band is given by the equation (2.18)¹:

$$I_{\text{Raman}} = K I_L (\tilde{\nu}_0 - \tilde{\nu}_k)^4 \left(\frac{\partial \alpha}{\partial Q} \right)^2, \quad (2.18)$$

where I_L is the power of the laser at the sample, $(\tilde{\nu}_0 - \tilde{\nu}_k)$ is the wavenumber at which the peak is measured and $(\partial \alpha / \partial Q)$ is the change in polarizability with the normal coordinate of the vibration. The value of the constant of proportionality, K , is dependent on the efficiency at which Raman-scattered light may be collected, as well as on some other factors.

The ratio of the intensity of the anti-Stokes and Stokes Raman lines is predicted to be⁹:

$$\frac{I_{AS}}{I_S} = \frac{(\nu_0 + \nu_k)^4}{(\nu_0 - \nu_k)^4} e^{-h\nu_k/kT}, \quad (2.19)$$

where h is Planck's constant, k is Boltzmann's constant, and T is temperature in Kelvin.

The Boltzmann exponential factor is the dominant term in equation (2.19), which makes the anti-Stokes features of the spectra much weaker than the corresponding Stokes lines.

The relative intensities and polarization properties of spectral lines in scattered radiation depend on different factors, such as the scattering geometry, the orientation of the

10 *Theoretical Background*

molecule with respect to the incident light, and the state of polarization of the incident light. Determination of the state of polarization may be of great importance because it can be correlated with the symmetry of the scattering species and the symmetry of the individual vibrational modes.¹⁻⁹

We are interested in the radiant intensity I of the light scattered at an angle θ and in its polarization characteristics described by the so-called depolarization ratio ρ . The latter one can be defined in different ways. For the case of illumination with radiation polarized perpendicular to the scattering plane, it is denoted ρ_{\perp} and defined as^{1, 8}:

$$\rho_{\perp}(\theta) = \frac{{}^{\perp}I_{\parallel}(\theta)}{{}^{\perp}I_{\perp}(\theta)}, \quad (2.20)$$

where the superscript preceding I refers to the polarization of the incident radiation (perpendicular to the scattering plane for both ${}^{\perp}I_{\parallel}$ and ${}^{\perp}I_{\perp}$), and the subscript following I stands for the direction of polarization of the scattered light (parallel and perpendicular, respectively, to the scattering plane).

Similarly, if the electric vector of incident light was polarized parallel to the scattering plane, the corresponding depolarization ratio ρ_{\parallel} would be defined as^{1, 8}:

$$\rho_{\parallel}(\theta) = \frac{{}^{\parallel}I_{\perp}(\theta)}{{}^{\parallel}I_{\parallel}(\theta)}. \quad (2.21)$$

The intervals of the possible depolarization ratio values are^{1, 8}

$$0 \leq \rho_{\perp}\left(\frac{\pi}{2}\right) \leq \frac{3}{4}. \quad (2.22)$$

Depolarization results are, in principle, the same for 180° scattering when using polarized exciting radiation (i.e. $\rho_{\perp}(\pi)$) as for 90° scattering with incident light perpendicularly polarized with respect to the scattering plane ($\rho_{\perp}(\pi/2)$)^{1, 8}:

$$0 \leq \rho_{\perp}(\pi) \leq \frac{3}{4}. \quad (2.23)$$

The actual values of ρ_{\perp} are determined by the symmetry properties of the derived polarizability tensor, that reflect the symmetry of the corresponding normal mode of vibration. Thus the following cases can be distinguished¹⁻⁸:

- a) For non-totally symmetric vibrations $\rho_{\perp} = 3/4$, and such Raman bands are said to be depolarized.
- b) For totally symmetric vibrations $\rho_{\perp} < 3/4$, and such bands are said to be partially depolarized.

11 *Theoretical Background*

- c) At an extreme, for totally symmetric vibrations of molecules belonging to cubic point groups $\rho_{\perp} = 0$, and the observed band is considered completely polarized.

Before the mid-1980s, Raman spectroscopy was often considered to be less desirable than IR spectroscopy, because only one out of about 10^8 of the incident photons undergoes Raman scattering. However, the distinct advantage of Raman to IR is that in Raman, there is little or no sample preparation, and the ability to use glass optics and work in aqueous media. Therefore, samples can often be examined in the form in which they are submitted, and can usually be returned unaffected after the measurements. Furthermore, low wavenumber measurements are possible and hence, signals can be observed easily below 100 cm^{-1} . Thus, IR and Raman spectroscopy are powerful complementary tools for obtaining precise and detailed information about the structure of organolithium compounds, particularly since lasers have been developed in optical spectroscopy¹⁻⁸. The advent of multiplex (usually FT) and multichannel (monochromators with array detectors) techniques have greatly increased the sensitivity of modern Raman spectrometry.

However, the high frequency of the laser irradiation in the visible region may lead to photochemical reactions in the laser focus. Besides this, fluorescence can often cover the whole Raman spectrum. Such problems can be avoided by using an excitation wavelength in the near infrared (NIR) region, e.g. with an Nd:YAG laser operating at 1064 nm. Deficits arising from the ν^4 dependence of the Raman intensity and the lower sensitivity of NIR-detectors are compensated by the Fourier-Transform (FT) technique, which is widely spread in IR spectroscopy.^{1, 3, 10, 11}

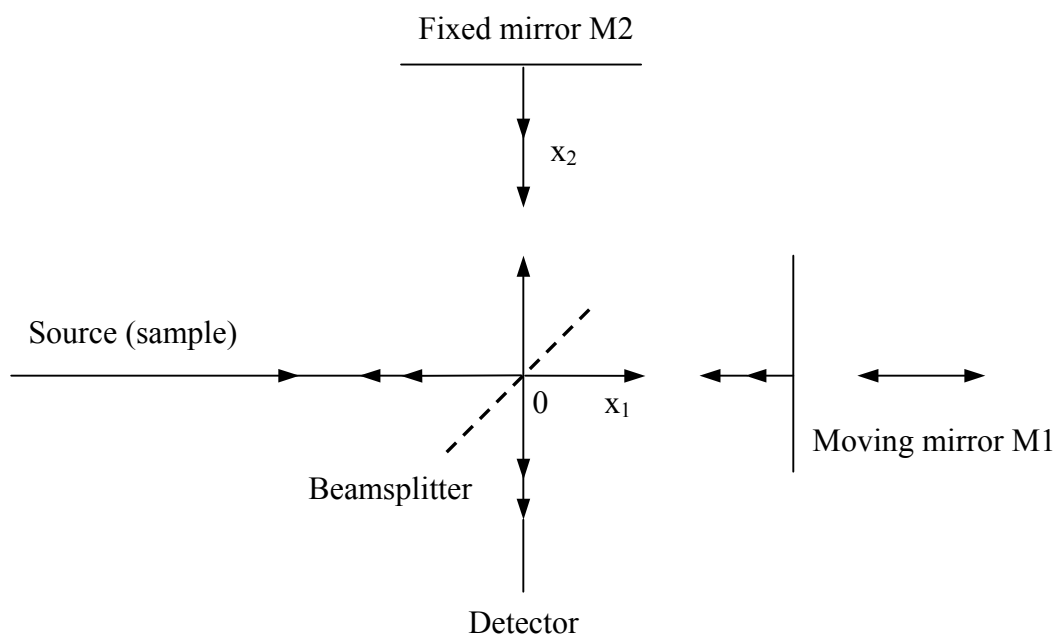


Figure 2.3. An idealized diagram of a Michelson interferometer.

The heart of each FT-Raman spectrometer is an interferometer and nowadays, all commercial FT-systems are based on a Michelson interferometer. In its simplest form, as shown in Figure 2.3, it consists of a beamsplitter, two mirrors, M1 and M2, and a means of altering the distance between one of the mirrors, M1, and the beamsplitter. To understand how the interferometer works, we consider a beam of light incident on the beamsplitter. Assuming a perfect beamsplitter, half of the light is transmitted to mirror M1 and half is reflected to mirror M2. After reflection at M1 and M2, the two rays are recombined at the beamsplitter. Again, half of the light is transmitted and half is reflected. The net effect is that half of the light is returned to the source and hence lost. Therefore, only half reaches the detector. Thus, the theoretical maximum efficiency of an interferometer is 50%. In practice, no beamsplitter is perfect and losses occur every time the light is transmitted or reflected in addition to the reflection losses at the mirrors. All of these factors conspire to reduce the efficiency below 50%.

The fact that every point in the interferogram contains information about every frequency in the spectrum constitutes the basis of the multiplex advantage, which was first described by Paul Fellgett.¹² The net effect of the Fourier transform is to obtain a wavelength dispersed spectrum without having to physically disperse the light. The absence of slits or gratings leads to the throughput advantage (or Jacquinot advantage^{13, 14}) of interferometers over dispersive instruments. Together, the two factors give a major improvement in signal-to-noise ratio (per unit time) over that obtainable from a dispersive instrument under equivalent conditions, i.e., the same laser power at the sample, detector, measurement time, resolution and scattered light collection efficiency.

2.1.2 *Surface enhanced Raman spectroscopy*

Surface enhanced Raman spectroscopy (SERS) was first demonstrated by Fleischmann and coworkers in 1974.¹⁵ They used Raman spectroscopy to study the adsorption of pyridine at a Ag electrode and strong Raman scattering was observed when the surface was electrochemically roughened. Jeanmaire and Van Duyne,¹⁶ and Albrecht and Creighton¹⁷ reported in 1977 that the Raman scattering from pyridine adsorbed on a roughened metal surface was enhanced by a factor of 10^6 compared to the equivalent scattering for the same concentration of pyridine in solution. This enhancement phenomenon was called SERS and it depended upon the surface roughness and the effective adsorption of the analyte to that surface.¹

13 *Theoretical Background*

Many of the advantages of normal Raman scattering are applicable to this technique. These include molecular specific vibrational spectra, simple versatile sampling and ready determination of analytes in air, under vacuum and in water.¹ However, using SERS, increased sensitivity is obtained and much wider concentration ranges can be studied. Detection limits are considerably lower (down to 10^{-9} mol L⁻¹) than those for resonance Raman scattering.^{18, 19} In addition to providing vibrational information, electronic information is available through surface enhanced excitation profiles.²⁰ However, in practice the sensitivity of these experiments to interference and the requirement for adsorption to specific metal surfaces has limited the development of the technique. Surface photolysis and fluorescence have proved to be a problem in some experiments.¹

Despite these difficulties, SERS has become an increasingly popular analytical tool, which has been applied to numerous fields as diverse as catalysis and forensic science.¹

The SERS phenomenon arises from an interaction between an adsorbate and the surface plasmons, which can be considered to be a wave of electrons present on the surface of the metal substrate.¹

Most of the theories proposed to explain the enhancement associated with the SERS effect can be divided into two broad categories. Those dealing with *electromagnetic (EM) enhancement mechanisms* are based on the interaction of light with matter from a spectroscopic-physical perspective. In general, EM enhancement theories predict large increases in E in the vicinity of the adsorbed molecule as a result of its proximity to a conducting surface with the “right” optical properties. Theories involving *chemical, or charge transfer (CT) enhancement mechanisms* generally propose that a chemisorbed species, either in combination with atomically small clusters of Ag atoms or through the formation of surface complexes, scatter the incident light more efficiently than the free molecule does. Therefore, chemical enhancement theories are focused on mechanisms related to increasing the molecule’s polarizability α .⁹ One theory that does not fit into these broad classifications has been proposed by Cooney and coworkers.²¹ They interpreted the large Raman signals from some species to be the result of surface laser damage leading to the concentration of the adsorbate at carbonized sites on the metal surface (intercalation).

A theory that seeks to explain SERS must account for the wide variety of experimental observations that have been reported by various groups. The following is a partial listing of many of the major observations associated with SERS-active systems that have proven to be repeatable by several independent investigations.⁹

14 *Theoretical Background*

Surface roughness. The magnitude of the surface roughness (either atomic (e.g., clusters, dislocations, steps, kink sites, and grain boundaries) scale or microscopic (≥ 5 nm)) necessary to observe SERS is still undetermined. However, Raman scattering from pyridine adsorbed to either atomically flat or step-terraced single crystal Ag surface is unenhanced.^{22, 23}

Metal specificity. By far, the largest number of SERS studies have been on Ag, and to a lesser extent, the other group IB (coinage) metals, Cu and Au. Other metals whose optical properties were used to predict enhancements that were later confirmed by experiment, are Li, Na, and K. Some reports of enhancement by Hg, Fe, Al, Ni, NiO, Pt, Pd, Rh, Ir, In, Sn, Co, Si, Ti, and TiO₂ also appeared in the literature.^{24, 25}

Adsorbate specificity. In his publication,²⁴ Seki lists over 130 different compounds that have been reported to exhibit enhancement at Ag electrode surfaces. However, most of the confirmed surface-enhanced (resonance) Raman spectroscopy active species reported so far are nitrogen- and/or sulfur-substituted Lewis bases. Generally, specifically adsorbed surfactants, polymers, colloid peptizers (e.g., gelatin), and many inorganic ions generally do not produce high S/N SERS spectra. SERS has seldom been reported in nonaqueous electrolytes. The SERS spectrum of H₂O has been obtained only in electrolytes with high molar concentrations of halides.²⁶

Wavenumbers and relative intensities. Large differences are often observed in spectral comparisons of the relative intensities of Raman bands obtained from a molecule under SERS conditions with those obtained from the same molecule in the bulk or in solution. Band-specific wavenumber shifts of about 5-20 cm⁻¹ for SERS active molecules are also common, but tend to be more system-specific than differences in relative intensities.

Selection rules. It is common for spectroscopic selection rules to be relaxed by the SERS environment to the extent that bands, which are normally both Raman and IR inactive (forbidden) for the bulk species, appear unexpectedly in the SERS spectra of a molecule.^{27, 28}

Wavelength dependence. Excitation profiles (Raman intensity of a vibrational mode versus $h\nu_0$) of SERS active species increase with decreasing wavenumber. By contrast, normal Raman intensities vary with $1/\lambda^4$.

Distance dependence. Raman scattering falls off rapidly with distance from the SERS active surface ($(a/r)^{12}$, where a is the radius of curvature of the surface roughness feature and r is the distance between the molecule and the center of the radius of the curvature).²⁹ Apparently, a molecule does not have to be in intimate contact with the metal surface to experience enhancement, although the greatest enhancements are observed from molecules within the first monomolecular layer of the surface.³⁰

Potential dependence. Both the wavenumbers and relative intensities of Raman bands from certain species adsorbed to SERS active electrode surfaces can vary with the applied potential.³¹ It is common for SERS activity to be quenched when the potential of the electrode is made more negative than the point of zero charge of the electrode metal.

Laser-assisted enhancement. The SERS activity of an electrode surface that has been oxidized and reduced while illuminated with laser light is much larger than that of a similar electrode prepared in the dark.³² Larger enhancements are also typically observed when the adsorbate molecule is present in the electrolyte solution during the oxidation-reduction cycle (ORC).

Separately, neither EM nor CT enhancement theories have been able to explain all of the experimental observations listed above. In particular, EM theories generally predict that when certain optical conditions are satisfied, all molecules at a given distance of a particular roughened metal surface should experience similar scattering enhancement resulting in a SERS spectrum resembling a normal Raman spectrum of the molecule in solution. EM theories thus fail to satisfy observations 3 and 4, and possibly 5 and 8. On the other hand, CT theories cannot fully account for either the requirement for metal roughness, observation 1, or the distance dependence of SERS, observation 7. Also, even under favorable conditions, CT theories by themselves can account for only a relatively small fraction of the total SERS observed.

2.1.2.1 Electromagnetic enhancement mechanism

According to the EM theories for rough surfaces, SERS is a result of three factors. The first is that small particle plasmon resonances, which are similar to those observed in metal sol solutions, exist on the surface of roughened metals. The second is that the dipole moment induced in the molecule is due to the EM field created by the incident light combined with the elastically scattered light resulting from resonance excitation of the metal particle surface plasmon. As a result, very high field gradients are produced when an adsorbed molecule is positioned near the tip of a surface protrusion (*lightning rod* or *antenna effect*).³³ Third, provided that the bandwidth of the optical particle resonance is wide and the Raman shift relatively small, the inelastically scattered field will be resonant or nearly resonant with the surface plasmon. Following absorption by particle, the Raman scattered field can then be amplified and reemitted by the oscillating particle dipole.

The classical treatment of small particle resonances developed by Kerker and coworkers³⁴⁻³⁹ provides considerable insight into the factors that are important in designing

16 Theoretical Background

systems tailored for SERS activity from a strictly EM perspective. The following is an overview of this treatment.

The optics of very small ($\leq \lambda_0/15$) metal colloid spheres are approximated by the expressions³⁴⁻³⁹:

$$Q_s = \frac{(8\sigma^4)}{3} \left| \frac{m^2 - 1}{m^2 + 2} \right|^2 \quad (2.24)$$

and

$$Q_a = -4\sigma \operatorname{Im} \left\{ \frac{m^2 - 1}{m^2 + 2} \right\}. \quad (2.25)$$

In these expressions Q_a and Q_s represent the fractions of light that are, respectively, adsorbed and scattered by the particle; σ is a size parameter equal to $2\pi a/\lambda$, where a is the radius of the particle and λ is the wavelength in the medium surrounding the particle; and m is the complex refractive index relative to the medium³⁴⁻³⁹:

$$m = n(1 - K_a i) \quad (2.26)$$

where n is the real refractive index and K_a is the absorption coefficient. As $m \rightarrow i\sqrt{2}$, the denominators of these expressions become very small. Accordingly, scattering and absorption of light by the particle become very efficient, i.e., resonance occurs. These equations are approximations of complex expressions with higher order series expansion terms that prevent the division by zero when $m^2 = -2$.

Silver is one of the few metals, along with Na, K, and Li, whose complex refractive indexes in the visible region of the EM spectrum satisfy the conditions for resonance as defined in the expressions above. At $\lambda_0 = 382$ nm, $m_{Ag} = 0.04 - 1.40i$ in H_2O , which explains the bright yellow color of sols composed of well-dispersed small ($a \leq 10$ nm) spherical Ag particles, i.e., the particles absorb blue light.

The modification of colloid scattering theory, which accounts for SERS, involves the effect of metal particle plasmon resonance on the emission from a molecule in the dielectric medium surrounding the particle. Assuming a monolayer of adsorbed molecules whose oscillating dipoles are normal to the surface of a small spherical particle and 90° scattering geometry, the expression for the Raman enhancement factor, $\mathcal{S}_{EM} = I_R/I_R^0$ (where I_R^0 is the Raman intensity in the absence of the sphere), due to the optical properties of the metal surface is given by³⁴⁻³⁹:

$$\mathcal{S} = \left| (1 + 2g)(1 + 2g_0) \right|^2, \quad (2.27),$$

17 *Theoretical Background*

where³⁴⁻³⁹

$$g = \frac{m^2 - 1}{m^2 + 2} \quad (2.28)$$

and

$$g_0 = \frac{m_0^2 - 1}{m_0^2 + 2}. \quad (2.29)$$

In calculating the enhancement factor, g , m , g_0 , and m_0 are evaluated at the Raman scattering (emission) frequency and at the incident (plane wave) (excitation) frequency, as indicated by the subscript. As with the isolated particle, the resonance causes the scattering yield from the system to increase dramatically. However, this expression indicates that EM resonance enhancement of the Raman emission from the system can be induced by either the excitation (laser) frequency or by the Raman emission from the adsorbed molecule itself.

Blatchford and coworkers⁴⁰ experimentally demonstrated that triphenylphosphine and pyridine adsorbed to electrochemically roughened Ag electrodes exhibit SERS excitation profiles that maximize between $\lambda_0 = 600\text{-}750$ nm. Based on the description of the EM theory outlined above for small Ag particles, it might be predicted that the largest enhancement would occur near 382 nm, where $m_{Ag} \approx i\sqrt{2}$ (in H₂O). However, this prediction assumes that the particles that promote SERS activity on the roughened electrode surfaces behave as isolated small spheres of Ag. Further refinements of the EM theory take into account the effect of both size and shape of the metal particles, as well as the dielectric constant of the medium. Generally, the best agreements with experimental excitation profiles are found using nanometer sized prolate (football-shaped) particles with high semimajor to semiminor (i.e., length to girth) axial ratios.

Systematic deviations from classical EM theory have also been observed in the excitation profiles of solutions of small metal colloid particles (sols). For sols, the peak for the maximal intensity in the SERS excitation profile is also typically red shifted relative to the λ_{max} of the sol. This behavior has been explained by the presence of large groupings (or *aggregates*) of the smaller individual spheroid particles. While the concentration of these aggregates may be too small to produce a distinct peak in the absorption spectrum, the field between aggregate particles is predicted to be considerably larger than that at the surface of a single particle.⁴¹

The largest EM enhancements are predicted for adsorption sites at the ends (i.e., smallest radius of curvature) of the particles. In extreme extensions of the particle shape

factor, SERS enhancements as large as 10^{11} have been predicted for the tips of sharp, needlelike surface protrusions. If enhancements of this magnitude are typical, then to account for experimentally measured enhancements of approximately 10^6 , the SERS active system must be populated with a relatively small number of “SERS active sites”.

Recent developments in SERS, among them the observation of SERS from single adsorbed molecules⁴²⁻⁴⁹ have, not only reinvigorated the field, but have demonstrated once again the operation of the EM mechanism. The enhancement calculated from these observations is approximately 10^{14} . This is some three to four orders of magnitude larger than what is predicted for hot spots in the interstices of aggregates or in fractal clusters. The fact that enhancements large enough to allow single-molecule spectra to be detected have only been observed for a handful of adsorbates (generally colored molecules) and unobserved for many other molecules suggests that the extra three order of enhancement is due to some form of resonance.⁵⁰

Single molecule SERS has inspired other optical observation on silver aggregates including optical non-linear effects, which should benefit especially greatly from the inordinately high EM fields at hot spots. A report of SERS-pumping of excited vibrational states has also been reported.⁵¹ Unfortunately, the explanation was found to be spurious.⁵²

2.1.2.2 Charge transfer enhancement mechanism

From the foregoing discussion on EM enhancement theory, it might be inferred that the large majority of SERS experimental observations can be satisfactorily explained by modifications of classical scattering theory to account for the effect of small particle plasmon resonances on the electric field of adsorbed molecules and vice versa. But a considerable body of experimental evidence has been acquired supporting the view that some type of chemical interaction between the adsorbed species and the SERS active surface must occur before large intensity increases in Raman scattering are observed. For example, Moskovits and DiLella⁵³ found that the Raman enhancement for CO adsorbed to cold-deposited Ag films was approximately 100 times more intense than that obtained for N₂ under identical conditions, even though the molecular polarizabilities of the molecules are virtually the same. While the surface Raman spectrum obtained from N₂ was relatively unchanged by adsorption, the Raman peak from CO was broadened and shifted by approximately 28 cm^{-1} from that of unbounded CO. Also, the absence of Raman activity from molar concentrations of species in which the SERS-active surface is immersed or embedded (e.g., H₂O or colloid stabilizers) has been used to challenge the exclusive application of EM theory to all SERS systems.

In fact, numerous studies have been carried out in order to establish or disqualify the existence of this mechanism.⁵⁴⁻⁵⁶ Its supporters also use it to explain why the enhancement factor of the first adsorbate layer is much greater than those of the subsequent layers.

In general, chemical mechanisms involve the formation of a surface complex between the substrate metal and adsorbate. The adsorbed complex may involve adsorbed metal atoms (adatoms or anions)⁵⁷ or clusters⁵⁸. In one theory of CT enhancement, Raman scattering enhancement is due to resonance involving electronic transitions to eigenstates that are created when the molecule is chemisorbed.⁵⁹ Accordingly, the differences between the Raman intensities obtained from the unbound and the adsorbed molecule are due to the changes in the polarizabilities of molecular vibrational modes that occur when new bonds are formed between the molecule and the metal surface.⁶⁰ The process is analogous to spectroscopic changes that are observed when ligands are combined with metal ions to form metal coordination complexes in solution. In support of this model, early work of Van Duyne and coworkers¹⁶ and later, in more detailed spectroscopic evaluations by Pettinger and coworkers,^{61, 62} showed that many features of a SERS spectrum from the Ag/pyridine/Cl⁻ electrochemical system could be explained by the formation of a complex involving an 1:2 pyridine/Cl⁻ complex with Ag.

All chemical enhancement theories are related to changes in the polarizability α of the metal-molecule system due to the formation of chemisorptive bonds. While the general features of EM particle-plasmon theory, which largely deals with electric field (E) enhancement, can be described in classical terms, explanation of CT enhancement theories necessarily involve quantum mechanics to describe spectroscopic changes that occur as a result of chemisorption. Consequently, it has often been easier to explain experimental results or to test enhancement theories within the framework of EM theory than to predict the outcome of an experiment using CT theory.

Lombardi and coworkers^{59, 63} demonstrated that under irradiation, charge can be transferred from an adsorbate (adcluster) complex to the metal or vice versa, depending on the excitation frequency and donor or accepted level of the adsorbate relative to the metal Fermi level. An estimate of the CT enhancement contribution to SERS activity has been obtained by Persson⁶⁴ using a quantum mechanical model based on Anderson-Newns resonances, i.e., brief excursions of metal electrons into an unfilled orbital of the chemisorbed molecule. In this model, it is assumed that the energy levels of the adsorbate are broadened to the extent that they overlap with the Fermi level E_F of the metal enabling charge flow from the metal into the lowest unoccupied orbital of the adsorbate. Persson⁶⁴ calculated the CT enhancement

factor \mathcal{G}_{CT} as the ratio of the Raman scattering intensity of the adsorbed molecule to that of the free molecule, namely,

$$\mathcal{G}_{CT} = \left| (ed)^2 \varepsilon'_a(0) G(\omega_0, \omega_S) / \alpha'(0) / 2 \right|^2, \quad (2.30)$$

where $G(\omega_0, \omega_S)$ is associated with resonance scattering due to photon-assisted CT from the metal to adsorbate; ω_0 is the incident laser frequency; ω_S is the Stokes scattered frequency; $\alpha'(0)$ is the derivative of the electronic polarizability of the free molecule with respect to the normal coordinate of the vibration (normal Raman scattering); d is the distance between the “center of charge” of orbital $|a\rangle$ of the molecule and the metal image plane; e is the charge of an electron; and $\varepsilon'_a(0)$ originates from the expansion of the energy ε_a of $|a\rangle$ in the free molecule with respect to the normal coordinate of the vibration. Using experimental values for CT resonances created by chemisorption of pyridine on Ag (111), Persson calculated a CT enhancement factor of approximately 30.

In conclusion, the EM theory predicts enhancements up to 10^{11} , while the CT theory⁶⁵ enhancements between 10 and 10^3 . Alone, neither can fully account for all of the confirmed experimental idiosyncrasies inherent to SERS. However, when taken together, EM and CT can be used with some degree of success in predicting the overall behavior of systems that exhibit SERS activity. In this regard, it is important to understand that the total SERS enhancement is very likely a *product* of the two individual enhancement mechanisms,⁹ namely,

$$\mathcal{G}_{SERS} = \mathcal{G}_{EM} \mathcal{G}_{CT}. \quad (2.31)$$

In theory, Raman excitation profiles can provide information on the nature of the SERS enhancement mechanism. Chemical enhancement theories predict that different Raman excitation profiles should be observed for different adsorbate molecules because the electron donor-acceptor levels of the adsorbate participate in the enhancement mechanism. On the contrary, EM theories predict that the SERS excitation profiles should depend on the optical and morphological properties of the metal surface and are largely independent of the adsorbate molecule.

2.1.2.3 Surface enhanced Raman scattering substrates

Since SERS was first observed from pyridine on an electrochemically roughened silver electrode,¹⁵ numerous SERS active substrates have been developed and explored for

both theoretical insights and practical applications of the effect. *Electrodes* were originally used and developments within this field are continuing.⁶⁶ *Thin metal films* roughened by chemical or mechanical means were also found to be sensitive.^{67, 68} However, the production of the films is difficult to control and hence it is difficult to obtain reproducible results.⁶⁹ *Colloidal suspensions* represent another widely used class of SERS substrates. But there are many other SERS active substrates. For example, metal colloidal particles formed upon porous membranes such as filter papers, gels, beads, polymers, etc. have been developed and investigated.^{70, 71} Although these adsorbed substrates are prepared easily, they are unpopular probably because they can be expensive and in some cases irreproducible. They involve more complicated preparations and are more susceptible to contamination.

The most common types of substrates together with their strengths and weaknesses are briefly presented below.

Electrodes. One of the principal advantages of the use of electrodes is that it is possible to control the surface potential. However, electrode pretreatment is crucial to obtain maximum SERS signals. An excellent discussion of the electrochemical techniques utilized in SERS may be found in the review of Chang and Laube⁷². In most cases, polycrystalline Ag wires or rods are sealed into an inert holder (glass or Teflon). The surface is then polished mechanically using increasingly smaller sizes of alumina powders (to 0.05 μm). This step is sometimes followed by a chemical etching procedure. For example, a mixture of ammonia⁷³ or sodium cyanide⁷⁴ and hydrogen peroxide has been used. Finally, the electrode is subjected to an oxidation-reduction cycle (ORC) in an electrochemical cell. This anodization step further cleans the electrode and also produces surface roughness. The resulting surface consists of sponge-like Ag deposits in the size range 25-500 nm.

Experimental variables in the ORC include the oxidation and reduction potentials, the type of potential-time function utilized (triangular-wave potential sweep or double potential step), and the amount of charge passed during the oxidation step. The oxidation potential is dictated by the electrolyte used. The amount of charge passed during the oxidation step has an appreciable effect upon the SERS enhancement. In the case of Ag, it has been observed that the optimum SERS signals are obtained following the passage of 20-50 mC cm^{-2} charge. This is equivalent to approximately 100-200 monolayers of Ag atoms.⁷⁵ Anodization of gold electrodes requires more positive potentials and multiple cycles for optimal SERS activity.⁷⁶

There are two other variants of electrode pretreatments that should be mentioned. First, it has been observed that cathodic treatment of the electrode prior to the anodization step can produce as much as a 10-fold increase in signal intensity.⁷⁷ The cathodization is believed

to cause reduction of organic materials on the electrode to hydrocarbons, which are then desorbed. Also, the presence of H₂ bubbles formed at the reducing potential may affect the surface morphology during the ORC of the silver surface. Second, it has also been observed that illumination of the electrode during anodization in the presence of halide can yield stronger SERS signals^{32, 78-80}. This has been attributed to partial photoreduction of the Ag⁺, which produces microstructure on the surface.

In many of the reported SERS experiments utilizing electrodes, the adsorbate was present during the anodization procedure. In some cases, it was shown that the same SERS signal intensity resulted when the adsorbate was present during anodization as when the adsorbate was added after the anodization step.⁷² However, it was found that biological samples can be very sensitive to the presence of Ag⁺ generated in the diffusion layer during the anodization step. This can lead to cleavage in covalently bound chromophores, e.g. hemes, or dissociation of non-covalently bonded substances, e.g. flavins. Protein denaturation may not be a problem if detection of a specific chromophore is the objective of the experiment. Under these conditions, enhanced sensitivity may be observed when the anodization is performed in the presence of the biomolecule. If, on the other hand, the goal is to monitor a biologically active substance, the adsorbate should be added after the anodization step.

Electrochemical SERS has been extensively investigated to obtain a better understanding of the surface and of the key process, such as prevention of copper corrosion, and as a detector for chromatography.^{81, 82} The main disadvantage of the technique is the reproducibility of the electrode surface. It is incredibly difficult to ensure that the same degree of surface roughness and potential is achieved for each experiment. This may result in different degrees of surface enhancement. Additionally, selection rules depend upon the analyte adsorption process and orientation. Therefore the surface chemistry must be closely controlled.

Colloids. A second frequently used substrate is the metal sol. Chemical reduction of silver, copper, or gold salts, has been used to produce the colloidal state. These systems are easy to prepare, and this is an attractive feature for the non-electrochemist. Furthermore, the ability to flow the colloid through the laser beam or stir the solution is another particularly attractive feature of colloids in overcoming sample degradation that can result during static experiments at electrode surfaces because of photochemical or thermal effects. Other advantages of the colloidal suspensions (Ag or Au sols) include the ability to compare the morphology with the theory, the defined surface area, the ability to control the particle size and shape, and the ability to directly measure the extinction spectrum.⁹

However, the use of sols suffers from several disadvantages. These include instability caused by the tendency of the colloid particles to aggregate and settle out of solution, especially when an adsorbate is added. This can be avoided by adding stabilizers,^{83, 84} by utilizing more elaborate preparation,⁴¹ or by sedimentation classification⁸⁵ schemes, which permit the preparation of smaller and more homogeneous particle sizes. Another problem is the inability to control the surface potential, which depends upon the solution potential and can vary considerably from one method to another or with time for a given method. This is a very important aspect, taking into account that the effect of the sol surface potential on the SERS spectrum of a biological species can be significant.^{86, 87}

Several methods were suggested for the preparation of the well-known silver colloid. Each produces silver particles of different diameters and uniformities.⁸⁸⁻⁹⁰ The Carey-Lea preparation is reported to produce particles with diameters in the range 14-22 nm,⁸⁸ whereas Creighton and coworkers obtained particles with diameters of 18-22 nm⁸⁹. However, both substrates were relatively unstable. One process that yields reproducible and reliable results is a controlled citrate reduction of silver nitrate, originally reported by Lee and Meisel⁹⁰ and modified by Munro and coworkers⁹¹. It produces monodispersed colloidal particles with a diameter of 28 nm. The difference in colloidal particle size may account for the varying stability of colloid preparations. There is a natural tendency for small particles to reduce their surface area and energy in a bid to increase their stability by self-aggregating. As a Lee and Meisel colloid has a lower surface area and energy than colloids prepared by other methods, it is less likely to self-aggregate.

The effectiveness of surface enhancement depends on efficient adsorption of the analyte to the Ag surface. Positively charged analytes will adsorb readily to the colloid surface, although problems with neutral and negatively charged analytes arised. This problem may be overcome by the introduction of surface modifiers.¹

Aggregating the colloidal particles⁹² can further increase the SERS enhancement. The act of aggregation forms clusters of colloid, within which are interstices. The electric field established in these regions is predicted to be very large; hence the surface enhancement experienced from this is very intense. Many different methods of aggregation have been suggested including acids, salts, and surfactants even using the analyte itself to induce aggregation.⁹³⁻⁹⁵ This aggregation process is detected by a change in color of the colloidal suspension and a bathochromic shift of the absorbance maximum.

Metal films. The third, very popular, substrate for SERS is the thin metal film. Generally, these substrates are easy to prepare, compact, transportable, and stable. A further

potential advantage over other types of SERS active substrates is the possibility to experimentally “tune” these SERS substrates for optimal enhancement at a desired excitation frequency by proper choice of the metal film preparation conditions.⁹⁶

The most representative of these are the island films, the coldly deposited films in ultrahigh vacuum, and the lithographically prepared substrates, since results obtained with these systems have been extensively used in fundamental studies aimed at pointing the origins of the SERS effect. Of these we will present in some detail, the island films, which we used in our experiments.

Metal island films are prepared by vapor depositing 50-150 Å equivalent mass thickness of metal on a substrate (usually quartz or glass) at room temperature and under high vacuum conditions.⁹⁷ When the metal atoms impinge on the surface, they have sufficient mobility to nucleate and form island structures, rather than an uniform overlayer of metal atoms. The morphology and topography of evaporated metal films depend on several factors including the amount of metal deposited, type of substrate, temperature of the substrate, deposition rate, angle of incidence of the metal atoms with respect to the surface, pressure and composition of the background gas in the vacuum system. Once the film is deposited, the annealing conditions (annealing temperature, rate of heating to annealing temperature, and the time of annealing) can cause the initial film structure to change dramatically. Morphologies of several metal island films structures have been examined by scanning electron microscopy and scanning transmission microscopy.^{98, 99} The structure of the films was shown to vary with deposition rate.⁹⁸ Slow rates produced more strongly aggregated films with more intense color, whereas rapid deposition produced thinner structures that were more uniformly distributed on the substrate. These differences in structure were rationalized in terms of atom migration on the surface. Higher temperatures of the substrates were also found to lead to increased aggregation. The structure of Au films was found to be very similar to that of Ag films, but Cu films were not as regular as the other metals studied. In addition to Ag, Au, and Cu, island films of Ni, Pt, and In have also been examined with respect to their SERS activities.^{100, 101}

2.2 *Density functional theory*

2.2.1 *The Kohn-Sham approach*

Density functional theory (DFT)¹⁰²⁻¹⁰⁵ is based on the Hohenberg-Kohn theorem,¹⁰⁶ which states that the total energy of a system in its ground state is a functional of that system's electronic density, $\rho(r)$, and that any density, $\rho'(r)$, other than the true density will necessarily lead to a higher energy. Therefore, the Hohenberg-Kohn theorem introduces an alternative approach to performing exact, variational, *ab initio* electronic structure calculations. In conventional *ab initio* methodology,¹⁰⁴ Schrödinger's equation

$$H\psi = E\psi \quad (2.32)$$

must be solved. Meanwhile, DFT requires only that we minimize the energy functional, $E[\rho(r)]$. The conceptual simplification thus offered cannot be overstated. Rather than working with a complex $3N$ -dimensional wavefunction, ψ , describing the behavior of each electron in an N -electron system, DFT allows us to work with a simple three-dimensional function, the total electronic density. Unfortunately, the exact nature of the energy functional is not known, and the total energy of a system cannot be simply output when a trial density, $\rho'(r)$, is given as input. Therefore, we must turn to approximate DFT methods, and though we will not have a wavefunction, we will have to make use of one-electron Kohn-Sham¹⁰⁷ molecular orbitals, which rather closely resemble molecular orbitals from the well-known Hartree-Fock (HF) method.^{108, 109}

Early applications of DFT tended to be within the physics community, concentrating on systems where the HF approximation is a particularly poor starting point.¹¹⁰ Therefore, the vast majority of the applications were on metallic systems, because a single determinantal approach is notoriously bad in such cases. Since DFT works with the density, and not the wavefunction, systems that would require a great number of electronic configurations to be well described by conventional *ab initio* approaches are in principle neither harder nor more expensive, for DFT than the systems that are well described by a single configuration. Correlation effects, absent within the HF approximation, are also built into the approximate energy functionals used in modern DFT applications. Therefore, DFT methods are in principle able to treat the entire periodic table with unvarying ease and accuracy.

Though the Hohenberg-Kohn theorem clearly established that one could, in principle, work directly with the density in *ab initio* calculations, it was the subsequent work of Kohn and Sham (KS)¹⁰⁷ that offered a practical approach to perform DFT calculations. In the KS

approach, the unknown Hohenberg-Kohn energy functional, $E[\rho(r)]$, is partitioned in the following manner^{104, 107}:

$$E[\rho(r)] = U[\rho(r)] + T[\rho(r)] + E_{XC}[\rho(r)]. \quad (2.33)$$

In this partitioning scheme, $U[\rho(r)]$ is simply the classical electrostatic energy, the sum of the electron-nucleus attractions and the electron-electron repulsions^{104, 107}:

$$U[\rho(r)] = \left(\sum_A \int \frac{-Z_A \rho(r)}{|r - R_A|} dr \right) + \frac{1}{2} \iint \frac{\rho(r)\rho(r')}{|r - r'|} dr dr'. \quad (2.34)$$

The next term, $T[\rho(r)]$, is defined as the kinetic energy of a system of noninteracting electrons with the same density, $\rho(r)$, as that of the real system of interacting electrons being studied. This may seem to introduce a severe error. However, this is not the case, because the final term, $E_{XC}[\rho(r)]$, is made to contain, in addition to the exchange and correlation (XC) contributions to the energy, the difference between $T[\rho(r)]$ and the true electronic kinetic energy of the system.

Following Kohn and Sham, $\rho(r)$ of an N -electron system (with N^α spin up electrons and N^β spin down electrons) is expressed as the sum of the square moduli of single occupied, orthonormal Kohn-Sham molecular orbitals,^{104, 107}

$$\rho(r) = \rho^\alpha(r) + \rho^\beta(r) = \sum_i^{N^\alpha} |\psi_i^\alpha(r)|^2 + \sum_i^{N^\beta} |\psi_i^\beta(r)|^2. \quad (2.35)$$

Having done this, $T[\rho(r)]$ can now be defined as^{104, 107}

$$T[\rho(r)] = \sum_{\sigma=\alpha,\beta} \sum_i^{N^\sigma} \int \psi_i^\sigma(r) \frac{-\nabla^2}{2} \psi_i^\sigma(r) dr. \quad (2.36)$$

One should note that $T[\rho(r)]$ is not a true density functional, because the KS orbitals are required. Alternate forms of $T[\rho(r)]$ that depend only on the electronic density and do not require KS orbitals have been proposed.¹⁰² However, they are too imprecise to be of any practical use in chemistry.

Finally, recalling the fact that the energy functional is minimized by the true ground state density, $\rho(r)$, the energy functional $E[\rho(r)]$ must be stationary with respect to any arbitrary variation in either of the spin densities, i.e.,^{104, 107}

$$\frac{\delta E[\rho(r)]}{\delta \rho^\alpha(r)} = \frac{\delta E[\rho(r)]}{\delta \rho^\beta(r)} = 0. \quad (2.37)$$

This condition yields the one-electron KS equations,^{104, 107}

$$\left\{ \frac{-\nabla^2}{2} - \left(\sum_A \frac{Z_A}{|r - R_A|} \right) + \int \frac{\rho(r')}{|r - r'|} dr' + \frac{\delta E_{XC}[\rho(r)]}{\delta \rho^\sigma(r)} \right\} \psi_i^\sigma(r) = \epsilon_i \psi_i^\sigma(r),$$

$$\sigma = \alpha, \beta. \quad (2.38)$$

Thus, a scheme for performing practical DFT calculations emerges. With an initial guess at the total spin densities, $\rho^\alpha(r)$ and $\rho^\beta(r)$, the KS equations are constructed and solved, and the resulting set of KS-orbitals, $\{\psi_i^\sigma(r)\}$, are then used to generate new guesses at $\rho^\alpha(r)$ and $\rho^\beta(r)$. This procedure is repeated until self-consistency is achieved, that is, the same densities and KS orbitals are regenerated.

In this preceding discussion, we avoided to deal with the precise nature of the XC energy functional, $E_{XC}[\rho(r)]$, and the XC potentials, which are the functional derivatives of $E_{XC}[\rho(r)]$ with respect to $\rho^\alpha(r)$ and $\rho^\beta(r)$; $v_{XC}^\alpha(r)$ and $v_{XC}^\beta(r)$ are formally given by:¹⁰⁴

$$v_{XC}^\sigma(r) = \frac{\delta E_{XC}[\rho(r)]}{\delta \rho^\sigma(r)}. \quad (2.39)$$

If the true XC energy functional, $E_{XC}[\rho(r)]$, were known, this scheme would yield the true ground state density, and in turn, exact values for all ground state properties. Unfortunately, the precise nature of $E_{XC}[\rho(r)]$ is not known, and at the first glance, it may seem that we are no further along to performing practical DFT calculations than when we had only the Hohenberg-Kohn theorem and an unknown total energy functional, $E[\rho(r)]$. However, very simple approximations to $E_{XC}[\rho(r)]$ can, perhaps surprisingly to some, yield fairly accurate results. The KS approach is therefore of great practical importance and has become the cornerstone of all modern DFT applications.

2.2.2 Exchange and correlation energy functionals

Since the quality of any DFT calculation is limited by the quality of its approximation to the true XC energy functional, $E_{XC}[\rho(r)]$, it is not surprising that a great deal of effort has been invested in the development of ever more sophisticated XC functionals. Fortunately, one of the simplest and most popular approximations of $E_{XC}[\rho(r)]$, the Local Spin Density Approximation (LSDA),¹¹¹ is capable of yielding results that favorably compete with those obtained using HF calculations.^{105, 112-116} In the LSDA, $E_{XC}[\rho(r)]$ is approximated by:^{104, 111}

$$E_{XC}[\rho(r)] = \int \rho(r) \epsilon_{XC}(\rho^\alpha(r), \rho^\beta(r)) dr, \quad (2.40)$$

where $\epsilon_{XC}(\rho^\alpha(r), \rho^\beta(r))$ is the XC energy density at a point r in the space. Within the LSDA, ϵ_{XC} is just a function of $\rho^\alpha(r)$ and $\rho^\beta(r)$ at that specific point r in space. When $E_{XC}[\rho(r)]$ is expressed in such a fashion, the XC potentials, $v_{XC}^\sigma(r)$, from equation (2.39) are given by:^{104, 111}

$$v_{XC}^{\sigma}(r) = \rho(r) \frac{d \in_{XC}(\rho^{\alpha}(r), \rho^{\beta}(r))}{d\rho^{\sigma}(r)} + \in_{XC}(\rho^{\alpha}(r), \rho^{\beta}(r)), \quad \sigma = \alpha, \beta. \quad (2.41)$$

The heart of the LSDA is the approximation that a particular point in space of an inhomogeneous distribution of electrons with densities $\rho^{\alpha}(r)$ and $\rho^{\beta}(r)$ has the same values of \in_{XC} , v_{XC}^{α} , and v_{XC}^{β} as those of any point in a homogeneous distribution of electrons of the exact same densities ρ^{α} and ρ^{β} . The value of $\in_{XC}(\rho^{\alpha}(r), \rho^{\beta}(r))$ has been determined for a large number of homogeneous gases of interacting electrons of varying total density, $\rho = \rho^{\alpha} + \rho^{\beta}$, and net spin density, $\rho^S = \rho^{\alpha} - \rho^{\beta}$, by means of quantum Monte Carlo methods^{117, 118}. The results have since been parameterized by Vosko, Wilk, and Nusair (VWN)¹¹¹ and by Perdew and Zunger (PZ),¹¹⁹ in such a way that the XC potentials can be easily evaluated via equation (2.41).

Though this may seem to be a crude approximation, theoretical considerations¹²⁰ do justify the LSDA's ability to provide quantitatively accurate geometries, charge distributions, and vibrational spectra on a wide variety of systems.^{105, 112-116} It should not be surprising to see the LSDA results surpass HF and even challenge correlated post-HF methods. One must remember that correlation effects are included within the LSDA XC functional. Systems that prove to be extremely problematic in HF theory, where correlation effects are by definition absent, are therefore not necessarily systems that offer any great challenge to the LSDA.

The most troubling aspect of the LSDA is its systematic overestimation of binding energies.^{116, 121, 122} For general chemistry, this means that the LSDA is not particularly well suited for thermochemical applications such as computing atomization energies, heats of reactions, or activation energies. For weakly bound systems, such as hydrogen-bonded systems¹²³ or van der Waals complexes,¹²⁴ the overestimation of the strength of certain interactions can disrupt what is often a delicate balance of forces, driving a system to a geometry that is in very poor agreement with the experiment. For a great deal of biomolecular applications this flaw is fatal.

For such applications, one must therefore go beyond the LSDA and adopt gradient-corrected XC energy functionals. The XC energy functional still has the general form of equation (2.40), but as the name suggests, the gradients of $\rho^{\alpha}(r)$ and $\rho^{\beta}(r)$ appear so that $E_{XC}[\rho(r)]$ is now given by:¹⁰⁴

$$E_{XC}[\rho(r)] = \int \rho(r) \in_{XC}(\rho^{\alpha}(r), \rho^{\beta}(r), \nabla\rho^{\alpha}(r), \nabla\rho^{\beta}(r)) dr. \quad (2.42)$$

Unfortunately, once we go to gradient-corrected functionals, the conceptual simplicity of the LSDA is lost and various methods may be adopted. Consequently, many gradient-corrected XC energy functionals have been proposed.¹²⁵⁻¹³⁰

Even though gradient-corrected XC functionals are local functionals (the values of $\epsilon_{XC}(r)$, $v_{XC}^{\alpha}(r)$, and $v_{XC}^{\beta}(r)$ at any point in space depend only on the values and derivatives of $\rho^{\alpha}(r)$ and $\rho^{\beta}(r)$ at that precise point in space), they do impose a significantly greater computational burden than the LSDA functionals do. Derivatives of $\rho^{\alpha}(r)$ and $\rho^{\beta}(r)$ must now be evaluated before $\epsilon_{XC}(r)$, $v_{XC}^{\alpha}(r)$, and $v_{XC}^{\beta}(r)$ can be synthesized. Fortunately, experience has shown that it is often not essential to include gradient corrections in the course of the self-consistent procedure.¹³¹ In other words, the KS equations can be iteratively solved using LSDA XC potentials. Once self-consistency is achieved, one should calculate the total energy and the forces acting on the atoms, the derivatives of the LSDA SCF density are evaluated and plugged into the gradient-corrected forms of $\epsilon_{XC}(r)$, $v_{XC}^{\alpha}(r)$, and $v_{XC}^{\beta}(r)$. Thus, gradient corrections are simply treated in a perturbative fashion. This simplification essentially renders gradient-corrected DFT calculations as inexpensive as their LSDA counterparts.

It has been suggested that the LSDA's propensity for generating hydrogen bonds that are too short and therefore too strong arises from the fact that the LSDA electronic densities decay too abruptly in the outer regions.¹³² However, the perturbative approach to incorporating gradient corrections does not alter the LSDA electronic structure, yet repairs the poor LSDA hydrogen bond lengths and strengths. The key would therefore seem to be the evaluation of the gradient-corrected XC functionals regarding the contribution of the tail regions to the XC energy, and not corrections to the electronic structure of the tail regions, as suggested.¹³²

The gradient-corrected exchange and correlation energy functionals are typically formulated so as to address either the exchange or the correlation component of $E_{XC}[\rho(r)]$. Popular gradient-corrected exchange functionals are those of Perdew and Wang¹²⁵ and Becke¹²⁷. Perdew's gradient-corrected correlation functional¹²⁶ has been extensively used, as that of Miehlich, Savin, Stoll, and Preuss has,¹²⁸ which is a reformulation of the Lee, Yang, and Parr correlation functional¹³³. Since each functional addresses a specific component of $E_{XC}[\rho(r)]$, any of the two exchange functionals can be coupled with any two of the correlation functionals. One of the most used functionals of this type is the coupled exchange and correlation gradient-corrected functional of Perdew and Wang.¹²⁵

Despite their often radically different forms, no particular gradient-corrected XC functional has emerged as being clearly superior. Partially, this may be due in part to the fact that the LSDA is very often a very good starting point: gradient corrections have little to correct. However, one promising example is Becke's, ^{134, 135} where the exact exchange energy, obtained in the same fashion as that of an HF calculation but with the KS orbitals replacing the HF orbitals, the LSDA XC energy, and gradient corrections to the LSDA XC energy are all mixed together to create a new XC energy functional.

2.2.3 *Basis set effects*

A basis set is the mathematical description of the orbitals within a system (which in turn combine to approximate the total electronic wavefunction) used to perform the theoretical calculation. Larger basis sets approximate the orbitals more accurately by imposing fewer restrictions on the location of the electrons in space. In the true quantum mechanical picture, electrons have a finite probability of existing anywhere in space. This limit corresponds to a infinite basis set expansion.

2.2.3.1 *Slater and Gaussian type orbitals*

There are two types of basis functions (also called *Atomic Orbitals*, AO, although in general they are not solutions to an atomic Schrödinger equation) commonly used in electronic structure calculations: *Slater Type Orbitals* (STO) and *Gaussian Type Orbitals* (GTO). The STOs have the functional form ^{103, 136}

$$\chi_{\zeta,n,l,m}(r, \theta, \varphi) = NY_{l,m}(\theta, \varphi)r^{n-1}e^{-\zeta r}, \quad (2.43)$$

where N is a normalization constant and $Y_{l,m}$ s are the usual spherical harmonic functions (angular momentum part). r , θ , and φ are the spherical coordinates and ζ is called the “orbital exponent”. n , m , and l are the quantum numbers: principal, angular momentum, and magnetic, respectively. The exponential dependence on the distance between the nucleus and the electron mirrors recalls the hydrogen atom orbitals. However, STOs do not have any radial nodes, nodes in the radial part are introduced by making linear combinations of STOs. The exponential dependence ensures a fairly rapid convergence with an increasing number of functions. However, the calculation of three- and four-centre two-electron integrals cannot be performed analytically. STOs are primarily used for atomic and diatomic systems where high accuracy is required, and in semi-empirical methods where all three- and four-centre integrals are neglected.

GTOs¹³⁷ can be written in terms of polar or Cartesian coordinates.^{103, 137}

$$\begin{aligned}\chi_{\zeta,n,l,m}(r, \theta, \varphi) &= NY_{l,m}(\theta, \varphi)r^{(2n-2-l)}e^{-\zeta r^2} \\ \chi_{\zeta,l_x,l_y,l_z}(x, y, z) &= Nx^{l_x}y^{l_y}z^{l_z}e^{-\zeta r^2},\end{aligned}\quad (2.44)$$

where the sum of l_x , l_y , and l_z determines the type of orbital. For example $l_x + l_y + l_z = 1$ is a p-orbital. Although a GTO appears similar in the two sets of coordinates, there is a subtle difference. A d-type GTO written in terms of the spherical functions has five components ($Y_{2,2}$, $Y_{2,1}$, $Y_{2,0}$, $Y_{2,-1}$, $Y_{2,-2}$), but there appear to be six components in the Cartesian coordinates (x^2 , y^2 , z^2 , xy , xz , yz). However, the later six functions may be transformed to the five spherical d-functions and one additional s-function ($x^2 + y^2 + z^2$). Similarly, there are 10 Cartesian f-functions, which may be transformed into seven spherical f-functions and one set of spherical p-functions. When only one d-function is present per atom, the saving obtained by removing the extra s-function is small, but if many d-functions and/or higher angular moment functions (f-, g-, h-, etc. functions) are present, the saving can be substantial. Furthermore, the use of only the spherical components reduces the problems of linear dependence for large basis sets.

The r^2 dependence in the exponential makes the GTO inferior to the STOs in two aspects. At the nucleus the GTO has zero slope, in contrast to the STO, which has a ‘‘cusp’’ (discontinuous derivative), and GTOs have problems representing the proper behavior near the nucleus. The other problem is that the GTO falls off far from the nucleus too rapidly in comparison with an STO. Consequently, the ‘‘tail’’ of the wavefunction is represented poorly. Both STOs and GTOs can be chosen to form a complete basis, but the above considerations indicate that more GTOs are necessary for achieving a certain accuracy in comparison with STOs. However, the increase in the number of basis functions is more than compensated for by the ease by which the required integrals can be calculated. In terms of computational efficiency, GTOs are therefore preferred, and used almost universally as basis functions in electronic structure calculations. Furthermore, essentially all applications take the GTOs to be centred at the nuclei. For certain types of calculation the center of a basis function may be taken not to coincide with a nucleus, for example being placed at the center of a bond.¹⁰³

Gaussian primitives are usually obtained from quantum calculations on atoms, i.e., Hartree-Fock plus some correlated calculations. Typically, the exponents are varied until the lowest total energy of the atom is achieved.¹³⁸ In some cases, the exponents are optimized independently. In others, they are related to each other by an equation, and the parameters in this equation are optimized, e.g. even-tempered or ‘‘geometrical’’ and well-tempered basis sets. The primitives derived this way describe isolated atoms and cannot accurately describe

deformations of atomic orbitals brought by the presence of other atoms in the molecule. Basis sets for molecular calculations are therefore frequently augmented with other functions. For molecular calculations, these Gaussian primitives (PGTOs) have to be contracted, i.e., certain linear combinations of them will be used as basis functions. The term contraction means “a linear combination of Gaussian primitives to be used as basis function”:¹⁰³

$$\chi(\text{CGTO}) = \sum_i^k a_i \chi_i(\text{PGTO}). \quad (2.45)$$

Such a basis function will have its coefficients and exponents fixed. The contractions are called Contracted Gaussian Type Orbitals (CGTO). A contraction is especially useful for orbitals describing the inner (core) electrons, because they require a relatively large number of functions to represent the wave function cusp near the nucleus, and furthermore are largely independent of the environment. Contracting a basis set will always increase the energy, because it is a restriction of the number of variational parameters. It will make the basis set less inflexible, but it will also reduce the computational costs significantly.

The *degree of contraction* is the number of PGTOs entering the CGTO, typically varying between 1 and 10. The specification of a basis set in terms of primitive and contracted functions is given by the notation (10s4p1d/4s1p) \rightarrow [3s2p1d/2s1p]. The basis in parentheses is the number of primitives with heavy atoms (first row elements) before the slash and hydrogen after. The basis in the square brackets is the number of contracted functions. But this will not tell how the contraction is done, it only indicates the size of the final basis (the size of the variational problem in HF calculations).¹⁰³

The way the contractions are derived is not easy to summarize. Moreover, it depends upon the intended use for the basis functions. Some basis sets are good for geometry and energies, some are aimed at properties, e.g. polarizability, some are optimized only with the Hartree-Fock in mind, and some are tailored for correlated calculations. Finally, some are good for anions and other for cations and neutral molecules. For some calculations, a good representation of the inner orbitals is necessary, while others require the best possible representation of valence electrons.

Below is a short description of the basis sets, which we used in the calculations.

2.2.3.2 Pople style basis sets

STO-nG basis set (*Slater Type Orbital* consisting of n PGTOs). This is a minimum type basis where the exponents of the PGTO are determined by fitting them to the STO, rather than optimizing them by a variational procedure. Although basis sets with $n = 2-6$ have been

derived, it has been found that using more than three PGTOs to represent the STO gives little improvement, and the STO-3G basis is a widely used minimum basis. This type of basis set has been determined for many elements in the periodic table. The designation of the carbon/hydrogen STO-3G basis is $(6s3p/3s) \rightarrow [2s1p/1s]$.

k-nlmG basis sets. These basis sets have been designed by Pople and coworkers, and are of the split valence type, with the k in front of the dash indicating how many PGTOs are used for representing the core orbitals. The nlm after the dash indicates both how many functions the valence orbitals are split into and how many PGTOs are used for their representation. Two values (e.g. nl) indicate a split valence, while three values (e.g. nlm) indicate a triple split valence. The values before the G (for Gaussian) indicate the s- and p-functions in the basis. The polarization functions are placed after the G. This type of basis sets has a further restriction in that the same exponent is used for both the s- and p-functions in the valence. This increases the computational efficiency, but of course decreases the flexibility of the basis set. The exponents in the PGTO have been optimized by variational procedures.

3-21G. This is a split valence basis, where the core orbitals are a contraction of three PGTOs, the inner part of the valence orbitals is a contraction of two PGTOs and the outer part of the valence is represented by one PGTO.¹³⁹ The designation of the carbon/hydrogen 3-21G basis is $(6s3p/3s) \rightarrow [3s2p/2s]$. We should mention that the 3-21G basis contains the same number of primitive GTOs as the STO-3G, however, it is much more flexible as there are twice as many valence functions which can freely combine to make MOs.

6-31G. This is also a split valence basis set, where the core orbitals are a contraction of six PGTOs, the inner part of the valence orbitals is a contraction of three PGTOs and the outer part of the valence represented by one PGTO.¹⁴⁰ The designation of the carbon/hydrogen basis is $(10s4p/4s) \rightarrow [3s2p/2s]$. In terms of contracted basis functions it contains the same number as 3-21G, but the representation of each functions is better since more PGTOs are used.

6-311G. This is a triple split valence basis, where the core orbitals are a contraction of six PGTOs and the valence split into three functions, represented by three, one, and one PGTOs, respectively.¹⁴¹

Diffuse and/or polarization functions can be added to each of the basis sets.¹⁴²

Diffuse functions are normally s- and p-functions and consequently go before the G. They are denoted + or ++, with the first + indicating one set of diffuse s- and p-functions on heavy atoms, and the second + indicating that a diffuse s-function is also added to hydrogen atoms. They allow orbitals to occupy a larger region of space. Basis sets with diffusion functions are important for systems where electrons are relatively far from nucleus: molecules

with lone pairs, anions, and other systems with significant negative charge, systems in their excited states, systems with low ionization potentials, descriptions of absolute acidities, and so on.

Polarization functions are indicated after the G, with a separate designation for heavy and hydrogen atoms. Split valence basis sets allow orbitals to change size, but not change shape. Polarized basis sets remove this limitation by adding orbitals with angular momentum beyond what it is required for the ground state for the description of each atom.

6-31+G(d). This is a split valence basis with one set of diffuse sp-functions on heavy atoms only and a single d-type polarization function on heavy atoms.

6-311++G(2df,2pd). This is similarly a triple split valence with additional diffuse sp-functions, and two d- and one f-functions on heavy atoms and diffuse s- and two p- and one d-functions on hydrogen atoms.

6-311++G(3df,3pd). This is the largest standard Pople style basis set.

These types of basis sets have been derived for hydrogen and the first row elements, and some of the basis sets have also been derived for the second and higher row elements.

2.2.4. *Population analysis and electron densities*

The physical meaning of the wavefunction is manifest in the square of the wavefunction: the probability of locating an electron at a given position r is given by the square of the wavefunction at that point:¹⁴³

$$\rho(r) = |\psi(r)|^2. \quad (2.46)$$

This electron density $\rho(r)$ can be expressed in terms of molecular orbitals (MO) (assuming doubly occupied MOs):¹⁴³

$$\rho(r) = 2 \sum_i^{N/2} |\phi_i(r)|^2. \quad (2.47)$$

Integration of the density over all space results in the total number of electrons in the system N (equation (2.48)):¹⁴³

$$\int dr \rho(r) = 2 \sum_i^{N/2} \int dr |\phi_i(r)|^2 = N. \quad (2.48)$$

The fundamental quest for the computational chemist is the extraction of chemically meaningful concepts from the wavefunction, taking into account that the electron density ρ does not directly supply the classical chemical notions. The computational approaches to interpret the wavefunction (*population analysis*) have split along two basic approaches.

The orbital-based method. The earliest procedures were based on distributing the electrons between the atoms in a molecule based on the occupancy of the atomic orbitals.

The spatially-based method. The major alternative approach is to subdivide physical space into regions that define the volume occupied by each atom in a molecule. Then, all electrons that are found in this volume are assigned to that atom. One simply integrates ρ within an atomic basin. The problem is to define the extent of the atomic basin.

However, some other methods for determining the atomic charge have been developed. Neither of them makes reference either to orbitals or to the space associated with a given atom. Two of them involve the calculation of the atomic polar tensor, and the fitting of the electrostatic potential to an expansion of charges at the atomic nuclei, respectively.¹⁴³

The *natural population analysis* (NPA), which we implied in the calculations and will briefly be described below, is a major procedure of the orbital-based method. It was developed by Reed, Weinstock, and Weinhold,¹⁴⁴⁻¹⁴⁶ and attempts to define atomic orbitals based on the molecular wavefunction, thereby obtaining different atomic orbitals depending on the chemical environment.

The NPA method is based on an analogy to natural orbitals first defined by Löwdin.¹⁴⁷ Suppose we have a many-electron wavefunction ϕ that is composed of many Slater determinants Γ_α . The product P is the probability of simultaneously finding electron 1 at x_1 , electron 2 at x_2 , etc.¹⁴³

$$P = \phi(x_1, x_2, \dots, x_N) \phi(x_1, x_2, \dots, x_N) \quad (2.49)$$

We are normally interested just in the probability of finding one electron regardless of the location of the remaining electrons. Integration over coordinates x_2, \dots, x_N leads to the reduced density function $P(x_1)$:¹⁴³

$$P(x_1) = \int dx_2, \dots, x_N, \phi(x_1, x_2, \dots, x_N) \phi(x_1, x_2, \dots, x_N). \quad (2.50)$$

This can be generalized to the first-order reduced density matrix $\gamma(x_l, x'_l)$ that depends on two continuous variables:^{108, 143, 148, 149}

$$\gamma(x_1, x'_1) = \int dx_2, \dots, x_N, \phi(x_1, x_2, \dots, x_N) \phi(x'_1, x_2, \dots, x_N). \quad (2.51)$$

The reduced density matrix can be converted into a discrete representation that involves sums over all the Slater determinants, MOs, and basis functions. This matrix will in general have many off-diagonal elements. The matrix is Hermitian. Therefore it can be diagonalized. The orbitals that result from the diagonal reduced-density matrix are called natural orbitals, and

the diagonal elements are the occupation numbers for these orbitals. The natural orbitals are orthonormal molecular orbitals having maximal occupancy.

By analogy, the natural atomic orbitals are the atomic orbitals having maximal occupancy and are obtained as eigenfunctions of atomic subblocks of the density matrix, instead of the entire density matrix. The trick is to define these subblocks and then obtain eigenfunctions that are orthonormal not only with the subblock, but with all other eigenfunctions.

The NPA¹⁴⁴ procedure begins by partitioning the density and overlap matrices into (Alm) subblocks, where A denotes the atom, l is the angular momentum, and m denotes the particular symmetry element of l . After averaging over the $2l + 1$ symmetry elements, these subblocks are independently diagonalized, forming pre-natural atomic orbitals (NAO). The pre-NAOs give the most compact description of the atomic density about the center, but the pre-NAOs of one center will overlap the pre-NAOs of other centers, leading to many of the same orbital population problems that plague Mulliken analysis.^{143, 149-153}

The next step is to remove the interatomic overlap and still preserve the atomic nature of the orbitals. The pre-NAOs are separated into two classes. The pre-NAOs with the highest occupancy are called the natural minimal basis (NMB), and all other orbitals are called the natural Rydberg basis (NRB). The NRB set is Schmidt orthogonalized relative to the NMB set. Next the NMB set and the NRB set are separately diagonalized using an occupancy-weighted symmetric orthogonalization. The resulting orbitals are reblocked and diagonalized to give the final NAOs. The diagonal elements of the density matrix formed from the NAOs are the atomic population of each NAO. Summing the atomic populations over all AOs centered on a particular atom gives the natural atomic population.

Taking this idea one step further, Weinhold and coworkers defined natural bond orbitals (NBO) by diagonalizing the two-center subblocks of the density matrix.^{146, 154, 155} These NBOs are the maximum occupancy of two-atom orbitals and are constructed from hybrids that are formed from the NAOs. The procedure begins with the NAOs and removes all orbitals that have high occupancy (> 1.999 e) such as unhybridized core orbitals. Next, all NAOs having an occupancy greater than 1.90 are defined as lone pairs and are removed. The remaining NAOs define a depleted density matrix, which is then blocked and diagonalized into two-center density matrix subblocks. The resulting eigenvectors are the NBOs.

Experimental section

3.1 Chemicals and procedures

All starting materials involved in syntheses, substrates and solutions preparation were purchased from commercial sources as analytical pure reagents.

3.1.1 Syntheses

The *nickel(II) cupferronato complexes*: NiL_2A_n , $\text{L} = \text{PhN}_2\text{O}_2^-$, $n = 1$, $\text{A} = o$ -phenanthroline (*o*-phen) (**1**), *o,o'*-bipyridine (*o,o'*-bip) (**2**) and $n = 2$, $\text{A} = \text{H}_2\text{O}$ (**3**), *o*- NH_2Py (**4**), *o*- $\text{C}_6\text{H}_4(\text{NH}_2)_2$ (**5**) were obtained by our coworkers: **Dr. Andrea Deák** and **Dr. Monica Venter**.¹⁵⁶

The complex **3** was prepared by the reaction of $\text{Ni}(\text{NO}_3)_2 \cdot 6\text{H}_2\text{O}$ with cupferron $[\text{PhN}_2\text{O}_2]\text{NH}_4$.¹⁵⁷ The reaction of **3** with neutral donor molecules [*o*-phen, *o,o'*-bipy, *o*- NH_2Py , and *o*- $\text{C}_6\text{H}_4(\text{NH}_2)_2$] in acetone yielded the new complexes **1**, **2**, **4**, and **5**, respectively.

The *silylene-bridged dinuclear iron complexes*: $[\text{Cp}(\text{OC})_2\text{Fe}]_2\text{SiX}_2$ with $\text{X} = \text{H}, \text{F}, \text{Cl}, \text{Br},$ and I (**6-10**) were synthesized by our coworkers **Dr. Matthias Vögler** and **Dr. Marco Hofmann**, in **Professor Dr. Wolfgang Malisch**'s workgroup.¹⁵⁸

The complexes **6** and **8** were prepared according to the literature procedures.^{159, 160} The new compounds **7**, **9**, and **10** have been obtained from the μ_2 - SiH_2 functional precursor $[\text{Cp}(\text{OC})_2\text{Fe}]_2\text{SiH}_2$ (**6**) by hydrogen/halogen exchange, using HBF_4 , CBr_4 , and CH_2I_2 , respectively. For a detailed description of their syntheses, see reference 158.

The *3-silaoxetane* and *3-silathietane* compounds: 3,3-dimethyl-2,2,4,4-tetraphenyl-1-oxa-3-silacyclobutane (**11**) and 3,3-dimethyl-2,2,4,4-tetraphenyl-1-sila-3-thiacyclobutane (**12**), respectively, were synthesized by our coworker **Katja Strohfelddt**, in **Professor Dr. Carsten Strohmman**'s workgroup. For more details please consult the reference 161.

3.1.2 Substrates and solutions preparation

Three different kinds of SERS substrates were prepared and used in our investigations: a sodium-citrate-reduced Ag colloid, thermally evaporated Ag films, and Ag electrodes, respectively.

The *sodium-citrate-reduced Ag colloid* was prepared according to the literature.⁹⁰ AgNO₃ (90 mg) was dissolved in 500 ml of H₂O and brought to boiling. A solution of 1% sodium citrate (10 mL) was added. The solution was kept on boiling for approximately 1 hour. The Ag sol prepared by this procedure was brownish and had the absorption maximum at 400 nm.

Small amounts of (a) DHPZ sulfate 10⁻³ M water solutions
(b) caffeine 8 x 10⁻² M water solutions
(c) 10⁻² M papaverine pH adjusted water solutions
(d) nickel(II) cupferronato complexes (**2**, **3**) 10⁻³ M ethanol solutions
were added to (a) 0.7 mL of colloid.
(b) 0.5 mL
(c) 2.5 mL
(d) 3 mL

NaCl solution (10⁻² M) was also added (10:1) to produce a stabilization of the colloidal dispersion and a considerable enhancement of the SERS spectrum.⁹ Final concentrations of the samples were (a) 6.9 x 10⁻⁷, 1.4 x 10⁻⁶, 4.2 x 10⁻⁶, 4.0 x 10⁻⁵, and 1.2 x 10⁻⁴ mol L⁻¹;
(b) 5.7 x 10⁻³ mol L⁻¹;
(c) 0.362 x 10⁻⁴ mol L⁻¹;
(d) 3.84 x 10⁻⁵ (**2**) and 2.59 x 10⁻⁵ mol L⁻¹ (**3**).

In case of caffeine, the yellowish sol presented a single extinction band at 406 nm and was aged for several weeks before being used in the SERS experiment. The Ag colloid was stored at 5°C.

Dilute HCl and NaOH solutions (10⁻¹ mol L⁻¹) were used to adjust the pH value of the mixtures (for caffeine and papaverine) and pH paper was used to measure the pH values.

Thermally evaporated Ag films with particle roughness of 49, 25, 11, and 6.5 Å, were prepared according to the procedure described in **Theoretical Background**, in the Institute of Physics of Würzburg University.⁹⁷

The surface of the *Ag working electrode* was subjected to careful electrochemical treatment prior to the recording of the SERS spectrum. The electrolyte was 1 M and 2 M KCl solution and the roughening process of the polished silver electrodes consisted of oxidation-reduction cycles between -3 and 3 V.

3.2 Instrumentation

The absorption spectra were measured with a UV-VIS-NIR Perkin-Elmer Lambda 19 spectrometer with a scan speed of 240 nm min^{-1} .

The IR spectra were recorded using a Perkin Elmer 283 spectrophotometer. Samples were prepared as solutions in a NaCl cell.

The FT-Raman measurements of the solid samples were performed using a Bruker IFS 120-HR spectrometer with an integrated FRA 106 Raman module. Radiation of 1064 nm from a Nd:YAG laser was employed for excitation. A Ge detector was used and cooling was with liquid nitrogen. The spectral data were analyzed using the OPUS 2.0.5 software. The spectral resolution was 1 cm^{-1} .

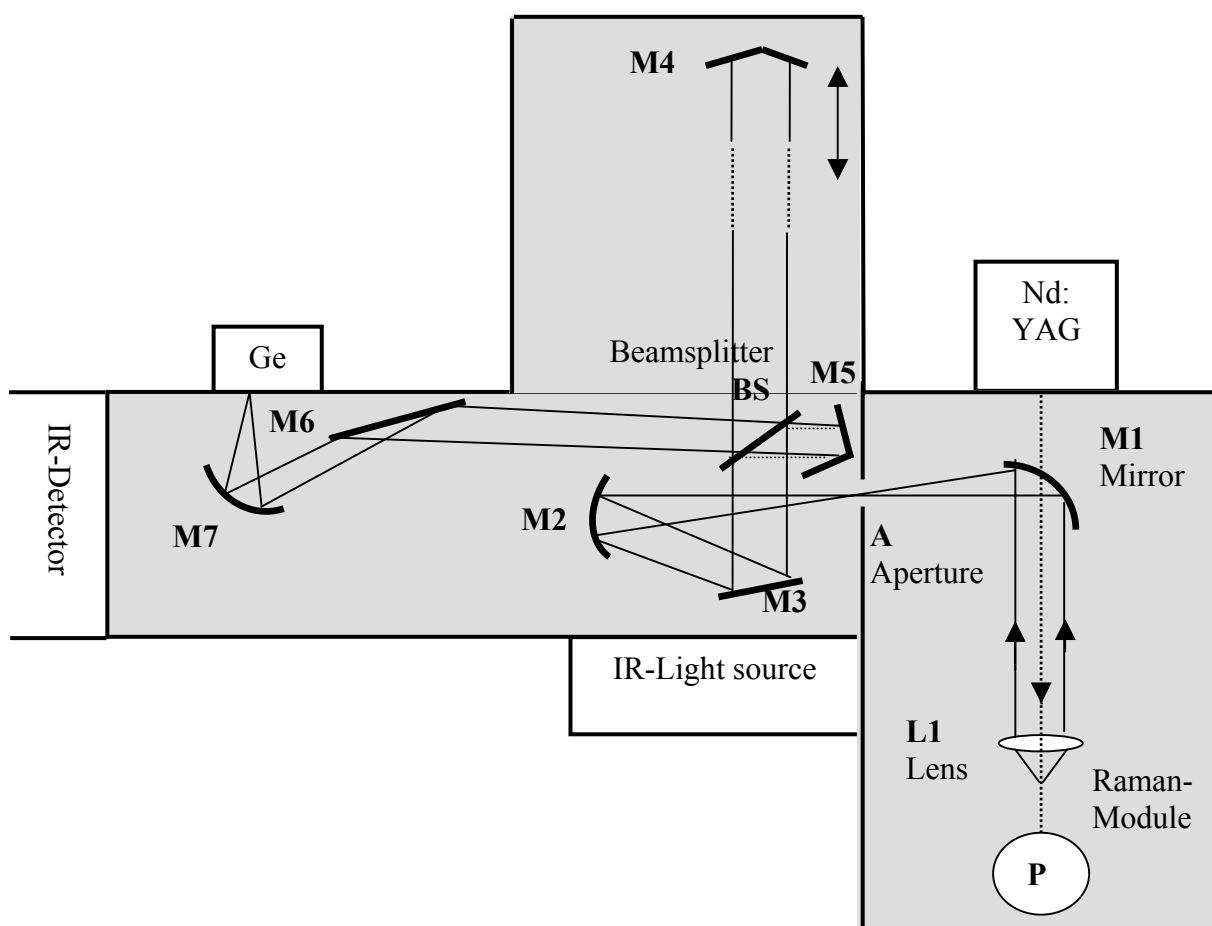


Figure 3.1. Brief optical diagram of the Bruker IFS 120-HR spectrometer with an integrated FRA 106 Raman module.

The micro-Raman and SERS spectra of all samples except for papaverine hydrochloride were recorded with a Spex 1404 double spectrometer with 2400 grooves/mm

gratings (Figure 3.2). The 514.5 nm and 647.088 nm output of a Spectra Physics argon or krypton ion laser respectively, were used as excitation lines. 90° (only for the nickel(II) cupferronato complexes) and back-scattering geometries were adopted for collecting the SERS spectra. The laser excitation was coupled to an optical microscope Olympus U-CMAD-2 with two objectives: DPLAN 20 160/0.17 and ULWD MS-PLAN 80/0.75. Noteworthy features of this instrumentation are a notch filter to reject Rayleigh scattering and a liquid nitrogen-cooled charge-coupled device (Photometrics model 9000 CCD camera) to provide state-of-the-art quantum efficiency in Raman detection. The MAPS VO 98.5 analyzing software package was used in this case for the acquisition of data. The spectral resolution was 2 cm^{-1} .

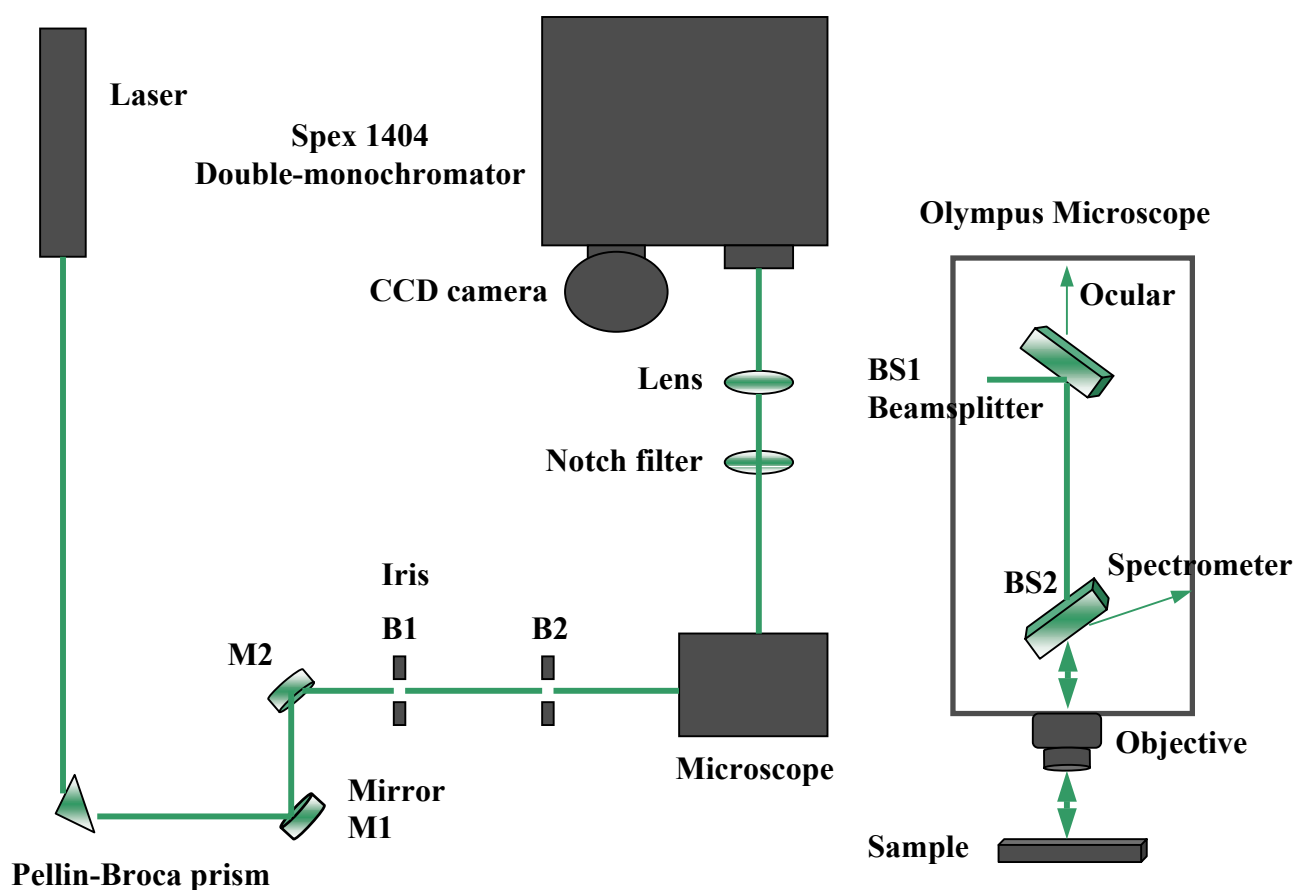


Figure 3.2. Brief optical diagram of the Micro-Raman and SERS setup.

The *3-silaonetane* (**11**) and *3-silathietane* (**12**) compounds were cooled with a closed-cycle helium cryostat at 10 K intervals in the range 10-300 K. The micro-Raman spectra of **11** and **12** were recorded in the $200\text{-}1800\text{ cm}^{-1}$ spectral region for both cooling and heating cycles. In this case, Raman wavenumbers were accurate to within 1 cm^{-1} .

The micro-Raman and SERS spectra of papaverine hydrochloride in the visible wavelength region were recorded by our coworker, **Lector Dr. Simona Cîntă**, with a Dilor-Jobin Yvon Spex Groupe Horiba spectrometer, which was equipped with 1800 grooves/mm holographic gratings. The 514.5 nm of a Spectra Physics argon ion laser was again used to collect the Raman and SERS spectra in the back-scattering geometry. A CCD camera detection system and the analysing software package LabSpec_3.01C were employed for the data acquisition. The spectral resolution was in this case 4 cm^{-1} .

3.3 *Computational details*

The DFT calculations were performed using Gaussian 98.¹⁶² Becke's 1988 exchange functional¹²⁷ in combination with the Perdew–Wang's 91 gradient-corrected correlation functional (BPW91),¹⁶³ and Becke's three-parameter hybrid exchange functional^{122, 135} using the LYP correlational functional of Lee, Yang, and Parr (B3LYP)¹³³ were employed in calculations. The 3-21G(d), 6-31G, 6-31+G(d), 6-311G(d), and/or 6-311+G(d) Pople split valence basis sets implemented in the Gaussian 98 program¹⁶² were chosen in the geometry optimization and normal modes calculations of almost all compounds, taking into account that results obtained with a split valence set are a significant improvement against those obtained with a minimal basis set.¹⁶⁴ Because of the presence of Ni atoms in complexes **1-5**, the calculations were performed in this case using the LANL2DZ basis.¹⁶⁵ It consists of the Dunning/Huzinaga valence double-zeta (D95V) for the first row and the Los Alamos ECP (effective core potential) plus DZ (Double-Zeta) for Na-Bi.

We chose this basis set with the intention to continue the calculations at the same level of theory for the Ag-adsorbed species of **1-5**.

DFT calculations on harmonic vibrational modes and Raman scattering activity of each band were performed by using the fully optimized molecular geometry with or without symmetry restrictions, according to each case, and the analytical harmonic vibrational wavenumbers for all structures confirmed that local minima on the potential energy surface have been found.

The partial charges (in e) situated on the selected atoms were then determined by the natural population analysis¹⁴⁴ at the levels of theory mentioned above. To obtain further information regarding the electronic structures, natural bond orbital analyses were also carried out^{145, 146, 154, 166}. The essential feature of NBO analysis is that the electron density is represented, as far as possible, by localized core orbitals, bonds and lone pairs. These orbitals comprise Lewis structures precisely corresponding to the chemist's view of molecules built

from atoms connected by localized two-electron bonds. However, for conjugated systems ideal Lewis structures are obviously not adequate. Deviations from idealized Lewis structures due to conjugation are shown in NBO analysis as orbital interactions between localized bonds and antibonds and between lone pairs and antibonds. The energetic contributions from these interactions can be quantified with the help of the second-order perturbation theory.

Chapter 4

Why SERS and DFT? A combination that can certainly help in analyzing pharmaceutical materials and their behavior near a biological artificial model

Raman spectroscopy is a useful tool for recording fingerprints of molecules.¹⁶⁷⁻¹⁷⁰ However, due to its low scattering cross-section, and the possibility of high background-fluorescence interference, the application of Raman spectroscopy to trace analysis is limited. Although the theories explaining SERS are not definite and still evolving, the experimental research and development in recent years has demonstrated SERS to be a potential technique for environmental and biological trace analysis, enabling the detection of even single molecules.¹⁷¹ Moreover, it can provide information about the changes of molecular identity or orientation to the metal surface with the concentration.¹⁷²⁻¹⁷⁴ In many cases the surface-adsorbed molecule may exist in a variety of forms related to one another by means of an acid–base reaction, complex formation, tautomerization, and the like. That is, previous works suggest that SERS can efficiently determine the changes of molecular identity on the metal surface with the pH value.¹⁷⁵⁻¹⁷⁸

But for a correct interpretation of the SERS data, it is necessary to have a reliable and complete vibrational assignment of the Raman spectra as a guideline. Therefore, the Raman and SERS spectra were discussed with the assistance of results obtained from DFT calculations (harmonic vibrational wavenumbers and Raman scattering activities). One should take into account that for a number of instances the theoretical calculations have aided the interpretation of Raman spectra and many previous incomplete assignments have been analyzed and improved.^{115, 116, 179} In addition, the geometries of the compounds, for which no crystal structure data were available, were theoretically characterized for the first time using DFT calculations.^{174, 179} The total electron density of the molecules and the partial charges situated on selected atoms (by the natural population analysis) were also determined theoretically in order to establish the probability of different atoms acting as an adsorptive site for the metal surface.^{174, 179} Moreover, the closer examination of the calculated orbitals of molecules brought further arguments about the presence or absence of the photoproducts at the Ag surface during the irradiation.

Overall, the results provide a benchmark illustration of the value of DFT for aiding interpretation of the rich vibrational spectra attainable for larger polyatomic adsorbates by using SERS, as well as furnishing detailed insight into the relation between the vibrational properties and the nature of the Ag substrate-adsorbate bonding.

4.1 *1,4-Dihydrazinophthalazine*

4.1.1 *Molecule presentation*

1,4 -Dihydrazinophthalazine (DHPZ) sulfate possesses a wide range of applications from the well-known antihypertensive agent^{180, 181} to the available pharmaceutical analytical reagent used in the spectrophotometric determination of napoton in bulk and tablets¹⁸². DHPZ was involved in the synthesis of some copper^{183, 184} and lead¹⁸⁵ complexes and new biologically active compounds¹⁸⁶⁻¹⁸⁸ characterized by ESR, NMR, or IR spectroscopy. Recently, physiologically compatible and water-insoluble hydrazine or hydrazide compound-crosslinked hyaluronic acid gels useful for making contact lenses, prosthetic parts, etc., were prepared by using DHPZ as crosslinker.¹⁸⁷ The action of DHPZ as a hypotensive drug on Na active cellular transport at different concentrations, in Ringer-frog medium was also studied.¹⁸⁸ Efforts have been directed toward studying the influence of these DHPZ drugs on arterial pressure, cardiac rate, and urinary excretion of catecholamines at low concentrations.¹⁸⁸⁻¹⁹⁰

In spite of their importance, no Raman or SERS studies on DHPZ derivatives have been reported so far. Therefore, Raman and SERS spectra of DHPZ sulfate were recorded at different concentrations and discussed with the assistance of results obtained from DFT calculations. Its vibrational behavior at low concentrations was closely examined to determine a possible unwanted surface photochemistry. A sodium citrate-reduced silver colloid served as an artificial biological interface in this case.

Several studies^{191, 192} have shown the acidic atoms of DHPZ derivatives to be quite mobile, allowing tautomeric equilibrium in solution. Protonation is usually formulated at the two terminal amino groups **1** (Figure 4.1). Obviously, this is in keeping with an assumed substituted hydrazine character of the base. For the alternative tautomeric form **2** (Figure 4.1), one proton is bonded to the phthalazine N2 and the other to the hydrazino N4. Therefore, to establish and characterize the tautomeric forms, the structures of those were calculated and optimized with density functional methods at different level of theory.

4.1.2 *Results and discussion*

4.1.2.1 *Geometry optimization*

The optimized structures of DHPZ sulfate tautomeric forms, which have been computed at a high level of theory using the B3LYP/6-311+G(d) method, are presented in Figure 4.1. Protonation is at the two terminal amino groups in **1** or at the N2 and N4 atoms in

2. The structural parameters of **1** and **2**, calculated with BPW91/6-31+G(d), BPW91/6-311+G(d), B3LYP/6-31+G(d) and B3LYP/6-311+G(d) methods are listed in Table 4.1. To assess the accuracy of the geometry optimizations, the computed structural parameters for tautomer **2** were compared to experimental values of the related crystal structure. The calculated bond distances and bond angles of tautomer **2** are very close to the reported parameters.¹⁹³ To the best of our knowledge, no crystal structure data for the tautomeric form **1** were yet published. The two theoretical methods agree quite well with each other, but the bond lengths and angles of **2** were better reproduced in almost all cases by the B3LYP/6-311+G(d) method, where the maximum discrepancy was only 3 pm and 2.5° with respect to the experimental data. Also, the agreement between computed and experimental values improved, but not very significantly, from 6-31+G(d) to 6-311+G(d) level of theory.

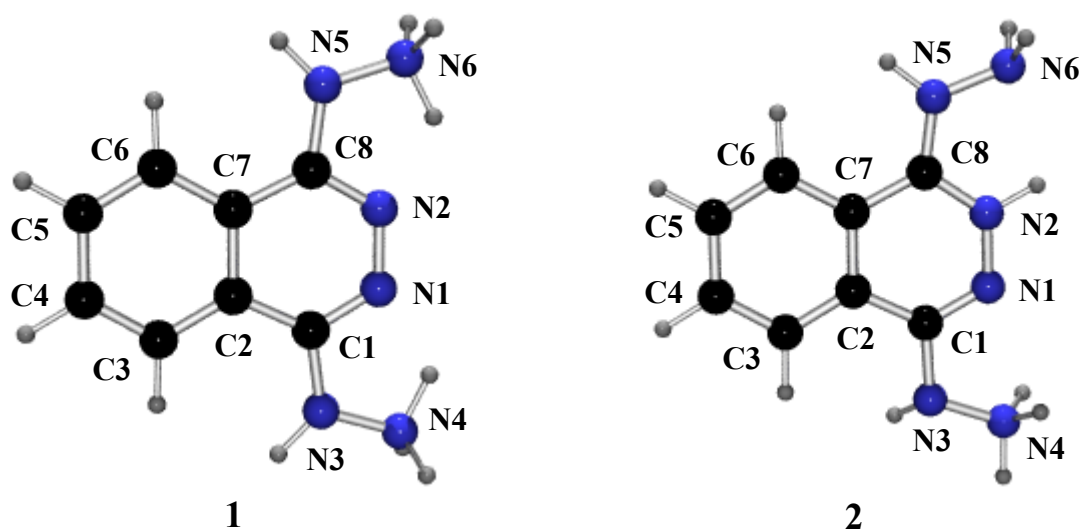


Figure 4.1. B3LYP/6-311+G(d) optimized geometry of DHPZ sulfate tautomers **1** and **2**.

On the basis of the geometry optimizations that have been carried out, the following conclusions can be reached. The phthalazine unit is almost planar in both diprotonated forms **1** and **2**. The fragment C2-C3-C4-C5-C6-C7 is planar and the deviations of the other atoms from this plane are similar in the two forms. The pyridazine rings deviate slightly from planarity, adopting distorted boat conformations with the N2 and C2 atoms out of the plane.¹⁹²⁻¹⁹⁵ The angle between the best planes through the benzene ring and the pyridazine is 1.45° and 1.36° for the tautomer **1** and **2**, respectively, with the best basis set 6-311+G(d) and the B3LYP functional. The BPW91/6-311+G(d) led to a value of 1.42° and 1.02° for **1** and **2**, respectively, also comparable to the literature value of 1.59° for tautomer **2**.¹⁹² The -NH-NH₂ substitute at C8 is in the plane of the ring and the experimental and calculated (Table 4.1)

Table 4.1. Selected calculated structural parameters for the DHPZ sulfate tautomers **1** and **2**, respectively, together with the experimental values found in tautomeric form **2**.

| | Exp in 2 ¹⁹³ | Calc for 2 | | | | Calc for 1 | | | |
|-------------------|--------------------------------|-------------------|------------|-----------|------------|-------------------|------------|-----------|------------|
| | | BPW91 | | B3LYP | | BPW91 | | B3LYP | |
| | | 6-31+G(d) | 6-311+G(d) | 6-31+G(d) | 6-311+G(d) | 6-31+G(d) | 6-311+G(d) | 6-31+G(d) | 6-311+G(d) |
| Bond lengths (pm) | | | | | | | | | |
| N1-C1 | 129.6(5) | 131.0 | 130.5 | 129.6 | 129.6 | 132.1 | 131.6 | 130.7 | 130.2 |
| N2-C8 | 131.3(5) | 135.4 | 135.0 | 134.4 | 134.1 | 132.1 | 131.6 | 130.7 | 130.2 |
| N3-N4 | 141.5(5) | 144.3 | 144.1 | 143.7 | 143.6 | 144.3 | 144.1 | 143.7 | 143.5 |
| N5-N6 | 141.5(5) | 140.9 | 140.7 | 140.6 | 140.4 | 144.3 | 144.1 | 143.7 | 143.5 |
| N3-C1 | 141.0(5) | 142.7 | 142.3 | 142.1 | 142.1 | 142.2 | 142.1 | 142.0 | 142.0 |
| N5-C8 | 134.0(5) | 134.7 | 134.5 | 133.9 | 133.6 | 142.3 | 142.1 | 142.0 | 142.0 |
| N1-N2 | 137.9(4) | 135.4 | 135.1 | 135.4 | 135.2 | 135.1 | 134.9 | 135.2 | 135.0 |
| C1-C2 | 142.1(5) | 144.7 | 144.4 | 144.6 | 144.4 | 143.7 | 143.5 | 143.5 | 143.3 |
| C7-C8 | 144.8(5) | 145.1 | 145.0 | 144.9 | 144.7 | 143.7 | 143.5 | 143.5 | 143.3 |
| C2-C3 | 140.7(5) | 141.3 | 141.0 | 140.6 | 140.3 | 141.6 | 141.2 | 141.0 | 140.7 |
| C6-C7 | 138.1(5) | 141.2 | 141.0 | 140.6 | 140.4 | 141.6 | 141.2 | 141.0 | 140.7 |
| C2-C7 | 141.8(5) | 143.6 | 143.3 | 142.6 | 142.4 | 143.9 | 143.5 | 142.8 | 142.5 |
| C4-C5 | 140.8(6) | 141.1 | 140.7 | 140.5 | 140.2 | 141.5 | 141.2 | 141.0 | 140.7 |
| C3-C4 | 135.7(6) | 139.0 | 139.3 | 139.0 | 138.7 | 139.4 | 139.0 | 138.7 | 138.3 |
| C5-C6 | 138.0(6) | 139.2 | 139.2 | 139.0 | 138.6 | 139.4 | 139.0 | 138.7 | 138.3 |

| | Exp in 2 ¹⁹³ | Calc for 2 | | | | Calc for 1 | | | |
|------------|--------------------------------|-------------------|------------|-----------|------------|-------------------|------------|-----------|------------|
| | | BPW91 | | B3LYP | | BPW91 | | B3LYP | |
| | | 6-31+G(d) | 6-311+G(d) | 6-31+G(d) | 6-311+G(d) | 6-31+G(d) | 6-311+G(d) | 6-31+G(d) | 6-311+G(d) |
| Angles (°) | | | | | | | | | |
| C1-C2-C3 | 124.3(3) | 124.0 | 124.0 | 123.8 | 123.9 | 125.0 | 125.0 | 125.0 | 125.0 |
| C6-C7-C8 | 123.9(3) | 123.3 | 123.2 | 123.2 | 123.2 | 125.0 | 125.0 | 125.0 | 125.0 |
| C1-C2-C7 | 117.4(3) | 116.4 | 116.4 | 116.5 | 116.5 | 115.4 | 115.4 | 115.4 | 115.3 |
| C2-C7-C8 | 116.1(3) | 117.3 | 117.5 | 117.3 | 117.3 | 115.4 | 115.4 | 115.4 | 115.3 |
| C3-C2-C7 | 118.3(3) | 119.6 | 119.3 | 119.6 | 119.6 | 119.6 | 119.6 | 119.6 | 119.6 |
| C2-C7-C6 | 120.1(3) | 119.4 | 119.5 | 119.5 | 119.4 | 119.6 | 119.6 | 119.6 | 119.6 |
| C2-C3-C4 | 120.9(4) | 120.0 | 120.1 | 120.0 | 120.0 | 119.8 | 119.8 | 119.7 | 119.7 |
| C5-C6-C7 | 120.7(4) | 120.1 | 120.2 | 120.0 | 120.1 | 119.8 | 119.8 | 119.7 | 119.7 |
| C3-C4-C5 | 120.5(4) | 120.4 | 120.4 | 120.5 | 120.5 | 120.6 | 120.6 | 120.6 | 120.6 |
| C4-C5-C6 | 120.5(4) | 120.5 | 120.5 | 120.5 | 120.5 | 120.6 | 120.6 | 120.6 | 120.6 |
| N2-C8-N5 | 118.1(3) | 116.8 | 116.8 | 117.4 | 117.4 | 114.0 | 114.0 | 114.7 | 114.7 |
| N1-C1-N3 | 115.0(3) | 115.4 | 115.0 | 115.6 | 115.6 | 114.0 | 114.0 | 114.7 | 114.7 |
| N2-C8-C7 | 119.8(3) | 118.2 | 118.2 | 118.1 | 118.1 | 124.5 | 124.5 | 124.6 | 124.6 |
| N1-C1-C2 | 125.4(3) | 125.0 | 124.4 | 124.8 | 124.8 | 124.5 | 124.5 | 124.6 | 124.6 |
| N5-C8-C7 | 122.1(3) | 125.0 | 125.0 | 124.5 | 124.5 | 121.4 | 121.4 | 120.6 | 120.6 |
| N3-C1-C2 | 119.5(3) | 119.6 | 120.0 | 119.5 | 119.5 | 121.4 | 121.4 | 120.6 | 120.6 |
| N2-N1-C1 | 116.0(3) | 116.7 | 116.7 | 117.1 | 117.2 | 120.0 | 120.0 | 120.0 | 120.0 |
| N1-N2-C8 | 125.2(3) | 126.3 | 125.7 | 126.0 | 125.9 | 120.0 | 120.0 | 120.0 | 120.0 |
| N4-N3-C1 | 112.6(3) | 112.8 | 112.7 | 113.1 | 113.0 | 111.3 | 111.3 | 112.1 | 112.1 |
| N6-N5-C8 | 116.6(3) | 118.2 | 118.1 | 118.5 | 118.4 | 111.3 | 111.3 | 112.1 | 112.1 |

values for the N5-C8 interatomic distance indicate a partially double bond with the phthalazine unit. Indeed, the N2-C8-N5-N6 dihedral angle calculated for **2** with the B3LYP/6-311+G(d) and BPW91/6-311+G(d) methods is 0° , as expected. In the case of the $-\text{NH}-\text{NH}_3^+$ substitute at C1, the bonds at N3 are not planar and a much weaker conjugation with the phthalazine system can be inferred. This should lead to a higher value for the N1-C1-N3-N4 dihedral angle of **2**. The B3LYP/6-311+G(d) and BPW91/6-311+G(d) methods predicted an absolute value of 3.2° and 3.6° , which confirmed these aspects. For the tautomer **1**, these methods predicted an absolute value of 8.3° and 8.5° , respectively, which suggests a much weaker conjugation with the phthalazine system.

The positive charge resulting from the protonation of N2 is delocalized over the N2-C8-N5 fragment. The structure of **2** should therefore be represented in solution by a mesomeric equilibrium between the limiting formulas **2a** and **2b** (Figure 4.2). With the B3LYP/6-311+G(d) method, the N2-C8 bond is 4.5 pm longer than N1-C1 and N5-C8 is 8.5 pm shorter than N3-C1. The comparison of the same bond lengths, calculated with the BPW91/6-311+G(d), yields a similar difference of 4.5 and 7.8 pm, respectively, owing to the charge delocalization over the N2-C8-N5 moiety. Due to the protonation at the two terminal amino groups in tautomer **1**, the N2-C8 and N1-C1 bond lengths have identical values of 131.6 pm and 130.2 pm, respectively with the BPW91/6-311+G(d) and B3LYP/6-311+G(d) methods. For N5-C8 and N3-C1, the BPW91/6-311+G(d) and B3LYP/6-311+G(d) methods predict bond lengths of 142.1 and 142.0 pm.

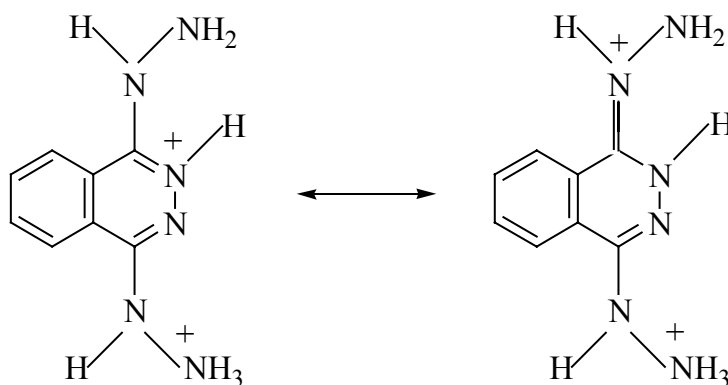


Figure 4.2. Depiction of the mesomeric equilibrium of **2**.

The absolute energy difference ΔE_0 between **1** and **2**, which contains the zero-point energy (ZPE) correction, has been determined to be 42.7 kJ/mol and 48.5 kJ/mol with the BPW91/6-31+G(d) and BPW91/6-311+G(d) methods. With the B3LYP/6-31+G(d) and

B3LYP/6-311+G(d) methods, ΔE_0 has been predicted to be at 63.7 kJ/mol and 54.9 kJ/mol, respectively. Therefore, according to our DFT calculations results, the tautomeric form **1** is thermodynamically the most favorized one.

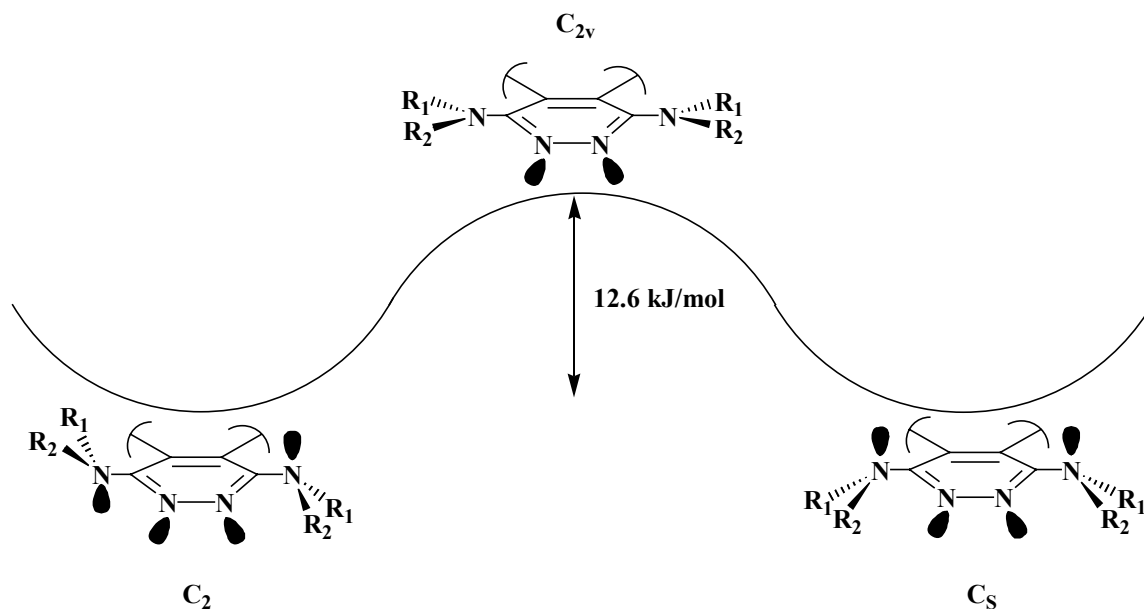


Figure 4.3. Calculated possible geometry of tautomeric form **1** of different symmetries.

After the geometry optimization of **1** with a C_2 , C_s , and C_{2v} restricted symmetry (BPW91/6-311+G(d) method), the absolute energy difference between these imposed structures of **1** has been also determined. Either with C_2 symmetry or C_s symmetry, the absolute energy difference with respect to C_{2v} has been found to be 12.6 kJ/mol (Figure 4.3). This seems to indicate the structure of C_2 or C_s symmetry as the most stable one, due probably to the fact that, in those cases, resonance interaction between the nitrogen lone-pair orbital and the ring is possible. As depicted in Figure 4.3, in the case of C_{2v} symmetry, the three groups around N are coplanar, with sp^2 hybridization, and the axis of symmetry of the lone-pair orbital is in the plane of the ring corresponding to no overlap and complete elimination of conjugation.

4.1.2.2 *Vibrational spectroscopy*

The FT-Raman spectrum of DHPZ sulfate recorded in the 3500-200 cm^{-1} spectral region is presented in Figure 4.4. The observed bands as well as the vibrational assignment are summarized in Table 4.2. The vibrational fundamentals from the Raman spectrum were

analyzed by comparing the vibrational modes with those assigned for phthalazine^{173, 196, 197} and naphthalene^{198, 199} in conjunction with theoretical calculations.

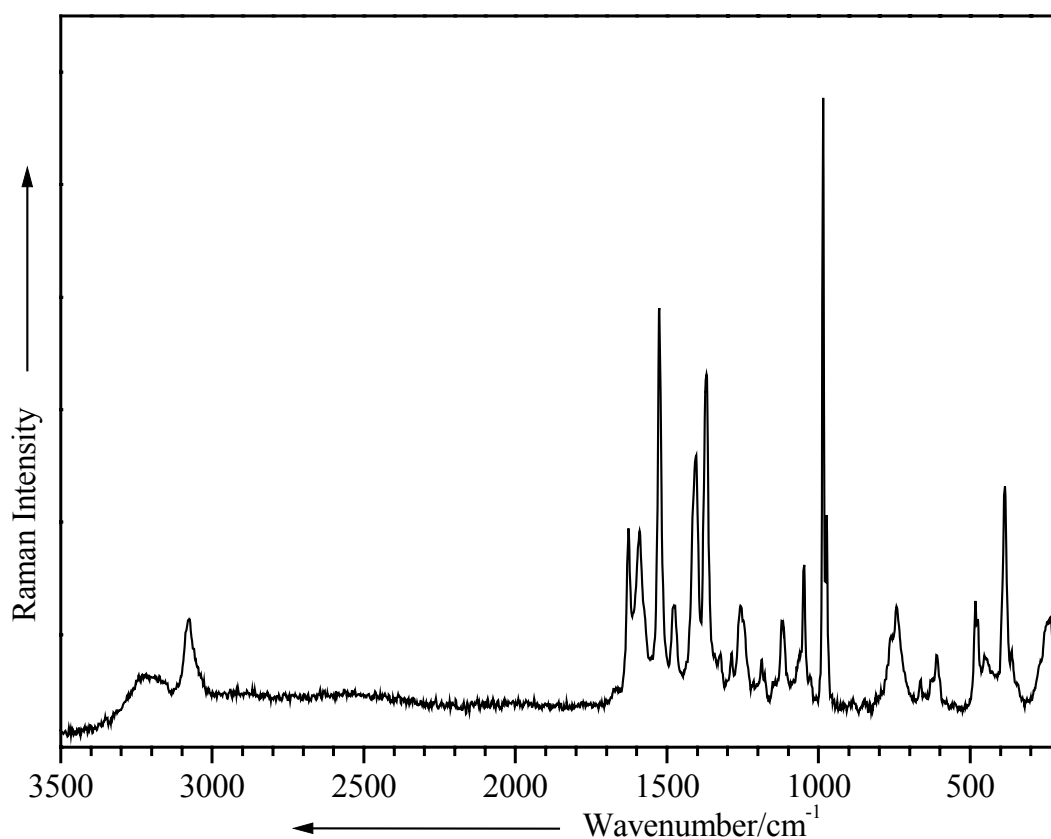


Figure 4.4. The FT-Raman spectrum of DHPZ sulfate solid powder.

Excitation line: $\lambda_0 = 1064$ nm.

Ab initio harmonic vibrational wavenumbers (ω) are typically larger than the fundamentals (ν) experimentally observed.¹⁰⁹ The vibrational assignment in the experimental spectrum was feasible with the help of the BPW91 calculations (Table 4.2), which was expected. Consistent with previous findings,²⁰⁰⁻²⁰² the B3LYP functional tends to overestimate fundamental modes. Indeed, the calculated vibrational wavenumbers using B3LYP are much larger than those using BPW91 compared to the experimental fundamentals and should be scaled in order to be in good agreement with the experiment.²⁰³ Major sources of this disagreement are the neglect of anharmonicity effects in the theoretical treatment and the incomplete incorporation of electron correlation. We wish to remark that vibrational modes calculated with the 6-311+G(d) basis set improved, but not significantly, the calculated values. The Raman scattering activities predicted at the B3LYP/6-311+G(d) level correlate

Table 4.2. Selected calculated and experimental Raman and SERS wavenumbers (cm^{-1}), together with their tentative assignment.

| Raman | Calc | | | | SERS $6.9 \times 10^{-7} \text{ mol L}^{-1}$ | Vibrational assignment |
|--------|-----------|------------|-----------|---------------|---|---|
| | BPW91 | | B3LYP | | | |
| | 6-31+G(d) | 6-311+G(d) | 6-31+G(d) | 6-311+G(d) | | |
| 1628m | 1622 | 1624 | 1674 | 1676 (12.96) | | NH_3^+ asym bending |
| 1591m | 1601 | 1596 | 1647 | 1641 (24.37) | 1606m | ring stretching + NH bending + CH bending |
| 1570sh | 1573 | 1568 | 1625 | 1618 (39.71) | 1577m | NH_3^+ sym bending + ring stretching |
| 1525s | 1521 | 1519 | 1565 | 1571 (47.23) | 1531m | CH bending + NH bending + NH_3^+ asym bending |
| 1477w | 1488 | 1483 | 1537 | 1523 (4.16) | 1491w | ring stretching + CH bending NH bending + NH_3^+ asym bending |
| 1404m | 1416 | 1412 | 1463 | 1457 (130.57) | 1452vs | ring stretching + CH bending |
| 1370ms | 1379 | 1370 | 1401 | 1395 (41.57) | 1382vs | ring stretching |
| 1323vw | 1363 | 1358 | 1387 | 1375 (23.08) | 1360m | ring stretching + CH bending |
| 1286vw | 1336 | 1335 | 1377 | 1373 (1.29) | 1313w | ring stretching + NH bending |
| 1258w | 1274 | 1276 | 1314 | 1313 (4.10) | | CH bending + NH_3^+ sym bending |
| 1248w | 1229 | 1233 | 1253 | 1250 (4.36) | 1240sh | CH bending + ring stretching + C-N stretching |
| 1189vw | 1194 | 1194 | 1220 | 1222 (11.41) | 1229w | + NH bending + NH_3^+ rocking |
| 1177vw | 1189 | 1187 | 1219 | 1217 (0.81) | | CH bending + NH_3^+ rocking |
| 1122vw | 1177 | 1177 | 1207 | 1207 (3.62) | 1161w | CH bending |
| 1115vw | | | | | | SO_4^{2-} asym stretching |
| 1063sh | 1091 | 1096 | 1126 | 1122 (31.74) | 1116vw | skeletal distortion |
| 1048w | 1074 | 1076 | 1110 | 1108 (27.83) | | SO_4^{2-} sym stretching + skeletal distortion + N-N stretching |
| | 1037 | 1040 | 1064 | 1060 (30.13) | 1061vw | CH bending + ring stretching |

53 *Why SERS and DFT?*

| | | | | | | |
|--------|------|------|------|-------------|-------|--|
| 1029vw | 1014 | 1015 | 1042 | 1042 (4.11) | | N-N stretching + CH bending |
| 986vs | 997 | 1001 | 1024 | 1021 (1.15) | 1019s | ring breathing |
| 974m | 999 | 994 | 988 | 984 (0.09) | 988m | CH wagging |
| | | | | | 943w | skeletal distortion |
| | 951 | 946 | 887 | 882 (0.84) | 924vw | CH wagging |
| 762sh | 760 | 764 | 790 | 787 (1.99) | 799ms | ring stretching + CH wagging |
| 744w | 750 | 748 | 766 | 766 (23.85) | 755vw | skeletal torsion |
| 663vw | 651 | 651 | 678 | 676 (1.00) | 668vw | skeletal distortion + CH wagging |
| | 648 | 648 | 672 | 674 (2.14) | 653vw | |
| 624sh | 630 | 629 | 648 | 649 (0.17) | 623vw | skeletal distortion + NH ₃ ⁺ rocking |
| 611vw | | | | | 607vw | SO ₄ ²⁻ asym bending |
| | | | | | 529m | skeletal distortion |
| | | | | | 519vw | skeletal distortion |
| 483w | 472 | 473 | 486 | 486 (2.96) | 483vw | skeletal torsion |
| 475vw | 465 | 466 | 479 | 479 (1.87) | | SO ₄ ²⁻ sym bending + NH bending |
| | | | | | | + skeletal bending |
| 386m | 392 | 389 | 401 | 406 (1.05) | | NH ₃ ⁺ bending + NH bending |
| | | | | | | + skeletal distortion |
| 362vw | 372 | 369 | 377 | 378 (12.90) | | NH ₃ ⁺ bending + NH bending |
| | | | | | | + skeletal distortion |
| 268sh | 288 | 288 | 240 | 240 (0.59) | | NH ₃ ⁺ torsion |
| 235vw | 223 | 224 | 214 | 216 (2.13) | | skeletal distortion |
| | | | | | 228m | Ag-N stretching |

Abbreviations: vw - very weak, w - weak, m - medium, ms - medium strong, s - strong, vs - very strong, sh - shoulder; sym - symmetric, asym - asymmetric. The calculated Raman scattering activities are in parentheses ($\text{\AA}^4/\text{amu}$).

pretty well with the relative intensities of the FT-Raman spectrum of the neat solid sample (Table 4.2).

The observed bands in the SERS spectrum of DHPZ sulfate (Figure 4.4) were also given in Table 4.2 after the complete analysis of the FT-Raman spectrum.

It is well known that there are two possibilities of molecules adsorption on the metal surface, namely physisorption and chemisorption. In the case of physisorption, the molecules have a SERS spectrum similar to that of the free molecules, due to a relatively larger distance between metal surface and adsorbed compound. Comparatively, in the case of chemisorption there is an overlapping of the molecular and metal orbitals, the molecular structure being changed, and consequently, the position of the bands and their relative intensities are dramatically changed.

Comparing the FT-Raman and SERS spectra of DHPZ sulfate (6.9×10^{-7} mol L⁻¹) (Figure 4.5) on Ag sol, one may notice that there are major differences between the band positions and their relative intensities. Therefore, we suppose that DHPZ sulfate is mainly chemisorbed on the silver surface. According to the adatom model proposed by Otto and coworkers,^{204, 205} chemisorption occurs in specific active sites of the metal surface and the SERS signal is mainly generated by a minority species formed at these surface sites. Indeed, all of the prominent lines (1452, 1382, 1019, 799, and 529 cm⁻¹) of the SERS spectrum are assignable to totally symmetric modes of phthalazine and the overall spectral feature has a striking resemblance to the SERS spectrum of phthalazine. That indicates a strong interaction of the molecule through the phthalazine part with the silver surface. Moreover, the NH₃⁺ asymmetric bending and torsion modes, which were attributed at 1628 and 268 cm⁻¹, respectively, in the FT-Raman spectrum of DHPZ sulfate and do not overlap with another vibrational modes, are absent or very weak in the SERS spectrum. Also, the NH bending, N-N stretching, and SO₄²⁻ stretching or bending modes, which were assigned at 1477, 1122, 1063 and 475 cm⁻¹, respectively in the FT-Raman spectrum, have a similar behavior. Therefore, the terminal parts may be far from the surface. Strong evidence for decreasing SERS intensity or absence of some vibrational modes, when a vibrational group is separated several Å from the surface, has been found in other studies too.²⁰⁶

Recently, the SERS spectrum of phthalazine adsorbed on silver colloid was reexamined on the basis of results obtained in a flow cell and the conclusion^{173, 207} was drawn that many of the spectroscopic changes attributed to various factors, such as excitation wavelength, concentration, and coadsorption of anions, were, in fact, due to the surface

photodecomposition of phthalazine. Its photoreaction was ascribed to a process in which the N-N bond of the molecule breaks to form an adsorbed species (with the newly free N ends forming two Ag-N bonds) resembling an ortho-disubstituted benzene. The suggested structure of the photoproduct implies that the vibrational signature of the benzene ring should dominate the SERS spectrum. Although the SERS spectrum of DHPZ sulfate was recorded again with a longer exposure time (100, 200, and 250s), the rapidly growing bands of ortho-substituted benzenes, which were observed in the SERS spectrum of phthalazine^{173, 207} on Ag colloid with the same excitation line, were either absent or very weak. Namely, the signals at 1547, 1465, 1432, 1332, 1278, and 545 cm^{-1} , respectively, due to the ν_{8a} , $19b$, $19a$, 14 , 3 , and $6a$ vibrational modes of ortho-substituted benzenes²⁰⁸ were absent, whereas the observed bands at 1244, 755, and 483 cm^{-1} , respectively, assigned to the ν_{7a} , 11 and $6b$ vibrational modes of the same species were very weak and did not dominate the SERS spectrum of DHPZ sulfate.

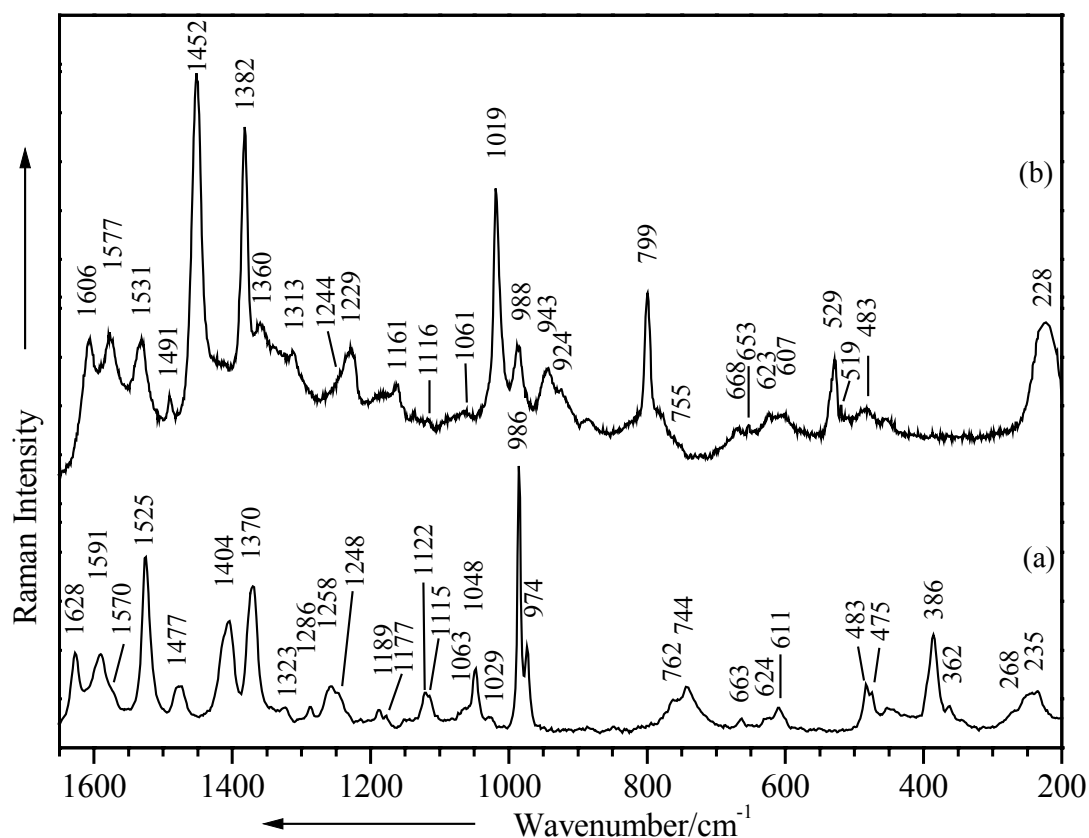


Figure 4.5. The FT-Raman spectrum of DHPZ sulfate solid powder (a) and the SERS (b) ($6.9 \times 10^{-7} \text{ mol L}^{-1}$) spectrum on Ag colloid.

Excitation line: (a) $\lambda_0 = 1064 \text{ nm}$ and (b) $\lambda_0 = 514.5 \text{ nm}$.

Therefore, we suggest that there are no photoproducts from a photoreaction of DHPZ sulfate at this concentration ($6.9 \times 10^{-7} \text{ mol L}^{-1}$) and the mentioned bands can be indeed assigned to the native adsorbate.

The highest occupied molecular orbital (HOMO), the lowest unoccupied molecular orbital (LUMO), and LUMO+1 are shown in Figure 4.6. Since the LUMO and LUMO+1 are energetically very close (9.56 and 9.40 eV), both of them should be taken into consideration when one analyzes the possible appearance of photoproducts during the irradiation of the adsorbate. The LUMO, which is partially situated at the N1-N2 atoms has a bonding character, whereas at the N2-C8 and N1-C1 atoms it has an antibonding one. A closer examination of the LUMO+1 shows a reverse behavior at the mentioned atoms.

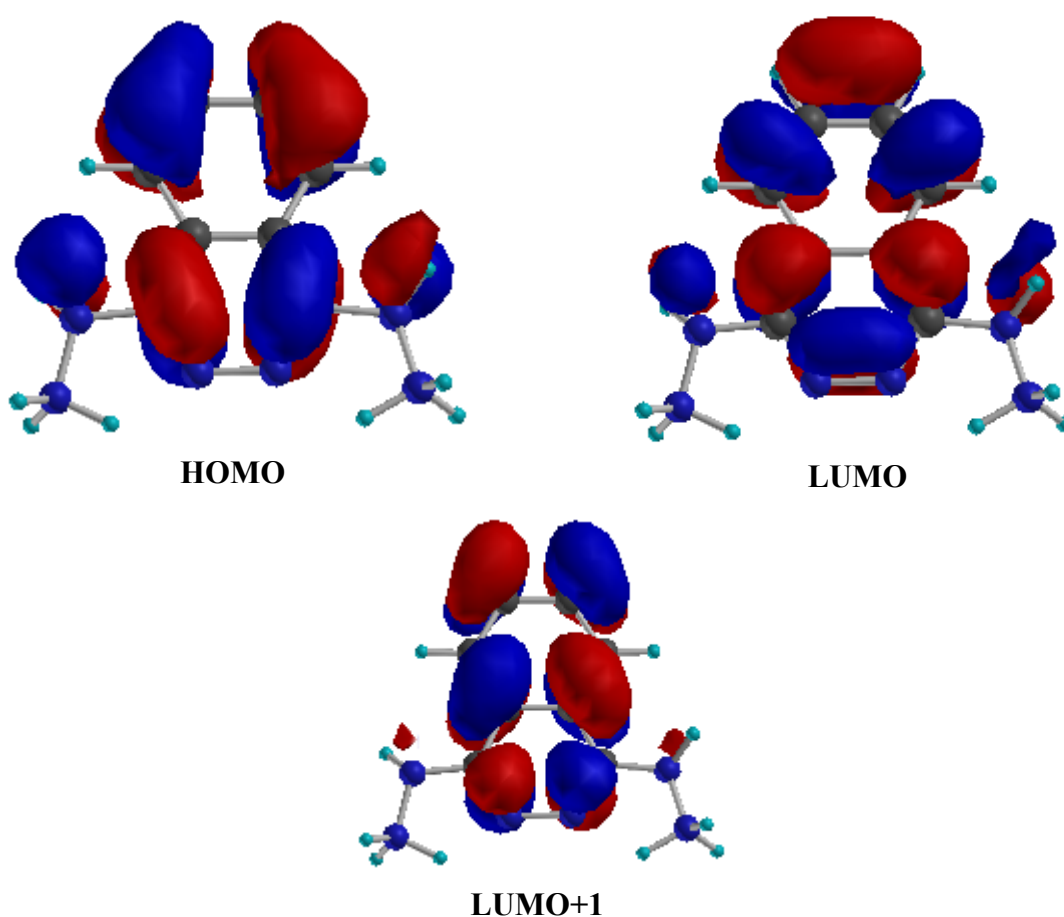


Figure 4.6. Calculated HOMO, LUMO, and LUMO+1 of DHPZ sulfate with BPW91/6-311+G(d). (Isocontour: 0.03 a.u.)

Populating these orbitals during the irradiation should lead in the first case (LUMO) to a breaking of the C1-N1 and C8-N2 bonds, followed by an N₂ emission, and in the second case (LUMO+1) to a breaking of the N1-N2 bond, as in the model proposed by Suh and

coworkers¹⁷³. But the HOMO-LUMO and HOMO-LUMO+1 gaps of DHPZ sulfate were calculated to be at 3.46 and 3.61 eV, which correspond to an absorption in the UV spectral region, namely at 358 and 343 nm, respectively. This could explain the absence of the photoproducts after the excitation of the sample with 514.5 nm, taking into account that the photoreaction reported on phthalazine is only a one-photon process.¹⁷³ However, one should take into consideration that the calculations refer to the gas phase and do not describe the interaction of the molecule with the Ag surface.

It is well-known that the determination of orientation of molecules adsorbed on metal surfaces is based on SERS surface selection rules.^{27, 28, 175, 209} These stated that vibrations deriving their intensities from a large value of α_{zz} (when z lying to the local metal surface normal) would be the most intense in the SERS spectrum when the molecule has an end-on orientation to the Ag surface. According to the mentioned rules, we have tried to establish the orientation of DHPZ sulfate on the Ag colloid, at different concentration.

The Figure 4.7 shows the SERS spectrum of DHPZ sulfate at different concentrations. Examining the SERS spectra of DHPZ sulfate recorded at 6.9×10^{-7} , 1.4×10^{-6} , and 4.2×10^{-6} mol L⁻¹ (Figure 4.7a-c, respectively), one can notice again that all of the strong bands (1452, 1382, 1019, 799, and 529 cm⁻¹, respectively, in the SERS spectrum (a)) are in-plane totally symmetric modes of phthalazine. In all these spectra, the mentioned bands are very little shifted in comparison to those of the SERS spectrum at lowest concentration (a) (Figure 4.7). The bands at 1452 (very strong), 1382 (very strong), and 799 cm⁻¹ (medium to strong) are good candidates for modes with a much higher α_{zz} term than the other Raman polarizability components, because they are in-plane (of the molecule) ring stretching vibrations. Moreover, according to our theoretical calculations, the bands at 1452 and 1382 cm⁻¹ are due to in-plane ring stretching modes, which involve stronger C-N, N-N, and C-C bonds, due to the bond delocalization. In the SERS spectrum, the strong band at 1019 cm⁻¹ is due to the skeletal breathing, while the medium signal at 529 cm⁻¹ is attributed to a skeletal distortion. All of these strong bands correspond according to the literature to a_g modes of naphthalene. This makes them also good candidates for enhancement.^{27, 28, 175, 209} All those may support the idea that DHPZ sulfate is adsorbed such that the skeletal plane is oriented perpendicular to, or significantly tilted with respect to the surface. Considering the steric hindrance that could occur at the approaching of the tautomeric form **2** to the surface, we suppose that the interaction of the tautomeric form **1** with the Ag surface is favored.

Also, the relative magnitude of the intensity of CH stretching bands can play a very important role in analyzing the surface geometry of compounds that have a planar structure.^{27,}

^{28, 175, 209} In the case of naphthalene, for example, the CH stretching vibrations contribute significantly only to the α_{xy} , α_{xx} and α_{yy} Raman polarizability components (where z is normal to the surface), when the molecule is lying down flat on surface. If, on the other hand, it is standing up on the surface, the CH stretching vibrations would obtain their intensities from α_{zz} , α_{xz} , and α_{yz} , resulting in a higher SERS intensity for those bands.^{27, 28, 175, 209} Taking into account that the studied molecule has a strong interaction through the phthalazine part with the Ag surface and that DFT-calculations led to an almost planar phthalazine system in both diprotonated forms **1** and **2**, the observation of strong or weak CH stretching bands in the SERS spectrum of DHPZ sulfate would constitute a simple rule for determining the surface geometry of molecule adsorbed on the Ag colloid surface at different concentrations.

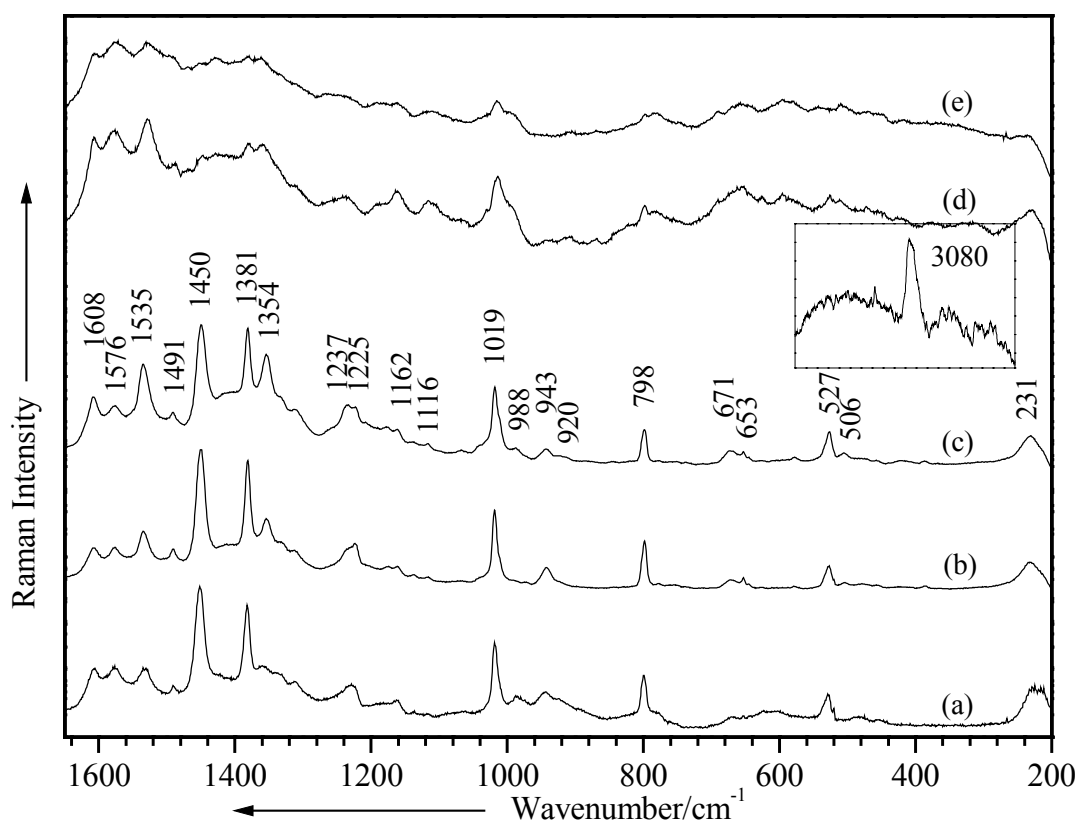


Figure 4.7. The SERS spectra of DHPZ sulfate on Ag colloid at different concentrations: 6.9×10^{-7} (a), 1.4×10^{-6} (b), 4.2×10^{-6} (c), 4.0×10^{-5} (d), and 1.2×10^{-4} mol L⁻¹ (e).
Excitation line: $\lambda_0 = 514.5$ nm.

The SERS spectrum of DHPZ sulfate at 4.2×10^{-6} mol L⁻¹ (Figure 4.7c) shows a weak to medium broad CH stretching band at 3080 cm⁻¹, not strong, as expected according to the

simple rule discussed. This case is similar to that of phthalazine,²⁰⁹ where the CH stretching bands are very weak even though the molecule stands up on the surface. This is probably due to the fact that the two CH bonds nearest the surface are parallel to the surface even when the molecule is standing and hence do not contribute greatly to the SERS intensity.²⁰⁹ However, the signal is stronger than in case of phthalazine, suggesting that the top two CH bonds are closer and rather tilted to the surface than in the case of phthalazine. Therefore, the DHPZ sulfate prefers probably in this case a significantly tilted orientation to the metal surface. The SERS spectrum of DHPZ sulfate at 4.2×10^{-6} mol L⁻¹ (c) is different from those at lower concentration (6.9×10^{-7} mol L⁻¹ (a)) but not dramatically (Figure 4.7). It is evident that relative intensities of the Raman lines change with a decrease in the DHPZ sulfate solution concentration. As the concentration is decreased, the band intensity of the CH stretching mode decreases. The molecule tends probably to lie flat on the Ag surface, but the flat orientation is not achieved even at the lowest concentration, because the ring breathing should be at least 10 cm⁻¹ shifted along with substantial band broadening in the SERS spectrum (Figure 4.7a), which has not been observed. Conspicuous differences in these SERS spectra are also found in the bands at 1608, 1535, 1354, 988, and 920 cm⁻¹, respectively. The relative intensities of the 1608, 1535, and 1354 cm⁻¹ bands decrease much in passing to lower DHPZ sulfate concentration. On the basis of the surface selection rule, these vibrational modes should have a large Raman polarizability change in the z direction (when z lying to the local metal surface normal). Indeed, according to the DFT calculations and previous studies,^{173, 196-199} all these modes are mostly due to in-plane CH bending or ring stretching modes, as shown in Figure 4.8, with large components parallel to the metal surface, when the molecule tends to lie flat on the surface. On the other hand, the 988 and 920 cm⁻¹ bands, which do not have components perpendicular to the metal surface when the planar portion of the molecule (Figure 4.8) has an end-on or at least significantly tilted orientation, exhibit intensity enhancement. Even though the SERS spectrum of DHPZ sulfate at the lowest concentration (Figure 4.7) is noisy in comparison with the other SERS spectra, the out-of plane skeletal and CH deformation modes could be observed with the same very weak relative intensity at 668 and 653 cm⁻¹.

As the concentration of adsorbate in the solution decreases, the occupancy of the adsorbed molecules on the surface must decrease. If our interpretation is correct, this could explain the changes observed in the SERS spectra at different concentrations. More specific, the effective molecular area of each adsorbed DHPZ sulfate on the Ag surface increases, that is, adsorbates prefer a less tilted orientation to the surface. Since an unequivocal SERS

selection rule is not available, the exact tilt angle of the adsorbate cannot be estimated at the moment, however.

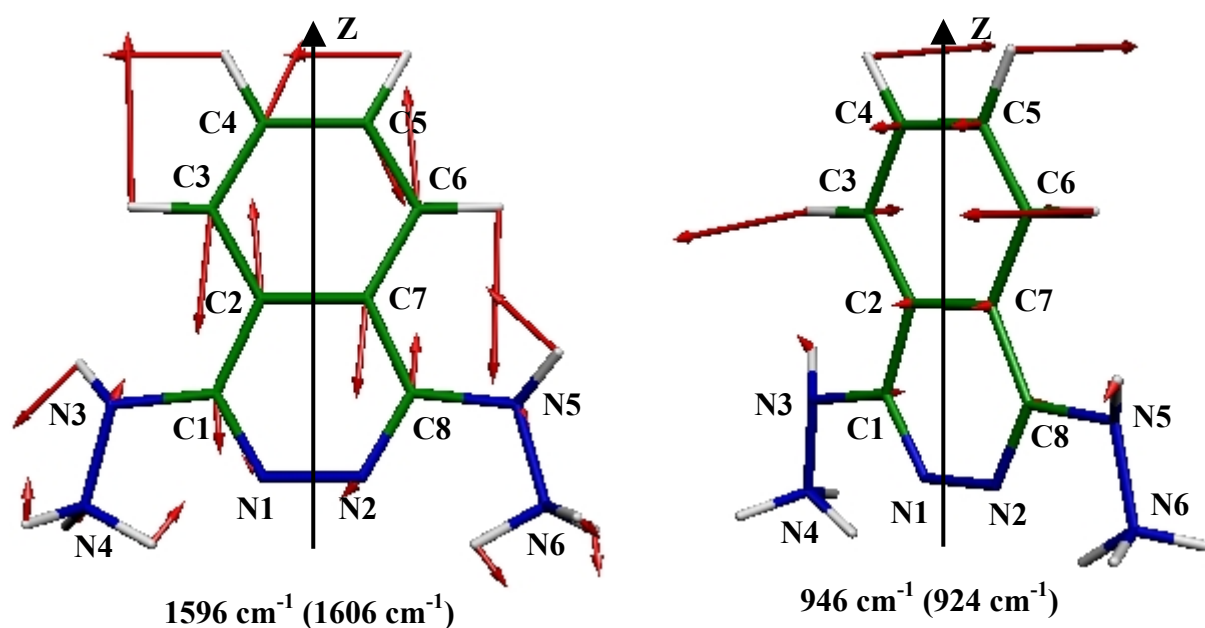


Figure 4.8. The fundamental calculated (BPW91/6-311+G(d)) vibrational modes of tautomeric form **1**, which imply in-plane CH bending and ring stretching modes and out-of-plane CH bending modes. The experimental SERS values are given in parentheses.

The SERS spectra of DHPZ sulfate (Figure 4.7a-c) present a medium broad band at around 230 cm^{-1} , which can be due to the Ag-N stretching mode, characteristic for the N-adsorbed species in SERS spectra under 250 cm^{-1} . This may indicate a bonding with the surface through the lone pairs of the nitrogen atoms located on the phthalazine system. Unfortunately, this cannot be a decisive argument, even if the band is broad enough and stronger than the very weak one at 235 cm^{-1} , which have been ascribed to an out-of-plane skeletal deformation in the FT-Raman spectrum of DHPZ sulfate and may overlap in the SERS spectrum with the Ag-N stretching mode. According to the proposed orientation and the surface selection rule, the relative intensity of this skeletal distortion mode should increase, whereas the Ag-N stretching mode should decrease with a decrease in the DHPZ sulfate solution concentration.

With an increase in the DHPZ sulfate solution concentration, the SERS spectrum of DHPZ sulfate (Figure 4.7d, e) becomes very noisy, and up $10^{-4} \text{ mol L}^{-1}$ no signal could be detected. This concentration may be sufficient to cause coverage with DHPZ sulfate of the surface, and therefore, no SERS spectrum can be recorded upper this concentration. However,

even if at about 10^{-5} mol L⁻¹ the SERS spectrum (Figure 4.7d) is noisy and presents a significant background, totally symmetric modes of phthalazine (1452, 1382, 799, and 529 cm⁻¹) could be observed at almost the same position as in the SERS spectrum at 4.2×10^{-6} mol L⁻¹ (Figure 4.7c), but with a smaller intensity. But other in-plane vibrational modes, as the in-plane CH stretching, ring stretching, CH deformation, and skeletal deformation modes, which have been assigned at almost the same wavenumbers, 1608, 1576, 1354, 1161, and 1116 cm⁻¹, respectively, as in the SERS spectrum at 4.2×10^{-6} mol L⁻¹, have higher or similar intensities. On the other hand, the 988 cm⁻¹ band, for example, which has been ascribed to an out-of-plane CH deformation, exhibit intensity enhancement. One can notice that the 230 cm⁻¹ band has also a similar broad profile, as at 4.2×10^{-6} mol L⁻¹, but perhaps a little enhanced. Taking into account all these spectral changes, we suppose that at this concentration (4.0×10^{-5} mol L⁻¹) the adsorbate has a rather random orientation to the Ag surface, as phthalazine in solution. As one increases the concentration, the SERS signal becomes weaker due probably to the surface coverage with DHPZ sulfate.

4.1.3 Conclusions

In conclusion, the computed structural parameters for tautomer **2** agree very well with the reported experimental data, while for tautomer **1** no crystal structure data were yet published. The theoretical calculations and the SERS spectra suggest that there is no surface photodecomposition of 1,4-dihydrazinophthalazine sulfate on the metal surface. SERS spectra of 1,4-dihydrazinophthalazine sulfate could be recorded even at nanomolar concentration with a conventional SERS setup. At about 10^{-6} mol L⁻¹ the molecular skeletal plane is probably oriented perpendicular to, or at least significantly tilted with respect to, the Ag surface plane. As the concentration is decreased, the molecule tends to lie flat on the Ag surface. With the increase in solution concentration, a surface coverage with 1,4-dihydrazinophthalazine sulfate may occur.

4.2 *Caffeine (1,3,7-trimethyl-2,6-purinedione)*

4.2.1 *Molecule presentation*

Caffeine (1,3,7-trimethyl-2,6-purinedione) is a natural product widely distributed in coffee beans or several other plants.^{210, 211} Coffee beans contain relatively high concentrations of caffeine, which is perceived by some as having adverse effects on health.²¹² Nevertheless, caffeine is extensively used as a smooth muscle relaxant; it is often included in small doses in analgesics and cold remedies because of its stimulant action; and it is consumed in beverages such as coffee, tea and a variety of soft drinks. The drug's absorption processes at the human body level take place at different pH values, usually at nearly neutral pH values in blood and human plasma.^{213, 214} Also, the low solubility of caffeine (20g/L) makes it very difficult to obtain information from the pH dependent Raman spectra. Therefore, the SERS spectra of caffeine were recorded for the first time at different pH values and were discussed; taking into account that information about the species present under particular conditions could be of relevance to the interpretation of biochemical processes. A sodium citrate-reduced silver colloid served as a biological artificial model.

The vibrational fundamentals from the Raman spectrum were analyzed by comparing the vibrational modes with those from literature²¹⁵⁻²¹⁹ in conjunction with the results of our theoretical calculations. Additionally, the geometry of the anhydrous form of caffeine was characterized for the first time using DFT calculations.

4.2.2 *Results and discussion*

4.2.2.1 *Geometry optimization*

The optimized structure of caffeine, which has been computed at a high level of theory using B3LYP/6-311+G(d), is presented in Figure 4.9. The structural parameters of caffeine as calculated with the BPW91/6-31+G(d), BPW91/6-311+G(d), B3LYP/6-31+G(d), and B3LYP/6-311+G(d) methods are listed in Table 4.3. The previously reported crystal structure data of 1:1 caffeine and 5-chlorosalicylic acid complex²²⁰ are also shown in Table 4.3 to assess the accuracy of the geometry optimizations. The distances and angles for the nonhydrogen atoms of the crystal structure have standard deviations of 0.7 pm and 0.3°, respectively.²²⁰ The distances and angles for the hydrogen atoms have an average uncertainty of approximately 7 pm and 2°, respectively.²²⁰ As shown by Shefter,²²⁰ there are some differences between the structural parameters of this complex and that of caffeine hydrate as reported earlier by Sutor.²²¹ These discrepancies may reflect the higher uncertainty in the X-

ray study of Sutor or possibly the effect of intermolecular polarization bonding. Thus, with the help of DFT calculations we have tried to characterize the anhydrous form of caffeine and to get over these discrepancies.

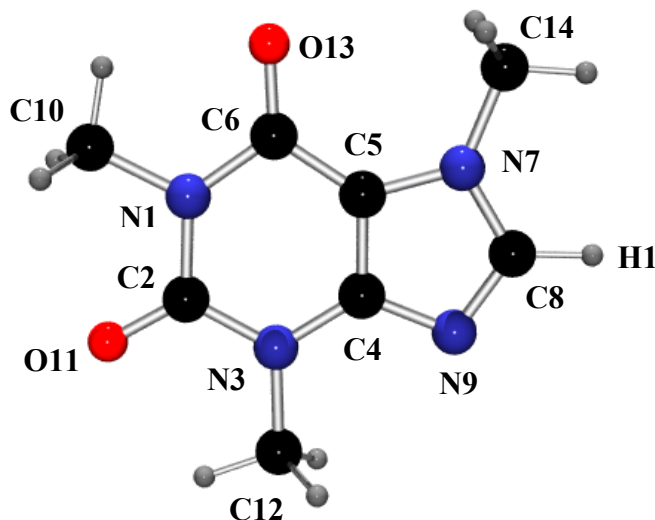


Figure 4.9. The B3LYP/6-311+G(d) optimized geometry of caffeine.

The theoretical methods described above were applied to a molecular geometry without symmetry restrictions and to a geometry that was restricted to C_s symmetry. Using the C_s symmetry, the rotational conformation of one of the methyl groups caused difficulties with convergence with the B3LYP functional and the optimization yielded structures with one low imaginary harmonic wavenumber corresponding to the N-CH₃ rotation, which indicated a saddle point. However, this difficulty was removed by freezing the geometry on the methyl group. The calculated geometry with C_1 symmetry was very close to that with C_s symmetry. The absolute energy difference, which contains the ZPE correction, between these imposed structures of caffeine has been determined to be insignificant (e.g., 0.06 kJ/mol with the BPW91/6-311+G(d) method). This seems to indicate the structure of C_s symmetry is possible. One may notice that the calculated bond distances and bond angles are very close to the reported crystal structure data (Table 4.3).²²⁰ For instance, the maximum difference between the calculated and experimental structural parameters was only 2 pm and 1.6°, respectively, with the B3LYP/6-311+G(d) method. However, there are some differences worth noting with respect to the reported study of Shefter.²²⁰ These are between the N9-C8-H1 and H1-C8-N7 bond angles and the C8-H1 bond length, which were not taken into consideration when we determined the maximum differences in comparison with the experimental data, because they involve intermolecular hydrogen bonds. However, note that the DFT calculations refer to the

Table 4.3. Selected calculated structural parameters compared to crystal structure data of caffeine.

| | Exp ²²⁰ | Calc BPW91 | | Calc B3LYP | |
|--------------------------|--------------------|------------|------------|------------|------------|
| | | 6-31+G(d) | 6-311+G(d) | 6-31+G(d) | 6-311+G(d) |
| Bond lengths (pm) | | | | | |
| N1-C2 | 139.7 | 141.6 | 141.5 | 140.8 | 140.8 |
| C2-N3 | 139.2 | 140.4 | 140.3 | 139.4 | 139.3 |
| N3-C4 | 137.3 | 137.9 | 137.7 | 137.5 | 137.3 |
| C4-C5 | 136.1 | 139.4 | 139.0 | 138.3 | 138.0 |
| C5-C6 | 144.1 | 143.6 | 143.4 | 143.3 | 143.1 |
| C6-N1 | 141.3 | 143.0 | 142.9 | 141.8 | 141.8 |
| C5-N7 | 138.8 | 139.3 | 139.2 | 138.8 | 138.7 |
| N7-C8 | 134.3 | 136.6 | 136.4 | 135.7 | 135.5 |
| C8-N9 | 134.1 | 134.0 | 133.6 | 133.2 | 132.8 |
| N9-C4 | 136.1 | 136.7 | 136.4 | 136.0 | 135.8 |
| N1-C10 | 148.2 | 147.0 | 146.7 | 146.9 | 146.8 |
| C2-O11 | 121.1 | 125.5 | 122.8 | 122.6 | 121.8 |
| N3-C12 | 147.8 | 146.6 | 146.5 | 146.9 | 146.3 |
| C6-O13 | 120.8 | 124.1 | 123.4 | 123.4 | 122.4 |
| N7-C14 | 147.0 | 146.7 | 146.1 | 145.9 | 145.8 |
| C8-H1 | 93.0 | 108.9 | 108.7 | 108.2 | 108.1 |
| Angles (°) | | | | | |
| C2-N1-C6 | 127.8 | 127.3 | 127.4 | 126.9 | 127.1 |
| N1-C2-N3 | 116.1 | 116.7 | 116.5 | 117.1 | 116.8 |
| C2-N3-C4 | 119.9 | 119.7 | 119.8 | 119.5 | 119.6 |
| N3-C4-C5 | 121.9 | 121.8 | 121.9 | 121.9 | 121.9 |
| C4-C5-C6 | 123.4 | 123.6 | 123.6 | 123.4 | 123.4 |
| C5-C6-N1 | 110.6 | 110.9 | 110.8 | 111.3 | 111.2 |
| N9-C4-C5 | 111.6 | 112.1 | 112.0 | 111.8 | 112.0 |
| C4-C5-N7 | 106.0 | 105.0 | 105.0 | 105.1 | 105.1 |
| C5-N7-C8 | 105.4 | 105.8 | 105.8 | 105.7 | 105.6 |
| N7-C8-N9 | 113.6 | 113.9 | 113.8 | 113.8 | 113.7 |
| C8-N9-C4 | 103.4 | 103.4 | 103.5 | 103.6 | 103.8 |
| C6-N1-C10 | 116.4 | 117.7 | 117.6 | 118.0 | 117.9 |
| C10-N1-C2 | 115.7 | 115.0 | 114.9 | 115.1 | 115.0 |
| N1-C2-O11 | 122.3 | 121.0 | 121.1 | 120.7 | 120.8 |
| O11-C2-N3 | 121.6 | 122.3 | 124.4 | 122.3 | 122.4 |
| C2-N3-C12 | 118.5 | 119.9 | 119.9 | 120.2 | 120.1 |
| C12-N3-C4 | 121.1 | 120.4 | 120.4 | 120.3 | 120.3 |
| N3-C4-N9 | 126.5 | 126.1 | 126.2 | 126.3 | 126.3 |
| N9-C8-H1 | 128.0 | 124.5 | 124.6 | 124.5 | 124.5 |
| H1-C8-N7 | 119.0 | 121.6 | 121.2 | 121.7 | 121.8 |
| C8-N7-C14 | 126.7 | 127.3 | 127.3 | 127.4 | 127.3 |
| C14-N7-C5 | 127.8 | 127.0 | 127.1 | 127.0 | 127.0 |
| N7-C5-C6 | 130.5 | 131.4 | 131.4 | 131.5 | 131.5 |
| C5-C6-O13 | 127.4 | 126.7 | 126.8 | 126.3 | 126.4 |
| O13-C6-N1 | 122.0 | 122.4 | 122.4 | 122.4 | 122.4 |

gas phase of anhydrous caffeine and not to the solid 1:1 caffeine and 5-chlorosalicylic acid complex or caffeine hydrate.

The C6-C5-C4-N9 and N3-C4-C5-N7 dihedral angles, which were determined to be 180° with all methods, indicate planarity between the two ring units. According to Sutor and Shefter's studies, the atoms comprising the purine ring show a significant degree of puckering, probably due to the contribution of some sp^3 character to the valence state of the nitrogen atoms²²⁰ or to the formation of some hydrogen bonds between the water molecule and N9 (caffeine),²²¹ (caffeine) C8H \cdots O11 (caffeine),²²⁰ and (5-chlorosalicylic acid) C4H \cdots O13 (caffeine)²²⁰.

In this case, the standard deviation in a bond angle was found to be about 1.0° .²²¹ A recent X-ray study on caffeine hydrate²²² proved the formation of those intermolecular hydrogen bonds. The DFT calculations performed on anhydrous caffeine in gas phase led to zero (C_s symmetry) or almost zero (C_1 symmetry) values for the other dihedral angles, as expected.

4.2.2.2 *Vibrational spectroscopy*

Of all the xanthenes, the caffeine molecule has the fewest possibilities of protonation, because the N1, N3, and N7 atoms are methylated. It behaves as a monoacid base, accepting a proton from strong acids. The protonation equilibrium of caffeine has been already studied by ^1H - and ^{13}C -NMR and UV spectroscopies in aqueous sulfuric and perchloric acids, and the $\text{p}K_{\text{BH}^+}$ value was determined to be -0.13 ± 0.03 and 0.18 ± 0.01 , respectively.²²³ The protonation site was established at the N9 atom.²²³ The hydrogen bonding formation at the N1, N3, or N7 atoms was excluded on the previously established grounds and from known experience with pyrrole salts.²²⁴⁻²²⁶ Moreover, arguments based on carbonyl wavenumber shifts were already used in an earlier IR study²¹⁶ to rule out the carbonyl group protonation and to indicate the N9 atom as the only protonation site.

In comparison to other purines and xanthine molecules of physiological interest, like theophylline or theobromine, which can exist in two ionized forms by gaining or losing a proton, caffeine can only accept a proton in acid media, but it can not loose one in basic media, because there is no ionizable proton.^{216, 227} Furthermore, previous NMR and UV studies on xanthenes in their neutral and ionic forms in aqueous solution indicate that caffeine does not present tautomeric forms because of the presence of methyl groups at the N atoms.²²⁷

Figure 4.10 shows a series of SERS spectra of caffeine on Ag colloid as obtained at pH 2.5-9.5. High quality SERS spectra could not be obtained at $\text{pH} > 10$ or < 2 because of the

instability of colloidal particles under extremely acid and basic conditions. In examining Figure 4.10 one can note that the overall SERS spectral pattern changes dramatically with the pH from acid to neutral and then to basic values. Because the tautomeric and deprotonated forms are excluded, the changes in the relative intensity and peak positions in the SERS spectra of caffeine with the pH could be explained by the presence of different caffeine adsorbed species and/or the reorientation of the molecule to the Ag surface. The two forms in which caffeine may exist at basic and acid pH values are called caffeine and protonated caffeine, respectively.

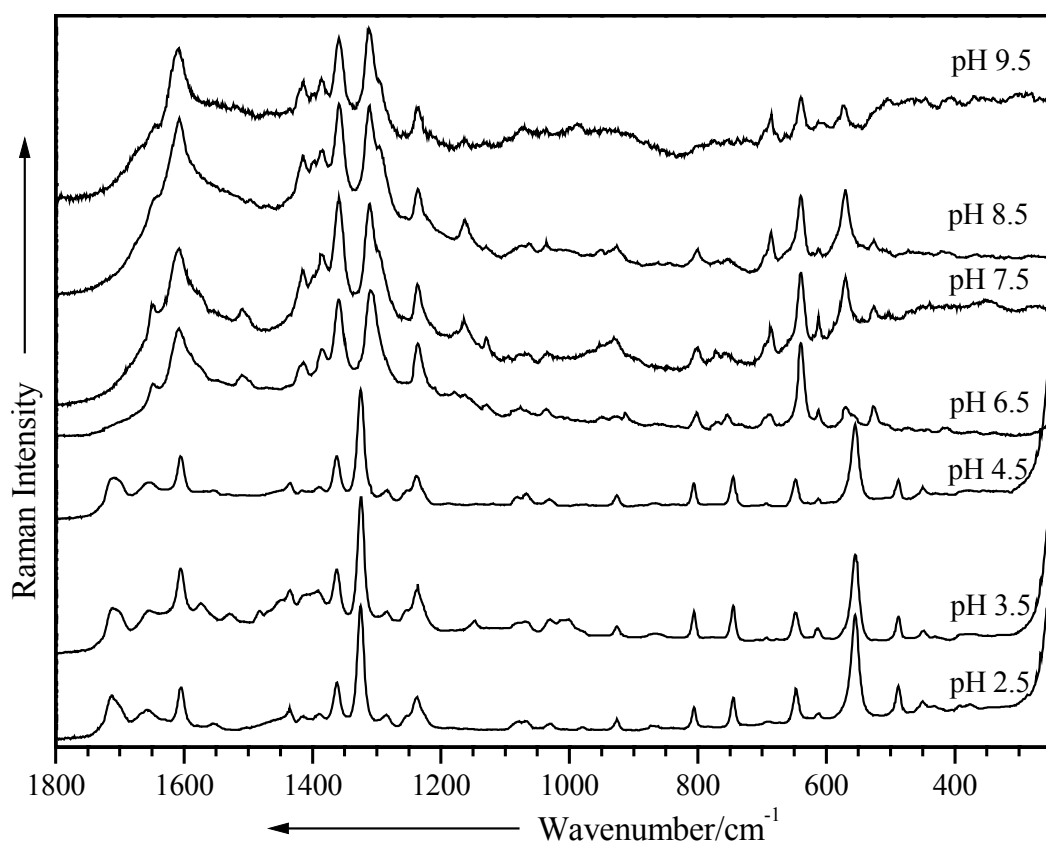


Figure 4.10. The SERS spectra of caffeine on Ag colloid at different solution pH values.

Excitation line: $\lambda_0 = 514.5$ nm.

To accurately determine the changes of molecular identity and the bonding geometry with the pH value, the SERS spectra of caffeine at acid and basic pH values have been discussed in comparison with the FT-Raman spectrum of the solid sample (Figures 4.11 and 4.12). The ordinary Raman spectra of caffeine in an aqueous medium could not be reliably obtained because of the solubility problem. The observed bands and the vibrational assignments are

summarized in Table 4.4. Earlier studies²¹⁵⁻²¹⁹ on caffeine and its derivatives have analyzed the IR and Raman spectra in only the 3800-500 cm^{-1} spectral region, and assignments for some bands have been already proposed. Therefore, in the present study we tried to improve the assignments by performing DFT calculations on caffeine. The calculated vibrational wavenumbers and their Raman scattering activities are also included in Table 4.4.

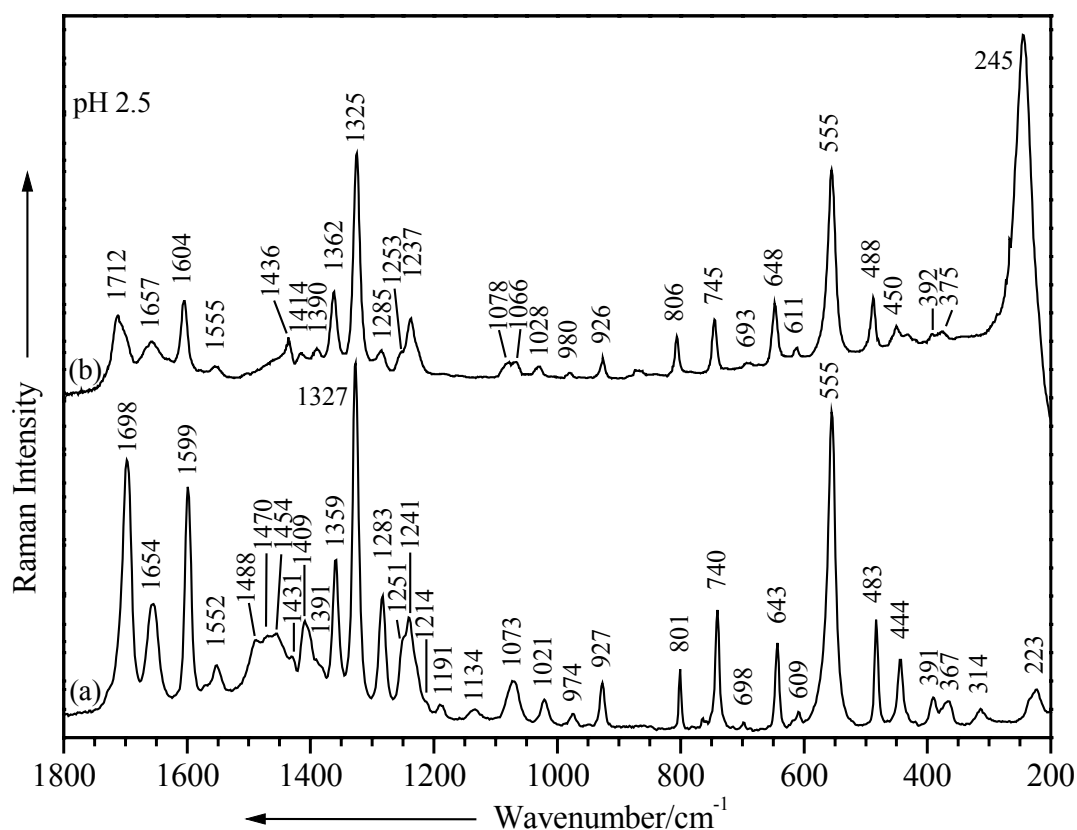


Figure 4.11. The FT-Raman spectrum of neat solid anhydrous caffeine (a) and the SERS spectrum of caffeine on Ag sol at pH 2.5 (b).

Excitation line: $\lambda_0 = 1064 \text{ nm}$ (a) and $\lambda_0 = 514.5 \text{ nm}$ (b).

The vibrational assignment in the experimental spectrum was feasible with the help of the BPW91 calculations (Table 4.4). As expected,²⁰⁰⁻²⁰³ the B3LYP functional overestimated the fundamental modes. Indeed, the calculated vibrational wavenumbers using B3LYP are much larger in the 2000-1000 cm^{-1} range (about 5%) than those using BPW91 with respect to the experimental fundamentals and should be scaled in order to be in good agreement with the experiment.²⁰²⁻²⁰³ In particular, the vibrations involving central atoms with lone pairs and CH vibrations, for which the anharmonicity is large, show important deviations. We wish to

Table 4.4. Selected calculated and experimental Raman and SERS wavenumbers (cm^{-1}), together with their tentative assignments.

| Raman | Calc BPW91 | | Calc B3LYP | | SERS | | Vibrational assignment |
|--------|------------|--------------|------------|--------------|--------|--------|--|
| | 6-31+G(d) | 6-311+G(d) | 6-31+G(d) | 6-311+G(d) | pH 2.5 | pH 8.5 | |
| 1698s | 1714 | 1708 (60.76) | 1762 | 1755 (58.59) | 1712m | broad | in-phase C=O stretching |
| 1654m | 1676 | 1670 (31.95) | 1722 | 1714 (33.16) | 1657w | 1649sh | out-of-phase C=O stretching + C=C sym stretching |
| 1599s | 1583 | 1577 (42.30) | 1632 | 1625 (44.16) | 1604m | 1607vs | C=C sym stretching + C-N sym stretching + CH ₃ sym bending |
| 1552w | 1537 | 1530 (3.33) | 1585 | 1577 (5.99) | 1555vw | 1540vw | imidazole, pyrimidine ring stretching + CH ₃ sym bending + CH bending |
| 1488w | 1497 | 1491 (4.86) | 1539 | 1535 (5.88) | sh | 1496vw | CH ₃ asym bending + CH bending + C ₈ -N ₇ sym stretching |
| 1470w | 1480 | 1475 (15.22) | 1524 | 1520 (11.63) | broad | | CH ₃ asym bending |
| 1454w | 1463 | 1455 (14.87) | 1506 | 1499 (11.20) | | | CH ₃ sym bending + imidazole ring stretching |
| 1431sh | 1458 | 1451 (10.60) | 1499 | 1494 (10.42) | 1436w | | CH ₃ asym bending |
| 1409m | 1420 | 1412 (26.43) | 1465 | 1459 (26.24) | 1414w | 1414ms | CH ₃ sym bending + C ₁₄ -N ₇ sym stretching |
| broad | | | | | | 1398m | |
| 1391sh | 1406 | 1399 (2.79) | 1455 | 1449 (3.57) | 1390w | 1384ms | CH ₃ sym bending |
| 1359m | 1382 | 1374 (5.88) | 1420 | 1411 (6.95) | 1362m | 1359vs | C=N, C-N stretching + CH ₃ sym bending |
| 1327vs | 1349 | 1342 (71.35) | 1393 | 1385 (60.57) | 1325vs | 1311vs | imidazole trigonal ring stretching |
| 1283m | 1275 | 1269 (20.99) | 1316 | 1307 (19.54) | 1285w | 1296sh | C ₂ -N ₃ sym stretching + CH ₃ rocking + imidazole ring stretching |
| 1251sh | 1238 | 1233 (10.90) | 1280 | 1272 (10.15) | 1253sh | 1236m | H-C=N bending + CH ₃ rocking |
| 1241m | 1229 | 1224 (16.49) | 1270 | 1265 (21.24) | 1237m | 1223sh | |
| 1214sh | 1199 | 1197 (2.20) | 1232 | 1230 (2.07) | | | C-N sym stretching + CH ₃ rocking + H-C-N bending |
| 1191vw | 1184 | 1181 (0.75) | 1220 | 1217 (1.22) | | 1162m | CH bending + CH ₃ rocking |
| 1134vw | 1129 | 1125 (0.56) | 1163 | 1162 (1.47) | | 1130vw | CH ₃ asym bending |
| 1073w | 1062 | 1059 (6.67) | 1095 | 1091 (7.38) | 1078vw | 1075vw | H-C=N bending |
| broad | | | | | 1066vw | 1063w | |
| 1021vw | 1007 | 1002 (1.98) | 1044 | 1036 (2.73) | 1028vw | 1036w | CH ₃ rocking + C-N stretching + C-N bending |

69 *Why SERS and DFT?*

| | | | | | | | |
|-------|-----|-------------|-----|-------------|-------|---------------|--|
| 974vw | 965 | 964 (1.21) | 992 | 991 (2.34) | 980vw | 952vw | i.p. pyrimidine deformation + CH ₃ rocking + i.p. C=O deformation |
| 927w | 916 | 914 (5.93) | 943 | 940 (6.60) | 926vw | 926w | imidazole, pyrimidine deformation + CH ₃ rocking + i.p. C=O deformation + CH bending |
| 801w | 786 | 789 (4.98) | 814 | 816 (3.82) | 806w | 800w | i.p. pyrimidine ring deformation + C4-N9=C8 trigonal bending + i.p. C=O deformation + CH ₃ rocking |
| 740m | 729 | 730 (5.47) | 750 | 750 (6.04) | 745m | 754vw | i.p. pyrimidine, imidazole ring deformation + CH ₃ sym bending + CH ₃ rocking |
| 698vw | 674 | 678 (0.18) | 703 | 709 (0.23) | 693vw | 697sh 686m | o.p. pyrimidine, imidazole ring deformation + o.p. C=O deformation + o.p. CH deformation |
| 643w | 627 | 626 (6.50) | 646 | 645 (5.05) | 648m | 640ms | i.p. imidazole ring deformation + i.p. O=C-N deformation + CH ₃ sym bending |
| 609vw | 591 | 592 (0.33) | 612 | 614 (0.26) | 611vw | 613w | o.p. CH deformation + o.p. imidazole ring deformation |
| 555vs | 542 | 540 (28.14) | 555 | 552 (24.83) | 555vs | 570ms | pyrimidine ring breathing + i.p. C14-N7-C deformation + CH bending + CH ₃ sym bending + CH ₃ rocking |
| 483m | 468 | 467 (4.47) | 484 | 483 (3.76) | 488m | 526w | i.p. pyrimidine, imidazole ring deformation + i.p. O=C-N deformation + CH bending |
| 444w | 431 | 431 (3.92) | 444 | 444 (3.37) | 450w | 472vw | + CH ₃ sym bending + CH ₃ rocking |
| 391vw | 380 | 383 (1.89) | 394 | 395 (1.70) | 392vw | 420vw | i.p. C=O deformation + i.p. imidazole ring deformation + CH ₃ rocking + CH ₃ sym bending + CH bending |
| 367vw | 355 | 351 (0.48) | 364 | 360 (0.61) | 375vw | 366vw | CH ₃ torsion + o.p. pyrimidine, imidazole ring deformation + o.p. CH deformation |
| 314vw | 292 | 293 (0.69) | 302 | 302 (0.62) | | 316vw | CH ₃ sym bending |
| 223vw | 217 | 210 (0.75) | 219 | 212 (0.29) | | | o.p. imidazole, pyrimidine ring deformation + CH ₃ torsion + o.p. H ₃ C-N deformation |

Abbreviations: vw - very weak, w - weak, m - medium, ms - medium strong, s - strong, vs - very strong, sh - shoulder; sym - symmetric, asym - asymmetric; i.p. - in-plane, o.p. - out-of-plane. The calculated Raman scattering activities are in parentheses ($\text{\AA}^4/\text{amu}$).

remark that the vibrational modes calculated with the 6-311+G(d) basis set were improved, but not very significantly. However, in the 1000-200 cm^{-1} spectral range, the B3LYP/6-31+G(d) and B3LYP/6-311+G(d) methods predicted the observed wavenumbers with good accuracy.

The Raman scattering activities predicted at the B3LYP/6-311+G(d) and BPW91/6-311+G(d) levels correlate pretty well with the relative intensities of the FT-Raman spectrum of neat solid caffeine (Table 4.4).

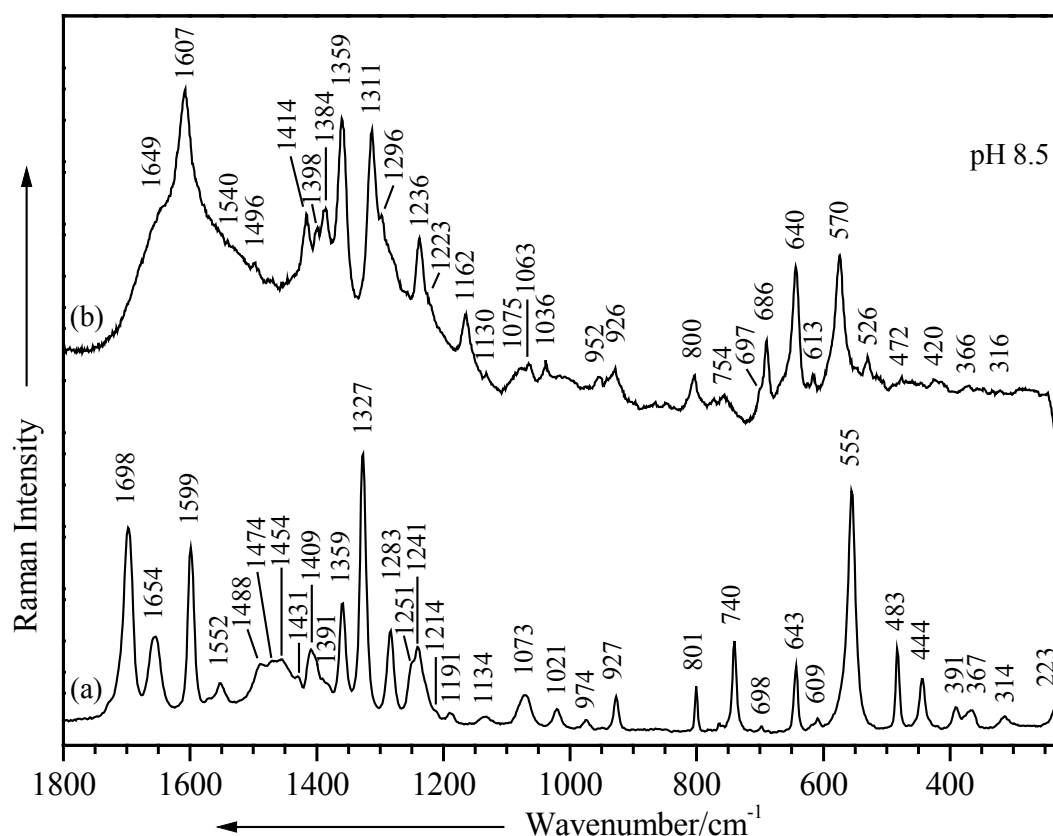


Figure 4.12. The FT-Raman spectrum of neat solid anhydrous caffeine (a) and the SERS spectrum of caffeine on Ag sol at pH 8.5 (b).

Excitation line: $\lambda_0 = 1064 \text{ nm}$ (a) and $\lambda_0 = 514.5 \text{ nm}$ (b).

The Raman spectrum of caffeine in the region of carbonyl stretching fundamentals consists of two major bands, namely at 1698 and 1654 cm^{-1} (Table 4.4). According to the study of Falk and coworkers,²¹⁷ the band at 1698 cm^{-1} is due to the stretching of the isolated carbonyl (C2=O11), while the band at 1654 cm^{-1} is due to the stretching of the conjugated carbonyl (C6=O13). Nevertheless, our DFT calculations are in good agreement with Nyquist

and Fiedler's experimental results,²¹⁹ in which the two C=O groups couple into an in-phase C=O stretching vibration and an out-of-phase C=O stretching vibration. As our theoretical calculations showed (Figure 4.13), during half of a cycle of the out-of-phase C=O vibrational mode only one of the carbonyl carbon atoms is compressed into the ring, while during half of a cycle of the in-phase C=O vibrational mode both carbonyl carbon atoms are compressed into the ring. Thus, less energy is required to compress one carbonyl carbon atom into the ring during a cycle of the out-of-phase C=O stretching mode than is required to compress both carbonyl carbon atoms into the ring during a cycle of the in-phase C=O stretching mode. Therefore, the out-of-phase C=O vibrational mode should occur at lower wavenumber than the in-phase C=O vibrational mode. The 1698 cm^{-1} Raman band is approximately twice as strong as the 1654 cm^{-1} Raman band (Figure 4.11), and this may support the assignment of the 1698 cm^{-1} band to the in-phase C=O stretching mode and the 1654 cm^{-1} band to the out-of-phase C=O stretching mode for caffeine. As one can notice (Figure 4.13), the out-of-phase C=O stretching mode mixes with the C=C stretching mode, which is probably due to the conjugated character of the C6=O13 carbonyl, which was also observed by Falk and coworkers²¹⁷.

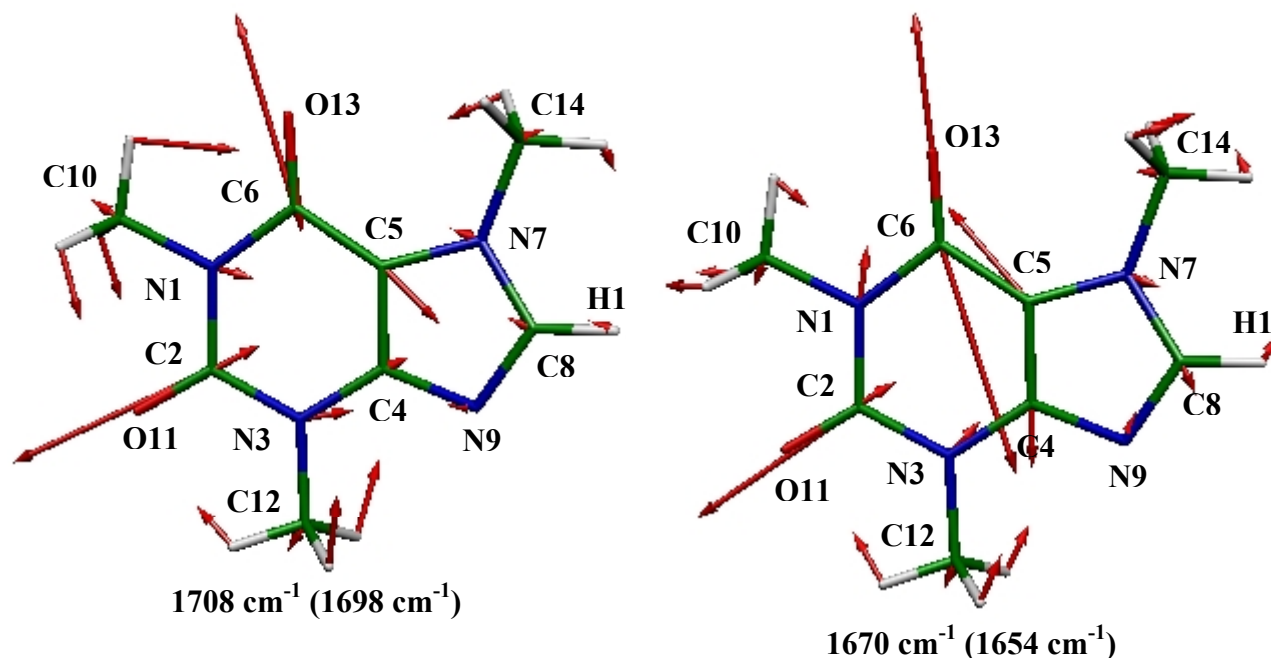


Figure 4.13. The fundamental calculated (BPW91/6-311+G(d)) vibrational modes of caffeine, which imply in-phase C=O and out-of phase C=O stretching modes. The experimental Raman values are given in parentheses.

To the best of our knowledge, no Raman bands corresponding to the ring breathing and trigonal stretching modes have been assigned so far for caffeine. Taking into account the earlier Raman and SERS studies on other purine bases, such as adenine, guanine, xanthine, and hypoxanthine,^{178, 228} and with the help of the DFT calculations, the band at 555 cm^{-1} that has a very strong relative intensity (Figure 4.11) has been tentatively assigned to the ring breathing mode of caffeine (Figure 4.14). However, de Matas et al's recent FT-Raman study on caffeine and caffeine hydrate ascribed this vibrational mode to an O=C-N deformation.²¹⁵

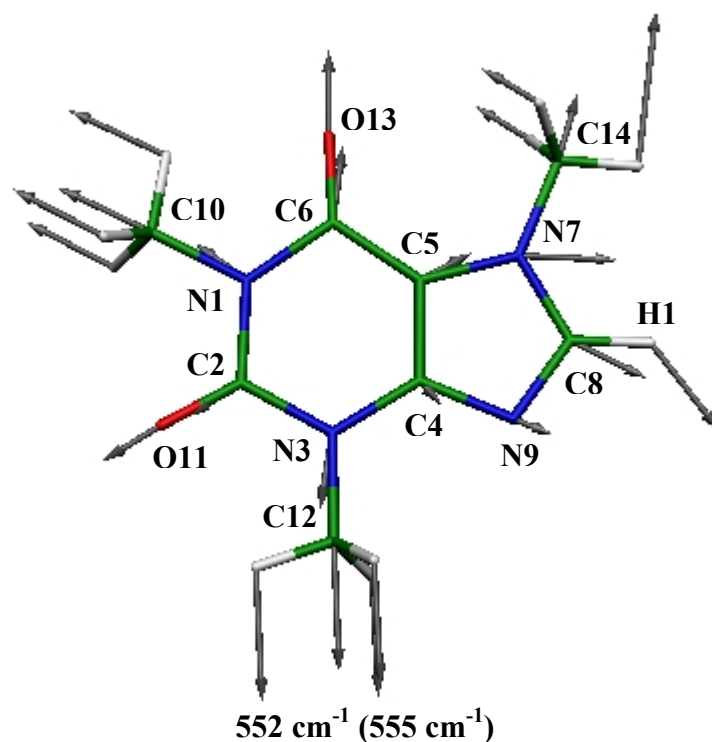


Figure 4.14. The fundamental calculated (B3LYP/6-311+G(d)) pyrimidine ring breathing mode of caffeine. The experimental Raman value is given in parentheses.

A further discrepancy appeared for the very strong peak at 1327 cm^{-1} in the Raman spectrum of anhydrous caffeine (Figure 4.11). Although de Matas and coworkers attributed the band to a C-N stretching mode,²¹⁵ our theoretical calculations suggested a skeletal vibration, namely, a trigonal stretching mode (Figure 4.15). However, consistent with previous findings, these two vibrational modes should be the most prominent bands in the Raman spectrum of such purine systems^{178, 228} and play a very important part in the characterization of the adsorbate-surface interactions, specifically the orientation of the adsorbed species on the metal surface.

The SERS spectrum of caffeine on Ag sol at pH 2.5 is presented in Figure 4.11 in comparison to the FT-Raman spectrum of neat solid anhydrous caffeine. It should be noted

that the band shifts are relatively small between the SERS and normal Raman spectra, excepting the shift of the in-phase C=O stretching mode. Further, large differences in the relative intensity of some bands, particularly in the same region of carbonyl stretching fundamentals, can be also observed. Therefore, we suppose that both electromagnetic and chemical mechanisms are involved in the interaction between caffeine and the Ag colloid, but the contribution of the electromagnetic mechanism to SERS seems to be dominant.

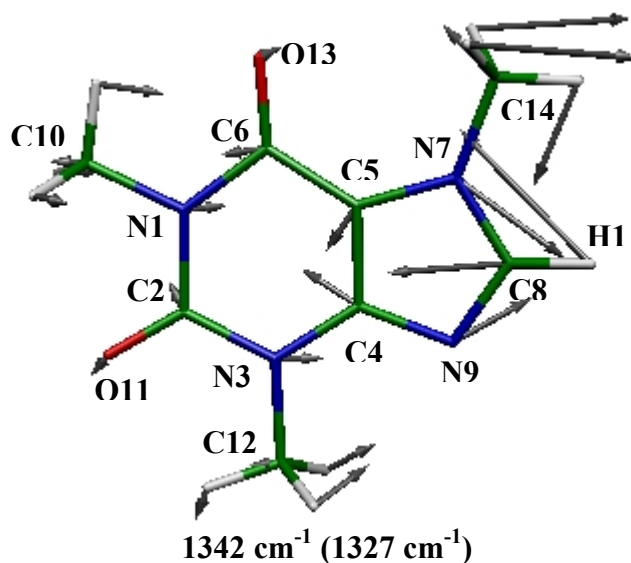


Figure 4.15. The fundamental calculated (BPW91/6-311+G(d)) imidazole trigonal ring stretching vibration of caffeine. The experimental Raman value is given in parentheses.

A closer examination of the region of carbonyl stretching fundamentals shows some interesting changes (Figure 4.11). The in-phase C=O stretching mode assigned in the FT-Raman spectrum at 1698 cm^{-1} is significantly shifted to 1712 cm^{-1} and drops substantially in intensity in the SERS spectrum of caffeine at pH 2.5. The out-of-phase C=O stretching mode, attributed to the peak at 1654 cm^{-1} in the FT-Raman spectrum, appears in the SERS spectrum at almost the same value (1657 cm^{-1}) and becomes weaker, but not so significant as the in-phase C=O stretching mode. Taking into account the mentioned variations, which are more pronounced for the band at 1698 cm^{-1} , and the conjugated character of the C6=O13 carbonyl, whose stretching mode strongly mixes with the C=C stretching mode to give rise to the signal at 1654 cm^{-1} , we presume an interaction of the molecule through one or both oxygen atoms, more probably through the O11 atom, with the silver surface. The precise determination of the adsorption site of the caffeine on the Ag surface is fraught with problems. One can see from the chemical structure (Figure 4.9) that caffeine has three atoms (O11, O13, and N9) capable

of forming bonds with the silver surface, while in the protonated form only the two oxygen atoms are available. The best way of treating this problem is to enumerate the negative charge density on each of these possible active sites. The higher the negative charge density is on the atom, the higher the probability of it acting as an adsorptive site for the Ag substrate.

Table 4.5. Partial charges (e) situated on selected atoms of caffeine as determined with the Natural Population Analysis.

| Atom | Calc BPW91 | | Calc B3LYP | |
|---------------------|------------|------------|------------|------------|
| | 6-31+G(d) | 6-311+G(d) | 6-31+G(d) | 6-311+G(d) |
| Caffeine | | | | |
| O11 | -0.609 | -0.608 | -0.643 | -0.640 |
| O13 | -0.597 | -0.597 | -0.630 | -0.629 |
| N1 | -0.479 | -0.484 | -0.507 | -0.512 |
| N3 | -0.437 | -0.444 | -0.466 | -0.472 |
| N7 | -0.353 | -0.357 | -0.370 | -0.374 |
| N9 | -0.495 | -0.500 | -0.519 | -0.523 |
| C2 | 0.775 | 0.781 | 0.830 | 0.833 |
| C4 | 0.341 | 0.352 | 0.364 | 0.376 |
| C5 | -0.018 | -0.012 | -0.026 | -0.022 |
| C6 | 0.597 | 0.600 | 0.649 | 0.650 |
| C8 | 0.190 | 0.231 | 0.222 | 0.262 |
| C10 | -0.514 | -0.383 | -0.480 | -0.353 |
| C12 | -0.509 | -0.380 | -0.476 | -0.350 |
| C14 | -0.499 | -0.367 | -0.467 | -0.338 |
| Protonated caffeine | | | | |
| O11 | -0.532 | -0.531 | -0.568 | -0.565 |
| O13 | -0.530 | -0.530 | -0.565 | -0.563 |
| N1 | -0.466 | -0.470 | -0.498 | -0.501 |
| N3 | -0.434 | -0.440 | -0.464 | -0.470 |
| N7 | -0.289 | -0.292 | -0.303 | -0.305 |
| N9 | -0.527 | -0.492 | -0.544 | -0.508 |
| C2 | 0.786 | 0.792 | 0.839 | 0.843 |
| C4 | 0.382 | 0.391 | 0.409 | 0.418 |
| C5 | 0.023 | 0.030 | 0.013 | 0.019 |
| C6 | 0.607 | 0.608 | 0.657 | 0.656 |
| C8 | 0.233 | 0.267 | 0.268 | 0.301 |
| C10 | -0.518 | -0.384 | -0.484 | -0.354 |
| C12 | -0.530 | -0.400 | -0.498 | -0.371 |
| C14 | -0.508 | -0.371 | -0.476 | -0.343 |

The representative plot of the total electron density of caffeine (Figure 4.16) indicates a build-up of charge density on the oxygen and nitrogen atoms and nodes at the other atoms. The DFT calculations at BPW91/6-311+G(d) level of theory (Table 4.5) led to negative charge densities of -0.608 , -0.597 , and -0.500 (e) in caffeine on the O11, O13, and N9 atoms,

respectively, and -0.531 and -0.530 (e), in the protonated form on the O11 and O13 atoms, respectively. One can note that the negative charge densities on the N1, N3, and N7 atoms are also large, but not as significant as on the oxygen atoms. The other methods led to similar values. Therefore, the negative charge density in both forms is higher on the oxygen atoms than on the N9 atom. As expected, the C2=O11 carbonyl group is a little more basic than the C6=O13 carbonyl group, because the C2=O11 carbonyl group is joined to two N-CH₃ groups while the C6=O13 carbonyl group is joined to one N-CH₃ group and to an sp² carbon atom. Therefore, it seems likely that both oxygen atoms can be active sites for the adsorption process, but the O11 atom has a little higher probability.

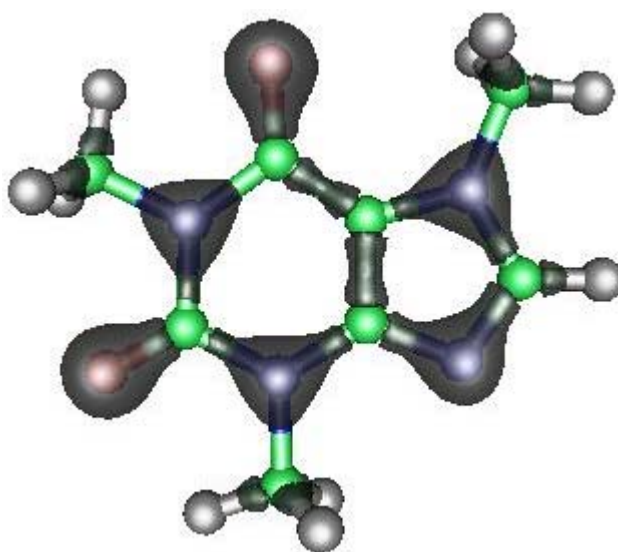


Figure 4.16. The total electron density of caffeine. The isosurface value is 0.26.

In order to gain more information about possible adsorptive sites for the Ag substrate, the spectral region around 200 cm^{-1} was examined more closely, because the Ag-O, Ag-N, and Ag-Cl stretching modes are generally observed in this low wavenumber spectral region. The SERS spectrum of caffeine at pH 2.5 presents a very strong broad band at about 245 cm^{-1} (Figure 4.11), which can be due to the Ag-O stretching mode. This may indicate a bonding with the Ag surface through the lone pairs of the oxygen atoms located on the pyrimidine system, but one should consider that at this pH value (2.5) a significant amount of HCl was added to the Ag colloid to adjust the pH. In examining the profile of the signal it seems that it is attributable to the Ag-Cl stretching mode, which appears normally at about 244 cm^{-1} ,²²⁹ and overlaps the possible Ag-O stretching bands. Moreover, the solid state FT-Raman

spectrum (Figure 4.11) also shows a very weak band at 223 cm^{-1} . Therefore, assignment of the 245 cm^{-1} SERS band is not unequivocal.

Moreover, at pH 2.5, when the protonation may occur at N9 atom according to the literature, the molecule is chemisorbed on the Ag surface through one of the oxygen atoms, probably through O11. However, the spectral features suggest that the electromagnetic mechanism predominates in this case.

To determine the orientation of caffeine adsorbed on the metal surface through oxygen, the SERS surface selection rules were used.^{27, 28, 175, 209} However, the orientation determination is quite difficult in this case, because the molecule is of very low symmetry (C_s point group) and therefore almost all the vibrations of the adsorbed molecules have a Raman polarizability component perpendicular to the surface in all orientations.

From Figures 4.10 and 4.11 it can be observed that as the pH of the solution is increased from 2.5 to 4.5, there is no sharp change (at most 2 cm^{-1}) in the peak position of the in-plane ring breathing and trigonal stretching modes with respect to the corresponding modes assigned in the FT-Raman spectrum at 555 and 1327 cm^{-1} . Moreover, as in the FT-Raman spectrum, these bands dominate the SERS spectra, which seems to suggest that caffeine is adsorbed on the metal surface with the molecular plane lying perpendicular to it. Also, the bands at 1359 , 801 , 740 , 643 , 483 , and 444 cm^{-1} are shifted very little in the SERS spectra in comparison with the FT-Raman spectrum, namely to 1362 , 806 , 745 , 648 , 488 , and 450 cm^{-1} in the SERS spectrum of caffeine at pH 2.5 (Figure 4.11) and have similar or higher relative intensity. Based on the surface selection rules, these vibrational modes should have a large Raman polarizability change in the z direction (when z is normal to the local metal surface). Indeed, according to the DFT calculations and previous studies,^{178, 215-219, 222, 228} all these modes are mainly due to in-plane vibrational modes, as shown in Table 4.4, with large components that are perpendicular to the metal surface when the molecule has an end-on orientation to the Ag surface.

Another band centered at 1599 cm^{-1} , which was ascribed in the FT-Raman spectrum to the C=C symmetric stretching mode in combination with a C-N symmetric stretching (involving the C4-N3 bond) and a CH₃ symmetric bending mode, shows some interesting changes. At pH values between 2.5 and 4.5, the signal also shifts very little like the other in-plane vibrational modes (5 cm^{-1} to higher wavenumbers), but its relative intensity drops substantially with respect to the FT-Raman spectrum (Figures 4.10 and 4.11). This unexpected change in relative intensity may be due to the protonation at N9, which may occur around these pH values, and its consequent inductive effect at the same atom. Similar behavior is

shown by the bands at 1409 and 1283 cm^{-1} , whose relative intensities decrease from medium to weak in the SERS spectra in comparison to the normal Raman spectrum. According to our DFT results, the intensity of the band at 1283 cm^{-1} comes about as a combination of some in-plane and out-of-plane vibrational modes ($\text{C}_2\text{-N}_3$ symmetric stretching, CH_3 rocking, and imidazole ring stretching modes). When the molecule is adsorbed on the Ag surface through the O11 atom with an end-on orientation (Figure 4.17), the $\text{C}_2\text{-N}_3$ symmetric stretching mode has large Raman polarizability components parallel to the Ag surface and it should therefore exhibit a decrease in intensity, like the CH_3 rocking modes. Analogously, the CH_3 symmetric bending modes, which in combination with a C14-N7 symmetric stretching mode give rise to the signal at 1409 cm^{-1} , also have large Raman polarizability components parallel to the Ag surface. Moreover, if the molecule is adsorbed on the Ag surface through the O11 atom with an end-on orientation as we mentioned above, the C14-N7 bond will be far away from the Ag surface (Figure 4.17).

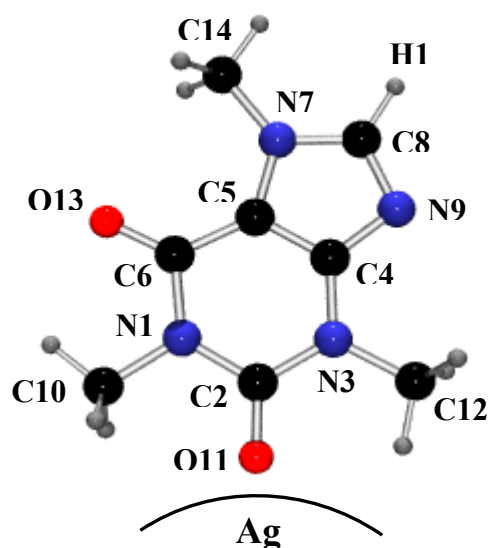


Figure 4.17. The proposed orientation for caffeine on the Ag surface at acid pH values.

Conspicuous differences between the FT-Raman and SERS spectra at these pH values are also found in the bands at 1488, 1470, 1454, 1431, 1191, 1134, and 1073 cm^{-1} (Figures 4.10 and 4.11). The bands in the 1488-1431 cm^{-1} region of the normal Raman spectrum decrease in intensity and overlap, giving rise in the SERS spectra to a weak peak at 1436 cm^{-1} along with a very weak broad shoulder. With the exception of the peak at 1073 cm^{-1} , whose relative intensity also decreases, all the other mentioned vibrational modes are absent in the

SERS spectra (Figures 4.10 and 4.11). According to the DFT calculations (Table 4.4), these vibrations mainly derive their intensities from large values of the α_{xx} , α_{yy} , and α_{xy} components (when z lying normal to the local metal surface). Therefore, based on the SERS surface selection rules, they should be the least intense in the SERS spectra when the molecule has a perpendicular orientation to the Ag surface.

All these aforementioned spectroscopic observations seem to indicate that, at pH values between 2.5 and 4.5, caffeine is adsorbed on the Ag surface with an end-on orientation (Figure 4.17).

At neutral and basic pH values the overall spectral quality deteriorates gradually and the SERS spectra present a sizable background in the 1700-1200 cm^{-1} region. This is probably attributable to the decomposition of the adsorbate on the Ag colloid during the irradiation, as was also observed by Kurokawa and coworkers for a similar compound (theobromine) on a fine Ag particle-doped cellulose gel film using the same laser line.²³⁰ Nonetheless, in comparing the FT-Raman and SERS spectra of caffeine on Ag sol at pH 8.5 (Figure 4.12), one may notice that there are major band shifts and changes in the relative intensities of most of the vibrational modes. Similar differences were observed in all SERS spectra at pH values higher than 4.5 (Figure 4.10), which suggest a strong chemical adsorbate-substrate interaction. Because caffeine does not present tautomeric forms and cannot lose protons in basic media, these changes may be caused by a reorientation of the sample on the metal surface. Therefore, we need to find the group through which the molecule interacts with the Ag surface and how the molecule is anchored to it.

At pH 8.5 (Figure 4.12) a significant shift of the ring breathing mode from 555 cm^{-1} to 570 cm^{-1} with a substantial decrease in relative intensity can be observed. The band at 1327 cm^{-1} , which is assigned to the imidazole trigonal ring stretching, shifts to 1311 cm^{-1} but does not present such a decrease in the relative intensity. These changes may reflect a reorientation of caffeine at the metal surface from perpendicular to parallel upon increasing the solution pH to basic values (Figure 4.18). Moreover, the interesting reverse in the relative intensity of the ring breathing mode at pH 6.5 could also be explained through the reorientation of the molecule, which could occur at around this pH value. Unfortunately, experimental limitations did not enable the observation of possible Ag-O or Ag-N stretching modes under 250 cm^{-1} at these pH values.

There are interesting changes that also show the in-phase and out-of-phase C=O stretching modes. Previous studies on similar compounds have reported and explained the absence of these bands in SERS spectra through a strong interaction of the oxygen of the C=O

groups with the solvent.^{230, 231} But in this case, when passing from neutral to basic pH values, one can clearly distinguish the out-of-phase C=O stretching mode, which strongly mixes with the C=C symmetric stretching mode, as a peak at about 1649 cm^{-1} (Figure 4.10). However, the in-phase C=O stretching mode is barely observed as a very weak shoulder because of the sizable background. In any case, at higher pH values the two C=O vibrational modes can be identified as two broad shoulders of much lower relative intensity (pH 8.5 and 9.5, Figure 4.10). Such changes in the relative intensity of these modes may be attributed to a more favorable π -coordination of the C=O groups and possibly the C=C group at the Ag surface (Figure 4.18). This is further substantiated by the increase in relative intensity of the band at 1607 cm^{-1} (Figures 4.10 and 4.12), which comes about as a combination of the C=C symmetric stretching with a C-N stretching and a CH₃ bending.

A SERS study of similar species on silver colloid¹⁷⁸ showed that the adsorbate orientation is indeed sensitive to some out-of-plane and in-plane modes. In this respect, one can notice that the aforementioned in-plane vibrational modes at 740 , 483 , and 444 cm^{-1} decrease, becoming weak or very weak bands in the SERS spectrum at pH 8.5 compared to the FT-Raman spectrum, and shift to higher wavenumbers (Figure 4.12). However, the peaks at 1359 and 643 cm^{-1} , which also derive their intensities from in-plane vibrational motions, are markedly intensified with an increase in the pH (Figures 4.10 and 4.12). This may reflect a possible interaction with the Ag surface through the lone pair of the N9 atom on the imidazole ring (Figure 4.18), because these fundamentals, in spite of the coupling with in-plane CH₃ and O=C-N bending modes, mainly represent in-plane C=N and C-N stretching and imidazole ring deformation modes.

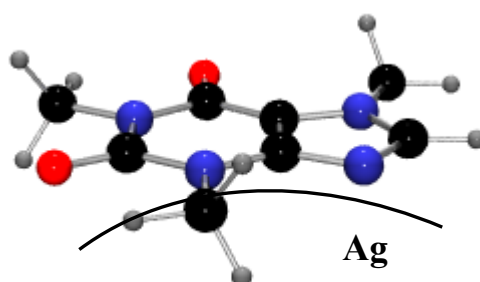


Figure 4.18. The proposed orientation for caffeine on the Ag surface at neutral and basic pH values.

The parallel orientation to the metal surface at high pH is further confirmed by the behavior of the out-of-plane vibrational modes at 1162, 1130, 697, 686 and 613 cm^{-1} , which either appear in the SERS spectrum in passing from neutral to basic pH or are significantly enhanced and shifted (Figures 4.10 and 4.12, Table 4.4). Even the SERS spectrum at pH 8.5 presents a sizable background in the CH_3 bending region; the bands at 1414, 1398, and 1384 cm^{-1} attributed to symmetric CH_3 bending modes also show considerable enhancement.

4.2.3 *Conclusions*

The structural parameters of caffeine and the vibrational fundamentals from FT-Raman spectrum were analyzed and discussed with the help of the DFT-calculations results in order to improve the previous assignments and for a reliable analysis of minute SERS spectra. The calculated structural parameters were very close to the reported crystalline data at both the B3LYP and BPW91 levels of theory: B3LYP/6-31+G(d) and B3LYP/6-311+G(d), and BPW91/6-31+G(d) and BPW91/6-311+G(d). Further, the BPW91 functional gave good results for the calculated harmonic vibrational wavenumbers and no scaling was required.

We tried to characterize the vibrational behavior of caffeine on an Ag surface at different pH values. The flat orientation of mainly chemisorbed caffeine, which is attached through the π -electrons and the lone pair of the N9 atom, was supposed to occur for neutral and basic pH values. At acid pH values caffeine was probably adsorbed on the Ag surface through one or both oxygen atoms, more probably through the O11 atom, with an end-on orientation. Nonetheless, the changes in the overall SERS spectral pattern seem to indicate the electromagnetic mechanism as being the dominant one. The surface selection rules along with the vibrational assignment of SERS spectra and our theoretical results have reasonably explained these adsorbate structures on the Ag surface.

4.3 *Papaverine hydrochloride*

4.3.1 *Molecule presentation*

Papaverine, a benzylisoquinoline alkaloid, is found in the plant *Papaver somniferum* L., and to an extent of 0.5-1% in opium.²³² It acts on smooth muscle throughout the body, causing vasodilatation and a general relaxation of smooth muscle tone.²³³ Papaverine has antispasmodic properties and has also been used as an analgesic. Today it is used as a minor constituent with morphine usually to enhance the analgesic properties of a weaker drug such as aspirin.^{234, 235}

Few N-acyl derivatives of papaverine and related compounds show a variety of activities against AIDS, glaucoma and fungal infections.²³⁶⁻²³⁸ In quest for biologically more potent compounds several substituted N-carbamoyl as well as N-thiocarbamoyl derivatives of tetrahydropapaverine were synthesized and their antispasmodic activity was studied.²³⁹

Natural narcotics and alkaloids are therapeutically used either in the form of natural vegetable drugs, of which they are the most effective component, as various galenic preparations made from these drugs, or in the form of chemical compounds isolated from these drugs or synthesized. In the last instance they occur most frequently in the form of salts readily soluble in water, or as suitable pharmaceutical preparations, the latter applying almost exclusively to synthetic narcotics. In evaluating narcotics and alkaloids the special conditions of the instances mentioned above are to be respected. The determination of salts is relatively the simplest case. Many accepted methods depend on determining the acid component with the aid of titration (hydrochlorides by argentometry, sulfates by alkalimetry, etc.). This method of determination cannot be considered fully adequate, as it is indirect and does not determine the physiologically active component, i.e., the organic base; furthermore it does not take into account the not entirely stoichiometric neutralization of the base during the manufacture of such salts. A very sensitive method to determine the changes in the identity of such compounds could be the pH dependent Raman study.

Therefore, the Raman and SERS spectra of papaverine hydrochloride were recorded for the first time at different pH values and discussed with the assistance of results obtained from DFT calculations in order to characterize the vibrational behavior of the adsorbed species on the metal surface.

4.3.2 Results and discussion

4.3.2.1 Geometry optimization

Since the molecular structure of papaverine is of interest in gaining a better understanding of its pharmacological action, we theoretically characterized for the first time the geometries of its neutral and protonated forms using DFT calculations (Figure 4.19) and then compared them with the previously reported crystal structure of papaverine hydrochloride²⁴⁰ in order to assess the accuracy of the geometry optimization.

The structural parameters of the protonated molecular species, calculated using the BPW91/P1, BPW91/P2, B3LYP/P1, and B3LYP/P2 methods, and the experimental data for papaverine hydrochloride²⁴⁰ are listed in Table 4.6. As one can notice, the calculated bond distances and bond angles agree very well with the reported parameters²⁴⁰ and the B3LYP/P2 method mostly provided the best results. In fact, the maximum differences between the calculated and experimental values were only 3.2 pm and 3°, respectively, with the mentioned method. For the neutral molecular species there are some small differences between the structural parameters, which involve the N2 atom, because in papaverine hydrochloride the N2 atom is protonated and forms a strong hydrogen bond with the chloride ion.²⁴⁰

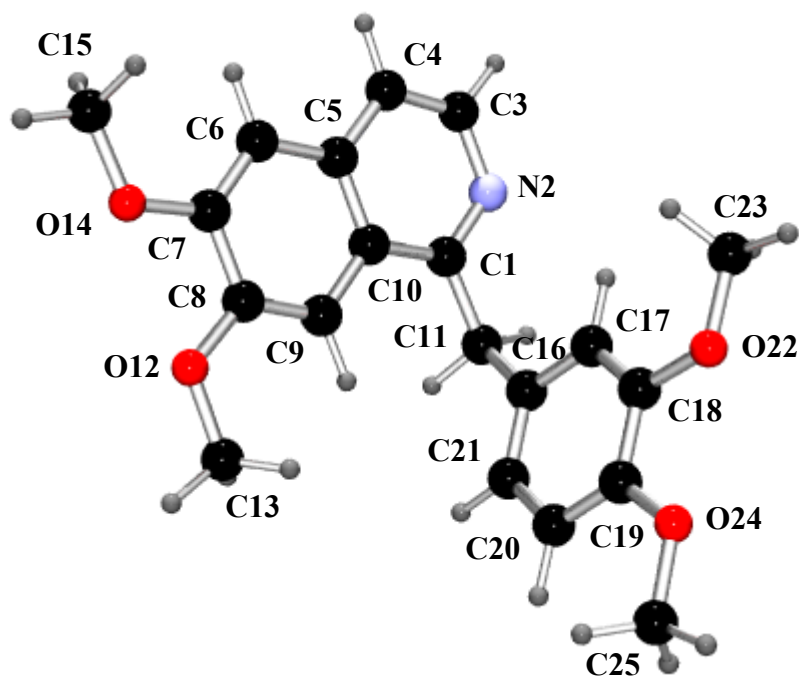


Figure 4.19. The B3LYP/P2 optimized geometry of the neutral form of papaverine.

Another interesting aspect for SERS is the planarity of the system. While the previous X-ray diffraction study indicated a slightly non-planar isoquinoline ring featuring a dihedral angle between the two phenyl planes of 3° ,²⁴⁰ our DFT calculations got closer to the planarity of the system. More exactly, the dihedral angle was calculated to be smaller than 1° . But the benzene ring was determined to be planar in both experimental and theoretical studies and the dihedral angle between the benzene ring and the best plane through the isoquinoline group was calculated to be 108° , which also agrees well with the experimental value of 109° .²⁴⁰

Table 4.6. Selected calculated structural parameters of the protonated form of papaverine in comparison with the crystal structure data of papaverine hydrochloride.

| | Exp ²⁴⁰ | Calc B3LYP | | Calc BPW91 | |
|-------------------|--------------------|------------|-------|------------|--------|
| | | P1 | P2 | P1 | P2 |
| Bond lengths (pm) | | | | | |
| C1-N2 | 133.9(3) | 135.5 | 135.4 | 136.4 | 136.4 |
| C1-C10 | 140.8(3) | 141.5 | 141.5 | 142.2 | 142.2 |
| C1-C11 | 150.9(3) | 151.3 | 151.2 | 151.5 | 151.5 |
| N2-C3 | 135.8(3) | 137.8 | 137.7 | 138.2 | 138.2 |
| C3-C4 | 135.0(4) | 136.8 | 136.8 | 137.7 | 137.7 |
| C4-C5 | 141.2(3) | 142.4 | 142.3 | 142.8 | 142.9 |
| C5-C6 | 140.8(3) | 141.2 | 141.2 | 141.8 | 141.8 |
| C5-C10 | 142.9(3) | 144.8 | 144.3 | 145.3 | 145.03 |
| C6-C7 | 136.7(3) | 138.7 | 138.7 | 139.6 | 139.6 |
| C7-C8 | 143.4(3) | 145.1 | 145.0 | 145.7 | 145.6 |
| C7-O14 | 134.7(3) | 134.4 | 134.2 | 135.2 | 135.1 |
| C8-C9 | 135.9(3) | 138.0 | 138.0 | 139.0 | 139.0 |
| C8-O12 | 135.1(2) | 135.1 | 134.9 | 135.7 | 135.6 |
| C9-C10 | 142.4(3) | 142.4 | 142.4 | 142.7 | 142.7 |
| C11-C16 | 151.1(4) | 152.6 | 152.6 | 153.0 | 153.0 |
| O12-C13 | 143.2(3) | 145.3 | 145.1 | 146.3 | 146.2 |
| O14-C15 | 144.5(3) | 145.6 | 145.4 | 146.5 | 146.5 |
| C16-C17 | 140.1(3) | 141.1 | 141.1 | 141.7 | 141.7 |
| C16-C21 | 137.1(3) | 139.5 | 139.5 | 140.3 | 140.4 |
| C17-C18 | 138.3(3) | 139.5 | 139.5 | 140.3 | 140.3 |
| C18-C19 | 139.4(3) | 142.6 | 142.5 | 143.5 | 143.4 |
| C18-O22 | 137.0(2) | 136.8 | 136.5 | 137.5 | 137.3 |
| C19-C20 | 137.8(3) | 139.5 | 139.5 | 140.4 | 140.4 |
| C19-O24 | 136.3(3) | 136.5 | 136.3 | 137.2 | 137.1 |
| C20-C21 | 139.6(4) | 140.5 | 140.5 | 141.1 | 141.1 |
| O22-C23 | 142.6(3) | 144.3 | 144.1 | 145.2 | 145.2 |
| O24-C25 | 141.3(3) | 144.7 | 144.5 | 145.6 | 145.5 |

| | Exp ²⁴⁰ | Calc B3LYP | | Calc BPW91 | |
|-------------|--------------------|------------|-------|------------|-------|
| | | P1 | P2 | P1 | P2 |
| Angles (°) | | | | | |
| C1-N2-C3 | 123.9(2) | 124.7 | 124.7 | 124.8 | 124.8 |
| C1-C10-C5 | 118.6(2) | 118.9 | 118.9 | 118.9 | 118.9 |
| C1-C10-C9 | 122.9(2) | 121.9 | 121.9 | 121.8 | 121.8 |
| C1-C11-C16 | 112.2(2) | 115.2 | 115.2 | 115.5 | 115.5 |
| N2-C1-C10 | 118.6(2) | 118.2 | 118.2 | 118.1 | 118.1 |
| N2-C1-C11 | 116.4(2) | 116.7 | 116.7 | 116.7 | 116.6 |
| N2-C3-C4 | 120.2(2) | 119.1 | 119.1 | 119.0 | 119.0 |
| C3-C4-C5 | 119.8(2) | 120.3 | 120.3 | 120.4 | 120.3 |
| C4-C5-C6 | 121.3(2) | 121.8 | 121.8 | 121.9 | 121.9 |
| C4-C5-C10 | 118.9(2) | 118.8 | 118.8 | 119.4 | 118.8 |
| C5-C6-C7 | 120.1(2) | 120.8 | 120.9 | 120.9 | 120.9 |
| C5-C10-C9 | 118.6(2) | 119.2 | 119.2 | 119.2 | 119.2 |
| C6-C5-C10 | 119.9(2) | 119.4 | 119.4 | 119.4 | 119.3 |
| C6-C7-C8 | 120.5(2) | 119.9 | 119.9 | 119.8 | 119.8 |
| C6-C7-O14 | 125.2(2) | 125.6 | 125.4 | 125.8 | 125.6 |
| C7-C8-C9 | 120.2(2) | 120.0 | 120.0 | 120.0 | 120.0 |
| C7-C8-O12 | 114.0(2) | 114.3 | 114.5 | 114.2 | 114.3 |
| C7-O14-C15 | 116.9(2) | 118.5 | 119.3 | 118.0 | 118.6 |
| C8-C7-O14 | 114.3(2) | 114.5 | 114.7 | 114.4 | 114.6 |
| C8-C9-C10 | 120.7(2) | 120.7 | 120.7 | 120.7 | 120.7 |
| C8-O12-C13 | 117.7(2) | 117.9 | 118.7 | 117.5 | 118.1 |
| C9-C8-O12 | 125.8(2) | 125.7 | 125.5 | 125.9 | 125.7 |
| C10-C1-C11 | 124.9(2) | 125.1 | 125.1 | 125.2 | 125.3 |
| C11-C16-C17 | 119.6(2) | 120.6 | 120.7 | 120.7 | 120.7 |
| C11-C16-C21 | 121.9(2) | 120.1 | 120.1 | 120.0 | 120.0 |
| C16-C17-C18 | 120.6(2) | 120.8 | 120.8 | 120.8 | 120.8 |
| C16-C21-C20 | 121.5(2) | 120.5 | 120.5 | 120.5 | 120.5 |
| C17-C16-C21 | 118.5(2) | 119.2 | 119.2 | 119.3 | 119.2 |
| C17-C18-C19 | 120.1(2) | 119.6 | 119.7 | 119.6 | 119.6 |
| C17-C18-O22 | 124.4(2) | 125.1 | 125.0 | 125.3 | 125.1 |
| C18-C19-C20 | 119.6(2) | 119.2 | 119.2 | 119.2 | 119.2 |
| C18-C19-O24 | 115.6(2) | 115.4 | 115.6 | 115.2 | 115.4 |
| C18-O22-C23 | 117.8(2) | 117.8 | 118.5 | 117.2 | 117.8 |
| C19-C18-O22 | 115.5(2) | 115.2 | 115.4 | 115.0 | 115.2 |
| C19-C20-C21 | 119.7(2) | 120.6 | 120.6 | 120.6 | 120.6 |
| C19-O24-C25 | 117.7(2) | 117.6 | 118.3 | 117.0 | 117.6 |
| C20-C19-O24 | 124.8(2) | 125.4 | 125.2 | 125.6 | 125.4 |

The standard 6-31G basis set was used for H and C in conjunction with the 6-31+G(d) (combination denoted P1) or 6-311+G(d) (combination denoted P2) basis sets for N and O.

4.3.2.2 *Vibrational spectroscopy*

The FT-Raman spectrum of papaverine hydrochloride in solid state is displayed in Figure 4.20.

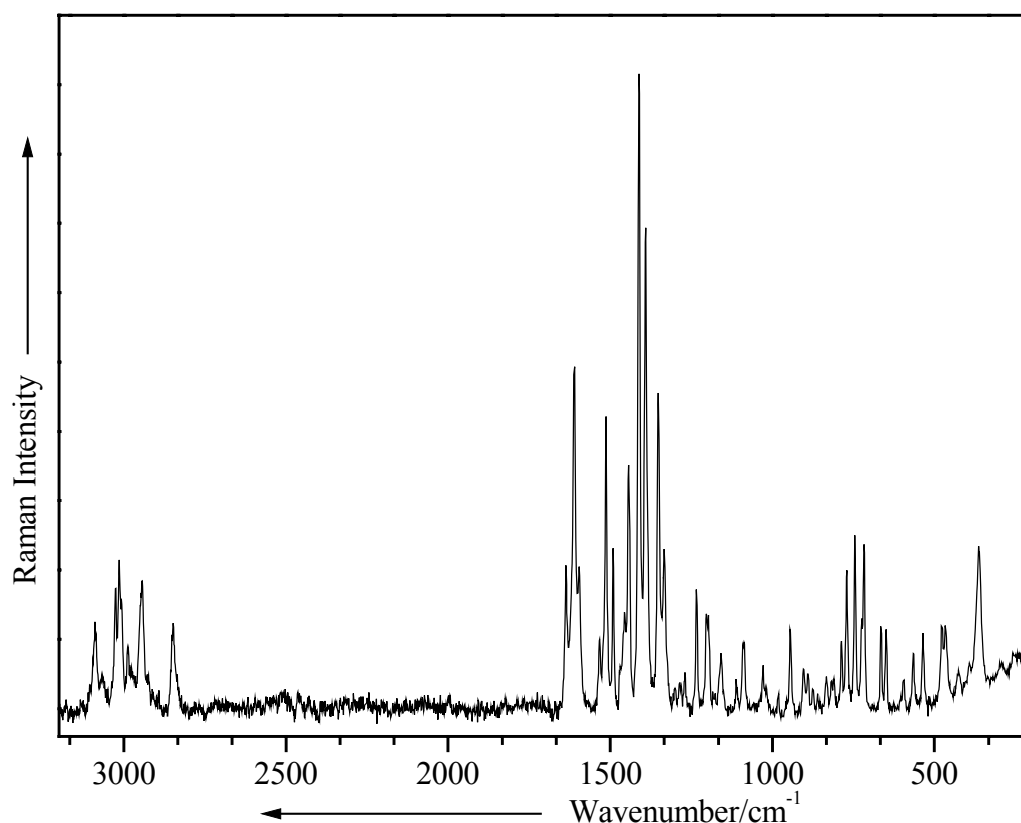


Figure 4.20. The FT-Raman spectrum of solid papaverine hydrochloride.

Excitation line: $\lambda_0 = 514.5$ nm.

The observed bands and the vibrational assignment are summarized in Table 4.7. Again, for a correct interpretation of the SERS data it was necessary to have a complete vibrational assignment of the papaverine hydrochloride Raman spectrum as a guideline. Consequently, the vibrational fundamentals from the Raman spectrum (Figure 4.20) were analyzed by comparing the vibrational modes with those assigned in the literature for quinoline, isoquinoline,²⁴¹⁻²⁴³ naphthalene,^{198, 199, 244, 245} and benzene,²⁴⁶ in conjunction with our theoretical calculations.

As expected, the vibrational assignment in the experimental spectrum was feasible with the help of the BPW91 calculations (Table 4.7), while the B3LYP functional overestimated the fundamental modes.²⁰⁰⁻²⁰³ Also, the 6-311+G(d) basis set improved, but not significantly, the values calculated with the smaller 6-31+G(d) basis set. In spite of the neglect of anharmonicity and of the fact that the DFT calculations refer to the gas phase, the BPW91/

Table 4.7. Selected calculated and experimental wavenumbers (cm^{-1}), together with their tentative assignments.

| Raman | Calc BPW91 | | Calc B3LYP | | Vibrational assignment |
|--------|------------|---------------|------------|------|--|
| | P1 | P2 | P1 | P2 | |
| 1637w | 1621 | 1620 (62.17) | 1671 | 1671 | isoq skeletal stretching (CC sym) + i.p. isoq CH deformation |
| 1610ms | 1611 | 1611 (74.00) | 1660 | 1660 | ph quadrant ring stretching + i.p. ph CH deformation + CH ₂ wagging |
| 1596w | 1592 | 1592 (29.40) | 1642 | 1641 | ph quadrant ring stretching + isoq skeletal stretching (CC, CN sym) + i.p. isoq, ph CH deformation + CH ₂ twisting + CH ₃ sym bending |
| 1532vw | 1522 | 1522 (8.76) | 1568 | 1569 | ph semicircle ring stretching + i.p. ph CH deformation + CH ₃ asym bending + CH ₂ scissoring |
| 1513m | 1516 | 1517 (15.69) | 1559 | 1561 | isoq skeletal stretching (CC) + CH ₃ asym bending |
| 1491w | 1489 | 1489 (31.88) | 1538 | 1539 | CH ₃ asym bending |
| 1468sh | 1457 | 1459 (5.76) | 1501 | 1503 | CH ₃ sym bending + ph semicircle ring stretching |
| 1455w | 1450 | 1453 (12.78) | 1494 | 1497 | CH ₃ sym bending + i.p. ph CH deformation |
| 1443m | 1444 | 1446 (26.06) | 1489 | 1490 | CH ₃ sym bending + i.p. isoq CH deformation |
| 1411vs | 1430 | 1429 (100.45) | 1464 | 1463 | isoq skeletal stretching (C sym gamma) + i.p. isoq, ph CH deformation + C ₁ C ₁₁ sym stretching + CH ₃ sym bending + CH ₂ wagging |
| 1391s | 1388 | 1387 (20.13) | 1403 | 1401 | ph ring stretching + CH ₂ wagging + CH ₃ rocking |
| 1351ms | 1368 | 1364 (127.22) | 1399 | 1397 | isoq skeletal stretching (CC, CN sym) + i.p. isoq CH deformation + CH ₂ twisting |
| 1333w | 1314 | 1313 (12.31) | 1355 | 1354 | CH ₂ wagging + i.p. ph, isoq CH deformation + C ₁ C ₁₁ sym stretching |
| 1300vw | 1305 | 1304 (3.03) | 1347 | 1345 | i.p. isoq, ph CH deformation + ph ring stretching + CH ₂ wagging |
| 1286vw | 1292 | 1291 (4.58) | 1334 | 1333 | CH ₂ wagging + i.p. isoq, ph CH deformation |
| 1269vw | 1278 | 1276 (2.06) | 1311 | 1309 | isoq skeletal stretching (CCC, CN) + i.p. isoq CH deformation + CH ₂ wagging + CH ₃ sym bending + C _{isoq} O sym stretching |
| 1234w | 1230 | 1228 (15.77) | 1258 | 1257 | i.p. isoq CH deformation + CH ₂ twisting + isoq skeletal stretching (CC, CN) |
| 1203w | 1195 | 1195 (23.70) | 1228 | 1228 | CH ₂ twisting + i.p. ph, isoq CH deformation + CH ₃ rocking |
| 1197w | 1190 | 1190 (6.63) | 1222 | 1224 | CH ₃ rocking + i.p. ph CH deformation + CH ₂ twisting + C ₁₁ C ₁₆ sym stretching |
| 1158vw | 1155 | 1154 (7.87) | 1189 | 1189 | CH ₃ rocking + i.p. isoq, ph CH deformation + isoq skeletal bending (CCC) |

87 *Why SERS and DFT?*

| | | | | | |
|--------|------|--------------|------|------|--|
| 1111vw | 1130 | 1133 (0.69) | 1165 | 1170 | + C _{isoq} OC _{methyl} asym stretching + CH ₂ twisting |
| 1088vw | 1084 | 1083 (20.21) | 1115 | 1114 | CH ₃ rocking |
| 1028vw | 1044 | 1043 (1.18) | 1077 | 1076 | isoq skeletal bending (CCN) + i.p. isoq CH deformation + CH ₂ twisting |
| 1017vw | 1016 | 1012 (3.07) | 1052 | 1049 | i.p. isoq skeletal bending + C _{13,15} O sym stretching + o.p. ph CH deformation + CH ₂ rocking + CH ₃ rocking |
| 981vw | 1004 | 998 (1.60) | 1040 | 1036 | C ₂₃ O sym stretching + ph ring stretching + i.p. ph CH deformation + CH ₃ rocking |
| 946w | 946 | 944 (3.78) | 980 | 979 | ph ring breathing + C ₂₅ O sym stretching + CH ₃ sym bending |
| 904vw | 915 | 913 (6.49) | 964 | 962 | CH ₂ rocking + o.p. ph, isoq CH deformation |
| 891vw | 889 | 888 (4.01) | 918 | 917 | CH ₂ rocking + o.p. ph CH deformation |
| 875vw | 870 | 867 (1.88) | 910 | 907 | o.p. isoq CH deformation + o.p. isoq skeletal distorsion (CCN) + CH ₂ rocking + i.p. ph CH deformation + o.p. C ₁ C ₁₁ bending |
| 861vw | 866 | 862 (1.75) | 905 | 902 | o.p. isoq CH deformation |
| 833vw | 857 | 852 (1.41) | 898 | 894 | o.p. isoq, ph CH deformation |
| 817vw | 823 | 820 (1.82) | 857 | 855 | o.p. isoq, ph CH deformation + CH ₂ rocking |
| 811vw | 812 | 809 (1.14) | 844 | 842 | o.p. isoq, ph CH deformation + CH ₂ twisting |
| 786vw | 784 | 780 (5.46) | 814 | 811 | o.p. isoq, ph CH deformation |
| 770w | 759 | 756 (35.24) | 782 | 779 | o.p. isoq, ph CH deformation + o.p. isoq skeletal distorsion + CH ₂ twisting + C ₁ C ₁₁ C ₁₆ bending |
| 745w | 736 | 735 (3.81) | 760 | 760 | i.p. isoq skeletal distorsion + i.p. ph ring bending + i.p. C _{23,25} OC _{ph} bending + CH ₃ rocking + CH ₂ twisting |
| 724sh | 730 | 729 (19.90) | 752 | 751 | o.p. isoq skeletal distorsion + o.p. ph ring bending + CH ₂ wagging + o.p. C _{ph} O bending + o.p. C ₁₁ C ₁₆ bending + CH ₃ rocking |
| 718w | 716 | 717 (1.54) | 742 | 744 | isoq skeletal breathing + CH ₂ wagging + o.p. ph ring bending + i.p. C _{13,15} OC _{isoq} bending + CH ₃ rocking |
| 665vw | 659 | 659 (1.76) | 682 | 682 | o.p. ph ring bending + o.p. isoq CH deformation + CH ₂ rocking |
| 649vw | 645 | 645 (5.44) | 665 | 665 | o.p. isoq skeletal distorsion + o.p. ph ring bending + CH ₂ wagging + o.p. C _{ph, isoq} O bending + C ₁ C ₁₁ C ₁₆ bending |
| 604vw | 603 | 604 (1.04) | 623 | 624 | i.p. isoq skeletal distorsion + CH ₃ rocking + i.p. C _{isoq} O bending |
| 594vw | 590 | 590 (0.69) | 610 | 611 | o.p. isoq skeletal distorsion + o.p. ph bending + CH ₂ wagging + CH ₃ rocking + i.p. C _{23,25} OC _{ph} bending |
| | | | | | o.p. ph ring bending + CH ₂ rocking + o.p. isoq skeletal bending + CH ₃ rocking |

| | | | | | |
|-------|-----|-------------|-----|-----|--|
| 565vw | 564 | 563 (1.88) | 583 | 582 | + o.p. CCO _{23,25} bending |
| 535vw | 528 | 528 (4.15) | 547 | 546 | o.p. isoq skeletal distorsion + o.p. ph ring bending + CH ₂ bending |
| 478vw | 485 | 484 (4.38) | 500 | 499 | o.p. isoq skeletal distorsion + CH ₂ bending + o.p. ph ring bending + C ₁ C ₁₁ C ₁₆ bending + CH ₃ rocking + o.p. CCO _{23,25} bending |
| 466vw | 464 | 463 (3.65) | 479 | 478 | o.p. isoq skeletal bending + i.p. C _{ph, isoq} OC bending + o.p. ph ring bending + CH ₃ rocking + CH ₂ bending |
| 426vw | 410 | 409 (0.75) | 424 | 423 | o.p. isoq skeletal bending + i.p. CCO _{23,25} bending + o.p. C _{13,15} OC _{isoq} bending + i.p. ph CH deformation + CH ₃ rocking + CH ₂ wagging |
| 392vw | 382 | 381 (2.98) | 394 | 393 | i.p. ph ring bending + CH ₂ rocking + CH ₃ rocking + i.p. C _{13,15} O bending |
| 364w | 352 | 352 (17.86) | 362 | 362 | o.p. isoq skeletal distorsion + o.p. CCO _{13,15} bending + o.p. ph CH deformation + i.p. C _{ph} OC bending + CH ₃ rocking |
| noisy | | | | | CH ₃ rocking + i.p. C _{13,15} O bending + i.p. isoq skeletal distorsion |
| 213vw | 209 | 208 (1.45) | 217 | 216 | o.p. isoq skeletal distorsion + o.p. ph ring deformation + i.p. C _{ph} OC bending + CH ₂ rocking + CH ₃ rocking |

Abbreviations: vw - very weak, w - weak, m - medium, ms - medium strong, s - strong, vs - very strong, sh - shoulder; sym - symmetric, asym - asymmetric; i.p. - in-plane, o.p. - out-of-plane; ph - phenyl, isoq - isoquinoline. The calculated Raman scattering activities are in parentheses ($\text{\AA}^4/\text{amu}$). The standard 6-31G basis set was used for H and C in conjunction with the 6-31+G(d) (combination denoted P1) or 6-311+G(d) (combination denoted P2) basis sets for N and O.

P2 computed wavenumbers and Raman intensities reproduced the experimental data and permitted the vibrational assignment well.

The Raman spectra of papaverine hydrochloride aqueous solution in the pH range from 1 to 6 were found to be unchanged (Figure 4.21). Increasing to higher pH's, over the pK_a value of 6.5, the sample soon solidifies and consequently, no Raman spectrum of the solution could be obtained. Notable differences in band positions and relative intensities appear between the Raman spectra at pH 6 and 6.5 in the 1300-1500 cm^{-1} spectral range. More specific, the bands at 1364 and 1423 cm^{-1} become dominant in the aqueous solution Raman spectrum at pH 6.5. These bands correspond to the ones at 1351 and 1411 cm^{-1} respectively, in the solid state Raman spectrum and are assigned to the isoquinoline skeletal stretching (C-C, C-N) and the C-H bending modes. Actually, in the solid state Raman spectrum only one band, namely the papaverine Raman fingerprint, can be observed in this region at 1411 cm^{-1}

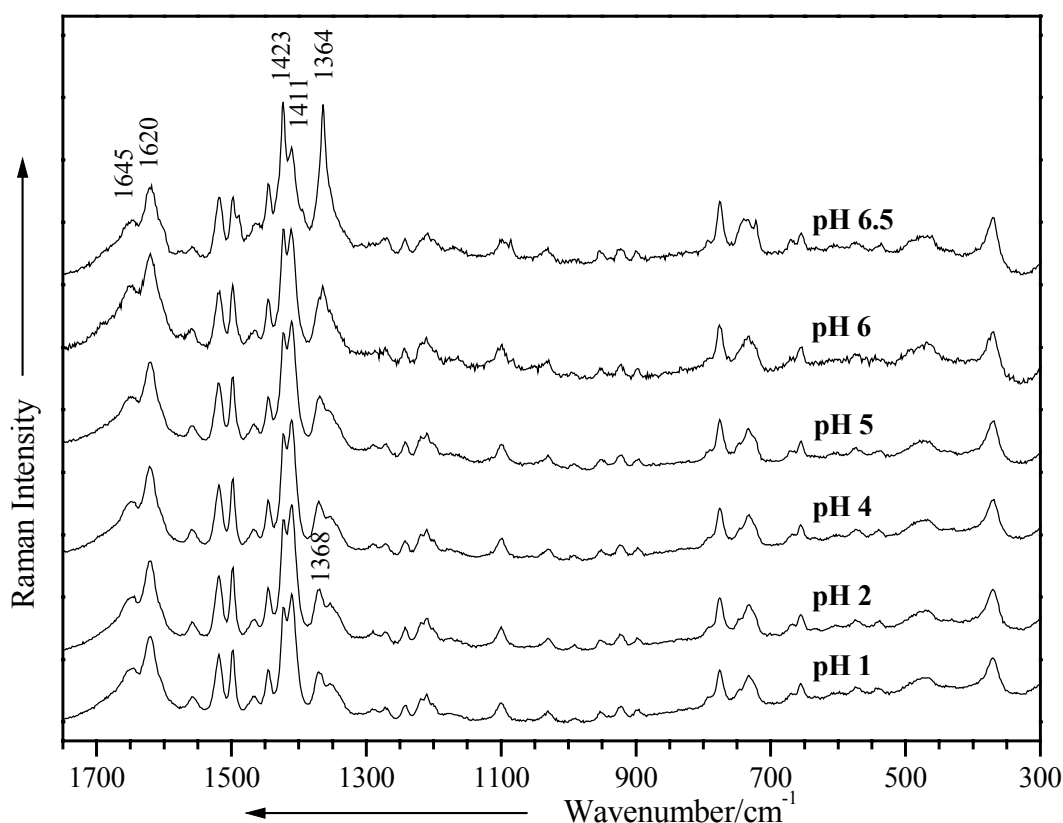


Figure 4.21. The Raman spectra of papaverine aqueous saturated solution at different pH values. Excitation line: $\lambda_0 = 514.5 \text{ nm}$.

and this splits up into a doublet 1411-1432 cm^{-1} in aqueous solution. These changes reflect the vibrational structure of the isoquinoline ring before and during deprotonation of the nitrogen atom, with consequence in the band positions of the adjacent involved modes.

A versatile tool to study the vibrational behavior with pH in the case of low solubility is the SERS spectroscopy, due to its sensitivity and potential of detection under the micromole level. Therefore, the SERS spectra in the pH range from 2 to 10 were obtained for the first time and discussed (Figure 4.22).

First, one can notice a substantially change in the band positions and their relative intensities while passing from Raman to SERS spectra at the same corresponding pH. According to the SERS theory,²⁰⁹ such modifications indicate a chemisorption of the protonated or neutral molecules at the Ag surface.

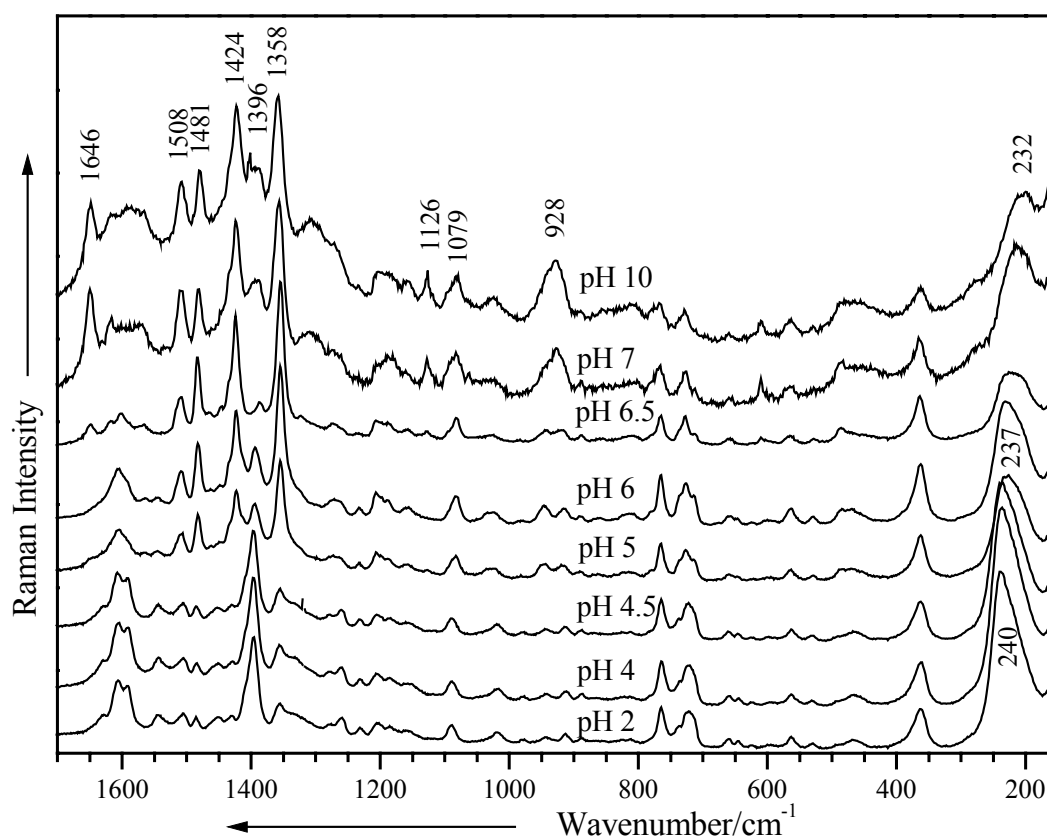


Figure 4.22. The SERS spectra of papaverine on Ag colloid at different pH values.

Excitation line: $\lambda_0 = 514.5 \text{ nm}$.

Second, while passing from the protonated molecular species (pH under 6.5) to the neutral ones, a dramatical change of the SERS band positions and their relative intensities was observed (Figure 4.22). More specific, when the protonated form (e. g., pH 2) is adsorbed onto the Ag particles, the bands assigned to the phenyl ring stretching modes (1606, 1592, and 1396 cm^{-1}) are mainly enhanced and red shifted from the corresponding ones in the pH dependent Raman spectrum. Therefore, after performing a complete vibrational analysis and on the basis of the surface selection rules,^{27, 28, 175, 209} an orientation with the phenyl ring tilted in the close vicinity of the Ag particles was concluded. An insignificant enhancement of any of the vibrational modes, which involves the oxygen atom, was also noticed. This reflects the absence of the interaction with the surface through one or more oxygen atoms.

To determine the possible adsorptive sites for the Ag substrate, the spectral region around 200 cm^{-1} was examined more closely. As we have already mentioned the Ag-O, Ag-N, and Ag-Cl stretching modes usually appear in this low wavenumber spectral region. The SERS spectra of papaverine hydrochloride at acid pH values exhibit a very strong broad band at about 240 cm^{-1} (Figure 4.22), which can be attributed to the Ag-O stretching mode. But one should consider that at these pH values a significant amount of HCl was added to the Ag colloid to adjust the pH. Examining the profile of the signal it seems again that it is due to the Ag-Cl stretching mode.²²⁹ Therefore, assignment of the 240 cm^{-1} SERS band is not unequivocal.

At pH values higher than 6.5, the bands assigned to the isoquinoline part of the papaverine structure (1646, 1508, 1424, 1358 cm^{-1}) present an enhancement (Figure 4.22). When the adsorbed unprotonated species are present, they adopt such an orientation that make the terminal oxygen atoms to be far from the surface because the vibrations involving the C-O modes are weakly represented in SERS, whereas those involving the C-N stretching mode from the isoquinoline ring (Figure 4.23) are significantly enhanced and downshifted from their corresponding Raman positions (e.g., 1358 cm^{-1} at pH 10 shifted from 1364 cm^{-1} at pH 6.5) (Figures 4.21 and 4.22). Besides, the band at 1126 cm^{-1} assigned to the methyl torsion was observed at basic pH values (Figure 4.22). Therefore, for the unprotonated species a different geometry on the silver surface was concluded, with the isoquinoline ring closer to the surface. Furthermore, a closer examination of the SERS spectra at pH values higher than 6.5 indicates the presence of a strong band at about 232 cm^{-1} , which may be assigned to the Ag-N stretching mode characteristic for the N-adsorbed species under 250 cm^{-1} .

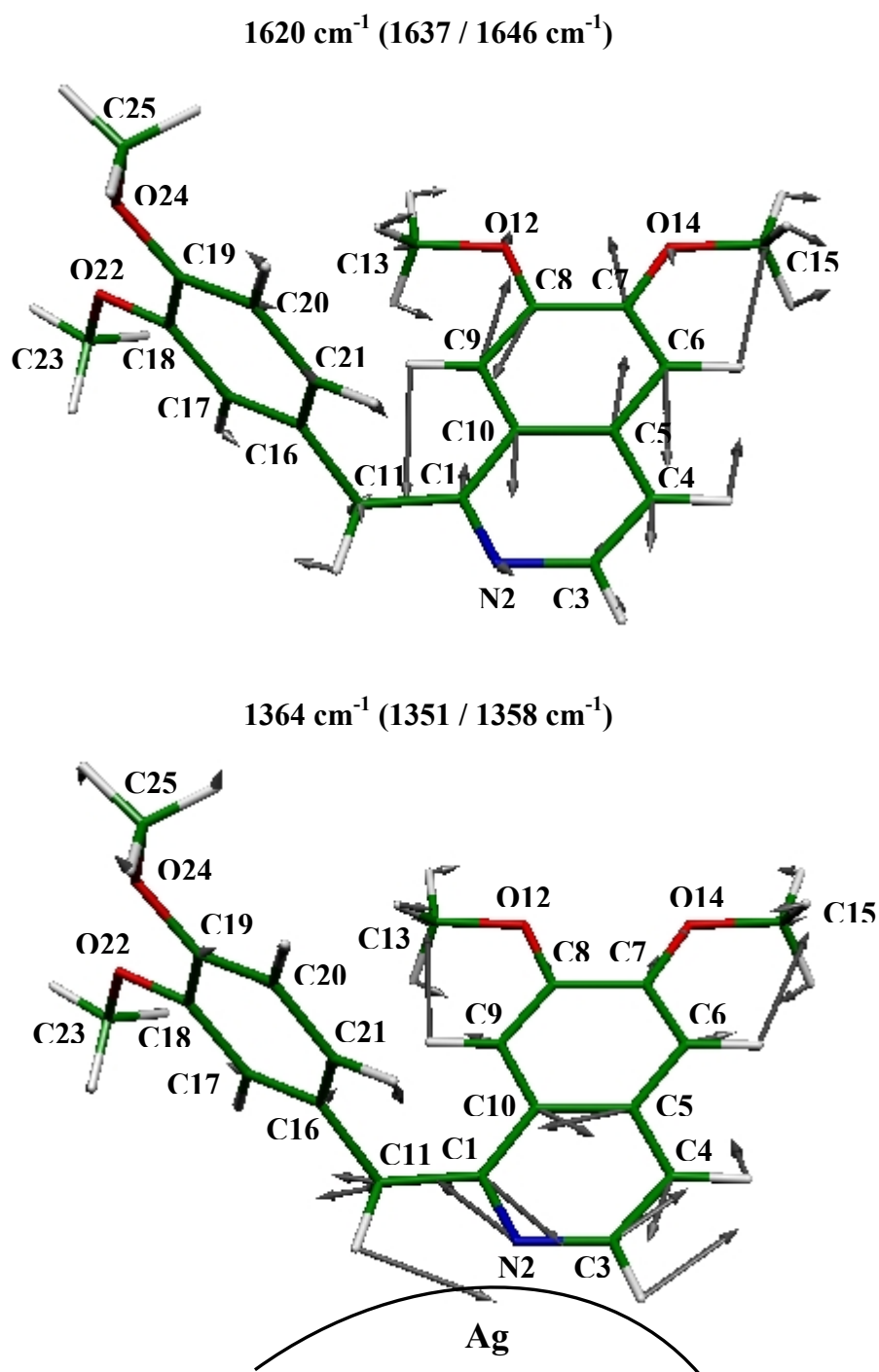


Figure 4.23. The fundamental calculated (BPW91/the 6-31G basis set for H and C in conjunction with the 6-311+G(d) basis set for N and O) vibrational modes of papaverine, which mainly involve isoquinoline skeletal stretching modes.

The experimental FT-Raman and SERS (pH 10) values are given in parentheses.

As one can note, the neutral form of papaverine has five atoms, namely N2, O12, O14, O22, and O24, capable of forming bonds with the silver surface (Figure 4.19). The representative plot of the total electron density of papaverine (Figure 4.24) indicates a build-

up of charge density on the oxygen and nitrogen atoms and nodes at the other atoms. Moreover, the DFT calculations at BPW91/P2 level of theory (Table 4.8) show that for the neutral species of papaverine, the negative charge density on the N2, O12, O14, O22, and O24 atoms are -0.578 , -0.567 , -0.559 , -0.563 , and -0.565 (e), respectively. The other methods led to similar values. One can notice that the negative charge density is significant in all five atoms. As the adsorption through the oxygen atoms was excluded, we suppose that the interaction with the Ag surface takes place through the isoquinoline part, with a higher probability through the nitrogen atom.

Table 4.8. Partial charges (e) situated on selected atoms of the neutral species of papaverine, as determined with the Natural Population Analysis.

| Atom | Calc | |
|------|----------|----------|
| | BPW91/P2 | B3LYP/P2 |
| N2 | -0.578 | -0.646 |
| O12 | -0.567 | -0.651 |
| O14 | -0.559 | -0.644 |
| O22 | -0.563 | -0.646 |
| O24 | -0.565 | -0.648 |
| C1 | 0.233 | 0.268 |
| C3 | 0.048 | 0.088 |
| C4 | -0.154 | -0.142 |
| C5 | 0.036 | 0.043 |
| C6 | -0.220 | -0.206 |
| C7 | 0.322 | 0.364 |
| C8 | 0.316 | 0.354 |
| C9 | -0.204 | -0.189 |
| C10 | 0.090 | 0.077 |
| C11 | -0.444 | -0.393 |
| C13 | -0.215 | -0.139 |
| C15 | -0.211 | -0.135 |
| C16 | 0.108 | 0.113 |
| C17 | -0.235 | -0.225 |
| C18 | 0.308 | 0.348 |
| C19 | 0.311 | 0.348 |
| C20 | -0.183 | -0.163 |
| C21 | -0.173 | -0.163 |
| C23 | -0.205 | -0.128 |
| C25 | -0.207 | -0.131 |

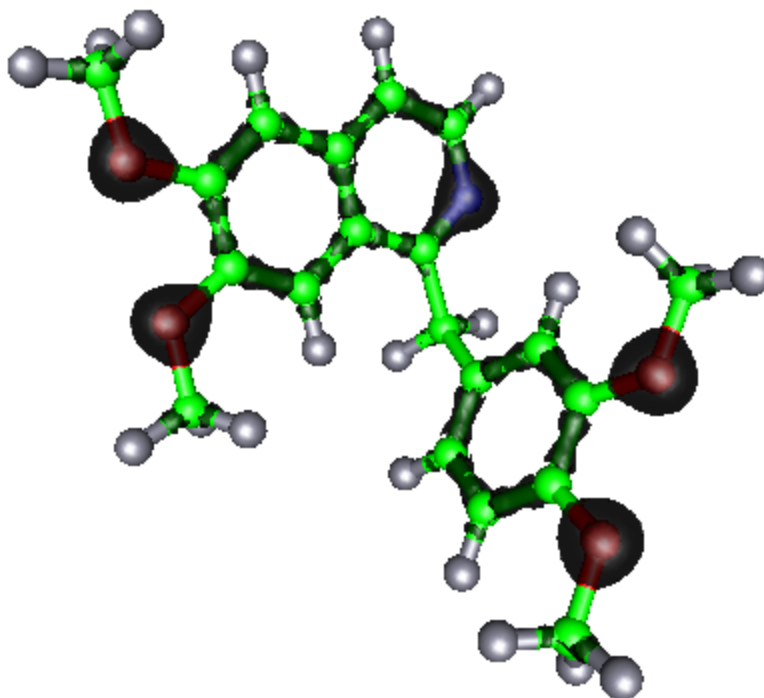


Figure 4.24. The total electron density of the neutral form of papaverine.
The isosurface value is 0.26.

4.3.3 Conclusions

Density functional theory calculations and an experimental vibrational characterization of papaverine hydrochloride and its neutral species were performed. The DFT computed structural parameters and harmonic vibrational wavenumbers reproduced the experimental data well and helped us to characterize the vibrational behavior of the adsorbed species.

A pH dependent Raman study was possible in the pH range under 6.5, for upper values the solubility being dramatically diminished. However, the vibrational analysis of the Raman spectra allowed to evidence the two species of papaverine, protonated and neutral, respectively.

The pH dependent SERS spectra of papaverine revealed again two different chemisorbed species on the Ag colloidal surface: protonated and neutral, the protonated one being adsorbed with the phenyl closer to the surface and the neutral one through the isoquinoline part, more probably through the nitrogen atom.

Either in acid or in basic media, the oxygen adsorption of papaverine species was excluded. The SERS spectra could evidence the protonated or neutral species under micromole level.

4.4 Nickel(II) cupferronato complexes

4.4.1 Molecules presentation

The ammonium salt of *N*-nitroso-*N*-phenylhydroxylamine (cupferron) (Figure 4.25 (a)) is a well known analytical reagent for the qualitative determination of Cu(II), Fe(II), and many other ions.²⁴⁷ Additionally, cupferron is a biologically active compound, which displays carcinogenic, genotoxic, mutagenic, and DNA-damaging effects.²⁴⁸⁻²⁵¹ It is also a donor that can release NO upon enzymatic,²⁵² electrochemical,²⁵³⁻²⁵⁵ as well as chemical oxidation²⁵⁶⁻²⁵⁹. The ligand is known to form complexes with many metals but only few of them have been structurally and spectroscopically characterized.^{157, 260-275} Thus, it is important to analyze the composition and vibrational properties of the *N*-nitroso-*N*-phenylhydroxylamine and its (organo)metallic species, not only from the analytical standpoint, but also from the biophysical one. The knowledge of cupferron chemistry could contribute to a better understanding of the interaction of nitrogen oxide with metal centers of biologically important species or enzymes.

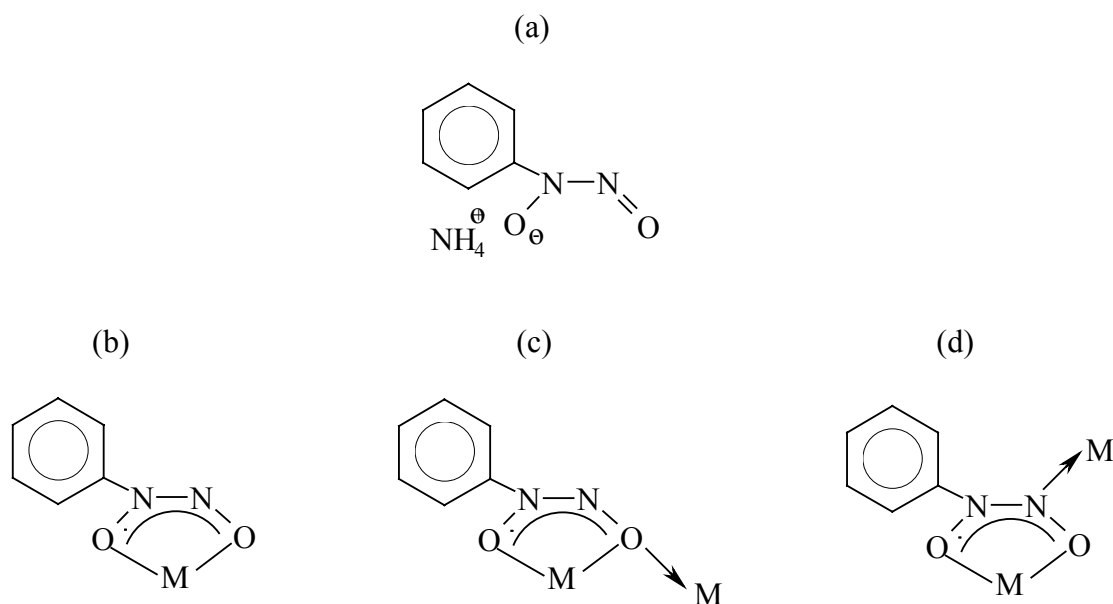


Figure 4.25. Schematic drawing of cupferron (a), $\text{NH}_4[\text{PhN}(\text{O})\text{NO}]$, and observed chelating patterns (b-c) of the cupferronato anion, $\text{PhN}(\text{O})\text{NO}^-$.

In a previous work we have reported on IR and/or Raman studies on new (organo)tin(IV),²⁴⁸ thallium(I),²⁶³ and cobalt(II)²⁷⁵ *N*-nitroso-*N*-hydroxylaminato complexes, to elucidate the coordination pattern of the anionic ligand. While we have characterized the

bidentate coordination (Figure 4.25 (b)), other studies^{262, 264, 272, 273, 276} have shown that the ligand can also act triconnectively (Figure 4.25 (c), (d)).

In this respect, we extended our vibrational studies on a larger range of cupferronato complexes, involving a different transition metal center. As one can see in this section, this has brought new information about the coordination behavior of the title ligand. Thus, the Raman and SERS spectra of the new nickel(II) cupferronato complexes: NiL_2A_n , $\text{L} = \text{PhN}_2\text{O}_2^-$, $n = 1$, $\text{A} = o$ -phenanthroline (*o*-phen) (**1**), *o,o'*-bipyridine (*o,o'*-bip) (**2**) and $n = 2$, $\text{A} = \text{H}_2\text{O}$ (**3**), *o*- NH_2Py (**4**), *o*- $\text{C}_6\text{H}_4(\text{NH}_2)_2$ (**5**) were recorded for the first time and discussed. (Figure 4.26).

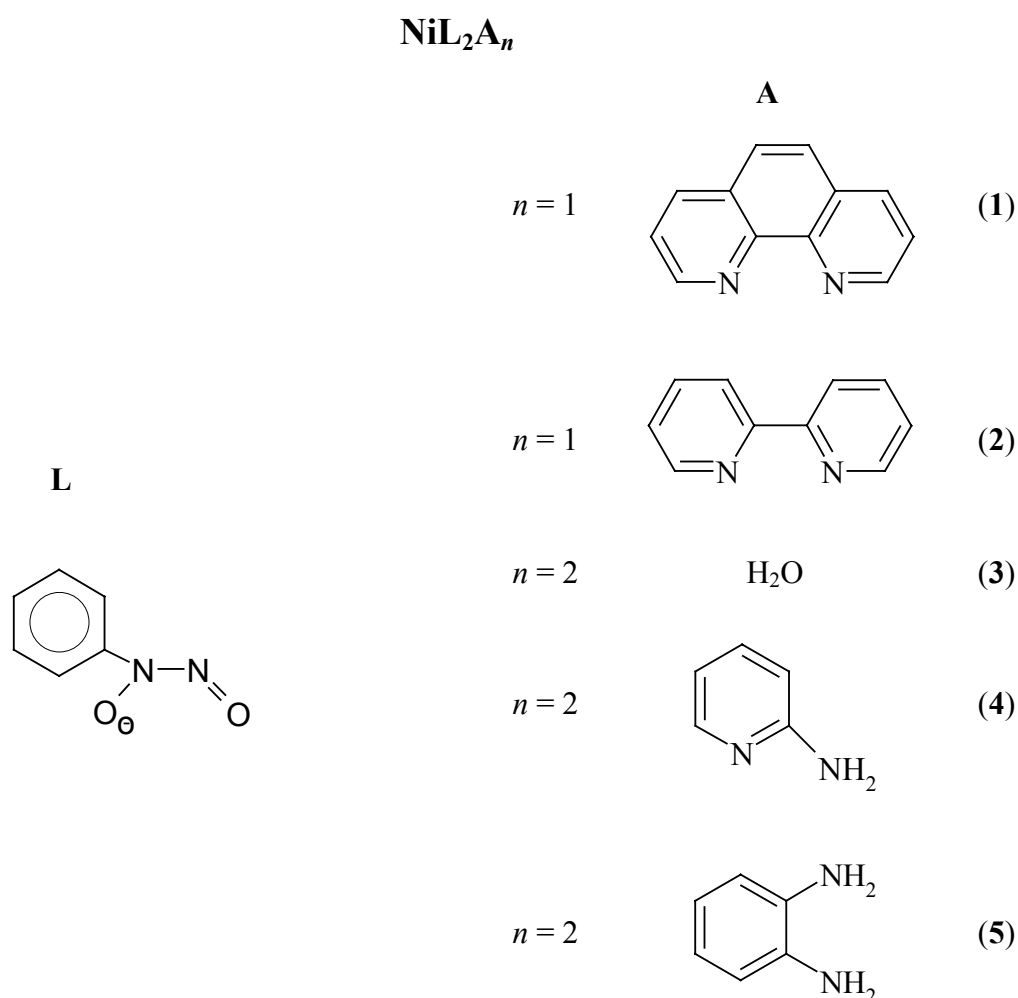


Figure 4.26. The chemical structure of the new nickel(II) cupferronato complexes.

The vibrational fundamentals from the Raman spectrum of cupferron were analyzed by comparing them with those from literature^{248, 272, 275, 277} in conjunction with the results of

our theoretical calculations. Additionally, the geometries of the nickel(II) cupferronato complexes **3**, **4**, and **5** were characterized for the first time using DFT calculations and compared with the only crystal structure that could have been obtained for complex **4** by our coworker Andrea Deák²⁶⁰. Unfortunately, the theoretical calculations for the other two organometallic compounds: **1** and **2** are still in progress.

4.4.2 Results and discussion

4.4.2.1 Geometry optimization

The optimized structures of the cupferronato anion, $\text{PhN}(\text{O})\text{NO}^-$, and the compound **4**, which have been obtained using the BPW91/LANL2DZ method, are illustrated in Figure 4.27. The structural parameters calculated for $\text{PhN}(\text{O})\text{NO}^-$ and complexes **3**, **4**, and **5**, respectively, are listed in Table 4.9.

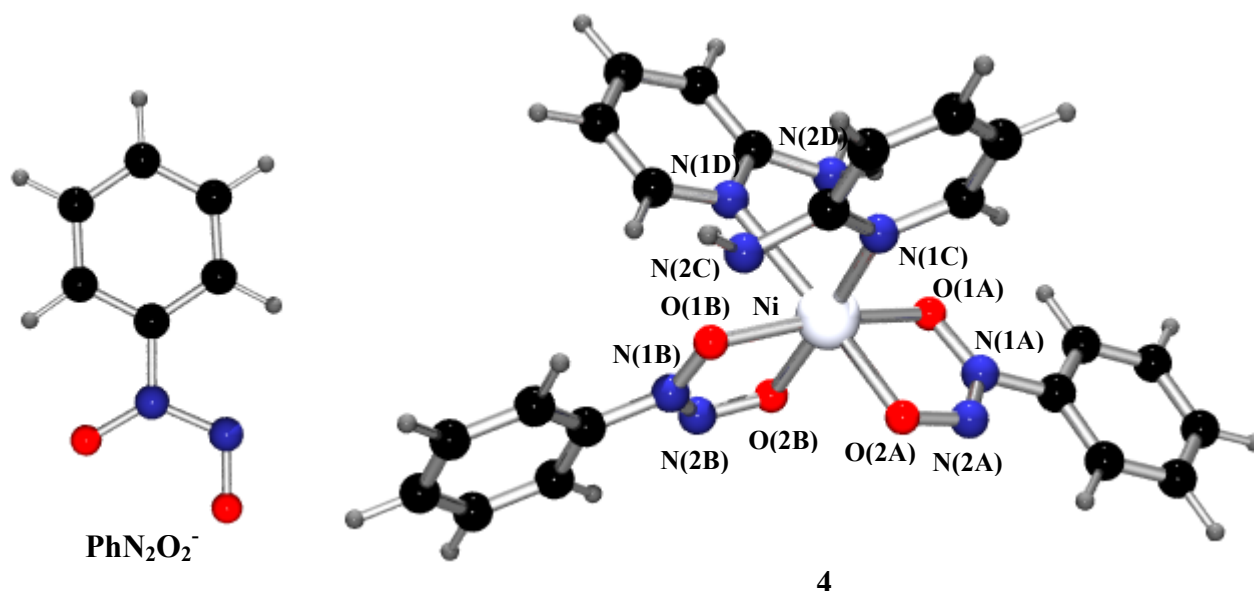


Figure 4.27. The BPW91/LANL2DZ optimized geometries of PhN_2O_2^- and its nickel(II) cupferronato complex **4**.

The molecular structure of complex **4** consists of discrete monomeric units with the nickel(II) atom in a distorted *cis*-octahedral configuration defined by two chelating cupferronato anions (A and B) and two neutral 2- NH_2Py ligands (C and D). The X-Ray study of Deák and coworkers²⁶⁰ showed intramolecular $\text{N-H}\cdots\text{O}$ hydrogen bonding between the NH_2 groups and the O atom of the cupferronato anion. Intermolecular $\text{N-H}\cdots\text{O}$ and $\text{N-H}\cdots\text{N}$ interactions between symmetry-related molecules led to hexameric aggregates, which connect

Table 4.9. Selected calculated structural parameters for PhN_2O_2^- and some of its new nickel(II) cupferronato complexes:

NiL_2A_n , $\text{L} = \text{PhN}_2\text{O}_2^-$, $n = 2$, $\text{A} = \text{H}_2\text{O}$ (**3**), *o*- NH_2Py (**4**), and *o*- $\text{C}_6\text{H}_4(\text{NH}_2)_2$ (**5**),
together with the experimental values found in (**4**).

| | PhN_2O_2^- | | 3 | Exp ²⁶⁰ | 4 | 5 |
|-------------------|----------------------------|---------|-----------------------|--------------------|-----------------------|-----------------------|
| | Calc BPW91 6-31+G(d) | LANL2DZ | Calc BPW91/LANL2DZ | | Calc BPW91/LANL2DZ | Calc BPW91/LANL2DZ |
| Bond lengths (pm) | | | | | | |
| Ni-O(1A) | | | 207.0 | 205.1(13) | 206.5 | 206.1 |
| Ni-O(2A) | | | 209.0 | 207.3(14) | 207.9 | 209.4 |
| Ni-N(1C) | | | | 209.9(15) | 211.5 | 214.6 |
| Ni-N(1D) | | | | 209.9(16) | 211.5 | 214.6 |
| Ni-O(1C) | | | 210.8 | | | |
| Ni-O(1D) | | | 210.7 | | | |
| O(1A)-N(1A) | 129.9 | 134.7 | 133.7 | 131.9(19) | 132.8 | 133.8 |
| O(2A)-N(2A) | 126.4 | 130.8 | 131.4 | 129.5(2) | 130.5 | 131.7 |
| N(1A)-N(2A) | 138.2 | 143.0 | 130.8 | 128.8(2) | 129.7 | 130.8 |
| Angles (°) | | | | | | |
| O(1A)-Ni-O(2A) | | | 74.3 | 75.2(5) | 75.2 | 75.3 |
| O(2A)-Ni-O(2B) | | | 86.9 | 88.2(6) | 88.1 | 88.1 |
| O(2B)-Ni-N(1D) | | | 91.7 | 92.3(6) | 92.0 | 96.3 |
| O(2A)-Ni-N(1C) | | | 88.3 | 90.2(6) | 91.5 | 96.1 |
| N(1C)-Ni-N(1D) | | | 88.9 | 89.5(6) | 89.4 | 93.5 |
| O(1B)-Ni-N(1D) | | | 91.9 | 93.6(6) | 92.9 | 94.2 |
| O(1A)-Ni-N(1C) | | | 92.8 | 94.7(6) | 93.7 | 94.1 |
| O(1A)-Ni-O(1B) | | | 162.1 | 159.0(5) | 160.8 | 161.8 |

through common edges into a two-dimensional supramolecular network of hexagonal-grid type.²⁶⁰

The N(1L)-N(2L) bond length of 128.8(2) pm in compound **4** is shorter than that of an N-N single bond (145.0 pm),²⁷⁸ but it is closer to that of an N=N double bond (121.0 pm)²⁷⁸. Furthermore, the averaged N(1L)-O(1L) and N(2L)-O(2L) bond lengths of 132.0(19) and 128.6(2) pm, respectively, are between that of a single bond (140.0 pm)²⁷⁸ and a double bond (121.0 pm)²⁷⁸. These structural features suggest significant electron delocalization along the *N*-nitroso-*N*-hydroxylaminate (ONNO) moiety.

All calculated structural parameters for complex **4** agree well with the experimental values of the related crystal structure, which determined us to perform further DFT calculations on the compounds **3** and **5**. As one can notice from Table 4.9, they are isostructural with the compound **4**.

4.4.2.2 *Vibrational spectroscopy*

The Raman spectra of cupferron and the new nickel(II) cupferronato complexes (**1-5**) recorded in the 1800-600 cm⁻¹ spectral region are presented in Figure 4.28.

Only poor FT-Raman spectra could be recorded for the complexes **2-5**, therefore higher energy excitation line was required. Alternatively, the micro-Raman spectra of **2-5** were successfully recorded using different laser excitation lines. Taking into account the absorption spectra of the title compounds,²⁷⁵ no significant resonance contributions in the spectra could be noticed.

The observed bands and the vibrational assignment are summarized in Table 4.10. The calculated harmonic vibrational wavenumbers for the cupferronato anion and their Raman scattering activities agree well with the experimental data but two modes, which involve the ONNO moiety. But one should take into account that the calculations refer to the gas phase of the cupferronato anion and not to the solid state of the ammonium salt of cupferron (Figure 4.25). The calculations were performed at two levels of theory, i.e., BPW91/6-31+G(d) and BPW91/LANL2DZ, but not to overload the table only the results which approached better the experimental data (using BPW91/6-31+G(d)) have been inserted.

The characteristic vibrational modes of aromatic groups were detected in the expected spectral region for all complexes.²⁷⁷ The specific differences between the spectra of **1-5** are due to the presence of different neutral molecules coordinated to the metal centers.

The assignments of the N-N, N=O stretching, and ONNO bending modes specific for the neutral ligand at 1336, 1265-1223, and 907 cm^{-1} , respectively (Figure 4.29), are in good agreement with the corresponding IR and Raman data of $\text{NH}_4[\text{PhN}(\text{O})\text{NO}]$.^{248, 263, 275}

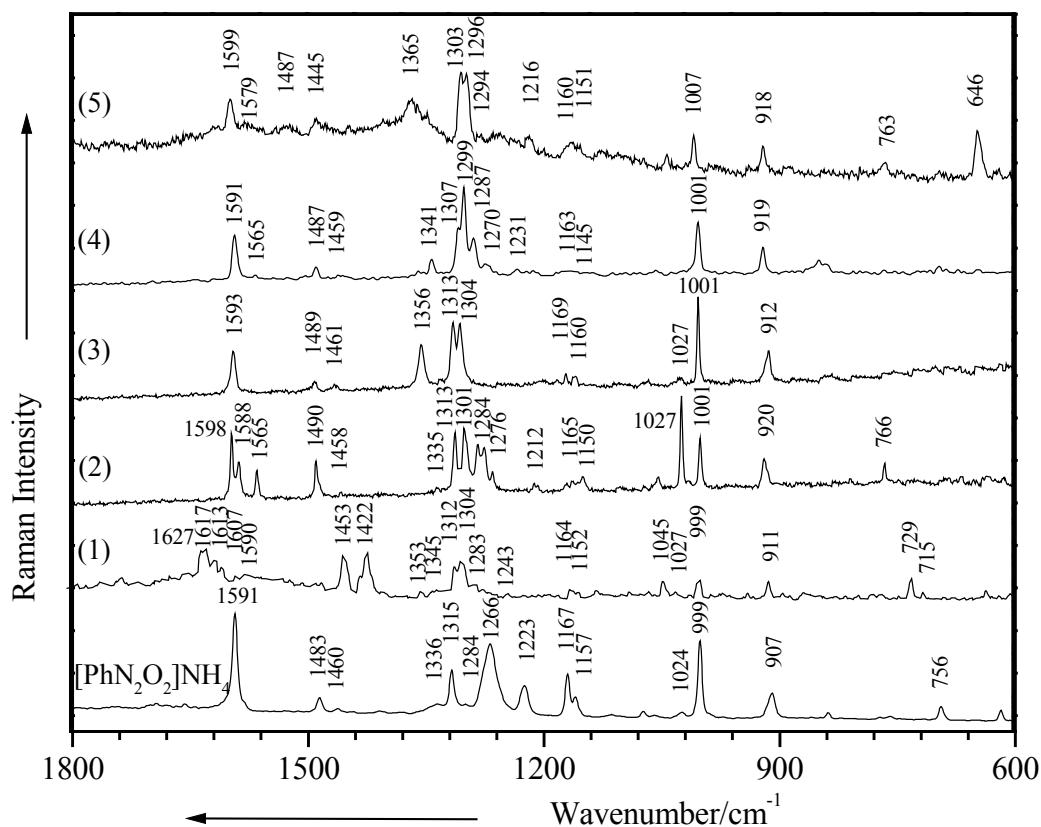


Figure 4.28. Raman spectra of the cupferron and its new corresponding nickel(II) complexes: NiL_2A_n , $\text{L} = \text{PhN}_2\text{O}_2^-$, $n = 1$, $\text{A} = o$ -phenanthroline (1), o,o' -bipyridine (2) and $n = 2$, $\text{A} = \text{H}_2\text{O}$ (3), o - NH_2Py (4), o - $\text{C}_6\text{H}_4(\text{NH}_2)_2$ (5). Excitation line: $\lambda_0 = 1064$ nm (cupferron and 1), $\lambda_0 = 647.1$ nm (2-4) and $\lambda_0 = 514.5$ nm (5). The molecular structure of the cupferron is inserted.

Comparing the Raman spectra of the complexes 1-5 with that of the cupferron, one may notice significant changes in the position of the three mentioned bands, due to the electron delocalization over the *N*-nitroso-*N*-hydroxylaminato unit and the bidentate coordination of the anionic ligand to the metal centers through the oxygen atoms. Thus, the N-N stretching and ONNO bending modes are shifted to higher wavenumbers up to 1365 and 920 cm^{-1} , respectively in the spectra of all complexes. The two N=O stretching vibrational modes were detected in the spectrum of cupferron at 1265 and 1223 cm^{-1} , respectively.^{248, 263}

The presence of these two bands is due to the *cis-trans* configuration of the ONNO group as it was previously described.²⁷⁵ Taking into account that the cupferronato ligand is expected to coordinate in a *cis*-configuration, only one band characteristic to the N=O stretching mode should be present in the spectra of **1-5**. More specifically, the band of weak or very weak relative intensity, in the 1243-1212 cm⁻¹ spectral range, is attributed to the new N=O stretching vibration in the spectra of all complexes.

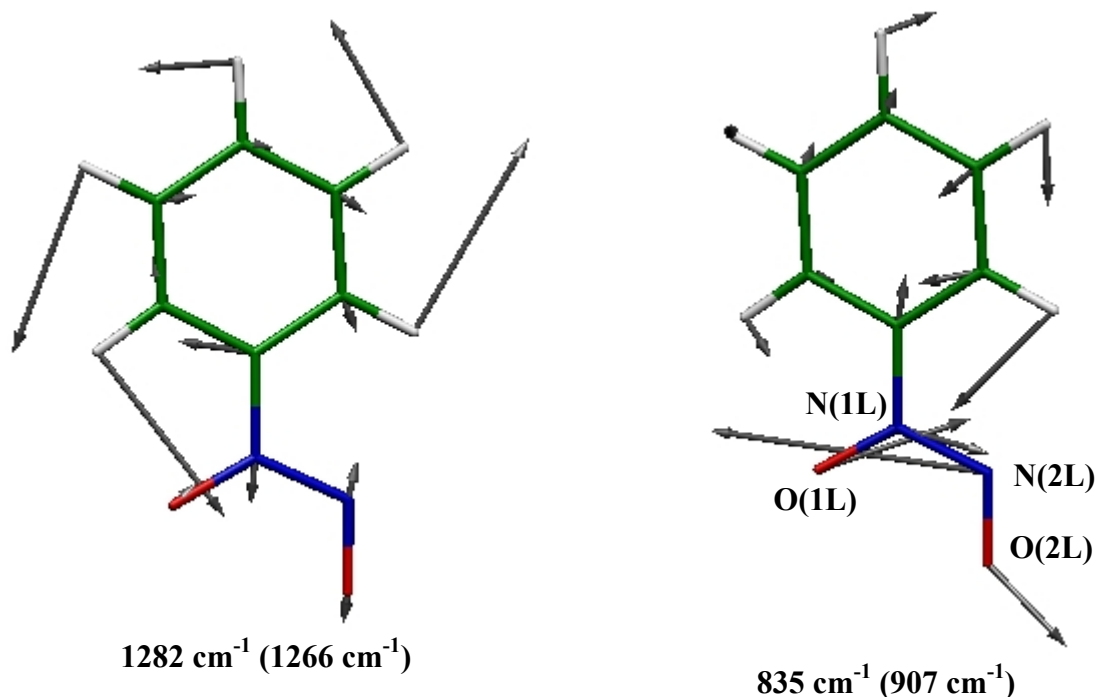


Figure 4.29. The fundamental calculated (BPW91/6-31+G(d)) vibrational modes of the cupferronato anion, which mainly involve CH bending, N=O stretching (left) and ONNO bending (right) modes. The experimental FT-Raman values are given in parentheses.

The assignment of the strong band at about 1304 cm⁻¹ in the Raman spectra of **1-5**, to the new symmetric mode of the ONNO group, is in good agreement with the vibrational data obtained by our coworkers for the cobalt(II) cupferronato homologues.²⁷⁵ The splitting of this band at 1312 cm⁻¹, specific for the complexes **1-3** (Table 4.10), still remain uncertain. A possible explanation could be the Fermi resonance due to the combination of the ONNO bending mode at about 912 cm⁻¹ and the ring mode of cupferronato at 401 cm⁻¹. The bands in the 1299-1283 cm⁻¹ spectral region are attributed to the C-N stretching vibrational modes. It must be mentioned that the presence of the amine molecules in the complexes **4** and **5** brings new contributions in the mentioned spectral region. Thus, for these complexes two bands are assigned to the C-N stretching mode.

Table 4.10. Raman data (cm^{-1}) of the cupferron, NH_4L , $\text{L} = \text{PhN}_2\text{O}_2^-$, and its corresponding nickel(II) complexes:
 NiL_2A_n , $n = 1$, $\text{A} = o$ -phenanthroline (**1**, **1'**), o,o' -bipyridine (**2**, **2'**) and $n = 2$, $\text{A} = \text{H}_2\text{O}$ (**3**, **3'**), o - NH_2Py (**4**), o - $\text{C}_6\text{H}_4(\text{NH}_2)_2$ (**5**).

| Raman | Calc BPW91/6-31+G(d) | Raman | | | | | SERS | | | Vibrational assignment |
|-----------------------|-------------------------|----------|----------|----------|----------|----------|-----------|-----------|-----------|---|
| NH_4L | | 1 | 2 | 3 | 4 | 5 | 1' | 2' | 3' | |
| | | 1627vs | | | | | 1625w | | | o -phen stretching |
| | | 1617vs | | | | | 1619w | | | |
| | | 1613m | | | | | | | | |
| | | 1607m | | | | | 1607w | | | |
| 1591vs | 1592 (158.36) | 1590vw | 1598vs | 1593ms | 1591s | 1599s | 1601w | | | $\text{C}_6\text{H}_5 + \text{C}_5\text{H}_4\text{N}$ quadrant stretching |
| | | | 1588ms | | 1565vw | 1579w | | 1600vs | 1594vs | |
| | | | 1565m | | | | | 1589sh | | |
| | | 1520vw | | | | | 1519m | 1568ms | | o -phen ring stretching |
| 1483m | 1471 (52.44) | | 1490m | 1489w | 1487w | 1487w | | 1494ms | | C_6H_5 semicircle stretching |
| 1460vw | 1447 (12.13) | 1453vs | 1458vw | 1461w | 1459vw | 1445v | 1453vs | 1451vw | 1450vw | + o -phen C-H bending |
| | | 1422vs | | | | w | 1424vs | | | |
| 1336w | 1363 (31.01) | 1353w | 1335vw | 1356ms | 1357vw | 1365s | | | | N-N stretching |
| | | 1345vw | | | | | 1347m | | | o -phen ring stretching |
| | | | | | 1340m | 1340sh | | | | $\text{C}_6\text{H}_4 + \text{C}_5\text{H}_4\text{N}$ ring stretching |
| 1315m | 1330 (29.72) | | | | | | | | | ONNO stretching |
| | | 1312s | 1313s | 1313s | | | | | | combined mode |
| | | 1304s | 1301vs | 1304s | 1307sh | 1303vs | 1310s | 1317s | 1308s | ONNO sym stretching |
| | | | | | 1299vs | 1296vs | 1296msh | | | C-N stretching |
| 1284sh | 1282 (1.22) | 1283w | 1284s | | 1287s | 1294sh | | 1287w | | |
| | | | 1276s | | | | | 1269w | | o,o' -bipy ring stretching |

103 *Why SERS and DFT?*

| | | | | | | | | | | | |
|--------|--------------|--------|--------|--------|--------|--------|--------|--------|-------|--|---|
| 1266s | 1282 (1.22) | | | | | | | | | | N=O stretching + CH bending |
| 1223m | | 1243vw | 1212w | | 1231vw | 1216w | 1243vw | | | | C-H bending |
| 1167m | 1185 (25.80) | 1164w | 1165w | 1169w | 1163vw | 1160w | 1169vw | 1174vw | | | |
| 1157w | 1143 (10.74) | 1152w | 1150w | 1160w | 1145vw | 1151sh | 1166vw | 1155vw | 1155m | | <i>o</i> -phen ring breathing |
| | | 1045m | | | | | 1057m | | | | |
| | | | | | | | 1049sh | | | | |
| 1024vw | 1013 (52.39) | 1027vw | 1027vs | 1027w | 1027sh | | | 1030s | | | <i>o,o'</i> -bipy breathing + aromatic ring stretching |
| 999s | 979 (56.75) | 998m | 1001s | 1001vs | 1001s | 1007s | 1003vw | 1001sh | 1004s | | aromatic ring breathing |
| 907m | 835 (22.93) | 911m | 920ms | 912m | 919m | 918m | | | 926m | | ONNO bending + CH bending |
| 756vw | 708 (13.46) | | 766m | | 765vw | 763w | | 768w | | | C-H and NH ₂ wagging |
| | | 729m | | | | | 735ms | | | | <i>o</i> -phen ring bending |
| | | 715w | | | | | 720m | | | | |
| | | | | | | | 238m | 238m | | | N-Ag stretching |

Abbreviations: vw - very weak, w - weak, m - medium, ms - medium strong, s - strong, vs - very strong, sh - shoulder; sym - symmetric, asym - asymmetric; *o*-phen – *o*-phenanthroline, *o,o'*-bipy - *o,o'*-bipyridine. The calculated Raman scattering activities are in parentheses (Å⁴/amu).

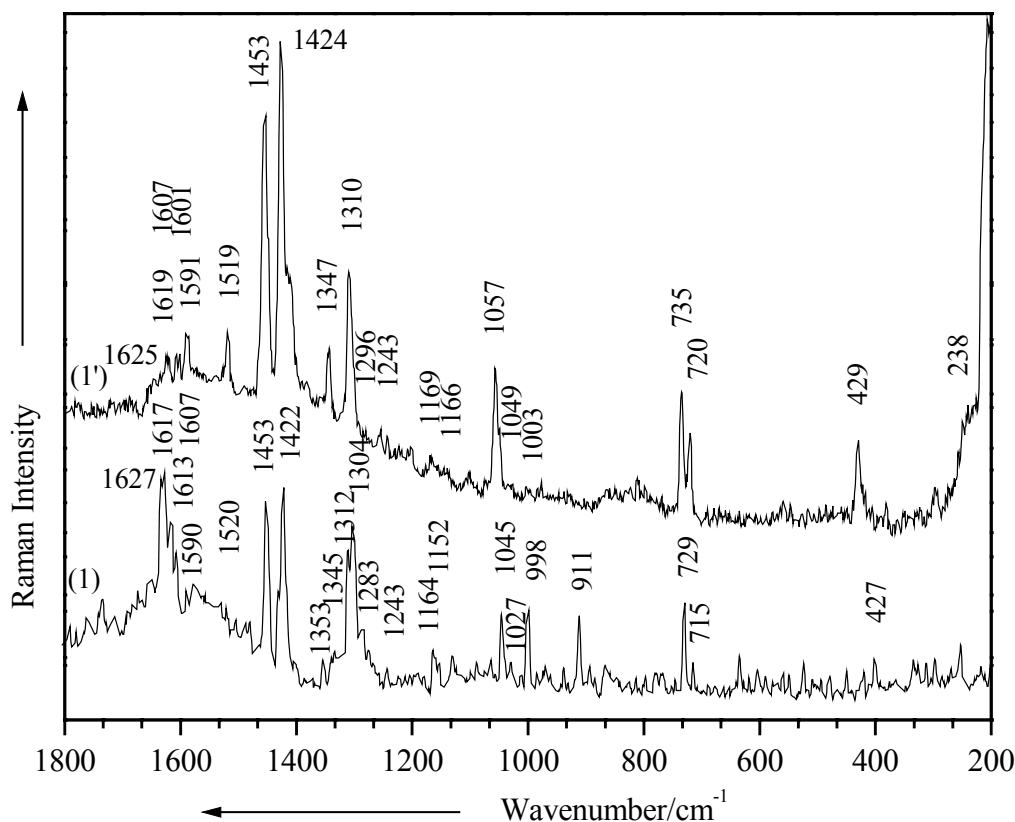


Figure 4.30. Raman (1) and SERS (1') spectra of NiL_2A_n , $\text{L} = \text{PhN}_2\text{O}_2^-$, $n = 1$, $\text{A} = o$ -phenanthroline, on Ag sol. Excitation line: $\lambda_0 = 1064 \text{ nm}$ (1) and $\lambda_0 = 514.5 \text{ nm}$ (1').

The SERS spectra (1'), (2') of NiL_2A_n , with $\text{L} = \text{PhN}_2\text{O}_2^-$, $n = 1$, $\text{A} = o$ -phenanthroline, and $\text{A} = o,o'$ -bipyridine complexes on Ag sol are shown in Figures 4.30 and 4.31, respectively, and compared to their corresponding Raman spectra. SERS spectra of the nickel(II) cupferronato complexes are different from those of the corresponding Raman spectra, which indicates a strong interaction of the nickel(II) cupferronato complexes with the Ag surface. The expected Ag-N stretching band characteristic for the N-adsorbed species in the SERS spectra under 250 cm^{-1} was observed in both spectra (1'), (2') at 238 cm^{-1} (Figures 4.30 and 4.31).

The SERS spectra of **1** and **2** present an enhanced blue shifted band at about 1311 cm^{-1} (Figures 4.30 and 4.31). It was attributed to the new symmetric mode, characteristic for the bidentate coordination of the ONNO unit in the interaction with the metal surface.²⁷⁹

Additionally, the π system interaction with the Ag surface is unfavorable because the phenyl vibrational modes are enhanced but not significantly shifted or broadened.²⁷

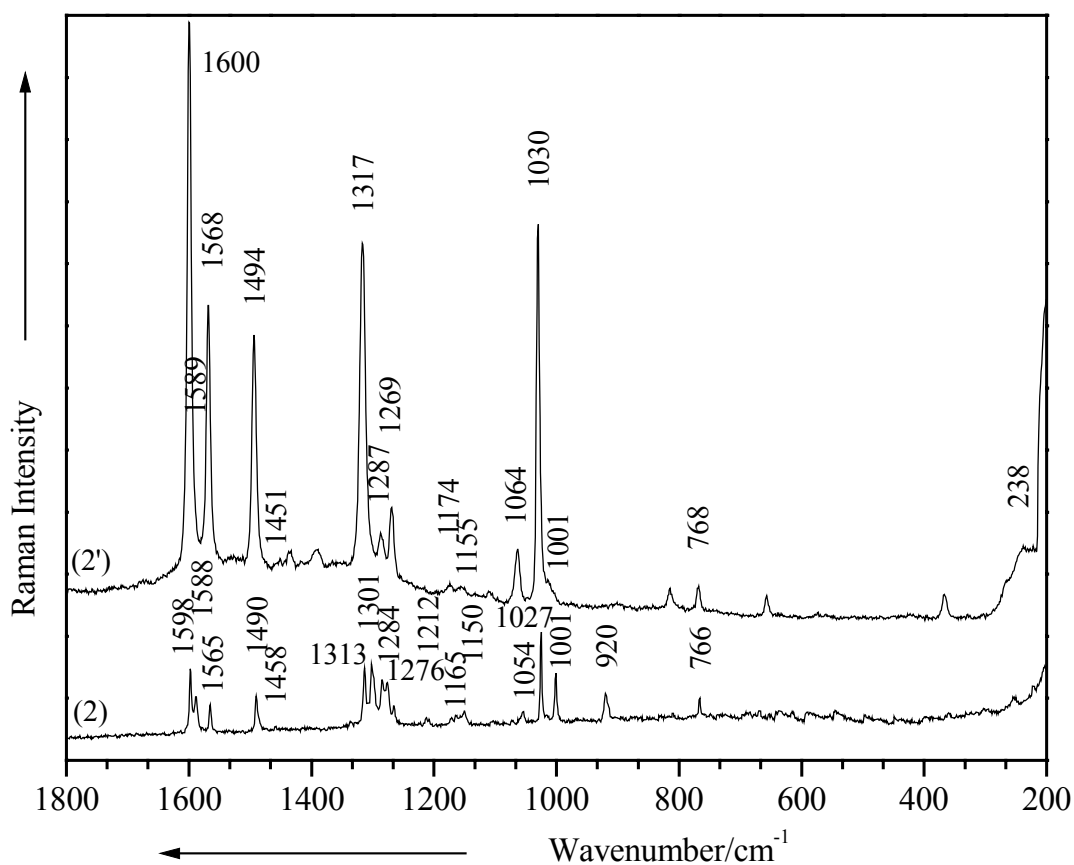


Figure 4.31. Raman (2) and SERS (2') spectra of NiL_2A_n , $\text{L} = \text{PhN}_2\text{O}_2^-$, $n = 1$, $\text{A} = o, o'$ -bipyridine complex, on Ag sol. Excitation line: $\lambda_0 = 647.1 \text{ nm}$ (2) and $\lambda_0 = 514.5 \text{ nm}$ (2').

A similar behavior regarding the *o*-phenanthroline and *o,o'*-bipyridine ring vibrational modes was noticed in the SERS spectra of the complex **1** and **2**. More specific, *o*-phenanthroline and *o,o'*-bipyridine ring breathing modes are less shifted and more enhanced in the SERS spectra. Also, the characteristic *o*-phenanthroline ring stretching modes at 1520, 1354, 729, and 715 cm^{-1} are enhanced but not importantly shifted to higher wavenumbers (Figure 4.30). Therefore, it can be concluded that the *o*-phenanthroline and *o,o'*-bipyridine structures are lying near the Ag surface.

Only a poor SERS spectrum of NiL_2A_n , $n = 2$, $\text{A} = \text{H}_2\text{O}$ complex on roughened Ag electrode could be recorded. However, the SERS fingerprint was detected at 1308 cm^{-1} (Figure 4.32).

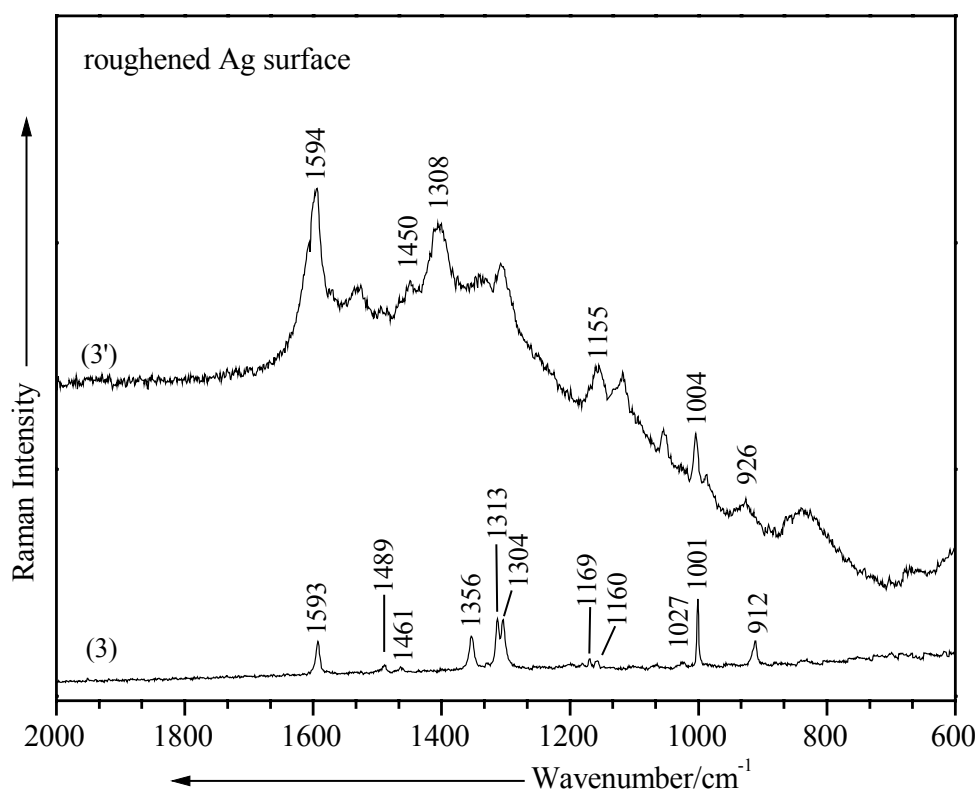


Figure 4.32. Micro-Raman (**3**) and SERS spectra (**3'**) of NiL_2A_n , $\text{L} = \text{PhN}_2\text{O}_2^-$, $n = 2$, $\text{A} = \text{H}_2\text{O}$ complex on roughened silver electrode.
Excitation line: $\lambda_0 = 647.1 \text{ nm}$ (**3**) and $\lambda_0 = 514.5 \text{ nm}$ (**3'**).

The above results obtained from the silver colloidal dispersion are confirmed by SERS experiments on nickel(II) cupferronato complex ($10^{-3} \text{ mol L}^{-1}$ solution) adsorbed on Ag films (Figure 4.33). A similar interaction between the ONNO unit and each Ag substrate was concluded based on the near coincidence both in wavenumbers and relative intensities of the observed bands.

The nickel(II) cupferronato complexes were found to adsorb on different Ag substrates. The best SERS spectra were recorded on the nanometer Ag colloid particles. The low solubility of the nickel(II) cupferronato complexes allowed to study the adsorbed structure only by SERS experiments.

Both electromagnetic resonance and charge-transfer mechanisms were supposed to be involved in the Raman enhancement.²⁸⁰

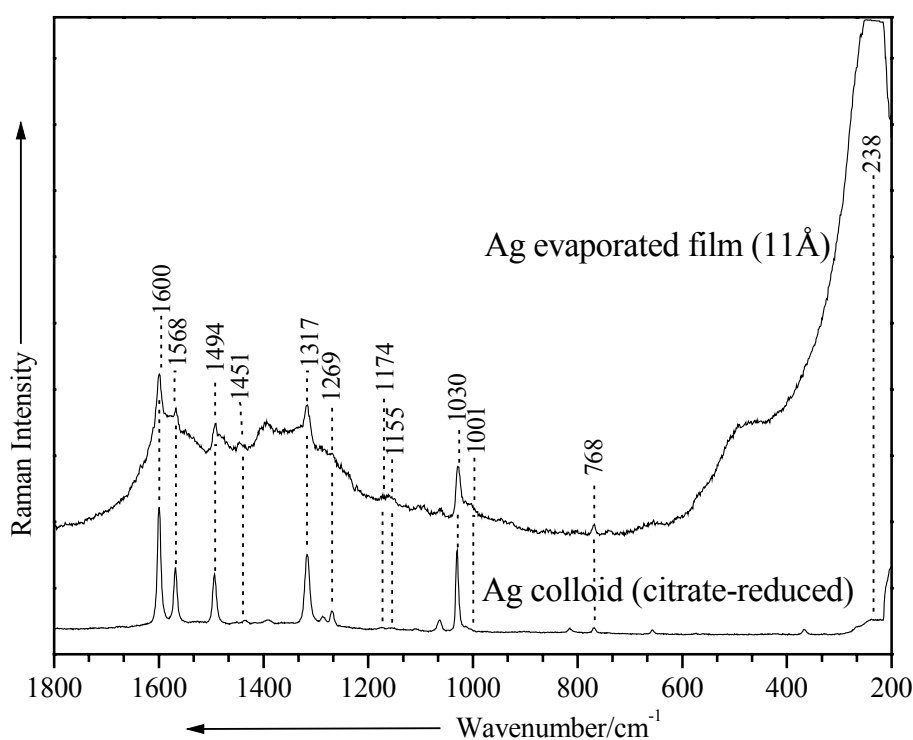


Figure 4.33. SERS spectra of NiL_2A_n , $\text{L} = \text{PhN}_2\text{O}_2^-$, $n = 1$, $\text{A} = o,o'$ -bipyridine complex on different substrates. Excitation line: $\lambda_0 = 514.5 \text{ nm}$.

For the NiL_2A_n complexes, with $\text{L} = \text{PhN}_2\text{O}_2^-$, $n = 2$, $\text{A} = o\text{-NH}_2\text{Py}$ and $o\text{-C}_6\text{H}_4(\text{NH}_2)_2$, there was a lack of solubility or decomposition to graphitic carbon under the laser excitation. The acquiring program allowed the visualization of the photodecomposition.

4.4.3 Conclusions

The FT-Raman study and the DFT calculations results on cupferron and its new nickel(II) cupferronato complexes suggests the electron delocalization through the coordinated ONNO unit and the bidentate coordination of the anionic ligand to the metal centers through the oxygen atoms. SERS spectra of the nickel(II) cupferronato complexes bring additional arguments for the assignment of the symmetric mode of the ONNO moiety in the Raman spectra. Additionally, the SERS spectra of the new compounds suggest a possible adsorption through the N atoms of the ONNO unit to the Ag surface.

Chapter 5

Why Raman and DFT? An already well-known method of studying new organometallic compounds

In the last twenty years, quantum chemical methods have so successfully been developed that now they are almost an indispensable complement of experimental studies in chemistry.^{103, 112, 138}

Density functional methods provide reliable results in the prediction of observed fundamentals modes, the assignment of coupled vibrational modes, and the molecular geometries. They are also more cost-effective from the computational point of view in comparison with scaled Hartree-Fock or many-body perturbation theory.^{103, 108, 109, 112} Bond lengths of transition-metal compounds can be predicted with an accuracy of ± 5 pm, which is a rather conservative estimate. In most cases the agreement with the experimental data is even better. Due to their high reliability, calculated metal-ligand bond lengths could even be used successfully to question experimental results.²⁸¹

Vibrational spectroscopy is one of the most reliable tools for obtaining information about the strength of the bonds in a molecule,^{1, 3, 6, 7, 21} as the vibrational modes of pure metal-ligand stretching modes are directly related to them. But the assignment of these bands may often be very difficult. In such cases theoretical calculations seem to be the best solution.

Without denying or overlooking the merits of other spectroscopic methods, such as X-ray diffraction analysis, it clear that by now vibrational spectroscopy in conjunction with DFT calculations have gained a firm place within the spectroscopic arsenal used to investigate new organometallic complexes. The X-Ray analysis of such compounds may often be very expensive and limited by the non-availability of single crystals.

The DFT calculations carried out on the model compounds analysed in these studies supplied harmonic vibrational wavenumbers and molecular geometries, which are in good agreement with the experimental results obtained from the corresponding isolated complexes. All these aspects, together with further NPA and NBO calculations,^{144-146, 154, 166} allowed us to study the special bonding situations in the new organometallic complexes or to monitor the structural changes observed with the change in temperature during the Raman experiments.

5.1 *Silylene-bridged dinuclear iron complexes*

This project is a collaboration with **Professor Dr. Wolfgang Malisch**'s workgroup, within the **SFB 347** program.

5.1.1 *Molecules presentation*

The chemistry of transition-metal silicon compounds has been an active field of research ever since the early works of Chalk and Harrod²⁸² on the transition-metal-catalyzed hydrosilylation of olefins. In the past decades, a huge number of silyl complexes of almost all transition metals have been synthesized and characterized.²⁸³⁻²⁸⁹ Especially, some palladium and platinum derivatives are encountered as crucial intermediates, not only in hydrosilylation reactions²⁹⁰⁻²⁹² but also in other catalytic processes (e.g., dehydrogenative coupling of SiH moieties²⁹³⁻²⁹⁵) or in ring-opening-metathesis polymerization (ROMP) reactions of cyclic disilanes.^{296, 297}

A central issue in understanding the mechanistic details of these catalytic processes is the strength of the metal-silicon bond. Some insight can be gained from structural data that are available for many transition-metal silyl complexes. For example, the bond lengths observed in $\text{H}_3\text{Si-Co}(\text{CO})_4$ (238.1 pm)²⁹⁸ and $\text{F}_3\text{Si-Co}(\text{CO})_4$ (222.6 pm)²⁹⁹ indicate that the presence of electronegative substituents on the Si atom can greatly increase the strength of the metal-silicon bond. The M-Si bond distances in many structurally characterized silyl complexes $\text{L}_n\text{M-SiR}_3$ (M = Mn, Fe, Co, Rh, Pt) were found to be up to 28 pm shorter than those that would be predicted on the basis of the covalent atom radii.²⁸⁶ These short bond distances are generally attributed to a π -type back-bonding from the d-orbitals of the transition metal into the antibonding $\sigma^*(\text{Si-R})$ orbitals of the silyl group $-\text{SiR}_3$.³⁰⁰⁻³⁰² Consequently, the M-Si bonds in silyl complexes of d^0 metals (Ti^{IV} , Zr^{IV}) show no significant shortening and closely match the predicted covalent values.³⁰³ In the Mössbauer and IR spectral investigations of Pannell and coworkers on $\text{Cp}(\text{OC})_2\text{Fe-R}$ (where R represents a large range of alkyl and silyl groups), the increase in s-electron density at the metal center for the silyl compounds has been attributed to a superior σ -donation from the silyl group, as compared with the alkyl group, rather than to significant iron-silicon π -back-bonding.³⁰⁴ Important π -type back-bonding effects were only observed for the $\text{Cp}(\text{OC})_2\text{Fe-SiMe}_{3-n}\text{Ph}_n$ complexes. However, valence photoelectron spectra that were recorded by Lichtenberger and Rai-Chaudhuri for the complexes $\text{Cp}(\text{OC})_2\text{Fe-SiR}_3$ (R = Me, Cl) have confirmed that silyl substituents can act as effective π -acceptors.³⁰⁵ In a more recent structural and theoretical study on a series of

osmium complexes $(\text{Ph}_3\text{P})_2(\text{OC})(\text{Cl})\text{Os-SiR}_3$ ($\text{R} = \text{F}, \text{Cl}, \text{OH}, \text{Me}$) Roper and coworkers examined the ionic and covalent contributions to the metal-silicon bond in detail.³⁰⁰

Five homologous complexes of the general formula $[\text{Cp}(\text{OC})_2\text{Fe}]_2\text{SiX}_2$ ($\text{X} = \text{H}$ (**6**), F (**7**), Cl (**8**), Br (**9**), I (**10**)) have been prepared by our coworkers (in **Professor Dr. Wolfgang Malisch's** workgroup) with the original intention of using these compounds as precursors for the synthesis of the bis(metallo)silanediol $[\text{Cp}(\text{OC})_2\text{Fe}]_2\text{Si}(\text{OH})_2$ ³⁰⁶ or the bis(metallo)silylene $[\text{Cp}(\text{OC})_2\text{Fe}]_2\text{Si}$. The availability of this series of compounds gave us the opportunity to study, in detail, the bonding situation in bismetalated silanes, which are among a class of compounds for which a growing number of representatives has been prepared in recent years.^{159, 160, 306-313} In this sense, the experimental research and development have demonstrated vibrational spectroscopy to be one of the most useful tools for obtaining information about the strength of the bonds in a molecule, even though the direct assignment of observed IR and Raman bands of comparatively complex molecules is fraught with problems. Theoretical calculations can certainly assist in obtaining a deeper understanding of vibrational spectra of larger organometallic arrangements, such as transition-metal silyl complexes. Thus, to complete the previous characterization of $[\text{Cp}(\text{OC})_2\text{Fe}]_2\text{SiH}_2$ (**6**)^{159, 313} and to obtain a better understanding of the influence of a wide range of SiX_2 groups on the nature of the Fe-Si and CO bonds, FT-IR and FT-Raman spectra of complexes **6-10** were recorded for the first time and discussed in combination with the results of our DFT calculations.

5.1.2 *Results and discussion*

5.1.2.1 *Geometry optimization*

The structural parameters of **6-10**, calculated using BPW91/6-311+G(d) are presented in Table 5.1 in comparison with experimental values of the related crystal structures obtained by our coworkers. For further details regarding the X-Ray measurements, please consult our paper (reference 158). Due to the presence of I atoms in complex **10**, the calculations were carried out in this case using the 3-21G(d) basis set for the I atoms and the 6-311G(d) basis set for the other atoms. As one can notice, the calculated bond distances and bond angles of **6-10** agree well with the reported parameters, which again confirms the experiment and the proposed structures. Unfortunately, for complex **10**, no crystal structure data could be obtained. The only structural parameters available at this time for compound **10** are the computed ones.

Table 5.1. Selected experimental crystal structure data of $[\text{Cp}(\text{OC})_2\text{Fe}]_2\text{SiX}_2$ with X = H, F, Cl, and Br (**6-9**), in comparison with the calculated structural parameters of **6-10**.

| | 6 (X = H) | | 7 (X = F) | | 8 (X = Cl) | | 9 (X = Br) | | 10 (X = I) |
|-------------------|------------------|-------------------|------------------|-------------------|-------------------|-------------------|-------------------|-------------------|-------------------|
| | Exp ^a | Calc ^b | Exp ^c | Calc ^b | Exp ^c | Calc ^b | Exp ^c | Calc ^b | Calc ^d |
| Bond lengths (pm) | | | | | | | | | |
| Si(1)-Fe(1) | 234.2 | 234.0 | 229.24(4) | 229.3 | 230.48(3) | 231.7 | 230.21(19) | 233.9 | 233.4 |
| Si(1)-Fe(2) | 234.0 | 237.2 | 229.55(4) | 232.2 | 230.48(3) | 234.6 | 230.21(19) | 233.9 | 233.4 |
| Si(1)-X(1) | - | 151.7 | 164.12(8) | 166.9 | 213.66(4) | 217.2 | 231.8(2) | 234.0 | 260.5 |
| Si(1)-X(2) | - | 151.3 | 163.23(9) | 166.9 | 213.66(4) | 216.5 | 231.8(2) | 234.0 | 260.5 |
| Fe(1)-C(1A) | 174.2(5) | 174.0 | 175.65(16) | 174.5 | 175.78(15) | 175.1 | 175.8(10) | 175.3 | 175.4 |
| Fe(1)-C(1B) | 175.5(4) | 174.1 | 175.34(15) | 174.4 | 175.12(15) | 174.8 | 173.9(9) | 174.0 | 174.1 |
| C(1A)-O(1A) | 113.6(5) | 116.4 | 115.21(19) | 116.1 | 114.23(18) | 115.9 | 115.6(10) | 115.9 | 115.8 |
| C(1B)-O(1B) | 114.5(7) | 116.4 | 115.28(19) | 116.2 | 114.64(18) | 116.1 | 116.0(9) | 116.5 | 116.5 |
| Fe(1)-Z(Cp) | 172.3(6) | - | 172.9(1) | - | 172.85(7) | - | 173.3 | - | - |

| | 6 (X = H) | | 7 (X = F) | | 8 (X = Cl) | | 9 (X = Br) | | 10 (X = I) |
|-------------------------|------------------|-------------------|------------------|-------------------|-------------------|-------------------|-------------------|-------------------|-------------------|
| | Exp ^a | Calc ^b | Exp ^c | Calc ^b | Exp ^c | Calc ^b | Exp ^c | Calc ^b | Calc ^d |
| Bond angles (Degree) | | | | | | | | | |
| X(2)-Si(1)-X(1) | 104.00 | 102.6 | 99.22(5) | 101.9 | 99.31(3) | 101.2 | 98.74(12) | 100.3 | 101.0 |
| Fe(1)-Si(1)-Fe(2) | 123.48(6) | 124.8 | 125.269(18) | 126.8 | 125.44(2) | 125.8 | 122.16(14) | 122.6 | 122.8 |
| Fe(1)-Si(1)-X(1) | 103.78 | 107.6 | 108.45(3) | 107.9 | 108.606(11) | 107.4 | 108.25(5) | 105.8 | 105.2 |
| C(1B)-Fe(1)-C(1A) | 94.0(2) | 92.9 | 95.99(7) | 93.0 | 93.80(7) | 93.4 | 95.0(4) | 93.9 | 94.1 |
| O(1A)-C(1A)-Fe(1) | 178.1(4) | 177.6 | 177.16(14) | 176.3 | 177.61(13) | 175.3 | 178.3(7) | 174.5 | 174.1 |
| O(1B)-C(1B)-Fe(1) | 178.1(5) | 178.3 | 178.55(14) | 177.3 | 178.10(14) | 176.1 | 178.5(7) | 175.9 | 175.5 |

^aReference 159; ^bCalculated using BPW91/6-311G(d); ^cReference 158; ^dCalculated using BPW91/3-21G(d) for the I atoms and BPW91/6-311G(d) for the other atoms. For **6** and **9** symmetry transformations were used to generate equivalent atoms: #1 -x+1,y,-z+1/2 and #1 -x+1,y,-z+1/2.¹⁵⁸

The most characteristic feature of all three solid-state structures of **7–9** is the coordination geometry of the central Si atom, which deviates significantly from the ideal tetrahedral form, as shown for the example of the fluoro derivative **7** (Figure 5.1). For the Fe-Si-Fe angle, values of 125.3° (**7**), 125.4° (**8**), and 122.2° (**9**) are found, in accordance with Bent's rule, which predicts an enlargement of the angles including the two most electropositive silicon substituents. The DFT calculations showed the same trend (126.8° (**7**), 125.8° (**8**), 122.6° (**9**), and 122.8° (**10**)). Consequently, the X-Si-X angles between the electronegative halogen substituents are considerably smaller (98.7° – 99.3°).

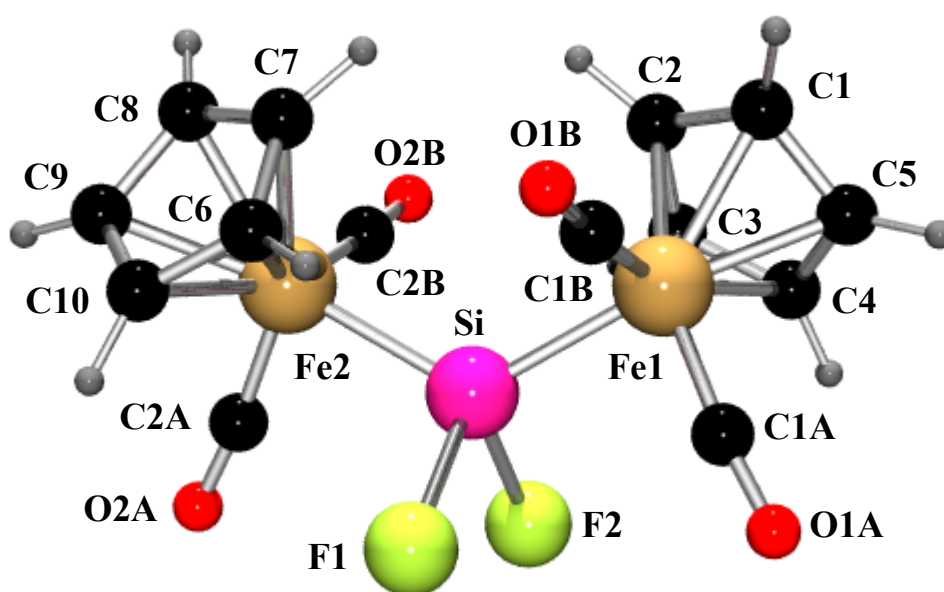


Figure 5.1. The BPW91/6-311G(d) optimized geometry of $[\text{Cp}(\text{OC})_2\text{Fe}]_2\text{SiF}_2$ (**7**).

In the solid state, **7–9** show C_2 symmetry. The view along one of the Fe-Si bonds, as shown in Figure 5.2 for the example of the bromo derivative **9**, reveals a distorted staggered conformation of the substituents in the bis(metallo)silanes **7–9**, with the following pairs adopting a mutually *trans* position: Cp/X, CO/X and CO/Fe.

The Fe-Si bond distances in the bismetalated silanes **7–9** (229.24 – 234.2 pm) are longer than those in comparable mono(ferrio)silanes $\text{Cp}(\text{OC})_2\text{Fe-SiR}_3$ (220.0 – 229.0 pm).^{305, 314} This is probably the result of a much lower Fe-Si π -type back-bonding in the bis(ferrio)silanes, which is due to the competition of two electron-releasing $\text{Cp}(\text{OC})_2\text{Fe}$ fragments on the same Si atom. Similar observations have been made for two other structurally characterized bis(ferrio)silanes: $[\text{Cp}(\text{OC})_2\text{Fe}]_2\text{SiH}_2$ (234.0 pm)¹⁵⁹ and

$[\text{Cp}(\text{OC})_2\text{Fe}]_2\text{Si}(\text{H})\text{OH}$ (234.0 pm).³⁰⁶ It is also remarkable that the Fe-Si bond length of **7-10** is almost invariant with respect to the type of halogen substituent on the silylene bridge, which means that no significant shortening of the Fe-Si bond is observed as the electronegativity of the substituents increases (Table 5.2).

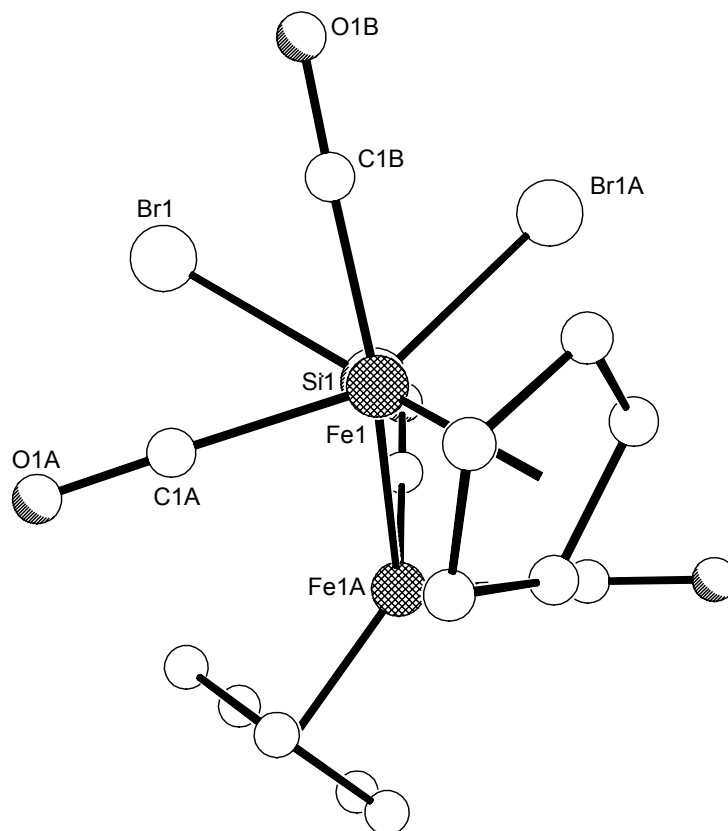


Figure 5.2. View along the Fe1-Si1 axis of $[\text{Cp}(\text{OC})_2\text{Fe}]_2\text{SiBr}_2$ (**9**).

As expected, all three halogen-substituted bis(ferrio)silanes **7-9** form intermolecular hydrogen bonds. In the case of $[\text{Cp}(\text{OC})_2\text{Fe}]_2\text{SiBr}_2$ (**9**), a simple chain structure can be observed. The two strongest hydrogen bridges are found between the cyclopentadienyl hydrogens (H4, H5) and the Br or O1B atoms, respectively (Figure 5.3(a)).

A similar arrangement is found for $[\text{Cp}(\text{OC})_2\text{Fe}]_2\text{SiCl}_2$ (**8**), which involves the interaction of the Cl substituents with the H1 atom and the interaction of the carbonyl oxygen atom O1B with the H2 atom (Figure 5.4(a)). In addition, hydrogen bridges between the cyclopentadienyl hydrogens (H3) and carbonyl groups (O1A) cross-link the chains of **8** in a plane (Figure 5.4(b)).

The solid-state structure of $[\text{Cp}(\text{OC})_2\text{Fe}]_2\text{SiF}_2$ (**7**) is more complex. Two molecules are linked, via hydrogen bridges between a cyclopentadienyl hydrogen (H2) and a carbonyl

oxygen atom (O2B), to a “dimer”. Each dimer is connected to other dimers via strong hydrogen bridges between the fluoro substituents and the cyclopentadienyl hydrogens atoms (H3, H8), with each fluoro atom forming two hydrogen bonds to different molecules, resulting in a three dimensional network (Figure 5.3(b)).

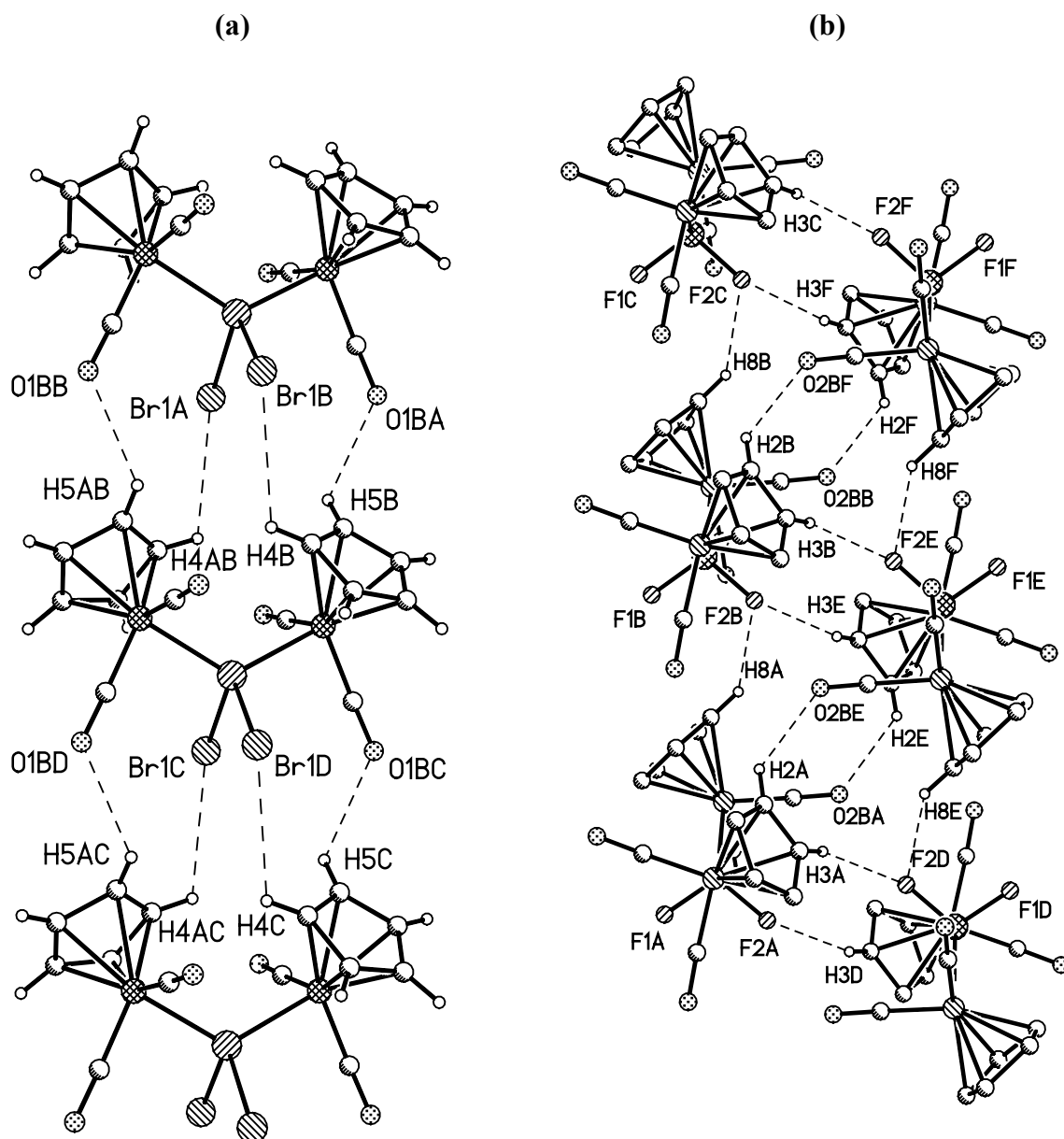


Figure 5.3. (a) Hydrogen bridges Br1-H4 (320.0 pm) and O1B-H5 (256.0 pm) forming the chain structure of **9**; (b) Segment of the three-dimensional network of **7**.

Only the three strongest hydrogen bonds are shown:

O2B-H2 (250.0 pm), F2-H3 (242.0 pm), and F2-H8 (242.0 pm).

The variety in the solid state structures of **7-9** can be explained by the different strength of the H···X hydrogen bonds, which is greatest for **7**, because of the small and hard F atoms, and decreases in the following order $7 \gg 8 > 9$. This can also be deduced from the fact that, in the case of **7**, every F atom forms two hydrogen bonds to cyclopentadienyl hydrogen atoms.¹⁵⁸

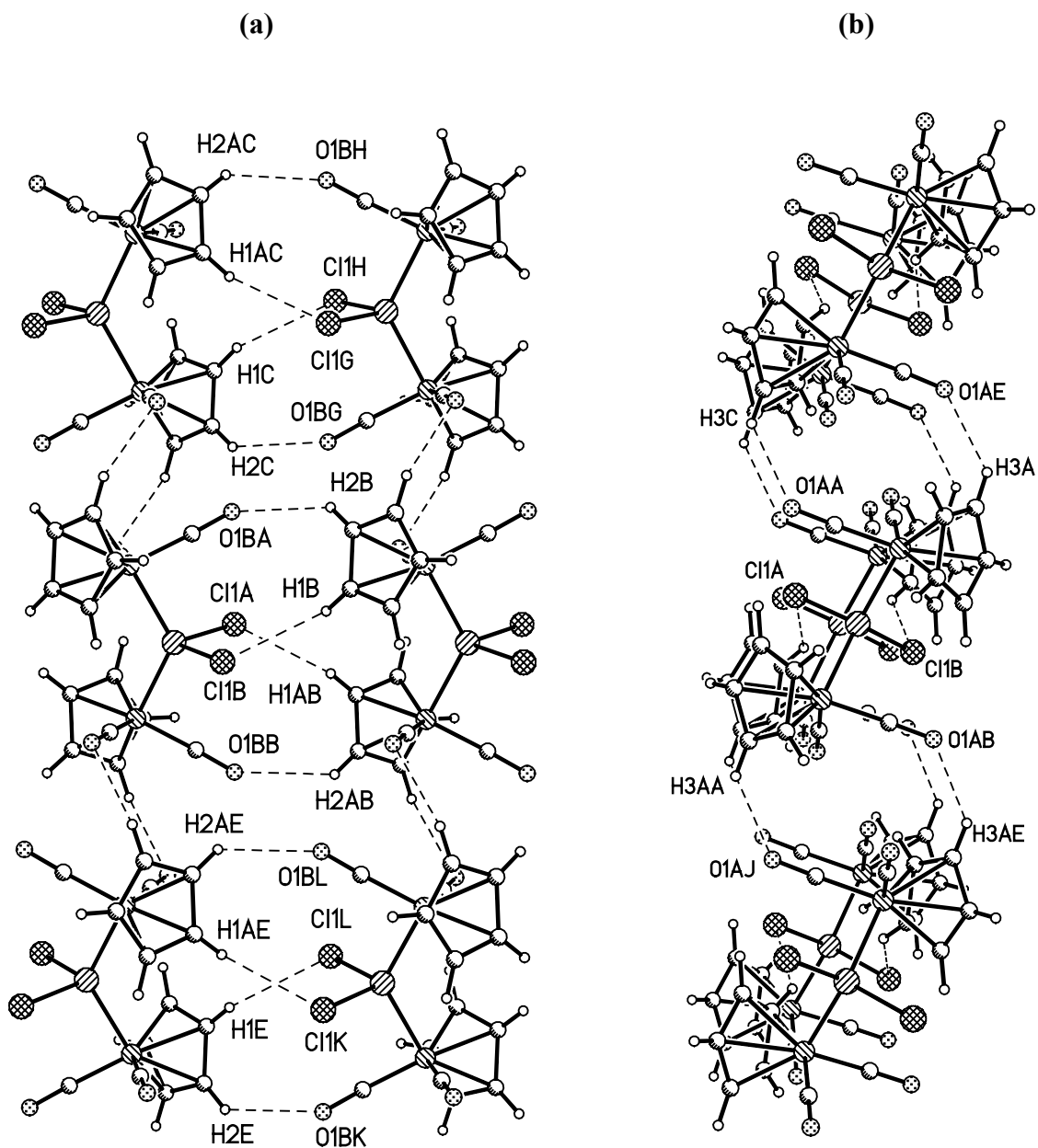


Figure 5.4. (a) View along the hydrogen-bridged chains of **8** with C11-H1 (288.0 pm) and O1B-H2 (258.0 pm); (b) View onto the cross-linked chains of **8** with O1A-H3 (256.0 pm).

5.1.2.2 *Vibrational spectroscopy*

The most significant calculated and experimental fundamental vibrational modes, together with their Raman scattering activities, are summarized in Table 5.2. As one can notice, the calculated values agree well with the experimental data. However, some deviations were observed for the vibrations involving lone-pair atoms and the SiH₂ vibrations in **6**, for which anharmonicity is large. The results were then scaled to better approach the experimental spectra in these regions (Table 5.2). All other calculated wavenumbers were in very good agreement with the experimental values and should not be scaled. The best conformity between calculation and experimental data was observed for the cyclopentadienyl ring breathing and ν (CC) modes, for which the maximum deviations were only 4 and 6 cm⁻¹, respectively (Table 5.2).

The FT-Raman spectra of **6-9** in the CO spectral region are presented in Figure 5.5. Unfortunately, no Raman spectrum could be measured for [Cp(OC)₂Fe]₂SiI₂ (**10**), because of its decomposition under the laser light.

A closer examination of the 2100-1850 cm⁻¹ spectral region in the FT-Raman spectra of **6-9** indicates the presence of two or more symmetric and asymmetric CO vibrational modes (Table 5.2, Figure 5.5). More exactly, **8** and **9** show only two ν (CO) vibrations, whereas more than two bands can be observed for **6** and **7** (Table 5.2, Figure 5.5). In the Raman spectrum of **6**, the bands at 2074 and 2043 cm⁻¹ were assigned to symmetric SiH stretching modes (Figure 5.6 (a)). For the other peaks at 2028, 1987, 1978, and 1928 cm⁻¹, the theoretical calculations and literature indicate CO stretching modes strongly mixed with symmetric and asymmetric SiH₂ stretching vibrations (Figure 5.6 (b)).^{316, 317} For **7-9**, these vibrations are “pure” CO stretchings and no other internal coordinates are involved (Figure 5.7).³¹⁶⁻³²³ As expected, the DFT calculations which were performed without any symmetry restriction, led to more than two ν (CO) modes in each case (**6-10**) (Table 5.2). Taking into account that the X-ray structure determination indicated a C₂ symmetry for all complexes, we believe that the appearance of more than two bands in the CO spectral region of **7** (1999, 1983, 1956, 1944, and 1931 cm⁻¹) is mostly due to the existence of different conformers, as previously reported for similar compounds.³¹⁸⁻³²⁰

For complexes **7-9**, the ν (CO) vibration is coupled only with other ν (CO) vibrations; therefore the wavenumber shift can be taken as a direct measure of bond strength. As one can

Table 5.2. Selected calculated and experimental fundamental vibrational wavenumbers (in cm^{-1}) for $[\text{Cp}(\text{CO})_2\text{Fe}]_2\text{SiX}_2$ with $X = \text{H, F, Cl, Br, and I}$ (**6-10**), together with their tentative assignments.^a

| X = F (7) | | | | X = Cl (8) | | | | X = Br (9) | | | | X = I (10) | | | X = H (6) | | | | Vibrational assignment | |
|------------|----------------|-------------------|-------------------|------------|--------|-------------------|-------------------|------------|--------|-------------------|-------------------|------------|-------------------|-------------------|-----------|--------|-------------------|-------------------|---|--------------------------------|
| IR | Raman | Calc ^b | Scal ^d | IR | Raman | Calc ^b | Scal ^d | IR | Raman | Calc ^b | Scal ^d | IR | Calc ^c | Scal ^d | IR | Raman | Calc ^b | Scal ^d | | |
| | | | | | | | | | | | | | | | | 2074vw | 2064 | 2028 | $\nu_{\text{sym}}(\text{SiH})$ | |
| | | | | | | | | | | | | | | | | 2034 | 2043vw | 2042 | 2006 | $\nu_{\text{sym}}(\text{SiH})$ |
| 2008 | 1999ms | 2025 (37.32) | 1990 | 2012 | 2003ms | 2031 | 1996 | 2015 | 2006ms | 2027 | 1992 | 2016 | 2027 | 1992 | 2027 | 2028ms | 2007 | 1972 | $\nu_{\text{sym}}(\text{SiH}_2) + \nu_{\text{sym}}(\text{CO})$ | |
| 1989 | 1983w | 2001 (27.40) | 1966 | 1998 | | 2006 | 1971 | 2000 | | 2020 | 1985 | 2002 | 2021 | 1986 | 1986 | 1987w | 1994 | 1960 | $\nu_{\text{asym}}(\text{SiH}_2) + \nu_{\text{asym}}(\text{CO})$ | |
| very broad | 1956w 1944w | 1982 (32.26) | 1948 | | | 1989 | 1955 | 1962 | | 1972 | 1938 | 1968 | 1974 | 1940 | 1967 | 1978vw | 1969 | 1934 | $\nu_{\text{sym}}(\text{SiH}_2) + \nu_{\text{sym}}(\text{CO})$ | |
| | | | | | | | | | | | | | | | 1921 | 1928s | 1949 | 1915 | $\nu_{\text{asym}}(\text{SiH}_2) + \nu_{\text{asym}}(\text{CO})$ | |
| 1932 | 1931ms | 1956 (29.42) | 1922 | broad | 1941s | 1960 | 1926 | 1945 | 1948vs | 1971 | 1937 | 1952 | 1973 | 1939 | 1913 | | | | $\nu_{\text{asym}}(\text{SiH}_2) + \nu_{\text{asym}}(\text{CO})$ | |
| 1434 | 1432vw | 1429 (10.62) | 1404 | 1433 | 1432vw | 1430 | 1405 | 1431 | 1430vw | 1432 | 1407 | 1430 | 1431 | 1406 | 1432 | 1430vw | 1431 | 1406 | $\nu(\text{CC}) + \text{i.p. } \delta(\text{CH})$ | |
| 1418 | 1419vw | 1414 (5.76) | 1390 | 1418 | 1418vw | 1415 | 1391 | 1417 | 1419vw | 1415 | 1391 | 1415 | 1415 | 1391 | 1413 | 1414vw | 1414 | 1390 | $\nu(\text{CC}) + \text{i.p. } \delta(\text{CH})$ | |
| 1367 | | 1365 (2.40) | 1341 | 1366 | | 1366 | 1342 | 1366 | | 1367 | 1343 | 1367 | 1367 | 1343 | 1366 | 1360vw | 1366 | 1342 | $\nu(\text{CC}) + \text{i.p. } \delta(\text{CH})$ | |
| | 1117s | 1117 | 1098 | | 1116vs | 1117 | 1098 | | 1115vs | 1119 | 1100 | | 1119 | 1100 | | 1113s | 1116 | 1097 | Cp ring breathing | |
| | | (101.21) | | | | | | | | | | | | | | | | | | |
| 1072 | 1070vw | 1063 (4.35) | 1045 | 1063 | 1063vw | 1064 | 1046 | 1062 | 1064vw | 1062 | 1044 | 1062 | 1062 | 1045 | 1065 | 1062w | 1062 | 1044 | $\text{i.p. } \delta(\text{CH})$ | |
| 843 | | 846 (0.61) | 831 | 847 | 848vw | 848 | 833 | 848 | 849vw | 848 | 833 | 851 | 852 | 837 | 843 | 846vw | 845 | 830 | $\omega(\text{SiH}_2) + \text{o.p. } \delta(\text{CH})$ | |
| 776 | | 764 (0.55) | 751 | | | | | | | | | | | | | | | | $\nu_{\text{asym}}(\text{SiF}_2) + \text{o.p. } \delta(\text{CH})$ | |
| 747 | | 726 (0.62) | 713 | | | | | | | | | | | | | | | | $\nu_{\text{sym}}(\text{SiF}_2) + \text{o.p. } \delta(\text{CH})$ | |
| 642 | | 650 (3.66) | 639 | 639 | | 646 | 635 | 636 | | 647 | 636 | 632 | 645 | 634 | 647 | 638vw | 653 | 642 | $\text{i.p. } \delta(\text{FeCO}) + \tau(\text{SiH}_2) + \text{o.p. } \delta(\text{CH})$ | |
| 605 | | 603 (0.48) | 593 | sh | | 602 | 592 | 602 | | 605 | 595 | 597 | 604 | 594 | 604 | 601vw | 602 | 592 | $\text{o.p. } \delta(\text{FeCO}) + \tau(\text{SiH}_2) + \text{o.p. } \delta(\text{CH})$ | |
| 531 | 531vw | 535 (3.42) | 526 | 521 | 526w | 527 | 518 | 519 | 525sh | 523 | 514 | 516 | 521 | 512 | 524 | 526w | 535 | 526 | $\text{i.p., o.p. } \delta(\text{FeCO})$ | |
| 520 | 521vw | 518 (0.96) | 509 | | 516sh | 518 | 509 | 515 | 519w | 512 | 503 | 508 | 509 | 500 | 516 | 513sh | 519 | 510 | $\text{o.p. } \delta(\text{CO})$ | |
| 467 | 464vw | 455 (1.28) | 447 | 466 | 463vw | 461 | 453 | 462 | 458w | 455 | 447 | 460 | 452 | 444 | 465 | 463vw | 464 | 456 | $\nu_{\text{asym}}(\text{SiCl}_2) + \nu_{\text{sym}}(\text{SiBr}_2) + \delta(\text{CO}) + \rho(\text{SiH}_2)$ | |

119 *Why Raman and DFT?*

| | | | | | | | | | | | | | | |
|-------|-------------|-----|-------|-----|-----|-------|-----|-----|-----|-----|-----|-------|-----|--|
| sh | 453 (2.37) | 445 | sh | 452 | 444 | sh | 453 | 445 | sh | 451 | 443 | 452 | 444 | $v_{\text{sym}}(\text{SiCl}_2) + \delta(\text{CO}) +$ |
| 435 | 435 (0.82) | | 425 | 428 | | | | | 420 | 398 | | 434 | 426 | $\rho(\text{SiH}_2) + \delta(\text{SiX}_2)$ |
| | | 427 | | | 421 | | | | | | 391 | | | |
| 426vw | 430 (0.92) | 423 | 426vw | 419 | 412 | 394vw | 384 | 377 | | 384 | 377 | | | $\text{o.p. } \delta(\text{CH}) + \text{o.p. } \delta(\text{FeCO})$ |
| | | | | | | | | | | | | | | $+ \omega(\text{SiF}_2) + v_{\text{sym}}(\text{SiCl}_2)$ |
| 398vw | 390 (6.69) | 383 | 387w | 384 | 377 | 374vs | 376 | 369 | | 374 | 368 | 397 | 390 | $v_{\text{asym}}(\text{FeCp}) + v_{\text{sym}}(\text{SiBr}_2) +$ |
| | | | | | | | | | | | | | | $\omega(\text{SiH}_2) + \text{o.p. } \delta(\text{FeCO})$ |
| | 385 (7.68) | 378 | | 379 | 372 | | 376 | 370 | | 370 | | 389m | 390 | $v_{\text{asym}}(\text{SiFeCp}) + \rho(\text{SiH}_2) +$ |
| | | | | | | | | | | | | | | $\omega(\text{SiX}_2) + \text{o.p. } \delta(\text{FeCO})$ |
| 376vs | 370 (5.88) | 364 | 369vs | 367 | 361 | 353m | 358 | 352 | | 358 | 352 | 365s | 364 | $v_{\text{sym}}(\text{FeCp}) + v_{\text{asym}}(\text{SiBr}_2) +$ |
| | | | | | | | | | | | | | | $\text{i.p., o.p. } \delta(\text{FeCO})$ |
| 350ms | 367 (23.60) | 361 | | 350 | 344 | | 344 | 338 | | 342 | 336 | | | $v_{\text{sym}}(\text{SiFeCp}) + \omega(\text{SiF}_2) +$ |
| | | | | | | | | | | | | | | $\text{o.p. } \delta(\text{FeCO})$ |
| | | | | | | | | | | 325 | 319 | 328vw | 334 | $v_{\text{sym}}(\text{SiI}_2) + \omega(\text{SiH}_2) + v_{\text{sym}}$ |
| | | | | | | | | | | | | | | $(\text{FeCp}) + \text{i.p., o.p. } \delta(\text{FeCO})$ |
| | | | | | | | | | | 321 | 315 | | | $v_{\text{asym}}(\text{SiI}_2) + v_{\text{asym}}(\text{FeCp}) +$ |
| | | | | | | | | | | | | | | $\text{i.p., o.p. } \delta(\text{FeCO})$ |
| | | | | | | | | | | | | 276vs | 276 | $\delta_{\text{sym}}(\text{FeCp}) + \text{i.p. } \delta(\text{SiH}_2) +$ |
| | | | | | | | | | | | | | | $\text{o.p. } \delta(\text{FeCO})$ |
| 242vw | 228 (1.56) | 224 | 245vs | 238 | 234 | | | | | | | | | $\delta_{\text{asym}}(\text{FeCp}) + \gamma(\text{SiCl}_2) +$ |
| | | | | | | | | | | | | | | $\omega(\text{SiF}_2) + \text{o.p. } \delta(\text{FeCO})$ |
| 224vs | 215 (19.19) | 211 | | | | | | | | | | | | $\text{i.p. } \delta(\text{SiF}_2) + \delta_{\text{sym}}(\text{FeCp}) +$ |
| | | | | | | | | | | | | | | $\text{o.p. } \delta(\text{FeCO})$ |
| | | | | | | 204s | 191 | 188 | | | | | | $v_{\text{sym}}(\text{SiBr}_2) + \delta_{\text{asym}}(\text{SiFeCp})$ |
| | | | | | | | | | | | | | | $+ \text{o.p. } \delta(\text{FeCO})$ |

^aAbbreviations: vw - very weak, w - weak, m - medium, ms - medium strong, s - strong, vs - very strong, sh - shoulder, sym - symmetric, asym - asymmetric, i.p. - in-plane, o.p. - out-of-plane, v - stretching, δ - bending, ω - wagging, τ - twisting, ρ - rocking, γ - scissoring; Cp - cyclopentadienyl. Calculated Raman scattering activities, shown in parentheses, are given in units of $\text{\AA}^4/\text{amu}$; ^bCalculated using BPW91/6-311G(d); ^cCalculated using BPW91/3-21G(d) for the I atoms and BPW91/6-311G(d) for the other atoms; ^dScaled by 0.9827, according to the value proposed by Shillady and coworkers.³¹⁵

notice (Figure 5.5, Table 5.2), the sequential replacement of the H atoms with either F, Cl, or Br atoms on the Si atom causes the $\nu(\text{CO})$ values to increase. Furthermore, the magnitude of this effect depends on the substituents in the following order: $\text{F} < \text{Cl} < \text{Br}$ (i.e., 1999, 2003, 2006 cm^{-1} and 1931, 1941, 1948 cm^{-1}). The same trend was observed in the IR spectra and confirmed by the DFT calculations ($\text{F} < \text{Cl} < \text{Br} \leq \text{I}$), although the experimental values differ in this case by almost 30 cm^{-1} from the experimental data (Table 5.2). However, when scaled by 0.9827 in this spectral region,³¹⁵ the calculated CO stretching modes come very close to the

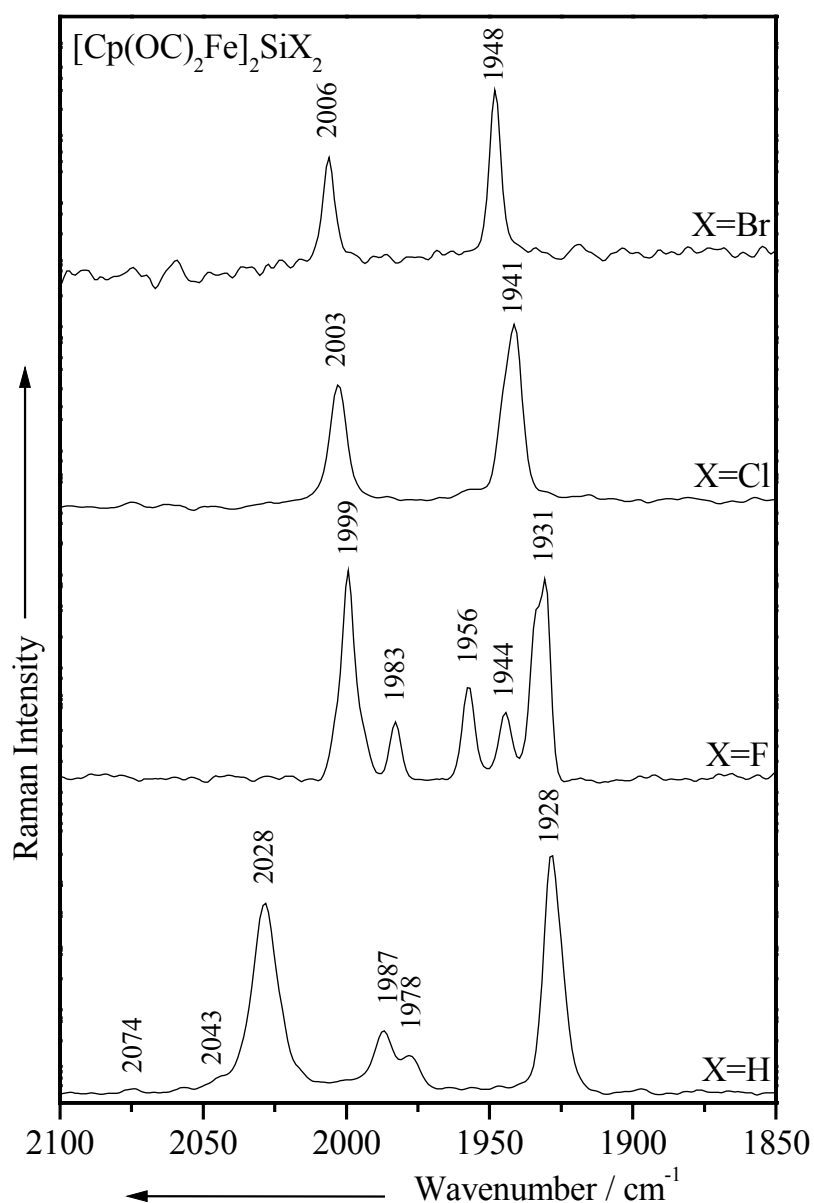


Figure 5.5. The FT-Raman spectra of **6-9** in the CO spectral region.

Excitation line: $\lambda_0 = 1064 \text{ nm}$.

experimental values (Table 5.2). This is a very surprising result, because it is contrary to the tendency observed for other homologous silyl complexes $(OC)_L M-SiR_3$,³⁰⁵ where the $\nu(CO)$ values decreased as the electronegativity of the silyl substituent decreased.

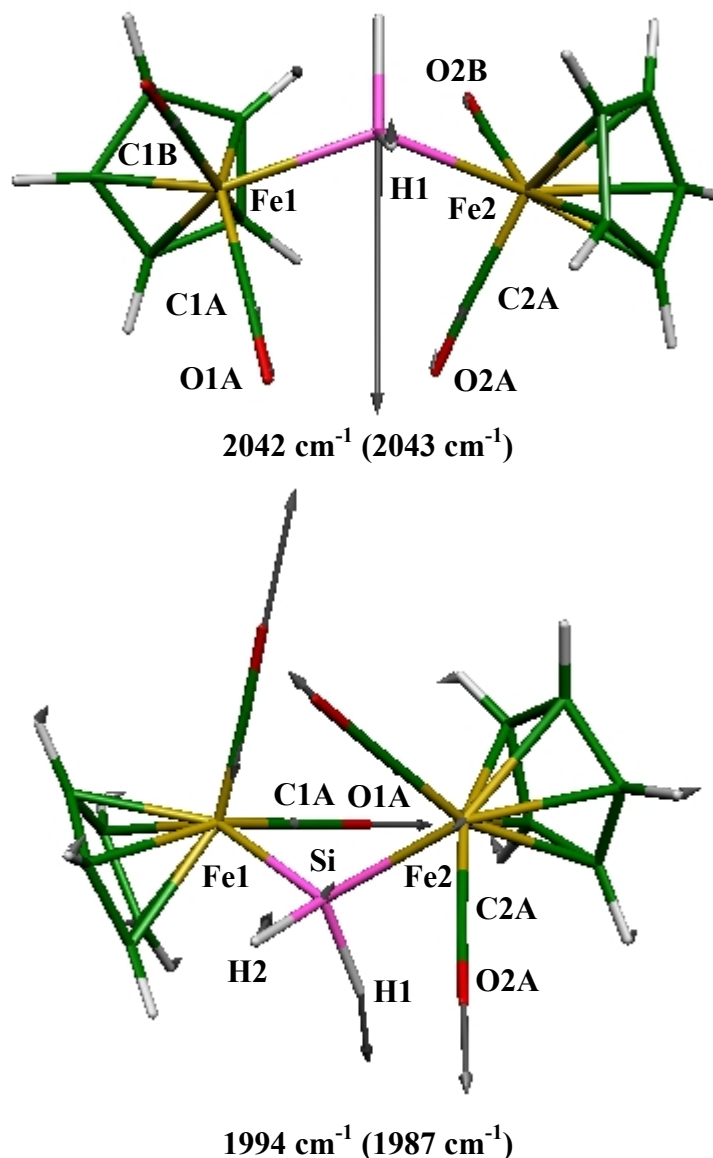


Figure 5.6. The fundamental calculated (BPW91/6-311G(d)) vibrational modes of $[Cp(OC)_2Fe]_2SiH_2$ (**6**), which imply (a) symmetric SiH stretching mode and (b) CO stretching modes strongly mixed with asymmetric SiH₂ stretching vibrations.

The experimental Raman values are given in parentheses.

This unexpected shift of the carbonyl stretching mode to higher wavenumbers could be explained by an increase of the electron density on the metal available for d- π -type back-bonding to the $\pi^*(CO)$ orbitals. The NPA (Table 5.3) actually reveals that the Fe atoms in **6**-

10 are positively charged, with the lowest formal charge being found for the fluorine derivative **7** (+0.698) and significantly higher charges being observed for the other halogen

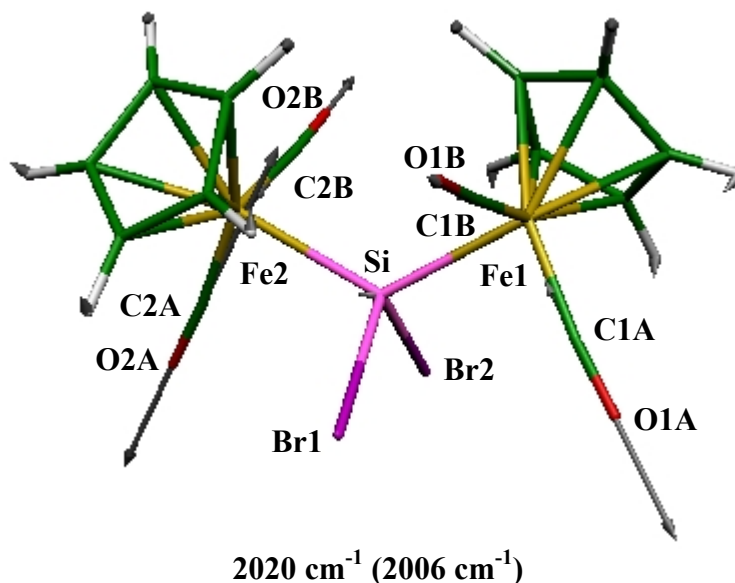


Figure 5.7. The fundamental calculated (BPW91/6-311G(d)) symmetric CO stretching mode of $[\text{Cp}(\text{OC})_2\text{Fe}]_2\text{SiBr}_2$ (**9**). The experimental Raman value is given in parentheses.

derivatives **8-10**. Despite the undoubtedly higher electronegativity of the SiF_2 unit, the Fe atom in **7** still bears the highest electron density. The reasons for these observations can be rationalized assuming a π -type bonding from the nonbonding halogen valence electrons to the unoccupied $d(\text{Si})$ or $\sigma^*(\text{Fe-Si})$ orbitals, respectively. Such a π -type overlap is more efficient for smaller orbitals (e.g., in F) than for the more diffuse orbitals of the larger halogen substituents and might therefore overcompensate the opposite ionic contributions to the Fe-Si bond.

For a better understanding of the π -type bonding from the nonbonding halogen valence electrons to the unoccupied $d(\text{Si})$ or $\sigma^*(\text{Fe-Si})$ orbitals, we performed an NBO analysis for quantitative information regarding these second-order interactions. Table 5.4 shows the occupancy of the lone-pair orbitals n_x at the halogen atoms and that of the $\sigma^*(\text{Fe-Si})$ orbitals. As one can notice, the ionic contribution decreases in the order $\text{F} > \text{Cl} > \text{Br} > \text{I}$, as indicated by the presence of four lone-pair orbitals of the fluoro and chloro derivatives (**7** and **8**); the most electronegative compound (**7**) presents a higher occupancy. As we have already mentioned, the NPA analysis indicates that the Fe atom in **7** has the highest electron density, in comparison with **8-10** (Table 5.3), which is further substantiated by the NBO results (Table 5.4), that show a decrease in the population of the $\sigma^*(\text{Fe-Si})$ orbitals while going from **7** to

10. The NBO analysis reveals that $\sigma_I^*(\text{Fe-Si})$ orbitals are a mixture of Fe- and Si-centered hybrids, which have sd form at the Fe atom and sp form at the Si atom. In contrast to this, $\sigma_2^*(\text{Fe-Si})$ orbitals have almost pure Si character (Table 5.4). Moreover, a lone-pair orbital - composed of a hybrid of a high p-character and an occupancy of 0.63 and 0.59 e, respectively (Table 5.4) - at the Si atom was detected only for **7** and **8**. We would like to mention that the possible discrepancies in the calculated values of complex **10** (in comparison with the other complexes **7-9**) may be caused by the different basis set employed in this case for the halogen atom (3-21G(d) for the I atoms and 6-31G(d) for the other atoms).

Table 5.3. Partial charges (e) situated on selected atoms of $[\text{Cp}(\text{OC})_2\text{Fe}]_2\text{SiX}_2$ with X = H, F, Cl, Br, and I (**6-10**), determined by the Natural Population Analysis.

| Atom | 6 ^a | 7 ^a | 8 ^a | 9 ^a | 10 ^b |
|------|-----------------------|-----------------------|-----------------------|-----------------------|------------------------|
| X | -0.063 | -0.402 | -0.336 | -0.265 | -0.128 |
| Si | -0.076 | +0.676 | +0.167 | +0.100 | -0.330 |
| Fe | +0.740 | +0.698 | +0.767 | +0.766 | +0.805 |
| C | -0.026 | -0.036 | -0.020 | +0.011 | +0.034 |
| O | -0.196 | -0.186 | -0.175 | -0.162 | -0.159 |

^aCalculated using BPW91/6-311G(d); ^bCalculated using BPW91/3-21G(d) for the I atoms and BPW91/6-311G(d) for the other atoms.

Table 5.5 presents the strengths of the perturbative donor-acceptor interactions, which involve an occupied and formally unoccupied NBOs. A closer examination of the stabilization energies in Table 5.5 reveals stronger π -type back-bonding for **7** and **8**, showing slightly higher energy values for the chlorine compound **8** (417.35 kJ/mol) and very small values for the other derivatives (**9** and **10**). However, for the $\sigma_I^*(\text{Fe-Si})$ orbital, the highest stabilization energy (120.88 kJ/mol) was found in the fluorine compound **7**. In addition, in the case of the fluoro derivative **7**, we also observed a strong $n_{\text{Si}} \rightarrow \sigma^*(\text{Fe-Si})$ interaction (929.27 kJ/mol) that should lead to a significant π -stabilization of **7**. This effect is negligible for the other three compounds (**8-10**).

Table 5.4. Orbital occupancy (e) and contributions of atomic orbitals (%) for [Cp(OC)₂Fe]₂SiX₂ with X = F, Cl, Br, and I (7-10).

| | 7 ^a | 8 ^a | 9 ^a | 10 ^b |
|----------------------|--|--|--|--|
| σ_1^* (Fe-Si) | 0.46858 e (sd ^{1.87} , sp ^{0.23}) | 0.40984/0.38207 e (sd ^{1.93} , sp ^{1.30}) | 0.38570/0.36686 e (sd ^{1.81} , sp ^{2.25}) | 0.34184 e (sd ^{1.92} , sp ^{1.21}) |
| Fe | 52.30 % | 56.56 % | 55.78 % | 47.25 % |
| Si | 47.70 % | 43.44 % | 44.22 % | 52.75 % |
| σ_2^* (Fe-Si) | 0.54904/0.38657 e (d, p) | 0.46016 e (d, p) | | 0.48267/0.90064 e (d, p) |
| Fe | 4.84 % | 4.83 % | | 4.24 % |
| Si | 95.16 % | 95.17 % | | 95.76 % |
| n_{Si} | 0.62590 e (sp ^{5.62}) | 0.58662 e (sp ^{7.43}) | | |
| n_x (1) | 1.97890 e (sp ^{0.67}) | 1.97684 e (sp ^{0.35}) | 1.97774 e (sp ^{0.27}) | 1.98099 e (sp ^{0.17}) |
| n_x (2) | 1.93219 e (p) | 1.94419 e (p) | 1.93461 e (p) | 1.93833 e (p) |
| n_x (3) | 1.92907 e (p) | 1.93430 e (p) | 1.92902 e (p) | 1.93250 e (p) |
| n_x (4) | 1.79020 e (sp ^{1.48}) | 1.57587 e (sp ^{2.86}) | | |

^aCalculated using BPW91/6-31G(d); ^bCalculated using BPW91/3-21G(d) for the I atoms and BPW91/6-31G(d) for the other atoms.

Table 5.5. Results of the NBO analysis for [Cp(OC)₂Fe]₂SiX₂ with X = F, Cl, Br, and I (**7-10**).

| | 7^a | 8^a | 9^a | 10^b |
|--|----------------------|--|----------------------|-----------------------|
| | | <i>n_x → σ₂[*](Fe-Si)</i> | | |
| <i>E</i> (2) (kJ/mol) ^c | 271.29 | 417.35 | | 72.59 |
| <i>ε</i> (<i>j</i>) - <i>ε</i> (<i>i</i>) (a.u.) | 0.74 | 0.38 | | 1.11 |
| <i>F</i> (<i>i</i> , <i>j</i>) (a.u.) | 0.205 | 0.174 | | 0.141 |
| | | <i>n_x → σ₂[*](Fe-Si)</i> | | |
| <i>E</i> (2) (kJ/mol) ^c | 92.88 | 106.60 | | 73.97 |
| <i>ε</i> (<i>j</i>) - <i>ε</i> (<i>i</i>) (a.u.) | 0.81 | 0.75 | | 0.05 |
| <i>F</i> (<i>i</i> , <i>j</i>) (a.u.) | 0.133 | 0.140 | | 0.031 |
| | | <i>n_x → σ₁[*](Fe-Si)</i> | | |
| <i>E</i> (2) (kJ/mol) ^c | 120.88 | 21.51 | 25.94 | 2.26 |
| <i>ε</i> (<i>j</i>) - <i>ε</i> (<i>i</i>) (a.u.) | 0.80 | 0.56 | 0.24 | 0.36 |
| <i>F</i> (<i>i</i> , <i>j</i>) (a.u.) | 0.146 | 0.049 | 0.036 | 0.013 |
| | | <i>n_{Si} → σ₂[*](Fe-Si)</i> | | |
| <i>E</i> (2) (kJ/mol) | 929.27 | | | |
| <i>ε</i> (<i>j</i>) - <i>ε</i> (<i>i</i>) (a.u.) | 0.01 | | | |
| <i>F</i> (<i>i</i> , <i>j</i>) (a.u.) | 0.059 | | | |
| | | <i>n_{Si} → σ₁[*](Fe-Si)</i> | | |
| <i>E</i> (2) (kJ/mol) | 245.60 | 38.28 | | |
| <i>ε</i> (<i>j</i>) - <i>ε</i> (<i>i</i>) (a.u.) | 0.12 | 0.20 | | |
| <i>F</i> (<i>i</i> , <i>j</i>) (a.u.) | 0.101 | 0.054 | | |

^aCalculated using BPW91/6-31G(d); ^bCalculated using BPW91/3-21G(d) for the I atoms and BPW91/6-31G(d) for the other atoms. ^cFor each lone pair, only the donor-acceptor interactions with the highest *E*(2) values have been taken into consideration.

$E(2) = q_i \frac{F(i, j)^2}{\varepsilon_j - \varepsilon_i}$, where *E*(2) is the second-order perturbational energy stabilization. *F*(*i*, *j*)

is the Fock matrix element between an occupied orbital *i* and an unoccupied orbital *j*. *F*(*i*, *j*) is proportional to the overlap between orbitals *i* and *j*. $\varepsilon_j - \varepsilon_i$ is the energy difference between orbitals *i* and *j*, and *q_i* is the occupancy of donor orbital *i*. Thus, NBO analysis can be used to examine conjugation effects in π-conjugated systems quantitatively.^{145, 146, 154, 166}

The introduction of halogen atoms at the Si site can be monitored in a straightforward manner by the disappearance of the SiH stretching modes of **6** at 2074 and 2043 cm⁻¹ and the simultaneous formation of new bands in the IR and Raman spectra of **7-10**, which is characteristic to the symmetric and asymmetric SiX₂ stretching vibrations (Table 5.2, Figures

5.5 and 5.8). One can notice that, upon substitution of H with either a F, Br, or Cl atom on the Si atom, the $\nu(\text{SiX}_2)$ modes are shifted significantly to lower wavenumbers, because of mass effects. Moreover, they strongly mix with other vibrations. Consequently, the wavenumber shift cannot give us any further information.

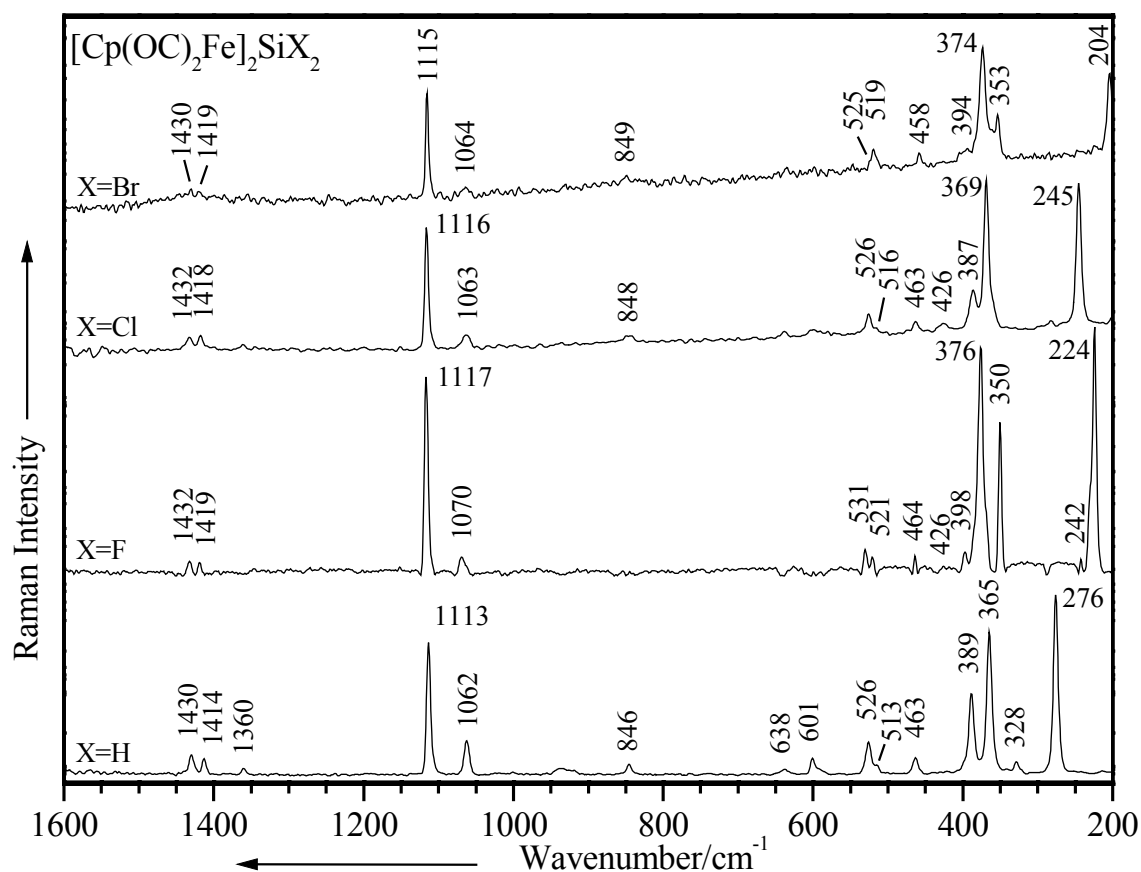


Figure 5.8. The FT-Raman spectra of **6-9** between 1600 and 200 cm^{-1} .

Excitation line: $\lambda_0 = 1064 \text{ nm}$.

Unfortunately, the very interesting symmetric and asymmetric Fe-Si stretching modes can be observed only in the Raman spectrum of **6**, as a medium signal at 390 cm^{-1} (symmetric $\nu(\text{Fe-Si})$), and in that of **7**, as a medium-strong peak at 350 cm^{-1} (asymmetric $\nu(\text{Fe-Si})$) (Table 5.2, Figure 5.8). The visualization of these vibrations shows a strong coupling with the symmetric and asymmetric Fe-Cp stretching mode, respectively. Hence, these motions should be better ascribed to a symmetric and asymmetric $\nu(\text{SiFeCp})$ mode (Table 5.2). Nevertheless, the calculated values are consistent with the assumed weakening of the Fe-Si bond, because of the π -type bonding of the nonbonding halogen valence electrons with the unoccupied d(Si) or

σ^* (Fe-Si) orbitals. More exactly, the asymmetric ν (SiFeCp) modes of **7-10** were found to decrease in the order F, Cl, Br, and I (385, 379, 376, and 370 cm^{-1}). A similar tendency is present for the symmetric ν (SiFeCp) modes, which were theoretically determined at 361, 350, 344, and 342 cm^{-1} in **7-10**.

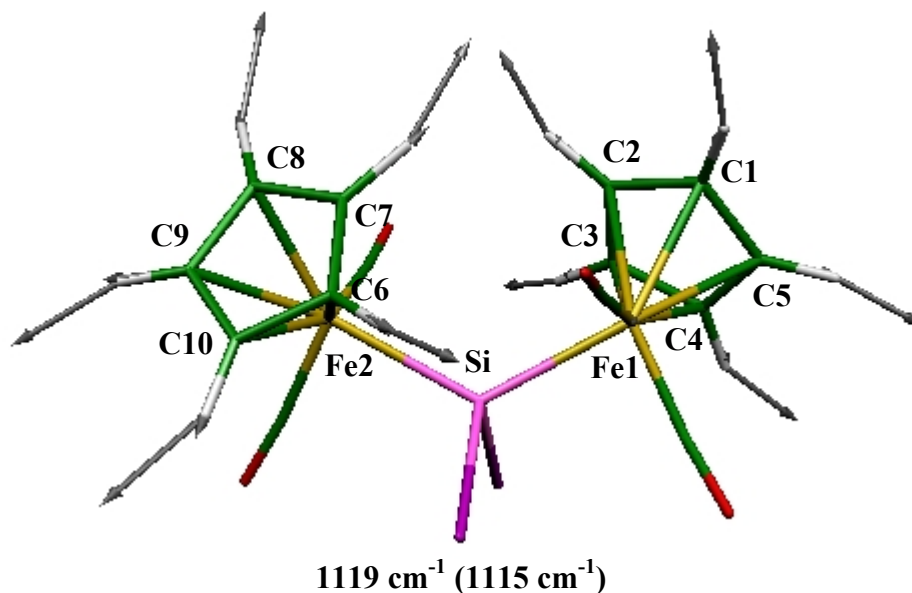


Figure 5.9. The fundamental calculated (BPW91/6-311G(d)) ring breathing mode of the cyclopentadienyl ring of $[\text{Cp}(\text{OC})_2\text{Fe}]_2\text{SiBr}_2$ (**9**). The experimental Raman value is given in parentheses.

Because of its relative intensity and characteristic wavenumber ($1110 \pm 10 \text{ cm}^{-1}$), the ring breathing mode of the cyclopentadienyl ring (Figure 5.9) can be considered to be the most evident vibration of the group (Figure 5.8). As also indicated by the calculated harmonic vibrational wavenumbers, the cyclopentadienyl ring breathing mode of **6-10** does not change substantially upon the substitution of X (Table 5.2, Figure 5.8). A similar behaviour is present in the CC stretching vibrations of the cyclopentadienyl ring, which strongly couple with the CH in-plane deformations and give rise to the peaks at 1435-1360 cm^{-1} in the Raman spectra of **6-10** (Figure 5.8, Table 5.2). So, we can conclude that the changes in the electronic density on the metal have no influence on these bonds.

5.1.3 Conclusions

The availability of a full series of homologous compounds, $[\text{Cp}(\text{OC})_2\text{Fe}]_2\text{SiX}_2$ (X = F, Cl, Br, I), gave us the opportunity to perform a systematic study of the bonding situation in these complexes using X-ray crystallography, vibrational spectroscopy, and DFT calculations.

In this context, the nature of the Fe-Si bond and the influence of the various substituents H, F, Cl, Br, and I on the silylene bridge seemed to be of particular interest.

The Fe-Si distance can be taken as a measure of the bond strength in these complexes. The experimental and calculated Fe-Si bond distances in **6-10** are generally larger than those in other mono(ferrio)silanes $\text{Cp}(\text{OC})_2\text{Fe-SiR}_3$. However, significant variation of the bond length, relative to the type of halogen substituent, could not be observed. The calculated Fe-Si stretching vibrations predict an increase in wavenumbers and, hence, bond strength, in the following order: $\text{I} < \text{Br} < \text{Cl} < \text{F}$. This is a typical consequence of the ionic bonding contribution between the iron fragment and the silylene unit SiX_2 , with increasing electronegativity of X.

A remarkable result was found for the wavenumbers of the CO stretching modes, which are increasing in the following order: $\text{F} < \text{Cl} < \text{Br} \leq \text{I}$. It must be assumed that the π -type back-bonding of the nonbonding orbitals of the halogen substituents X into unoccupied $\sigma^*(\text{Fe-Si})$ orbitals is responsible for this effect. All observed structural and vibrational properties are clearly indicating a strong electron-donating influence of the iron fragments on the silylene unit. This transition-metal effect has previously been invoked to rationalize some unusual characteristics and reactivities of mono- and bis(ferrio)silanes, e. g., the stabilization of Si(OH) units toward condensation or the activation of SiH moieties for halogenation and oxygenation reactions.

Further studies concerning the reactivity of this interesting class of compounds are currently in progress.

5.2 *3-Silaoxetane and 3-silathietane*

This project is a collaboration with **Professor Dr. Carsten Strohmann**'s workgroup, within the **SFB 347** program.

5.2.1 *Molecules presentation*

In spite of their stability in air and humidity resistance, the 1-hetero-3-silacyclobutane compounds with oxygen or sulfur were not intensively studied,^{324, 325} due to the absence of appropriate methods of preparation for these ring-systems³²⁶⁻³³⁴. Additionally, the transannular electronic interaction between silicon and oxygen or silicon and sulfur, respectively, in such systems is still a very discussed problem in literature.^{325, 335} In this respect, the 3-silaoxetane 3,3-dimethyl-2,2,4,4-tetraphenyl-1-oxa-3-silacyclobutane (**11**) (Figure 5.10), and the 3-silathietane 3,3-dimethyl-2,2,4,4-tetraphenyl-1-sila-3-thiacyclobutane (**12**) (Figure 5.11), were

synthesized (in **Professor Dr. Carsten Strohmann's** workgroup) and their structure investigated by X-ray diffraction and solid-state NMR spectroscopy.¹⁶¹ The results obtained by X-ray diffraction were consistent with those obtained from solid state ¹³C-NMR spectroscopy, and suggested an unusual bonding situation around the silicon atom of compound **11** in the solid state. Also, in spite of the ring strain in compound **11**, an unusual low reactivity was noticed (the synthesis was performed in water).

Vibrational spectroscopy has proved to be an important tool in the determination of structural parameters of new compounds. Also, Raman spectroscopy has widely and frequently been used to investigate structural changes in different types of materials,³³⁶ taking into account that variation of certain physical quantities (temperature, pressure) affects the polarizability tensor and results in changes of the measurable parameters of certain vibrational modes of the system. The measurement and analysis of linewidths, peak positions and integrated intensity yield information about the structure and dynamics of the system undergoing structural changes. That is, the micro-Raman spectra of **11** and **12** were recorded for the first time at different temperatures, and discussed with the help of our DFT results, hoping to bring new information about the title compounds, their reactivity and this unusual bonding situation.

5.2.2 Results and discussion

5.2.2.1 Geometry optimization

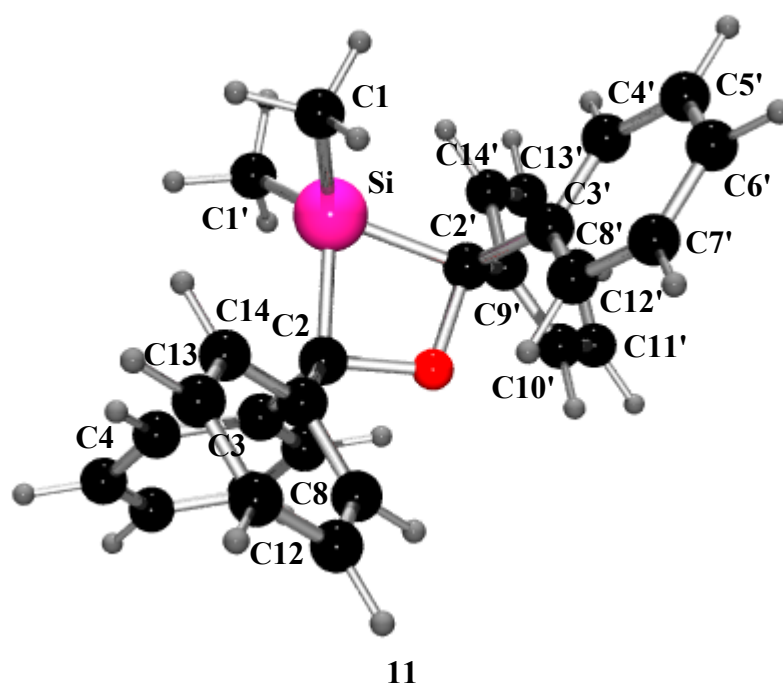


Figure 5.10. The BPW91/6-31+G(d) optimized geometry of **11**.

The structural parameters of **11** and **12**, which were calculated using the BPW91/6-31+G(d) and B3LYP/6-31+G(d) methods, are presented in Table 5.6 and compared with the experimental values of the related crystal structures obtained by our coworkers. For further details regarding the X-Ray measurements, please consult the reference 161.

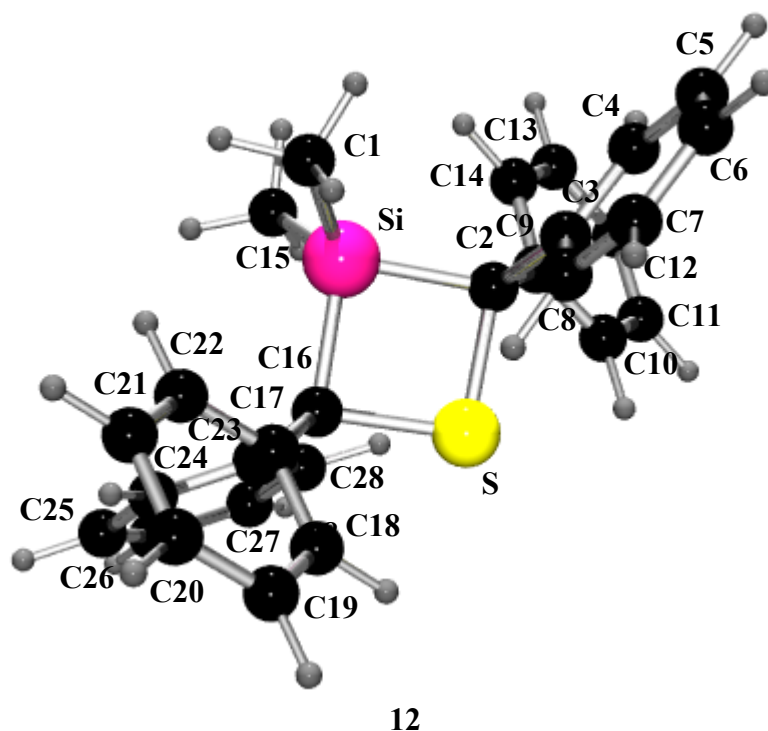


Figure 5.11. The BPW91/6-31+G(d) optimized geometry of **12**.

The two theoretical methods yielded similar results, but the bond lengths and angles of the two compounds were better reproduced by the B3LYP/6-31+G(d) method in almost all cases. Using the well-known B3LYP functional, the maximum discrepancies with respect to the experimental data were approximately 5 pm and 2°, respectively, for both compounds. Taking into account these small discrepancies and the methods implied in calculations, we can state that DFT works well even for large molecules at low costs (CPU time, disk space, and memory).

In both cases (**11** and **12**), the calculations were performed for a molecular geometry without symmetry restrictions and for a geometry that was restricted to C_2 symmetry. The calculated geometry with C_1 symmetry was very close to that with C_2 symmetry. The absolute energy difference, which contains the ZPE correction, between these imposed structures of compounds **11** and **12** has been determined to be small (e.g., 0.37 kJ/mol for **11**, using the

Table 5.6. Experimental and calculated bond lengths and bond angles for compounds **11** and **12**.

| | 11 | | | | 12 | | |
|---------|-------------------|-------------------|-------------------|----------|------------------|-------------------|-------------------|
| | Exp ^a | Calc ^b | Calc ^c | | Exp ^a | Calc ^b | Calc ^c |
| | Bond lengths (pm) | | | | | | |
| Si–C(1) | 183.6(3) | 188.5 | 189.6 | S–C(16) | 185.4(2) | 189.6 | 189.8 |
| Si–C(2) | 192.0(2) | 194.7 | 195.6 | S–C(2) | 185.5(3) | 189.6 | 189.9 |
| O–C(2) | 147.2(2) | 147.2 | 148.2 | Si–C(15) | 185.1(3) | 188.4 | 189.1 |
| Si⋯O | 241.5(3) | 242.8 | 244.7 | Si–C(1) | 185.1(3) | 188.5 | 189.3 |
| | | | | Si–C(16) | 192.1(3) | 195.3 | 196.4 |
| | | | | Si–C(2) | 192.5(2) | 195.4 | 196.4 |
| | | | | Si⋯S | 263.9(3) | 269.3 | 269.4 |

| | 11 | | | 12 | | |
|----------------|------------------|-------------------|-------------------|-------------------|-------------------|-------------------|
| | Exp ^a | Calc ^b | Calc ^c | Exp ^a | Calc ^b | Calc ^c |
| | Bond angles (°) | | | | | |
| C(1)–Si–C(1)' | 111.3(2) | 110.0 | 109.9 | C(16)–S–C(2) | 93.25(11) | 93.0 94.5 |
| C(1)–Si–C(2) | 118.73(12) | 119.6 | 120.1 | C(15)–Si–C(1) | 109.5(2) | 107.8 108.0 |
| C(1)–Si–C(2)' | 114.43(10) | 114.7 | 114.4 | C(15)–Si–C(16) | 112.92(12) | 112.3 112.1 |
| C(2)–Si–C(2)' | 75.07(9) | 74.7 | 74.6 | C(1)–Si–C(16) | 115.79(12) | 117.6 117.6 |
| C(1)–Si–O | 124.32(11) | 125.0 | 125.1 | C(15)–Si–C(2) | 117.63(13) | 116.4 115.9 |
| C(2)–O–C(2) | 105.3(2) | 105.3 | 106.5 | C(1)–Si–C(2) | 111.00(10) | 112.8 113.1 |
| O–C(2)–C(9) | 110.24(12) | 110.3 | 110.4 | C(16)–Si–C(2) | 89.00(11) | 89.5 89.5 |
| O–C(2)–C(3) | 110.07(13) | 109.6 | 109.7 | C(9)–C2–C(3) | 112.21(14) | 112.7 113.2 |
| C(9)–C(2)–C(3) | 111.3(2) | 111.0 | 111.2 | C(9)–C(2)–S | 111.71(12) | 111.4 111.2 |
| O–C(2)–Si | 89.80(9) | 89.4 | 89.6 | C(3)–C(2)–S | 113.42(12) | 112.3 112.6 |
| C(9)–C(2)–Si | 118.47(11) | 120.2 | 120.0 | C(9)–C(2)–Si | 116.33(12) | 114.9 115.2 |
| C(3)–C(2)–Si | 114.73(11) | 114.1 | 113.7 | C(3)–C(2)–Si | 112.60(11) | 114.6 113.6 |
| | | | | S–C(2)–Si | 88.60(11) | 88.8 88.5 |
| | | | | C(17)–C(16)–C(23) | 112.4(2) | 112.4 112.7 |
| | | | | C(17)–C(16)–S | 112.93(12) | 111.9 112.1 |
| | | | | C(23)–C(16)–S | 111.48(12) | 111.7 111.7 |
| | | | | C(17)–C(16)–Si | 113.88(11) | 114.4 114.6 |
| | | | | C(23)–C(16)–Si | 115.32(12) | 115.5 115.1 |
| | | | | S–C(16)–Si | 88.73(11) | 88.8 88.4 |

^aReference 161; ^bCalculated using B3LYP/6-31+G(d); ^cCalculated using BPW91/6-31+G(d).

B3LYP/6-31+G(d) method). This seems to indicate that the structure of C_2 symmetry is also possible for both compounds.

Examining the Table 5.6 one can note that the X-Ray analysis showed C_2 symmetry for compound **11** and C_1 symmetry for compound **12**.

The cyclobutane ring of **11** is planar with a C-Si-C angle of $75.07(9)^\circ$ and a C-O-C angle of $105.3(2)^\circ$. The B3LYP/6-31+G(d) calculated values are 74.7° and 105.3° , respectively. The C-O-C angle is only a little bit smaller than the angle one can find in the crystal structures of ethers (112°).³³⁷ The C-Si-C angle is much smaller, which demonstrates the high flexibility of silicon-carbon-bonds. The Si...O distance ($241.5(3)$ pm) is larger than the sum of the covalent radii of silicon and oxygen atoms (191 pm),³³⁸ that is, there is no interaction between the two atoms. The usual values given in literature for the Si-O bonds are about 164 pm.³³⁹

The highest ESD values (electron density synthesis with coefficients F_0-F_c) are outside the Si-C2 bond direction, meaning that they are experimental hints of bent bond (Figure 5.12). Therefore, small bent angles are not indicative for high reactivity.

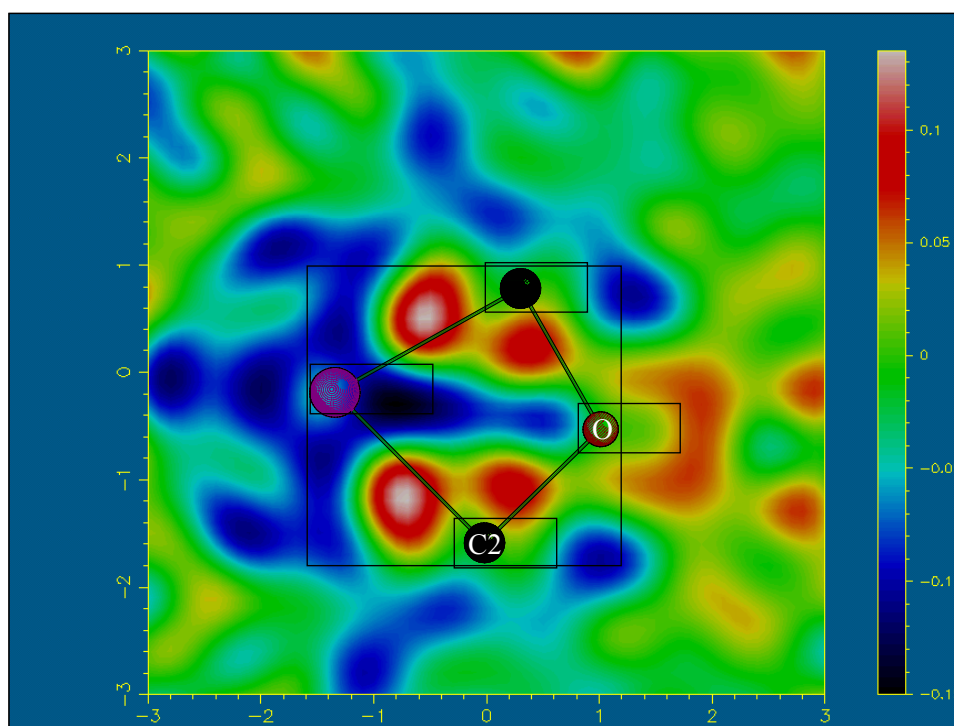


Figure 5.12. EDS of the crystal structure of **11**, determined in **Professor Dr. Carsten Strohmann's** workgroup.

The representative plot of the total electron density of **11** (calculated using the DFT-based method B3LYP/6-31+G(d)) indicates a build-up of charge density on the phenyl rings and oxygen atoms, and a node at the silicon atom (Figure 5.13).

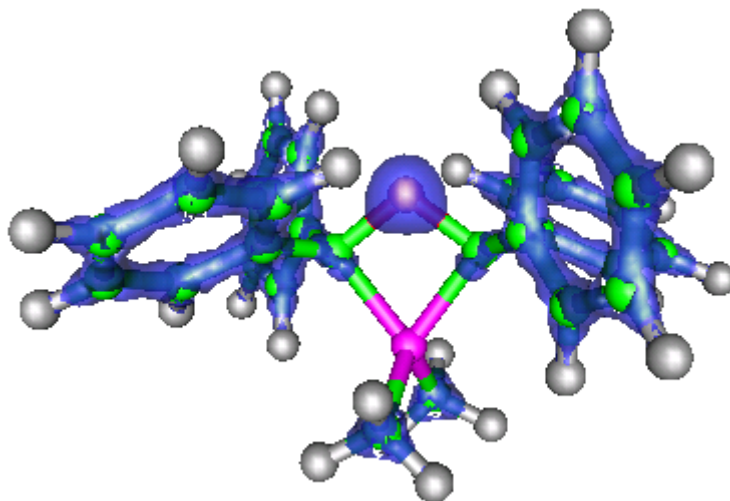


Figure 5.13. The total electron density of **11**. The isosurface value is 0.23.

Compound **12** crystallizes in a non-planar cyclobutane ring with a C-Si-C angle of $89.00(11)^\circ$ and a C-S-C angle of $93.25(11)^\circ$. The B3LYP/6-31+G(d) calculated values are in this case 89.5° and 93.0° , respectively. The C-S-C angle is similar to the angle found in sulfides (99°).³³⁷ The Si \cdots S distance of 263.9(3) pm is also larger than the sum of the covalent radii of silicon and oxygen atoms (220 pm).³³⁸ The average values given in literature for the Si-S bonds are about 214 pm.³³⁹

The Si \cdots O distance of 241.5(3) pm for **11** and the Si \cdots S distance of 263.9(3) pm for **12** are shorter than the sum of the van-der-Waals radii of these atoms (360 and 390 pm, respectively)³³⁸. At the first glance, it may seem that there is an interaction between these atoms. Swisher and coworkers tried to prove it by performing fluorescence measurements for compound **11** in solution.³²⁵ Strohmman and coworkers showed that they were actually due to the presence of some impurities in the sample, because **11** and **12** do not present fluorescence.¹⁶¹ Therefore, smaller Si \cdots O and Si \cdots S distances do not necessarily mean bonding interactions.

The loss of symmetry in compound **12** may be due to the unusual electronic or steric effects around the silicon atom, which were observed in the solid state.¹⁶¹ Also, one should not forget that the calculations refer to the gas phase of **12**, which probably does not describe

the real situation the best. In good agreement with our DFT results, *ab initio* calculations on the four-membered cyclic molecule of 3-silathietane indicate the title molecule as being nearly planar. However, electron diffraction results obtained for a similar compound, in which the H atoms are replaced by methyl, showed a fold angle of $20 \pm 2^\circ$.³⁴⁰

5.2.2.2 Vibrational spectroscopy

The micro-Raman spectra of 3-silaoxetane 3,3-dimethyl-2,2,4,4-tetraphenyl-1-oxa-3-silacyclobutane (**11**) (Figure 5.14) and 3-silathietane 3,3-dimethyl-2,2,4,4-tetraphenyl-1-sila-3-thiacyclobutane (**12**) (Figure 5.15) were recorded in the 1800-200 cm^{-1} at different temperatures (for both cooling and heating cycles).

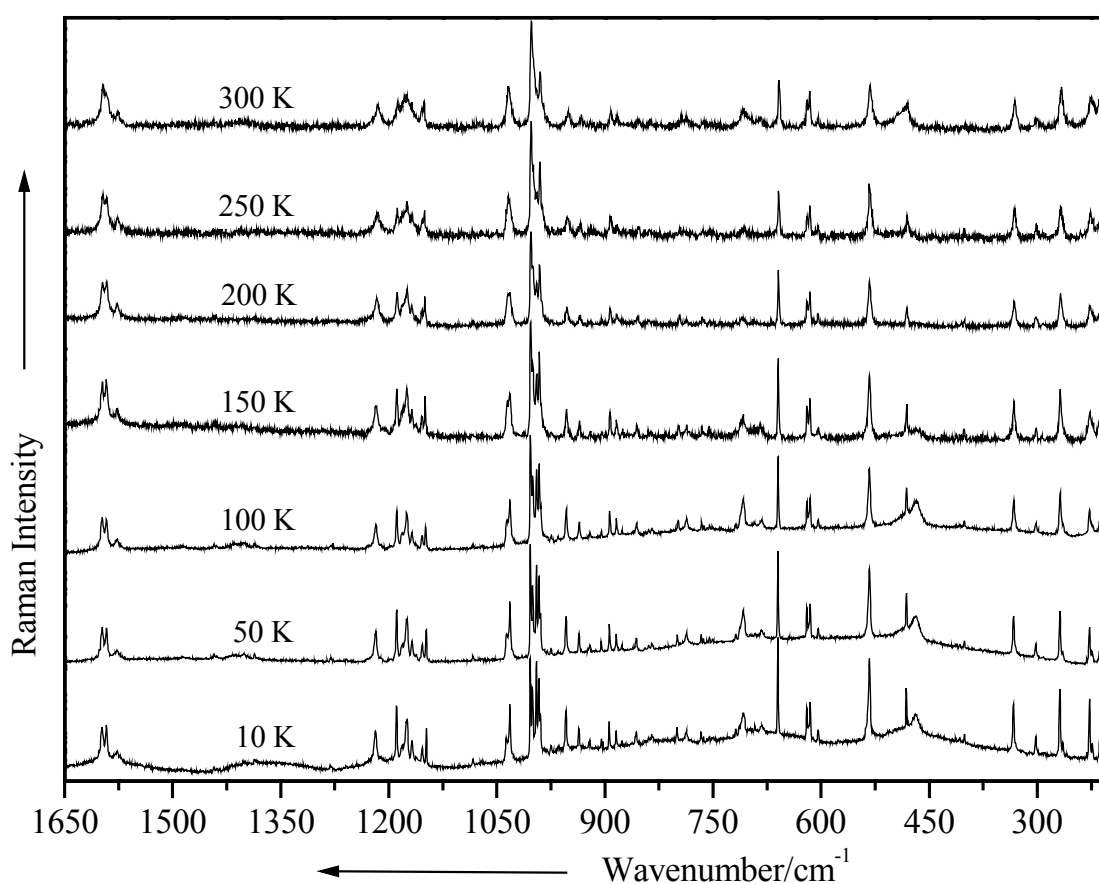


Figure 5.14. Micro-Raman spectra of compound **11** at different temperatures.

Excitation line: $\lambda_0 = 647.088 \text{ nm}$.

The spectral resolution was 1 cm^{-1} and all measurements were performed with a slit opening of $180 \mu\text{m}$. It is well known that the slit distortion may become a serious problem for

the bands having linewidths nearly of the same order as the slit width. Therefore, for a precise analysis of linewidths and to get an idea of the content of slit distortion, the fractional Lorentzian (L) character of some Raman bands have been calculated.³⁴¹⁻³⁴³ The calculation revealed that L is less than 0.90 for the bands under study, which suggests that the slit distortion is appreciable in every case and hence, deconvolution techniques^{342, 343} were applied to get the intrinsic Raman linewidth. For a detailed description of the deconvolution methods please consult the mentioned references.

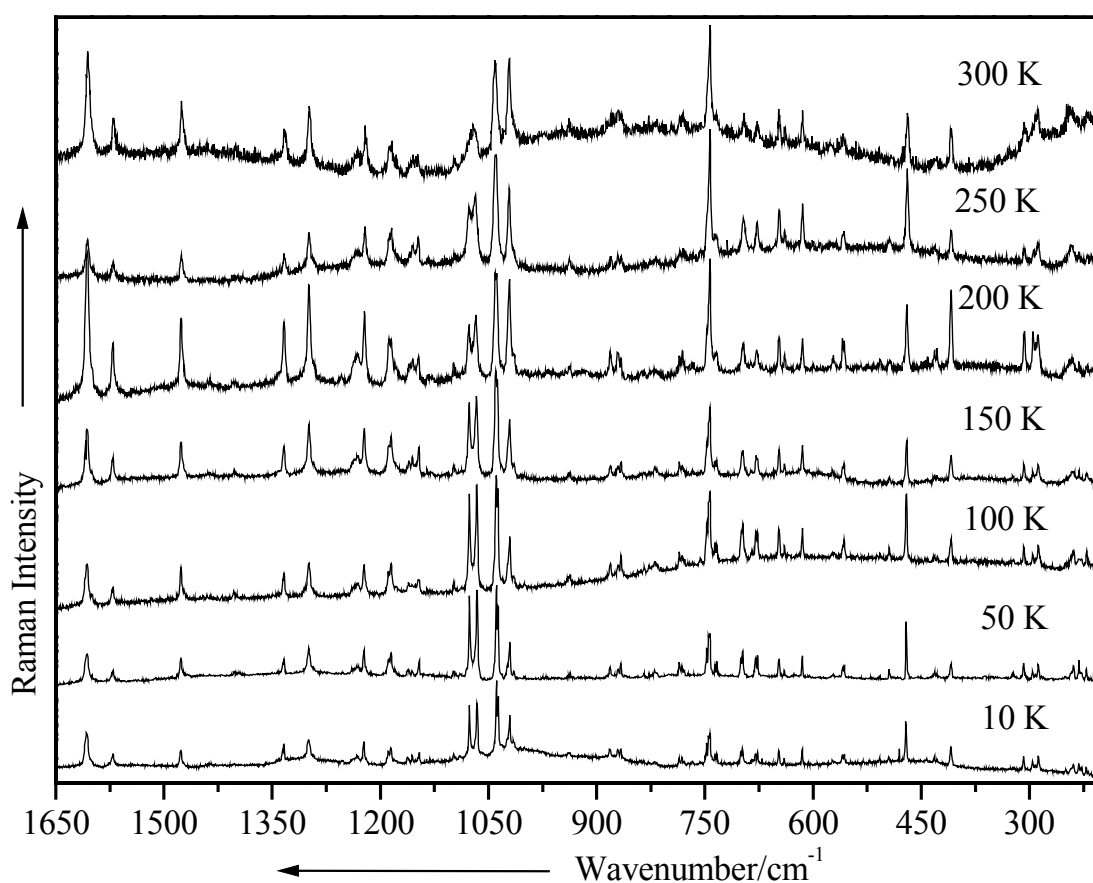


Figure 5.15. Micro-Raman spectra of compound **12** at different temperatures.

Excitation line: $\lambda_0 = 647.088$ nm.

As expected, the interpretation of the Raman spectra was feasible with the assistance of DFT calculations at the BPW91/6-31+G(d) and B3LYP/6-31+G(d) levels of theory. Taking into account the size of the calculated systems, we dare to say that both methods approached pretty well the measured spectra.

Table 5.7. Selected calculated and experimental fundamental vibrational wavenumbers (cm⁻¹) for compounds **11** and **12**, together with their tentative assignments.

| 11 | | | | 12 | | | | Vibrational assignment |
|-----------|--------|-------------------|-------------------|-----------|-------|-------------------|-------------------|--|
| Raman | | Calc ^b | Calc ^c | Raman | | Calc ^b | Calc ^c | |
| 10K | 300K | | | 10K | 300K | | | |
| 1037w | 1035m | 1040 | 1043 | 1077s | 1074m | 1072 | 1098 | i.p. ph CH deformation (18b) + sym Si-C-O stretching |
| 1032ms | broad | 1037 | 1039 | 1066s | 1072m | 1070 | 1098 | i.p. ph CH deformation (18a) |
| 1004vs | 1003vs | 1036 | 1009 | 1039vs | 1041s | 1037 | 1045 | ph trigonal ring breathing |
| 1001s | 999sh | 1035 | 1008 | 1037vs | 1040s | 1037 | 1042 | ph trigonal ring breathing |
| 995vs | 996m | 1032 | 1006 | 1024vw | 1021s | 1035 | 1008 | ph trigonal ring breathing |
| 992s | 990ms | 1002 | 1006 | 1021ms | broad | 1034 | 1007 | ph trigonal ring breathing |
| 990m | sh | 1001 | 991 | 1016vw | | 1028 | 988 | o.p. ph CH deformation (5) |
| 951m | 951w | 976 | 962 | 940vw | 938vw | 958 | 960 | o.p. ph CH deformation (17a) |
| 936w | 933vw | 945 | 938 | 937vw | broad | 923 | 934 | o.p. ph CH deformation (17b) |
| 470m | | 488 | 470 | 472ms | 469m | 515 | 497 | o.p. ph CH deformation (16b) + C-O-C bending |
| 401vw | 402vw | 426 | 410 | 409w | 408w | 431 | 415 | o.p. ph CH deformation (16a) |

^aAbbreviations: vw - very weak, w - weak, m - medium, ms - medium strong, s - strong, vs - very strong, sh - shoulder, i.p. - in-plane, o.p. - out-of-plane; sym - symmetric, asym - asymmetric; ph - phenyl.

^bCalculated using B3LYP/6-31+G(d). ^cCalculated using BPW91/6-31+G(d). The DFT calculations were performed for the room temperature. 18a, 5, 17a, 17b, 16a, 16b represent the Wilson's notation.²⁷⁷

The most significant calculated and experimental fundamental vibrational modes are summarized in Table 5.7.

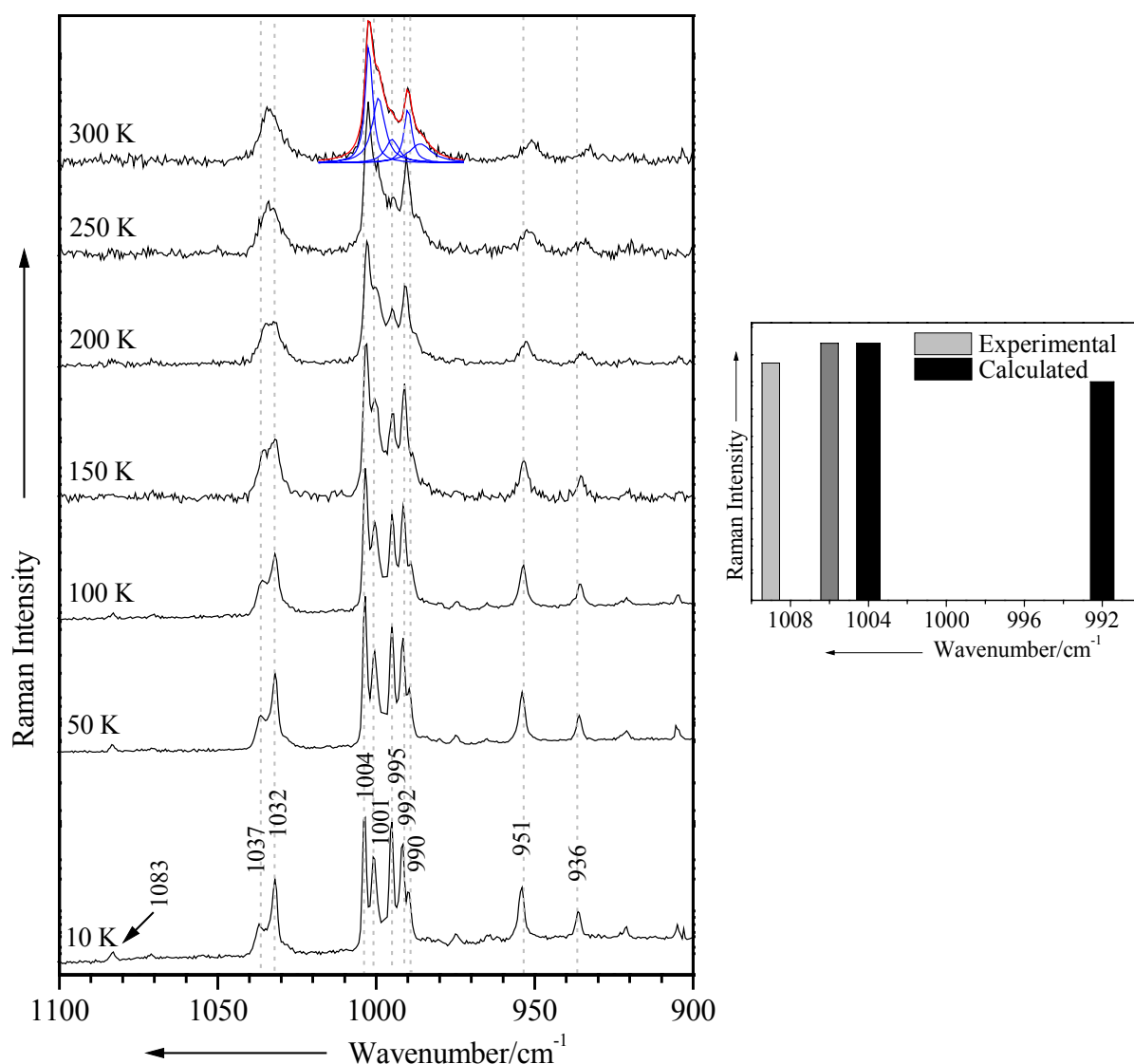


Figure 5.16. Micro-Raman spectra of compound **11** in the 1100-900 cm^{-1} spectral region at different temperatures. Excitation line: $\lambda_0 = 647.088$ nm.

At the right side, the Raman scattering activity of two of the BPW91/6-31+G(d) calculated vibrational modes (at room temperature) and the corresponding experimental values.

The characteristic vibrational modes of aromatic groups were detected in the expected spectral region for both compounds.²⁷⁷ However, the substitution of the oxygen atom in the 3-silaoxetane ring (**11**) with a sulfur atom (**12**) is reflected by some specific shifts. But our intention is to analyze the possible structural changes with the variation of temperature, and

not to make a detailed analysis of the well-known phenyl groups. Their IR and Raman spectra have been thoroughly discussed in literature.^{277, 344-346} Accordingly, out of the many various characteristic vibrations of these groups we will consider only some of the most representative ones, which show interesting changes.

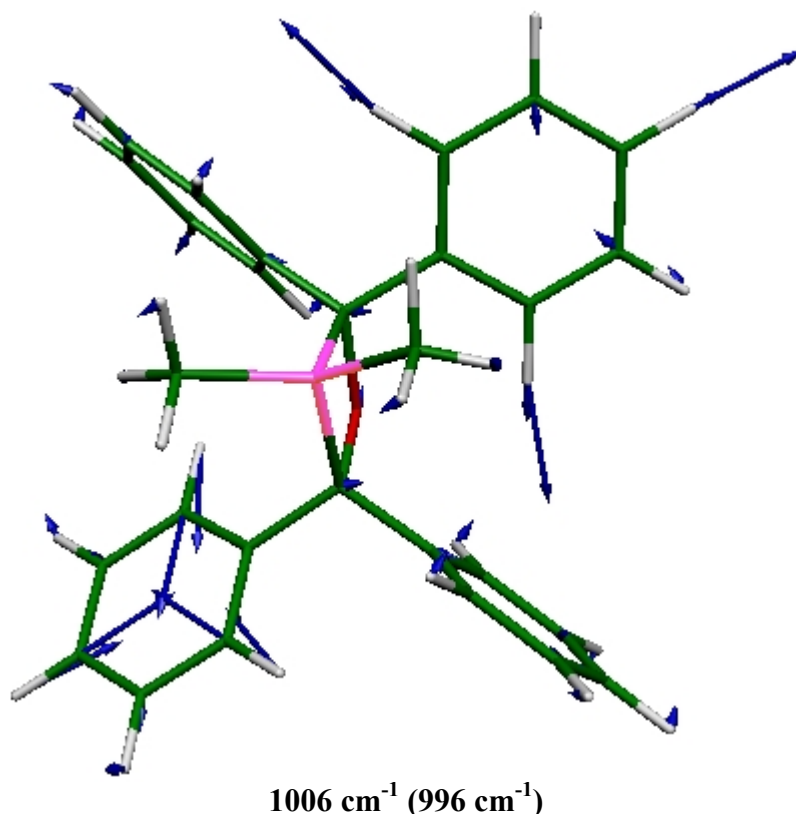


Figure 5.17. The fundamental calculated (BPW91/6-31+G(d)) trigonal ring breathing mode of phenyl in compound **11**. The experimental Raman value is given in parentheses.

Because of its relative intensity and characteristic wavenumber, the phenyl ring breathing mode can be considered to be the most evident vibration of the group (Figure 5.16). Although the wavenumber shifts observed with decreasing temperature are quite small, there are some subtle changes in the relative intensity of these bands, especially for compound **11** (Figure 5.17). More exactly, the peaks at 995 and 992 cm⁻¹, respectively, present a reverse in their relative intensity with the decrease in temperature from 300 to 10 K. This change becomes clearly in the 200-150 K range and is not reversible. A visualization of these vibrations shows that each of the trigonal ring breathing modes (observed at 995 and 992 cm⁻¹) involves only two of the four phenyl rings, namely the *trans* rings. This may be due to an electron delocalization of the system from one of the *trans* phenyls toward the 3-silaoxetane ring (Figure 5.13). Moreover, the band at 470 cm⁻¹ attributed to the C-O-C bending mode

disappears at higher temperatures (at about 200 K). The very strong 3-silaoxetane ring (660 cm^{-1}) and C-O-C (533 cm^{-1}) bending modes decrease significantly in intensity at higher temperatures. All these seem to indicate an unexpected restriction of the oxygen atom motion at higher temperatures, probably due to steric effects.

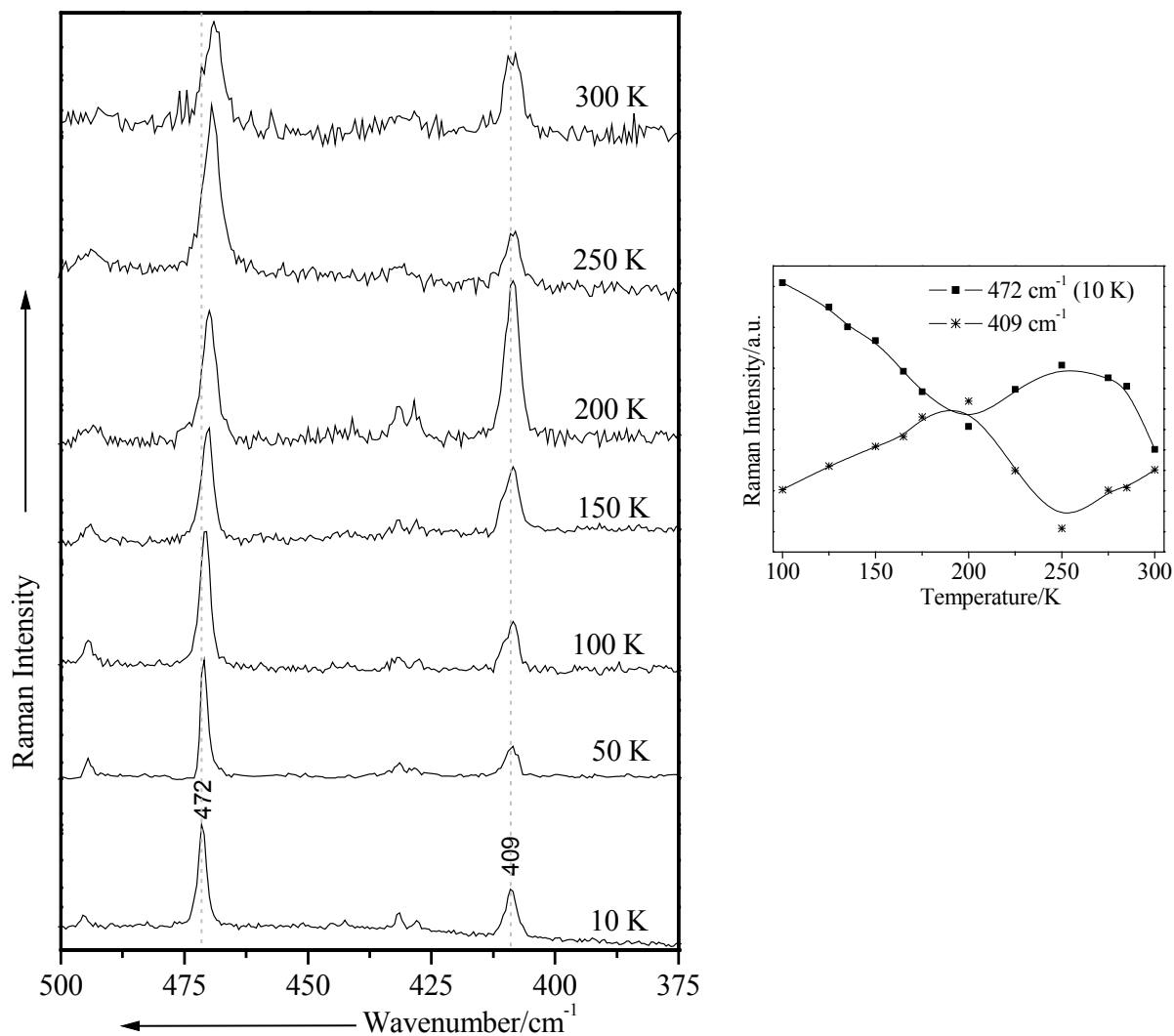


Figure 5.18. Micro-Raman spectra of compound **12** in the $500\text{-}375\text{ cm}^{-1}$ spectral region at different temperatures. Excitation line: $\lambda_0 = 647.088\text{ nm}$.

A reverse in relative intensity was also observed in compound **12** for the peaks at 472 and 409 cm^{-1} (Figure 5.18). They have been assigned to the out-of-plane phenyl CH deformations 16b and 16a. But in this case the transformation is reversible. Under 200 K the peaks recover the profile observed up to 250 K (Figure 5.18). Some unexpected changes were also observed for the well-known 8a (quadrant stretching – 1606 cm^{-1}) and 11 (out-of-plane

CH deformation – 743 cm^{-1}) modes of the phenyl rings at this temperature (200 K). Such observations might be correlated with a change in symmetry, taking into account that the two calculated structures (C_1 and C_2) are energetically comparable.

5.2.3 *Conclusions*

The DFT calculations carried out on the 3-silaoxetane and 3-silathietane compounds (**11** and **12**) analyzed in these studies supplied molecular geometries, which are in very good agreement with the experimental results obtained by X-Ray diffraction studies. The compound **11** was found to feature a planar cyclobutane ring with an unusual small angle at the silicon atom (74.7°), which could be explained only by bent bonds. In spite of the large ring strain, this substance showed a low reactivity. That is, small bent angles are not indicative for high reactivity.

The DFT calculations helped us accurately assign the Raman spectra of the title compounds and monitor the structural changes observed with the change in temperature during the Raman experiments.

Chapter 6

Summary

In the current work, several well-known pharmaceuticals (1,4-dihydrazinophthalazine sulfate, caffeine, and papaverine hydrochloride) and new organometallic compounds (nickel(II) cupferronato complexes NiL_2A_n , $\text{L} = \text{PhN}_2\text{O}_2^-$, $n = 1$, $\text{A} = o$ -phenanthroline (**1**), o,o' -bipyridine (**2**) and $n = 2$, $\text{A} = \text{H}_2\text{O}$ (**3**), o - NH_2Py (**4**), o - $\text{C}_6\text{H}_4(\text{NH}_2)_2$ (**5**); silylene-bridged dinuclear iron complexes $[\text{Cp}(\text{OC})_2\text{Fe}]_2\text{SiX}_2$ ($\text{X} = \text{H}$ (**6**), F (**7**), Cl (**8**), Br (**9**), I (**10**)); 3-silaoxetane 3,3-dimethyl-2,2,4,4-tetraphenyl-1-oxa-3-silacyclobutane (**11**) and 3-silathietane 3,3-dimethyl-2,2,4,4-tetraphenyl-1-sila-3-thiacyclobutane (**12**) compounds), which have successfully been characterized by using vibrational spectroscopy in conjunction with accurate density functional theory (DFT) calculations, are presented.

The DFT computed molecular geometries of the species of interest reproduced the crystal structure data very well and in conjunction with IR and Raman measurements helped us to clarify the structures of the compounds, for which no experimental data were available; and this, especially for the new organometallic compounds, where the X-Ray analysis was limited by the non-availability of single crystals (**3**, **5**, **10**).

Furthermore, a natural population analysis (NPA) and natural bond orbital (NBO) calculations together with a detailed analysis of the IR and Raman experimental as well as calculated spectra of the new organometallic compounds, allowed us to study some special bonding situations (**1-12**) or to monitor the structural changes observed with the change in temperature during the Raman experiments (**11**, **12**) (Chapter 5).

More exactly, the nature of the Fe-Si bond and the influence of the H, F, Cl, Br, and I substituents on the silylene bridge in complexes **6-10** was investigated. It was found that the Fe-Si distance can be taken as a measure of the bond strength. The experimental and calculated Fe-Si bond distances in **6-10** were generally larger than those in other mono(ferrio)silanes $\text{Cp}(\text{OC})_2\text{Fe-SiR}_3$. However, significant variation of the bond length, relative to the type of halogen substituent, could not be observed. The calculated Fe-Si stretching vibrations predict an increase in wavenumbers and, hence, bond strength, in the following order: $\text{I} < \text{Br} < \text{Cl} < \text{F}$. This is a typical consequence of the ionic bonding

contribution between the iron fragment and the silylene unit SiX_2 , with increasing electronegativity of X. A remarkable result was found for the wavenumbers of the CO stretching modes, which are increasing in the following order: $\text{F} < \text{Cl} < \text{Br} \leq \text{I}$. The π -type back-bonding of the nonbonding orbitals of the halogen substituents X into unoccupied σ^* (Fe-Si) orbitals was assumed to be responsible for this effect. All observed structural and vibrational properties are clearly indicating a strong electron-donating influence of the iron fragments on the silylene unit.

The compound **11** was found to feature a planar cyclobutane ring with an unusual small angle at the silicon atom (74.7°), which could be explained only by bent bonds. In spite of the large ring strain, this substance showed a low reactivity. That is, small bent angles are not indicative for high reactivity. The subtle changes observed in the relative intensity of some of the most representative vibrational modes of **11** and **12** at different temperatures (for both cooling and heating cycles 10-300 K) suggest an unexpected restriction of the oxygen atom motion in **11** at higher temperatures (up to 150 K), probably due to steric effects, and a possible change in symmetry for **12** at about 200 K, taking into account that the two calculated structures for this compound (of C_1 and C_2 symmetry) are energetically comparable.

Once again, it has been shown why these two complementary methods became so popular among chemists, especially since major progresses in Raman excitation (lasers), detection techniques (CCD cameras, FT-techniques) and unambiguous signal assignment by DFT calculations have been achieved.

By combining these two methods, the auspicious results obtained on the organometallic compounds **6-12** and overall in literature, made us confident of the power of theoretical calculations in aiding the interpretation of rich SERS spectra by solving some interesting issues. Consequently, the Raman and SERS spectra of well-known pharmaceuticals (1,4-dihydrazinophthalazine sulfate, caffeine, and papaverine hydrochloride) or new potentially biological active organometallic complexes (**1-5**) (Chapter 4), that were synthesized by our coworkers, were discussed with the assistance of the accurate results obtained from DFT calculations (structural parameters, harmonic vibrational wavenumbers, Raman scattering activities), and many previous incomplete assignments have been analyzed and improved. This allowed us to establish the vibrational behavior of these biological compounds near a biological artificial model at different pH values or concentrations (Ag substrate), taking into account that information about the species present under particular conditions could be of great importance for the interpretation of biochemical processes. The

total electron density of molecules and the partial charges situated on selected atoms, which were determined theoretically by NPA, allowed us to establish the probability of different atoms acting as an adsorptive site for the metal surface. Moreover, a closer examination of the calculated orbitals of molecules brought further arguments on the presence or absence of the photoproducts at the Ag surface during the irradiation (1,4-dihydrazinophthalazine sulfate).

SERS spectra of 1,4-dihydrazinophthalazine sulfate could be recorded even at nanomolar concentration with a conventional SERS setup. At about 10^{-6} mol L⁻¹ the molecular skeletal plane is probably oriented perpendicular to, or at least significantly tilted with respect to, the Ag surface plane. As the concentration is decreased, the molecule tends to lie flat on the Ag surface. With the increase in solution concentration, a surface coverage with 1,4-dihydrazinophthalazine sulfate may occur.

The vibrational behavior of caffeine on an Ag surface at different pH values was also characterized. The flat orientation of mainly chemisorbed caffeine, which is attached through the π -electrons and the lone pair of the N9 atom, was supposed to occur for neutral and basic pH values. At acid pH values caffeine is probably adsorbed on the Ag surface through one or both oxygen atoms, more probably through the O11 atom, with an end-on orientation. Nonetheless, the changes in the overall SERS spectral pattern seem to indicate the electromagnetic mechanism as being the dominant one.

A pH dependent Raman study for papaverine hydrochloride was possible in the pH range under 6.5, for upper values the solubility being dramatically diminished. However, the vibrational analysis of the Raman spectra allowed to evidence the two species of papaverine, protonated and neutral, respectively. The pH dependent SERS spectra of papaverine revealed again two different chemisorbed species on the Ag colloidal surface: protonated and neutral, the protonated one being adsorbed with the phenyl closer to the surface and the neutral one through the isoquinoline part, more probably through the nitrogen atom. Either in acid nor in basic media, the oxygen adsorption of papaverine species was excluded. The SERS spectra could evidence the protonated or neutral species under micromole level.

The FT-Raman study and the DFT calculations results on cupferron and its new nickel(II) cupferronato complexes (**1-5**) suggests the electron delocalization through the coordinated ONNO unit and the bidentate coordination of the anionic ligand to the metal centers through the oxygen atoms. SERS spectra of the title complexes brought additional arguments for the assignment of the symmetric mode of the ONNO moiety in the Raman spectra. Additionally, the SERS spectra of the new compounds indicated a possible adsorption through the N atoms of the ONNO unit to the Ag surface.

Overall, the results provide a benchmark illustration of the virtues of DFT in aiding the interpretation of rich vibrational spectra attainable for larger polyatomic adsorbates by using SERS, as well as in furnishing detailed insight into the relation between the vibrational properties and the nature of the Ag substrate-adsorbate bonding. Therefore, we strongly believe that theoretical calculations will become a matter of rapidly growing scientific and practical interest in SERS. That is, we already try to model the adsorption of very simple molecules on an Ag substrate (electrode) by the construction of a proper cluster. Regarding this aspect very few results have been reported so far and almost all have involved only a single or two metal atoms, which is clearly not a quantitative model of the metal surface.^{25, 347, 348} We also try to find out the method, which could fit the experimental results the best. We used the Hartree-Fock, the Moller-Plesset (MP2), and DFT methods (SVWN, BLYP, B3LYP, BPW91, B3PW91), and the basis sets were LANL2DZ, 3-21G, 6-31G, and 6-311G (when available). The first calculations indicate the BPW91/LANL2DZ combination as the most reliable for the noble-metal systems and less expensive, due to its accuracy and computational efficiency. In fact, almost all the DFT-based methods, particularly when allied with the LANL2DZ basis set, yielded results, which were significantly closer to the experimental values than those of the traditional Hartree-Fock and the Moller-Plesset electron correlation method. Supplementing this basis set by the addition of diffuse and/or polarization functions revealed no benefit.

It is now clear that quantum mechanical DFT calculations represent an indispensable complement not only for the spectroscopical studies in chemistry, but they can also help for a better understanding and exploring of other young fields in physical chemistry, such as SERS.

Zusammenfassung

In der vorliegenden Arbeit werden allgemein bekannte Pharmazeutika (1,4-Dihydrazin-phtalazinsulfat, Koffein und Papaverinhydrochlorid) und mehrere neue metallorganische Verbindungen (Nickel(II)-Kupferron-Komplexe NiL_2A_n , $\text{L} = \text{PhN}_2\text{O}_2^-$, $n = 1$, $\text{A} = o$ -phenanthrolin (**1**), o,o' -bipyridine (**2**) and $n = 2$, $\text{A} = \text{H}_2\text{O}$ (**3**), o - NH_2Py (**4**), o - $\text{C}_6\text{H}_4(\text{NH}_2)_2$ (**5**); Silicium-verbrückte dinucleare Eisen-Komplexe $[\text{Cp}(\text{OC})_2\text{Fe}]_2\text{SiX}_2$ ($\text{X} = \text{H}$ (**6**), F (**7**), Cl (**8**), Br (**9**), I (**10**)); 3-Silaoxetan 3,3-Dimethyl-2,2,4,4-tetraphenyl-1-oxa-3-silacyclobutan (**11**) und 3-Silathietan 3,3-Dimethyl-2,2,4,4-tetraphenyl-1-sila-thiacyclobutan (**12**) Verbindungen) vorgestellt, die erfolgreich unter Verwendung schwingungsspektroskopischer Methoden in Verbindung mit genauen DFT Rechnungen charakterisiert worden sind.

Die mittels DFT berechneten Molekülgeometrien der uns interessierenden Substanzen gaben die Daten, die aus Kristallstrukturanalyse erhalten worden sind, sehr gut wieder und halfen uns zusammen mit IR- und Raman-Messungen die Strukturen der Verbindungen aufzuklären, für die bisher keine experimentellen Daten erhältlich waren. Besondere Aufmerksamkeit wurde denjenigen neuen Metallorganika geschenkt, deren Röntgenstrukturanalyse (**3**, **5**, **10**) auf Grund der Fehlens von Einkristallen eingeschränkt war.

Desweiteren erlaubten uns "natural population analysis" (NPA)- und "natural bond orbital" (NBO)-Analysen, ebenso wie detaillierte Auswertungen der experimentellen und berechneten Spektren (IR, Raman) der metallorganischen Verbindungen, die Untersuchung spezieller Bindungssituationen (**1-12**) und die strukturellen Änderungen (**11**, **12**) zu verfolgen, die mit der Variation der Temperatur während der Raman-Messungen einhergehen (Kapitel 5).

Insbesondere wurde die spezifische Natur der Fe-Si-Bindung und der Einfluss der H-, F-, Cl-, Br- und I-Substituenten an der Siliciumbrücke der Komplexe **6-10** untersucht. Es konnte festgestellt werden, dass die Fe-Si-Bindungslänge ein Maß für die Bindungsstärke ist. Die experimentell bestimmten und berechneten Fe-Si-Bindungslängen waren generell länger als diejenigen in den anderen Mono(ferrio)silanen $\text{Cp}(\text{OC})_2\text{Fe-SiR}_3$. Jedoch konnten signifikante Bindungslängenunterschiede abhängig von der Art des Halogensubstituenten nicht beobachtet werden. Die berechneten Fe-Si-Streckschwingungen sagen ein Anstieg der Wellenzahlen und damit der Bindungsstärke in der folgenden Reihenfolge vorher: $\text{I} < \text{Br} < \text{Cl} < \text{F}$. Dies ist die typische Konsequenz des ionischen Bindungsanteils zwischen dem Eisenfragment und der Silaneinheit SiX_2 mit ansteigender Elektronegativität von X. Ein

bemerkenswertes Ergebnis konnte für die Wellenzahlen der CO-Streckschwingung gefunden werden, die in nachfolgender Reihenfolge ansteigen: $F < Cl < Br \leq I$. Die π -Rückbindung der nichtbindenden Orbitale der Halogensubstituenten X in unbesetzten $\sigma^*(Fe-Si)$ -Orbitale wurde für diesen Effekt verantwortlich gemacht. Alle beobachteten strukturellen und Schwingungseigenschaften indizieren einen starken elektronenschiebenden Einfluss vom Eisenfragment zur Silaneinheit.

Für die Verbindung **11** wurde ein planarer Cyclobutanring mit einem ungewöhnlich kleinem Winkel am Siliciumatom ($74,7^\circ$) gefunden, der nur mit "bent bonds" erklärt werden konnte. Trotz der großen Ringspannung zeigt diese Verbindung eine schwache Reaktivität. Das bedeutet, dass kleine Winkel keine hohe Reaktivität bedingen. Diese kleinsten Änderungen in der relativen Intensität von einigen ausgewählten Schwingungsmoden von **11** und **12** bei verschiedenen Temperaturen (für beide Kühlungs- und Heizzyklen 10-300 K) lassen eine unerwartet starre Bewegung des Sauerstoffatoms in **11** bei höheren Temperaturen vermuten (bis zu 150 K). Dies ist wahrscheinlich auf sterische Effekten und eine mögliche Änderung der Symmetrie von **12** bei ca. 200 K unter Berücksichtigung der Tatsache, dass die zwei berechneten Strukturen für diese Verbindung (C_1 und C_2 Symmetrie) energetisch vergleichbar sind, zurückzuführen.

Auch konnte gezeigt werden, weshalb die beiden komplementären Methoden der Schwingungsspektroskopie so beliebt bei Chemikern geworden sind, vor allem seitdem größere Fortschritte bei der Raman-Anregung (Laser), den Detektionstechniken (CCD Kameras, FT-Techniken) und den eindeutigen Zuordnungen durch DFT-Berechnungen gemacht worden sind.

Die vielversprechenden Ergebnisse der Untersuchungen an metallorganischen Verbindungen **6-12** sowie entsprechende bisher publizierte Ergebnisse, die durch Kombination dieser zwei Methoden erhalten worden sind, machten uns zuversichtlich, dass theoretische Berechnungen bei der Auswertung auch komplexer SERS-Spektren durch Lösung einiger interessanter Probleme sehr behilflich sein könnten. Folglich konnten die Raman- und SERS-Spektren von bekannten Pharmazeutika (1,4-Dihydrazin-phthalazinsulfat, Koffein und Papaverinhydrochlorid) oder von neuen, potentiell biologisch aktiven Organometall-Komplexen (**1-5**) (Kapitel 4), die von Mitarbeitern anderer Institute synthetisiert worden sind, unter Zuhilfenahme genauer Ergebnisse aus DFT-Rechnungen (strukturelle Parameter, harmonische Schwingungswellenzahlen, Raman-Streuaktivitäten) interpretiert werden. So war es möglich, viele bisher unvollständig zugeordnete Schwingungen zuzuordnen und zu erklären. Dies erlaubte uns, das Schwingungsverhalten

dieser biologischen Substanzen innerhalb eines künstlichen biologischen Modells (Ag-Substrat) bei verschiedenen pH-Werten und Konzentrationen zu ermitteln. Informationen über das Verhalten solcher Verbindungen unter besonderen Bedingungen könnten bei der Interpretation biologischer Prozesse eine wichtige Rolle spielen. Die totale Elektronendichte dieser Moleküle und die Partialladung an unterschiedlichen Atomen, die durch NPA bestimmt wurden, ermöglichten uns, die Adsorptionswahrscheinlichkeit verschiedener Atome an bestimmten Stellen der Metalloberfläche zu ermitteln. Ferner lieferte eine genauere Betrachtung der berechneten Molekülorbitale weitere Hinweise auf das Auftreten oder Fehlen von Photoprodukten auf der Silberoberfläche während der Bestrahlung (1,4-Dihydrazin-phtalazinsulfat).

Die SERS-Spektren von 1,4-Dihydrazin-phtalazinsulfat konnten selbst bei einer nanomolekularen Konzentration mit einem konventionellen SERS-Setup aufgenommen werden. Bei ca. 10^{-6} mol L⁻¹ ist die molekulare Ebene des Gerüsts wahrscheinlich senkrecht, oder zumindest deutlich gewinkelt zur Silberoberfläche angeordnet. Mit abnehmender Konzentration neigt das Molekül dazu, sich eher flach auf der Oberfläche zu orientieren. Ein Ansteigen der Konzentration der Lösung kann zu einer Bedeckung der Oberfläche mit 1,4-Dihydrazin-phtalazinsulfat führen.

Das Schwingungsverhalten von Koffein an der Silberoberfläche bei verschiedenen pH-Werten wurde ebenfalls untersucht. Die flache Orientierung des überwiegend chemisorbierten Koffeins, welches durch die π -Elektronen und das freie Elektronenpaar am N9-Atom gebunden ist, wurde für neutrale und basische pH-Werte angenommen. Bei sauren pH-Werten ist das Koffein vermutlich über ein oder beide Sauerstoffatome an der Silberoberfläche adsorbiert, wahrscheinlich mit "end-on"-Orientierung über das O11-Atom. Gleichwohl scheinen die Änderungen in den auftretenden Profilen der SERS-Spektren den elektromagnetischen Mechanismus als den dominierenden anzuzeigen.

Eine pH-Wert-abhängige Untersuchung am Papaverinhydrochlorid war im Bereich kleiner als 6,5 möglich, bei größeren Werten war die Löslichkeit dramatisch abgesenkt. Jedoch erlaubte uns die Schwingungsanalyse der Ramanspektren die zwei Formen des Papaverins, die neutrale und die protonierte, zu beweisen. Die pH-Wert-abhängigen SERS-Spektren des Papaverins lassen wieder zwei unterschiedliche chemisorbierte Formen, eine protonierte und eine neutrale, an der kolloidalen Silberoberfläche erkennen. Für die protonierte Form liegt der Phenylring näher an der Oberfläche; die neutrale Spezies ist über den Isochinolinteil adsorbiert, wahrscheinlicher hingegen über das Stickstoffatom. Weder im sauren noch im basischen Medium war es möglich, die Adsorption über das Sauerstoffatom

auszuschließen. Die SERS-Spektren konnten die protonierte oder neutrale Form im mikromolaren Bereich nachweisen.

Die FT-Raman-Messungen und die Ergebnisse der DFT-Rechnungen am Kupferron und seinen neuen Nickel(II)-Kupferron-Komplexen (**1-5**) lassen auf eine Elektronendelokalisierung über die koordinierte ONNO-Einheit und eine zweizählige Koordination des anionischen Liganden an das Zentralmetall über die Sauerstoffatome schliessen. Die SERS-Spektren der genannten Komplexe brachten zusätzliche Argumente für die Zuordnung der symmetrischen Schwingungsmode des ONNO-Fragmentes in den Raman-Spektren. Überdies deuten die SERS-Spektren der neuen Verbindungen eine mögliche Adsorption über die Stickstoffatome der ONNO-Einheit an der Silberoberfläche an.

Zusammenfassend zeigen die Ergebnisse die Vorteile von DFT-Rechnungen bei der Interpretation komplexer Schwingungsspektren größerer polyatomarer Adsorbate auf, die nur unter Ausnutzung des SERS-Effekts aufgenommen werden können. Auch tragen sie dazu bei, einen detaillierten Einblick in den Zusammenhang zwischen den Schwingungseigenschaften und der Natur der Silbersubstratadsorbat-Bindung zu liefern. Demzufolge sind wir davon überzeugt, dass theoretische Methoden einen größeren Stellenwert bei einem schnell wachsenden wissenschaftlichen und praktischen Interesse an SERS gewinnen werden. Diesbezüglich wurde ein Modellsystem erprobt, welches die Adsorption sehr einfacher Moleküle auf einer Silberoberfläche (Elektrode) durch den Aufbau eines geeigneten Clusters beschreibt. Diesbezüglich sind bislang nur wenige Ergebnisse publiziert worden, die allerdings größtenteils nur ein oder zwei Metallatome berücksichtigen, was offensichtlich keine quantitative Beschreibung der Metalloberfläche darstellt.^{25, 347, 348} Desweiteren haben wir untersucht, welche Methode die experimentellen Daten am besten wiedergibt. Es wurden Hartree-Fock-, Moller-Plesset- (MP2) und DFT-Methoden (SVWN, BLYP, B3LYP, BPW91, B3PW91) unter Verwendung der Basissätze LANL2DZ, 3-21G, 6-31G und 6-311G (wenn möglich) angewandt. Erste Rechnungen zeigen auf, dass die Kombination BPW91/LANL2DZ die verlässlichsten und kostengünstigsten Resultate für die Edelmetallsysteme im Rahmen der gewünschten Genauigkeit und des Rechenaufwandes liefert. Vielmehr wiesen fast alle DFT-basierenden Methoden insbesondere in Kombination mit dem LANL2DZ-Basissatz Ergebnisse auf, die deutlich näher an den experimentellen Werten lagen als die traditionellen Hartree-Fock- und Moller-Plesset-Elektronenkorrelations-Methoden. Ergänzende diffuse und/oder polarisierende Funktionen erzielten keine Verbesserungen.

Im Rahmen dieser Arbeit konnte gezeigt werden, dass quantenmechanische DFT-Rechnungen einen unverzichtbaren Bestandteil nicht nur für die spektroskopischen

Untersuchungen in der Chemie darstellen, sondern auch dazu beitragen, andere, neuere Gebiete in der physikalischen Chemie, wie beispielsweise SERS, zu verstehen.

REFERENCES

1. J. M. Chalmers, P. R. Griffiths, *Handbook of Vibrational Spectroscopy*, Vol. 1, J. Wiley & Sons, Chichester Baffins Lane, UK, **2002**.
2. J. M. Hollas, *Modern Spectroscopy*, 2nd Ed., Chap. 6, p. 128-183, J. Wiley & Sons, Baffins Lane, UK, **1992**.
3. A. J. Barnes, W. J. Orville, *Vibrational Spectroscopy – Modern Trends*, Elsevier Scientific Publishing Company, Amsterdam, The Netherlands, **1977**.
4. W. Demtröder, *Laser Spectroscopy. Basic Concepts and Instrumentation*, Springer-Verlag Berlin Heidelberg, **1981**.
5. P. R. Bunker, *Molecular Symmetry and Spectroscopy*, Academic Press Inc., New York, **1979**.
6. H. J. Jodl, *Vibrational spectra and structure. A series of advances*, Vol. 13, J. R. Durig Ed., Elsevier Science Publishers BV, Amsterdam, The Netherlands, **1984**.
7. R. A. Niquist, *Intepreting Infrared, Raman, and Nuclear Magnetic Resonance Spectra*, Vol. 1, Academic Press, San Diego, CA 92101-4495, **2001**.
8. D. A. Long, *Raman Spectroscopy*, McGraw-Hill, Great Britain, **1977**.
9. E. S. Brandt, T. M. Cotton, *Physical Methods of Chem. Series*, 2nd Ed., Vol. IXB, B. W. Rossiter and R. C. Baetzold Eds., Wiley, **1993**.
10. D. C. Champeney, *Fourier Transforms and their Physical Applications*, Academic Press, London, **1973**.
11. A. G. Marshall, F. R. Verdun, *Fourier Transforms in NMR, Optical and Mass Spectroscopy*, Elsevier, Amsterdam, **1990**.
12. P. B. Fellgett, *Infrared Phys.* **1984**, 24, 95.
13. P. Jacquinot, *J. Opt. Soc. Am.* **1954**, 44, 761.
14. P. Jacquinot, *Infrared Phys.* **1984**, 24, 99.
15. M. Fleischmann, P. J. Hendra, A. J. McQuillan, *Chem. Phys. Lett.* **1974**, 26, 163.
16. D. J. Jeanmaire, R. P. Van Duyne, *J. Electroanal. Chem.* **1977**, 84, 1.
17. M. G. Albrecht, J. A. Creighton, *J. Am. Chem. Soc.* **1977**, 99, 5215.
18. J. M. Sequaris, E. Koglin, *Anal. Chem.* **1985**, 321, 758.
19. E. L. Torres, J. D. Winefordner, *Z. Anal. Chem.* **1987**, 59, 1626.

20. C. H. Munro, W. E. Smith, D. R. Armstrong, P. C. White, *J. Phys. Chem.* **1995**, 99, 879.
21. R. P. Cooney, M. R. Mahoney, A. J. McQuillan, *Advances in Infrared and Raman spectroscopy*, Vol. 9, p. 188, R. J. H. Clark and R. E. Hester Eds., Heyden, Philadelphia, **1982**.
22. A. Campion, D. R. Mullins, *Chem. Phys. Lett.* **1983**, 54, 576.
23. A. Campion, D. R. Mullins, *Surf. Sci.* **1985**, 158, 263.
24. H. Seki, *J. Electron Spectrosc. Relat. Phenom.* **1986**, 39, 289.
25. M. F. Mrozek, A. S. Wasileski, M. J. Weaver, *J. Am. Chem. Soc.* **2001**, 123, 12817.
26. R. K. Chang, *Ber. Bunsenges. Phys. Chem.* **1987**, 91, 296.
27. J. A. Creighton, *Spectroscopy of Surface*, Eds. R. J. H. Clark, R. E. Hester, Wiley, New York, **1988**.
28. M. Moskovits, *J. Chem. Phys.* **1982**, 77, 4408.
29. C. A. Murray, *Surface Enhanced Raman Scattering*, p. 203, R. K. Chang and T. E. Furtak Eds., Plenum, New York, **1982**.
30. T. M. Cotton, R. A. Uphaus, D. Möbius, *J. Phys. Chem.* **1986**, 90, 6701.
31. R. K. Chang, B. L. Laube, *CRC Crit. Rev. Solid State Mater. Sci.* **1984**, 12, 1.
32. F. Barz, J. G. Gordon II, M. R. Philpott, M. J. Weaver, *Chem. Phys. Lett.* **1982**, 91, 291.
33. A. Wolkaun, *Solid State Phys.* **1984**, 38, 223.
34. H. Chew, Pj. McNulty, M. Kerker, *Phys. Rev. A* **1976**, 13, 396.
35. D. -S. Wang, H. Chew, M. Kerker, *Appl. Opt.* **1980**, 19, 2256.
36. M. Kerker, D. -S. Wang, H. Chew, *Appl. Opt.* **1980**, 19, 4159.
37. D. -S. Wang, M. Kerker, *Phys. Rev. B* **1981**, 24, 1777.
38. H. Chew, D. -S. Wang, M. Kerker, *Phys. Rev. B* **1983**, 28, 4169.
39. M. Kerker, O. Siiman, D. -S. Wang, *J. Phys. Chem.* **1984**, 88, 3168.
40. C. G. Blatchford, J. R. Campbell, J. A. Creighton, *Surf. Sci.* **1981**, 108, 411.
41. O. Siiman, L. A. Bumm, R. Callaghan, C. G. Blatchford, M. Kerker, *J. Phys. Chem.* **1983**, 87, 1014.
42. W. A. Lyon, S. M. Nie, *Anal. Chem.* **1997**, 69, 3400.
43. S. R. Emery, W. E. Haskins, S. M. Nie, *J. Am. Chem. Soc.* **1998**, 120, 8009.
44. K. Kneipp, H. Kneipp, R. Manoharan, E. B. Hanlon, I. Itzkan, R. R. Dasari, M. S. Feld, *Appl. Spectrosc.* **1998**, 52, 1493.
45. J. T. Krug, G. D. Wang, S. R. Emery, S. M. Nie, *J. Am. Chem. Soc.* **1999**, 121, 9208.

46. K. Kneipp, H. Kneipp, I. Itzkan, R. R. Dasari, M. S. Feld, *Chem. Phys.* **1999**, 247, 155.
47. A. M. Michaels, M. Nirmal, L. E. Brus, *J. Am. Chem. Soc.* **1999**, 121, 9932.
48. H. Xu, E. J. Bjerneld, M. Käll, L. Börjesson, *Phys. Rev. Lett.* **1999**, 83, 4357.
49. C. J. L. Constantino, T. Lemma, P. A. Antunes, R. Aroca, *Anal. Chem.* **2001**, 73, 3674.
50. M. Moskovits, *Proceedings of the XVIIIth International Conference on Raman Spectroscopy*, p. 53, J. Minsk, G. Jalsovszky and G. Keresztury Eds., Budapest, Hungary, **2002**.
51. K. Kneipp, Y. Wang, H. Kneipp, I. Itzkan, R. R. Dasari, M. S. Feld, *Phys. Rev. Lett.* **1996**, 76, 2444.
52. T. L. Haslett, L. Tay, M. Moskovits, *J. Chem. Phys.* **2000**, 113, 1641.
53. M. Moskovits, D. P. DiLella, *Surface Enhanced Raman Scattering*, p. 243, R. K. Chang and T. E. Furtak Eds., Plenum, New York, **1982**.
54. A. Otto, *Appl. Surf. Sci.* **1980**, 6, 309.
55. A. Otto, *J. Raman Spectrosc.* **1991**, 22, 743.
56. D. A. Guzonas, D. E. Irish, G. F. Atkinson, *Langmuir* **1990**, 6, 1102.
57. T. Watanabe, O. Kawanabe, K. Honda, B. Pettinger, *Chem. Phys. Lett.* **1983**, 102, 565.
58. D. Roy, T. E. Furtak, *Chem. Phys. Lett.* **1986**, 124, 299.
59. J. R. Lombardi, R. L. Birke, T. H. Lu, J. J. Xu, *J. Chem. Phys.* **1986**, 84, 4174.
60. F. J. Adrian, *J. Chem. Phys.* **1982**, 77, 5302.
61. H. Wetzel, H. Gerisher, B. Pettinger, *Chem. Phys. Lett.* **1981**, 78, 392.
62. B. Pettinger, H. Wetzel, *Chem. Phys. Lett.* **1981**, 78, 398.
63. R. L. Birke, J. R. Lombardi, *Spectroelectrochemistry: Theory and Practice*, p. 263, R. J. Gale Ed., Plenum, New York, **1988**.
64. B. J. N. Persson, *Chem. Phys. Lett.* **1981**, 82, 561.
65. J. I. Gersten, R. L. Birke, J. R. Lombardi, *Phys. Rev. Lett.* **1979**, 43, 147.
66. L. Markwort, P. J. Hendra, *J. Electroanal. Chem.* **1995**, 397, 225.
67. K. Suzan, A. Baiker, M. Meier, J. Wokaun, *J. Chem. Soc., Faraday Trans.* **1984**, 80, 1305.
68. G. Xue, J. Dong, M. Zhang, *Anal. Chem.* **1991**, 63, 2393.
69. A. Ruperez, J. J. Laserna, *Anal. Chim. Acta* **1994**, 291, 147.
70. J. J. Laserena, A. D. Campiglia, J. D. Winefordner, *Anal. Chim. Acta* **1988**, 208, 21.
71. W. S. Sutherland, J. D. Winefordner, *J. Colloid Interface Sci.* **1992**, 148, 129.
72. R. K. Chang, B. L. Laube, *CRC Crit. Rev. Solid State Mater. Sci.* **1984**, 12, 1.
73. T. E. Furtak, G. Trott, B. H. Loo, *Surface Sci.* **1980**, 101, 374.

74. B. Pettinger, U. Wenning, *Chem. Phys. Lett.* **1978**, 56, 253.
75. S. Efrima, *Modern Aspects of Electrochemistry*, Vol. 16, p. 253ff, B. E. Conway, R. E. White and J. O'M. Bockris Eds., Plenum, New York, **1985**.
76. P. Gao, M. L. Patterson, M. A. Tadayyoni, M. J. Weaver, *Langmuir* **1985**, 1, 173.
77. F. Barz, J. G. Gordon II, M. R. Philpott, M. J. Weaver, *Chem. Phys. Lett.* **1983**, 94, 168.
78. S. H. Macomber, T. E. Furtak, T. M. Devine, *Chem. Phys. Lett.* **1982**, 90, 439.
79. T. T. Chen, K. U. Von Raben, J. F. Owen, R. K. Chang, B. L. Laube, *Chem. Phys. Lett.* **1982**, 91, 494.
80. T. M. Devine, T. E. Furtak, S. H. Macomber, *J. Electroanal. Chem.* **1984**, 164, 299.
81. B. H. Loo, *Ann. Rep. INCRA*, Project No. 341, **1982**.
82. K. T. Carron, G. I. Xue, M. L. Lewis, *Langmuir* **1991**, 1, 2.
83. P. C. Lee, D. Meisel, *Chem. Phys. Lett.* **1983**, 99, 262.
84. S. M. Heard, F. Grieser, C. G. Barraclough, M. Kerker, *Chem. Phys. Lett.* **1983**, 95, 154.
85. R. -S. Sheng, L. Zhu, M. D. Morris, *Anal. Chem.* **1986**, 58, 1116.
86. C. G. Blatchford, O. Siiman, M. Kerker, *J. Phys. Chem.* **1983**, 87, 2503.
87. H. Wetzell, H. Gerischer, B. Pettinger, *Chem. Phys. Lett.* **1982**, 85, 187.
88. M. Carey Lea, *Am. J. Sci.* **1889**, 37, 476.
89. J. A. Creighton, C. G. Blatchford, M. G. Albrecht, *Trans. Faraday Soc.* **1979**, 75, 790.
90. P. C. Lee, D. P. J. Meisel, *J. Phys. Chem.* **1982**, 86, 3391.
91. C. H. Munro, W. E. Smith, M. Garner, J. Clarkson, P. C. White, *Langmuir* **1995**, 11, 3712.
92. O. Siiman, H. Feilchenfeld, *J. Phys. Chem.* **1988**, 92, 453.
93. P. Hildebrandt, M. Stockburger, *J. Raman Spectrosc.* **1986**, 17, 55.
94. Y. Xu, Y. Zheng, *Anal. Chim. Acta* **1989**, 225, 227.
95. S. Fu, P. Zhang, *J. Raman Spectrosc.* **1992**, 23, 93.
96. R. Aroca, F. Martin, *J. Raman Spectrosc.* **1985**, 16, 156.
97. E. V. Albano, S. Daiser, R. Miranda, K. Wandelt, *Surf. Sci.* **1985**, 150, 367.
98. R. S. Sennett, G. D. Scott, *J. Opt. Soc. Am.* **1950**, 40, 203.
99. V. Schlegel, T. M. Cotton, *Anal. Chem.* **1991**, 63, 241.
100. H. Yamada, Y. Yamamoto, *Chem. Phys. Lett.* **1981**, 77, 520.
101. C. Jennings, C. R. Aroca, A. -M. Hor, R. O. Loutfy, *Anal. Chem.* **1984**, 56, 2033.

102. R. G. Parr, W. Wang, *Density Functional Theory of Atoms and Molecules*, Oxford University Press, New York, **1989**.
103. F. Jensen, *Introduction to Computational Chemistry*, J. Wiley & Sons, Baffins Lane, UK, **1999**.
104. A. St-Amant, *Reviews in Computational Chemistry*, Vol. 7, p. 217, K. B. Lipkowitz and D.B. Boyd Eds., Wiley-VCH, New York, **1996**.
105. T. Ziegler, *Chem. Rev.* **1991**, 91, 651.
106. P. Hohenberg, W. Kohn, *Phys. Rev. B* **1964**, 136, 864.
107. W. Kohn, L. J. Sham, *Phys. Rev. A* **1965**, 140, 1133.
108. A. Szabo, N. S. Ostlund, *Modern Quantum Chemistry: Introduction to Advanced Electronic Structure Theory*, 1st Ed. Revised, McGraw-Hill, New York, **1989**.
109. W. J. Hehre, L. Radom, P. v. R. Schleyer, J. A. Pople, *Ab Initio Molecular Orbital Theory*, J. Wiley & Sons, New York, **1986**.
110. *Local Density Approximations in Quantum Chemistry and Solid State Physics*, J. P. Dahl, J. Avery Eds., Plenum, New York, **1984**.
111. S. H. Vosko, L. Wilk, M. Nusair, *Can. J. Phys.* **1980**, 58, 1200.
112. J. K. Labanowski, K. Jan, *Density Functional Methods in Chemistry*, J. W. Andzelm Ed., Springer-Verlag, New York, **1991**.
113. I. Papai, A. St.-Amant, J. Ushio, D. Salahub, *Int. J. Quantum Chem., Quantum Chem. Symp.* **1990**, 24, 29.
114. R. J. Bartlett, J. F. Stanton, *Reviews in Computational Chemistry*, Vol. 5, p. 65-169, K. B. Lipkowitz and D.B. Boyd Eds., VCH Publishers, New York, **1994**.
115. J. Andzelm, E. Wimmer, *J. Chem. Phys.* **1992**, 96, 1280.
116. B. G. Johnson, P. M. W. Gil, J. A. Pople, *J. Chem. Phys.* **1993**, 98, 5612.
117. D. M. Ceperley, *Phys. Rev. B* **1978**, 18, 3126.
118. D. M. Ceperley, B. J. Alder, *Phys. Rev. Lett.* **1980**, 45, 566.
119. J. P. Perdew, A. Zunger, *Phys. Rev. B* **1981**, 23, 5048.
120. A. D. Becke, *The challenge of d and f electrons*, ACS Symp. Ser. 394, p. 165, D. R. Salahub and M. C. Zerner Eds., American Chemical Society, Washington, DC, **1989**.
121. A. D. Becke, *J. Chem. Phys.* **1992**, 96, 2155.
122. A. D. Becke, *J. Chem. Phys.* **1992**, 97, 9173.
123. F. Sim, A. St-Amant, I. Papai, D. R. Salahub, *J. Am. Chem. Soc.* **1992**, 114, 4391.
124. P. Mlynarski, D. R. Salahub, *Phys. Rev. B* **1991**, 43, 1399.
125. J. P. Perdew, Y. Wang, *Phys. Rev. B* **1986**, 33, 8800.

126. J. P. Perdew, *Phys. Rev. B* **1986**, 33, 8822.
127. A. D. Becke, *Phys. Rev. A* **1988**, 38, 3098.
128. B. Miehlich, A. Savin, H. Stoll, H. Preuss, *Chem. Phys. Lett.* **1989**, 157, 200.
129. J. P. Perdew, J. A. Chevary, S. H. Vosko, K. A. Jackson, M. R. Pederson, D. J. Singh, C. Fiolhais, *Phys. Rev. A* **1992**, 46, 6671.
130. D. C. Langreth, M. J. Mehl, *Phys. Rev. B* **1983**, 28, 1809.
131. L. Y. Fan, T. Ziegler, *J. Chem. Phys.* **1991**, 94, 6057.
132. K. Laasonen, F. Csajka, M. Parrinello, *Chem. Phys. Lett.* **1992**, 194, 172.
133. C. Lee, W. Yang, R. G. Parr, *Phys. Rev. B* **1988**, 37, 785.
134. A. D. Becke, *J. Chem. Phys.* **1993**, 98, 1372.
135. A. D. Becke, *J. Chem. Phys.* **1993**, 98, 5648.
136. J. C. Slater, *Phys. Rev.* **1930**, 36, 57.
137. S. F. Boys, *Proc. R. Soc. (London) A* **1950**, 200, 452.
138. E. Clementi, G. Corongiu, M. Aida, *Modern Techniques in Computational Chemistry*, E. Clementi Ed., ESCOM Science Publishers, Leiden, **1990**.
139. J. S. Binkley, J. A. Pople, *J. Am. Chem. Soc.* **1980**, 102, 939.
140. W. J. Hehre, R. Ditchfield, J. A. Pople, *J. Chem. Phys.* **1972**, 56, 2257.
141. R. Krishnan, J. S. Binkley, R. Seeger, J. A. Pople, *J. Chem. Phys.* **1980**, 72, 650.
142. M. J. Frisch, J. A. Pople, J. S. Binkley, *J. Chem. Phys.* **1984**, 80, 3265.
143. S. M. Bachrach, *Reviews in Computational Chemistry*, Vol. 5, p. 171, K. B. Lipkowitz and D.B. Boyd Eds., VCH Publishers, New York, **1994**.
144. A. E. Reed, R. B. Weinstock, F. Weinhold, *J. Chem. Phys.* **1985**, 83, 735.
145. A. E. Reed, F. Weinhold, *J. Chem. Phys.* **1985**, 83, 1736.
146. A. E. Reed, L. A. Curtiss, F. Weinhold, *Chem. Rev.* **1988**, 88, 899.
147. P. -O. Löwdin, *Phys. Rev.* **1955**, 97, 1474.
148. E. R. Davidson, *Reduced Density Matrices in Quantum Chemistry*, Academic Press, New York, **1976**.
149. R. McWeeney, B. T. Sutcliffe, *Methods of Molecular Quantum Mechanics*, Academic Press, New York, **1969**.
150. R. S. Mulliken, *J. Chem. Phys.* **1955**, 23, 1883.
151. R. S. Mulliken, *J. Chem. Phys.* **1955**, 23, 1841.
152. R. S. Mulliken, *J. Chem. Phys.* **1955**, 23, 2338.
153. R. S. Mulliken, *J. Chem. Phys.* **1955**, 23, 2343.
154. J. P. Foster, F. Weinhold, *J. Am. Chem. Soc.* **1980**, 102, 7211.

157 **References**

155. A. E. Reed, F. Weinhold, *J. Chem. Phys.* **1983**, 78, 4066.
156. I. Pavel, S. Cîntă, M. Venter, A. Deák, I. Haiduc, P. Rösch, O. Cozar, T. Iliescu, W. Kiefer, *Vib. Spectrosc.* **2000**, 23, 71.
157. N. Okabe, K. Tamaki, *Acta Crystallogr.* **1995**, C51, 2004.
158. M. Vögler, I. Pavel, M. Hofmann, D. Moigno, M. Nieger, W. Kiefer, W. Malisch, *Inorg. Chem.* **2003**, 42, 3274.
159. W. Malisch, M. Vögler, H. Käß, H.-U. Wekel, *Organometallics* **2002**, 21, 2830.
160. W. Malisch, W. Ries, *Chem. Ber.* **1979**, 112, 1304.
161. C. Strohmann, *Chem. Ber.* **1995**, 128, 167.
162. M. J. Frisch, G. W. Trucks, H. B. Schlegel, P. M. W. Gill, B. G. Johnson, M. A. Robb, J. R. Cheeseman, T. Keith, G. A. Petersson, J. A. Montgomery, K. Rhaghavachari, M. A. Al-Laham, V. G. Zakrzewski, J. V. Ortiz, J. B. Foresman, J. Ciolowski, B. B. Stefanov, A. Nanayakkara, M. Challacombe, C. Y. Peng, P. Y. Ayala, W. Chen, M. W. Wong, J. L. Andres, E. S. Replogle, R. Gomberts, R. L. Martin, D. J. Fox, J. S. Binkley, D. J. Defrees, J. Baker, J. P. Stewart, M. Head-Gordon, C. Gonzalez, J.A. Pople, *Gaussian 98*, Revision A7, Gaussian Inc., Pittsburg PA, **1998**.
163. J. P. Perdew, Y. Wang, *Phys. Rev.* **1992**, B45, 13244.
164. Y. Yamguchi, M. Frisch, J. F. Gaw, H. F. Schaefer, S. Binkley, *J. Chem. Phys.* **1986**, 84, 2262.
165. T. H. Dunning, Jr. and P. J. Hay, *Modern Theoretical Chemistry*, III, p. 805-888, H. F. Schaefer Ed., Plenum, New York, **1976**.
166. U. Salzner, T. Kiziltepe, *J. Org. Chem.* **1999**, 64, 764.
167. M. Tasumi, *Kobunshi* **1974**, 23, 362.
168. M. Tasumi, S. Takahashi, *Seibutsu Butsuri* **1973**, 13, 319.
169. M. Tasumi, *Kagaku no Ryoiki* **1980**, 34, 14.
170. *Surface Enhanced Raman Scattering*, R. K. Chang and T. E. Furtak Eds., Plenum, New York, **1982**.
171. S. Nie, S. R. Emory, *Science* **1997**, 275, 1102.
172. M. Takahashi, M. Fujita, M. Ito, *Chem. Phys. Lett.* **1984**, 109, 122.
173. J. S. Suh, N. H. Jang, D. H. Jeong, M. Moskovits, *J. Phys. Chem.* **1996**, 100, 805.
174. I. Pavel, D. Moigno, S. Cîntă, W. Kiefer, *J. Phys. Chem. A* **2002**, 106, 3337.
175. M. Moskovits, J. S. Suh, *J. Phys. Chem.* **1984**, 88, 1293.
176. X. Gao, J. P. Davies, M. J. Weaver, *J. Phys. Chem.* **1990**, 94, 6858.
177. T. C. Streckas, P. S. Diamondopoulos, *J. Phys. Chem.* **1990**, 94, 1986.

178. J. Chowdhury, K. M. Mukherjee, T. N. Misra, *J. Raman Spectrosc.* **2000**, 31, 427.
179. I. Pavel, A. Szeghalmi, D. Moigno, S. Cîntă, W. Kiefer, *Biopolymers* **2003**, 72, 25.
180. H. J. Bein, H. Brunner, *Ger. Offen.* **1972** (patent).
181. H. Brunner, Ph. R. Hedwall, *Ger. Offen.* **1973** (patent).
182. V. Dorneanu, I. Popovici, M. Dorneanu, *Rom. Rev. Chim.* **1996**, 35, 357.
183. R. Micu-Semeniuc, R. F. Semeniuc, O. Cozar, L. David, *Synth. React. Inorg. Met. – Org. Chem.* **1994**, 28, 501.
184. L. K. Thompson, T. C. Woon, *Inorg. Chim. Acta* **1986**, 111, 45.
185. S. S. Tandon, L. K. Thompson, R. C. Hynes, *Inorg. Chem.* **1992**, 31, 2210.
186. S. K. Talwar, V. K. Rastogi, R. C. Saxena, *J. Indian Chem. Soc.* **1991**, 68, 402.
187. J. Kyota, N. Ueno, *Jpn. Kokai Tokkyo Koho* **1997** (patent).
188. G. Conte, S. Lauro, A. Ruol, *Clin. Ter.* **1966**, 39, 441.
189. S. Campus, A. Rappelli, F. Fabris, I. Mathis, *Ital. Biol. Sper.* **1967**, 43, 1847.
190. S. Campus, F. Fabris, A. Rappelli, I. Mathis, *Ital. Biol. Sper.* **1967**, 43, 1851.
191. C. Herrstadt, D. Mootz, H. Wunderlich, H. Möhrle, *J. Chem. Soc. Perkin Trans. II* **1979**, 6, 735.
192. K. Stadnicka, L. Lebioda, *Acta Crystallogr.* **1979**, B35, 770.
193. O. Carugo, C. B. Castellani, A. Perotti, *Acta Crystallogr.* **1995**, C51, 1683.
194. D. Cremer, J. A. Pople, *J. Am. Chem. Soc.* **1975**, 97, 1354.
195. N. S. Zefirov, V. A. Palyulin, E. E. Dashevskaya, *J. Phys. Org. Chem.* **1990**, 3, 147.
196. R. W. Mitchell, R. W. Glass, J. A. Merritt, *J. Mol. Spectrosc.* **1970**, 36, 310.
197. M. Muniz-Miranda, G. Sbrana, *J. Raman Spectrosc.* **1996**, 27, 105.
198. A. L. McClellan, G. C. Pimentel, *J. Chem. Phys.* **1955**, 23, 245.
199. E. R. Lippincott, E. J. O' Reilly, *J. Chem. Phys.* **1955**, 23, 238.
200. A. P. Scott, L. Radom, *J. Phys. Chem.* **1996**, 100, 16502.
201. M. W. Wong, *Chem. Phys. Lett.* **1996**, 256, 391.
202. G. Rauhut, P. Pulay, *J. Phys. Chem.* **1995**, 99, 3093.
203. R. Fleischer, B. Walfort, A. Gbureck, P. Scholz, W. Kiefer, D. Stalke, *Chem. Eur. J.* **1998**, 4, 2266.
204. J. Billmann, J. Kovacs, A. Otto, *Surf. Sci.* **1980**, 92, 153.
205. A. Otto, *Light Scattering in Solids*, Eds. M. Cardona and G. Guntherodt, Vol. 4, Springer: Berlin, **1984**.
206. M. Moskovits, J. S. Suh, *J. Am. Chem. Soc.* **1985**, 107, 6826.
207. D. H. Jeong, N. H. Jang, J. S. Suh, M. Moskovits, *J. Phys. Chem B.* **2000**, 104, 3594.

208. G. Varsany, *Assignments for Vibrational Spectra of Seven Hundred Benzene Derivatives*, J. Wiley & Sons, New York, **1974**.
209. M. Moskovits, J. S. Suh, *J. Phys. Chem.* **1988**, 92, 6327.
210. T. Robinson, *The Biochemistry of Alkaloids*, Springer, New York, **1968**.
211. H. Ashihara, A. Crozier, *J. Agric. Food Chem.* **1999**, 47, 3425.
212. P. Mazzafera, A. Crozier, A. C. Magalhães, *Phytochem.* **1991**, 30, 3913.
213. T. Kumazawa, H. Seno, X.-P. Lee, A. Ishii, K. Watanabe-Suzuki, K. Sato, O. Suzuki, *Anal. Chim. Acta* **1999**, 387, 53.
214. P. Bosson, *Rev. Pathol. Genet. Physiol. Clin.* **1956**, 56, 681.
215. M. de Matas, H. G. M. Edwards, E. E. Lawson, L. Shields, P. York, *J. Mol. Struct.* **1998**, 440, 97.
216. D. Cook, Z. R. Regnier, *Can. J. Chem.* **1967**, 45, 2895.
217. M. Falk, M. Gil, N. Iza, *Can. J. Chem.* **1990**, 68, 1293.
218. J. de Taeye, Th. Zeegers-Huyskens, *J. Pharm. Sci.* **1985**, 74, 660.
219. R. A. Nyquist, S. L. Fiedler, *Vibrat. Spectrosc.* **1995**, 8, 365.
220. E. Shefter, *J. Pharm. Sci.* **1968**, 57, 1163-1168.
221. D. J. Sutor, *J. Acta Crystallogr.* **1958**, 11, 453.
222. H. G. M. Edwards, E. Lawson, M. de Matas, L. Shields, P. York, *J. Chem. Soc. Perkin Trans. II* **1997**, 10, 1985.
223. R. L. Benoit, M. Fréchet, *Can. J. Chem.* **1985**, 63, 3053.
224. D. Cook, *Can. J. Chem.* **1966**, 44, 335.
225. R. J. Abraham, E. Bullock, S. S. Mitra, *Can. J. Chem.* **1959**, 37, 1859.
226. Y. Chiang, E. B. Whipple, *J. Am. Chem. Soc.* **1963**, 85, 2763.
227. D. Lichtenberg, F. Bergmann, Z. Nelman, *J. Chem. Soc. C* **1971**, 9, 1676.
228. R. Sheng, F. Ni, T. M. Cotton, *Anal. Chem.* **1991**, 63, 437.
229. S. Sánchez-Cortés, J. V. Garcia-Ramos, *J. Raman Spectrosc.* **1998**, 29, 365.
230. Y. Kurokawa, Y. Imai, Y. Tamai, *Analyst* **1997**, 122, 941.
231. R. Aroca, R. E. Clavijjo, *Spectrochim. Acta A* **1988**, 44A, 171.
232. K. W. Bentley, *The isoquinoline alkaloids*, Harwood Academic Publishers, Amsterdam, **1998**.
233. M. Kitamura, Y. Hsiao, M. Ohta, M. Tsukamoto, T. Ohta, H. Takaya, R. Noyori, *J. Org. Chem.* **1994**, 59, 297.
234. R. Santi, M. Ferrari, A. R. Contessa, *Biochem. Pharmacol.* **1964**, 13, 153.

235. T. Uruno, I. Takayanagi, M. Tokunaga, K. Kubota, K. Takagi, *Jap. J. Pharmacol.* **1974**, *24*, 681.
236. G. R. Lenz, C. M. Woo, *J. Org. Chem.* **1982**, *47*, 3049.
237. S. Chulia, M. D. Ivorra, S. Martinez, M. Elorriaga, M. Valiente, M. A. Noguera, C. Lugnier, C. Advenier, P. D'Ocon, *Br. J. Pharmacol.* **1997**, *122*, 409.
238. A. P. Venkov, I. I. Ivanov, *Tetrahedron* **1996**, *52*, 12299.
239. R. Chandra, J. Kaur, A. Talwar, N. N. Ghosh, *Arkivoc VIII* **2001**, 129.
240. C. D. Reynolds, R. A. Palmer, B. Gorinsky, *J. Cryst. Mol. Struct.* **1973**, *4*, 213.
241. A. R. Katritzky, R. A. Jones, *J. Chem. Soc., Abstracts* **1960**, 2942.
242. S. C. Wait Jr., J. C. McEnerney, *J. Mol. Spectrosc* **1970**, *34*, 56.
243. P. J. Chappell, I. G. Ross, *J. Mol. Spectrosc.* **1977**, *66*, 192.
244. S. S. Mitra, H. J. Bernstein, *Can. J. Chem.* **1959**, *37*, 553.
245. W. L. F. Armarego, G. B. Barlin, E. Spinner, *Spectrochim. Acta* **1966**, *22*, 117.
246. C. H. Kline, Jr., J. Turkevich, *J. Chem. Phys.* **1944**, *12*, 300.
247. F. J. Welcher, *Organic Analytical Reagents*, Vol. III, p. 355, Van Nostrand, New York, **1947**.
248. L. Parkanyi, A. Kalman, A. Deák, M. Venter, I. Haiduc, *Inorg. Chem. Commun.* **1999**, *2*, 265.
249. *Bioassay of cupferron for possible carcinogenicity*, in *Carcinogenesis*, National Cancer Institute Technical Report Series 100, National Cancer Institute, Bethesda, MD, **1978**.
250. D. F. V. Lewis, C. Ioannides, D. V. Parke, *Mutation Res.* **1993**, *291*, 61.
251. J. Ashby, D. Paton, *Mutation Res.* **1993**, *286*, 3.
252. T. A. Alston, D. J. T. Porter, H. J. Bright, *J. Bio. Chem.* **1985**, *260*, 4069.
253. J. G. Lawless, M. D. Hawley, *Anal. Chem.* **1968**, *40*, 948.
254. A. D. McGill, Y. -F. Yang, L. Echegoyen, P. G. Wang, *Methods Enzymology, Nitric Oxide, Part C: Biological and Antioxidant Activities*, Ed. L. Packer, **1999**, *301*, 235.
255. A. D. McGill, W. Zhang, J. Wittbrodt, J. Wang, H. B. Schlegel, P. G. Wang, *Bioorg. Med. Chem.* **2000**, *8*, 405.
256. A. T. Balaban, R. E. Garfield, M. J. Lesko, W. A. Seitz, *Org. Prep. Proced. Int.* **1998**, *30*, 439.
257. R. E. Garfield, A. T. Balaban, W. A. Seitz, D. J. Klein, M. J. Lesko, *Int. Pat. Appl.* **1996** (PCT/US/96/694).
258. A. T. Balaban, N. Negoita, I. Pascaru, *Rev. Roum. Chim.* **1971**, *16*, 271.

259. D. K. Taylor, I. Bytheway, D. H. R. Barton, C. A. Bayse, M. B. Hall, *J. Org. Chem.* **1995**, 60, 443.
260. A. Deák, A. Kalman, L. Parkanyi, I. Haiduc, *Acta Crystallogr.* **2001**, B57, 303.
261. Y. Hou, W. Xie, A. J. Janczuk, P. G. Wang, *J. Org. Chem.* **2000**, 65, 4333.
262. A. Deák, I. Haiduc, L. Parkanyi, M. Venter, A. Kalman, *Eur. J. Inorg. Chem.* **1999**, 9, 1593.
263. S. Cîntă, M. Venter, I. Haiduc, Spectroscopy of Biological Molecules: New Directions, European Conference on the Spectroscopy of Biological Molecules, 8th, p. 559, Enschede, Netherlands, **1999**.
264. A. Deák, L. Parkanyi, A. Kalman, M. Venter, I. Haiduc, *Acta Crystallogr.* **1998**, C54, CIF access.
265. G. -B. Yi, M. A. Khan, G. B. Richter-Addo, *Inorg. Chem.* **1995**, 34, 5703.
266. Y. Ellerman, O. Akatol, I. Svoboda, M. Gesselle, *Acta Crystallogr.* **1995**, C51, 1520.
267. Y. Ellerman, N. Kabak, I. Svoboda, H. Fuess, K. Griessar, W. Haase, *Z. Naturforsch.* **1995**, 50b, 1587.
268. S. S. Basson, J. G. Leipoldt, W. Purcell, J. A. Venter, *Acta Crystallogr.* **1992**, C48, 171.
269. S. S. Basson, J. G. Leipoldt, J. A. Venter, *Acta Crystallogr.* **1990**, C46, 1324.
270. S. S. Basson, J. G. Leipoldt, A. Roodt, J. A. Venter, *Inorg. Chim. Acta* **1987**, 128, 31.
271. S. S. Basson, J. G. Leipoldt, A. Roodt, J. A. Venter, *Inorg. Chim. Acta* **1986**, 118, 45.
272. S. Amirkhaili, A. J. Conwey, J. D. Smith, *J. Organometal. Chem.* **1978**, 149, 407.
273. R. Kellner, A. J. Prokopowski, *Anal. Chim. Acta* **1976**, 86, 175.
274. S. T. Srivastava, *J. Inorg. Nucl. Chem.* **1975**, 37, 1546.
275. M. Bolboacă, S. Cîntă, M. Venter, A. Deák, I. Haiduc, O. Cozar, T. Iliescu, P. Rösch, W. Kiefer, *Spectrosc. Lett.* **2000**, 33, 857.
276. K. Tamaki, N. Okabe, *Acta Crystallogr.* **1996**, C52, 1612.
277. F. R. Dollish, W. G. Fateley, F. F. Bentley, *Characteristic Raman Frequency of the Organic Compounds*, Wiley, New York, **1973**.
278. J. E. Huheey, E. A. Keiter, R. L. Keiter, *Inorganic Chemistry: Principles of Structure and Reactivity*, 4th Ed., p. A31, Harper Collins, New York, **1993**.
279. S. Cîntă, M. Venter, W. Kiefer, P. Scholz, T. Iliescu, O. Cozar, *Balk. Phys. Lett.* **1997**, 5, 317.
280. M. Moskovits, *Rev. Mod. Phys.* **1985**, 57, 783.
281. I. Antes, G. Frenking, *Organometallics* **1995**, 14, 4263.

282. A. J. Chalk, J. F. Harrod, *J. Am. Chem. Soc.* **1967**, 89, 1640.
283. J. Y. Corey, J. Braddock-Wilking, *Chem. Rev.* **1999**, 99, 175.
284. C. Zybilla, H. Handwerker, H. Friedrich, *Adv. Organomet. Chem.* **1994**, 36, 229.
285. T. D. Tilley, *Transition Metal Silyl Derivatives*, p. 245, S. Patai and Z. Rappoport Eds., Wiley, New York, **1991**.
286. C. S. Cundy, B. M. Kingston, M. F. Lappert, *Adv. Organomet. Chem.* **1973**, 11, 253.
287. U. Schubert, *Adv. Organomet. Chem.* **1990**, 30, 151.
288. B. J. Aylett, *Adv. Inorg. Chem. Radiochem.* **1982**, 25, 1.
289. W. Malisch, M. Kuhn, *Chem. Ber.* **1974**, 107, 979.
290. J. L. Speier, *Adv. Organomet. Chem.* **1979**, 407.
291. I. Ojima, *The Chemistry of Organic Silicon Compounds*, p. 1479, S. Patai and Z. Rappoport Eds., Wiley, Chichester, **1989**.
292. A. J. Chalk, J. F. Harrod, *J. Am. Chem. Soc.* **1965**, 87, 16.
293. M. Yamashita, M. Tanaka, *Bull. Chem. Soc. Jpn.* **1995**, 68, 403.
294. T. D. Tilley, *Acc. Chem. Res.* **1993**, 26, 22.
295. E. Hengge, *Organosilicon Chemistry*, p. 275, N. Auner and J. Weis Eds., Wiley-VCH, Weinheim, **1994**.
296. Y. Uchimaru, Y. Tanaka, M. Tanaka, *Chem. Lett.* **1995**, 164.
297. C. A. Recatto, *Aldrichimica Acta* **1995**, 28, 85.
298. B. J. Aylett, *Adv. Inorg. Chem. Radiochem.* **1968**, 11, 249.
299. N. J. Archer, R. N. Haszeldine, R. V. Parish, *Chem. Commun.* **1971**, 524.
300. K. Hübler, P. A. Hunt, S. M. Maddock, C. E. F. Rickard, W. R. Roper, D. M. Salter, P. Schwerdtfeger, L. J. Wright, *Organometallics* **1997**, 16, 5076.
301. F. R. Lemke, K. J. Galat, W. J. Youngs, *Organometallics* **1999**, 18, 1419.
302. S. T. N. Freeman, L. L. Lofton, F. R. Lemke, *Organometallics* **2002**, 21, 4776.
303. K. W. Muir, *J. Chem. Soc. A* **1971**, 2663.
304. K. H. Pannell, C. C. Wu, G. J. Long, *J. Organomet. Chem.* **1980**, 186, 85.
305. D. L. Lichtenberger, A. Rai-Chaudhuri, *J. Am. Chem. Soc.* **1991**, 113, 2923.
306. W. Malisch, M. Vögler, D. Schumacher, M. Nieger, *Organometallics* **2002**, 21, 2891.
307. W. Malisch, W. Ries, *Angew. Chem.* **1978**, 90, 140.
308. W. Malisch, W. Ries, *Angew. Chem., Int. Ed. Engl.* **1978**, 17, 120.
309. H. Ogino, H. Tobita, *Adv. Organomet. Chem.* **1998**, 42, 223.
310. L. S. Luh, Y. S. Wen, H. Tobita, H. Ogino, *Bull. Chem. Soc. Jpn.* **1997**, 70, 2193.
311. K. H. Pannell, H. Sharma, *Organometallics* **1991**, 10, 954.

312. K. Ueno, N. Hamashima, M. Shimoi, H. Ogino, *Organometallics* **1991**, 10, 959.
313. B. J. Aylett, H. M. Colquhoun, *J. Chem. Res. S* **1977**, 1, 148.
314. W. Malisch, S. Möller, O. Fey, H.-U. Wekel, R. Pikl, U. Posset, W. Kiefer, *J. Organomet. Chem.* **1996**, 507.
315. D. D. Shillady, J. Craig, S. Rutan, B. Rao, *Int. J. Quantum Chem.* **2002**, 90, 1414.
316. W. Malisch, H. Jehle, S. Möller, G. Thum, J. Reising, A. Gbureck, V. Nagel, C. Fickert, W. Kiefer, M. Nieger, *Eur. J. Inorg. Chem.* **1999**, 1597.
317. V. Nagel, C. Fickert, M. Hofmann, M. Vögler, W. Malisch, W. Kiefer, *J. Mol. Struct.* **1999**, 480-481, 511.
318. W. Jetz, W. A. G. Graham, *J. Am. Chem. Soc.* **1967**, 89, 2773.
319. W. Malisch, M. Kuhn, *Chem. Ber.* **1974**, 107, 2835.
320. W. Malisch, P. Panster, *Chem. Ber.* **1975**, 108, 2554.
321. J. Dalton, I. Paul, F. G. A. Stone, *J. Chem. Soc. A* **1969**, 2744.
322. M. Höfler, J. Scheuren, D. Spilker, *J. Org. Chem.* **1975**, 102, 205.
323. G. Thum, W. Malisch, *J. Organometal. Chem.* **1984**, 264, C5-C9.
324. M. G. Voronkov, S. V. Kirpichencko, E. N. Suslova, V. V. Keiko, *J. Organomet. Chem.* **1981** 204, 13.
325. J. V. Swisher, J. Perman, P. D. Weiss, J. R. Ropchan, *J. Organomet. Chem.* **1981**, 215, 373.
326. A. G. Brook, S. S. Hu, W. J. Chatterton, A. J. Lough, *Organometallics* **1991**, 10, 2752.
327. A. G. Brook, W. J. Chatterton, J. F. Sawyer, D. W. Hughes, K. Vorspohl, *Organometallics* **1987**, 6, 1246.
328. N. Wiberg, G. Preiner, K. Schurz, G. Fischer, *Z. Naturforsch. B* **1988**, 43, 1468.
329. N. Wiberg, G. Preiner, G. Wagner, H. Köpf, *Z. Naturforsch. B* **1987**, 42, 1062.
330. S. M. Bachrach, A. Streitwieser Jr., *J. Am. Chem. Soc.* **1985**, 107, 1186.
331. T. J. Barton, G. P. Hussmann, *Organometallics* **1983**, 2, 692.
332. W. Ando, A. Sekiguchi, T. Sato, *J. Am. Chem. Soc.* **1982**, 104, 6830.
333. N. Wiberg, G. Preiner, O. Schieda, *Chem. Ber.* **1981**, 114, 3518.
334. A. Maercker, *Methoden Org. Chem.*, 4th Ed, p. 448, Bd. E19d, **1952-1993**.
335. L. E. Gusel'nikov, V. V. Volkova, V. G. Zaikin, N. A. Tarasenko, A. A. Tishenkov, N. S. Nametkin, M. G. Voronkiv, *Zh. Struc. Khim.* **1997**, 28, 49.
336. D. Bist, S. Sathaiah, V. N. Sarin, *Recent trends in Raman spectroscopy*, p. 340, S. S. Banerjee and S.S.Jha Eds., World Scientific, Singapore, **1989**.

337. I. Goldberg, *The Chemistry of Ethers, Crown Ethers, Hydroxyl Groups and their Sulphur Analogues*, Part I, p. 175, S. Patai Ed., John Wiley & Sons, Chichester, **1980**.
338. A. Bondi, *J. Phys. Chem.* **1964**, 441.
339. W. S. Sheldrick, *The Chemistry of Organic Silicon Compounds*, Part I, p. 227, S. Patai and Z. Rappoport Eds., John Wiley & Sons, Chichester, **1989**.
340. V. S. Mastryukov, L. V. Khristenko, L. V. Vilkov, Yu. A. Pentin, J. E. Boggs, *Zh. Fiz. Kh.* **1994**, 68, 853.
341. R. K. Singh, A. L. Verma, *J. Raman Spectrosc.* **1997**, 28, 301.
342. R. K. Singh, S. N. Singh, B. P. Asthana, *J. Raman Spectrosc.* **1994**, 25, 423.
343. B. P. Asthana, W. Kiefer, *Vibrational Spectra and Structure*, Vol. 20, p. 67, Elsevier Science, J. R. Durrant Ed., Amsterdam, **1993**.
344. A. Langseth, R. C. Lord Jr., *Kgl. Dan. Vidensk. Selsk. Math-fys. Medd.* **1938**, 16, 1.
345. K. W. F. Kohlrausch, *Ramanspektren*, Akademische Verlagsges., Leipzig, **1943**.
346. G. Varsanyi, *Vibrational Spectra of Benzene Derivatives*, Academic Press, New York, **1969**.
347. G. Cardini, M. Muniz-Miranda, *J. Phys. Chem. B* **2002**, 106, 6875.
348. J. W. Mdelin, M. A. Barteau, *J. Phys. Chem. B* **2002**, 105, 10054.

ABBREVIATIONS and SYMBOLS

| | |
|---------------|---|
| ° | degree |
| Å | Ångström = 10^{-10} m |
| Ag | silver |
| amu | atomic mass unit = 1.6605402×10^{27} kilograms |
| AO | Atomic Orbital |
| a.u. | atomic unit of energy = 27.2 eV atomic unit of length = 0.053 nm |
| c | velocity of light = $2.99792458 \times 10^{10}$ cm s ⁻¹ |
| cal | 1 calory = 4.184 Joules |
| Calc | calculated |
| Cp | cyclopentadienyl |
| CT | charge transfer |
| DFT | density functional theory |
| DHPZ | 1,4 –dihydrazinophthalazine |
| D95V | Dunning/Huzinaga valence double-zeta |
| DZ | Double-Zeta basis sets |
| e | 1 electronic charge = 1.602188×10^{19} Coulomb |
| E | electric field vector |
| ECP | effective core potential |
| ESD | electron density synthesis |
| EM | electromagnetic |
| ESR | electron spin resonance |
| eV | 1 electron Volt = 23.06035 kcal mol ⁻¹ |
| Exp | experimental |
| f | quadratic force constant |
| FT | Fourier-Transform |
| \mathcal{G} | enhancement factor |
| GTO | Gaussian Type Orbital |
| h | Planck's constant = 6.6260755×10^{34} Joule s |
| HF | Hartree-Fock |

| | |
|--------------------|---------------------------------------|
| IR | infrared |
| I_L | power of the laser at sample |
| I_{Raman} | Raman intensity |
| isoq | isoquinoline |
| J | Joule = $\text{m}^2 \text{kg s}^{-2}$ |
| K | constant of proportionality |
| K_a | absorption coefficient |
| kJ/mol | kJoule/mol |
| KS | Kohn and Sham |
| L | Lorentzian character of a Raman band |
| LSDA | Local Spin Density Approximation |
| m | complex refractive index |
| m_i | molecular mass of atom i |
| MIR | middle infrared |
| MO | Molecular Orbital |
| n | real refractive index |
| N | number of atoms |
| NAO | natural atomic orbitals |
| NBO | natural bond orbitals |
| NIR | near infrared |
| NMB | natural minimal basis |
| NMR | nuclear magnetic resonance |
| NPA | natural population analysis |
| NRB | natural Rydberg basis |
| <i>o,o'</i> -bipy | <i>o,o'</i> -bipyridine |
| <i>o</i> -phen | <i>o</i> -phenanthroline |
| ORC | oxidation-reduction cycle |
| ph | phenyl |
| pm | picometer = 10^{-12} m |
| Q | normal mode |
| r | internal coordinate |
| Scal | scaled |
| SERS | surface enhanced Raman spectroscopy |
| S/N | signal-to-noise ratio |

| | |
|---------------|---|
| STO | Slater Type Orbital |
| SVWN | Slater exchange functional and Vosko-Wilk-Nusair correlation functional |
| t | time |
| UV | ultraviolet |
| ν_i | vibrational quantum number i |
| V | potential energy |
| XC | exchange and correlation |
| YAG | Yttrium Aluminum Garnet |
| ZPE | zero-point energy |
| α | polarizability |
| β | hyperpolarizability |
| γ | the second hyperpolarizability |
| Γ | integrated absorption intensity |
| ϵ_0 | permittivity of free space |
| μ | dipole moment |
| $\tilde{\nu}$ | wavenumber |
| ρ | depolarization ratio |

Vibrational modes

| | |
|----------|---------------|
| asym | asymmetric |
| i.p. | in-plane |
| m | medium |
| ms | medium strong |
| o.p. | out-of-plane |
| s | strong |
| sh | shoulder |
| sym | symmetric |
| vs | very strong |
| vw | very weak |
| w | weak |
| v | stretching |
| δ | bending |

| | |
|----------|------------|
| ω | wagging |
| τ | twisting |
| ρ | rocking |
| γ | scissoring |

Curriculum Vitae

Personal information

Pavel Ioana-Emilia
Date of Birth (dd/mm/yy): 08.08.1974
Citizenship: Romanian
Address: Kittelstraße 14, D-97074 Würzburg, Germany

Education

- 10.1999-currently Institution: Bayerische Julius-Maximilians University of Würzburg
Department: Institute of Physical Chemistry
Location: Am Hubland, D-97074 Würzburg, Germany
Anticipated ending: September 2003
Research topics: *“Vibrational spectroscopy and density functional theory calculations, a powerful approach for the characterization of pharmaceuticals and new organometallic complexes”*
Degree sought: Ph.D.
- 09.1998–06.1999 Institution: Babeş-Bolyai University
Department: Physics Faculty
Location: Kogălniceanu 1, 3400 Cluj-Napoca, Romania
Field: *Atom Physics*
Degree: MSc.
- 09.1997-06.1998 Institution: Babeş-Bolyai University
Department: Physics Faculty
Location: Kogălniceanu 1, 3400 Cluj-Napoca, Romania
Field: *Biophysics and medical physics*
Degree: MSc.
- 09.1997-06.1999 Institution: Technical University of Cluj-Napoca
Department: Faculty of Automation and Computer Science (English class)
Location: Daicoviciu 15, 3400 Cluj-Napoca, Romania
Study interrupted due to the scholarship received at the Würzburg University.
- 09.1993–06.1997 Institution: Babeş-Bolyai University
Department: Physics Faculty
Location: Kogălniceanu 1, 3400 Cluj-Napoca, Romania
Field: *Physics*
Degree: Bachelor of Physics

09.1993-06.1997 Institution: "Tiberiu Popoviciu" High School of Informatics
Location: Calea Turzii 140-142, 3400 Cluj-Napoca, Romania
Specialty: *Informatics*
Degree: **High school diploma, diploma of assistant
programmer**

Honors/Awards

01.1999–04.1999 Having graduated as the top student during the master study I
was offered a **SOCRATES fellowship** at University of
Würzburg.

Numerous awards received at different scholar competitions of
physics and foreign languages.

Work experience

04.2000-currently Teaching assistant at the physical chemistry department of
University of Würzburg in the special research project SFB 347.
Supervision of practicum.

Responsible for the upkeep of two Raman laboratories and a
Linux cluster.

Word of gratitude

“The most beautiful experience we can have is the mysterious.
It is the fundamental emotion, which stands at the cradle of true art and true science.”

Albert Einstein

Coming here, in a totally unknown country for me, to pursue a PhD, was probably the most courageous and at the same time the luckiest act of my life. It opened the doors to another world, a beautiful one, and gave me the chance to *grow*, not only scientifically but also as a human being.

The person who made all this possible was Professor Dr. Wolfgang Kiefer. Thank you for offering me the chance to join your workgroup and pursue the PhD degree. I am very grateful for the confidence that you showed to me and the extraordinary support. Every time I knocked at your door, you were there with a smile on face and a solution to my problems. The possibility of taking part at many international conferences has continuously motivated me and offered me the chance to get in contact with new perspectives.

I would also like to thank Professor Dietmar Stalke for the interesting discussions and the wonderful lessons of chemistry. Your words increased the confidence in myself and my work.

I also want to express my special thanks to Lector Dr. Simona Cîntă-Pînzaru. Her guidance concerning the SERS aspects helped me to progress a lot. I enjoyed the free discussions with you very much. Thank you for your continuous encouragement and interest in my work.

I would also like to thank Professor Dr. Volker Engel for having accepted to read my thesis and express his opinion upon the theoretical calculations.

Also, special thanks go to my colleague Dr. Damien Moigno. Without your help and understanding I would have never come so far. Thank you for passing on all your experience regarding the DFT calculations.

I am very grateful to Professor Dr. W. Malisch, Professor Dr. C. Strohmann and Professor Dr. W. Werner's workgroups for providing me with new substances and for the very constructive discussions. I will certainly miss the scientific conversations and the funny

moments spent in Berta Callejas-Gaspar, Simona Dragotă, and Marco Bosch's chemistry laboratories.

I would like to say a truly special word of thanks to Mrs. Müller and Mrs. Mühlrath for their continuous effort in solving the administrative problems and for their personal support.

I also want to thank Belinda Leimeister, Melanie Grom, Peter Popp, Rainer Eck, Jürgen Zimmermann, Peter Lang and all others in the mechanics and electronic workshop for their technical support.

My appreciation goes to Professor Dr. Arnulf Materny and all other "*femto guys*" (Dr. Achim Vierheilig, Dr. Günter Flachenecker, Dr. Mario Heid, and Dr. Chen Tao) for giving me a hand in the laboratory and for the very relaxing coffee breaks. And how could I forget to acknowledge the support and friendship that my other colleagues: Marion Strehle, Bianca Schreder, Petra Rösch, Petra Meuer, Adriana Szeghalmi, Niculina Peica, Ralph Geßner, and Nicolae Tarcea, showed to me?

A special thank goes to Stefanie Gräfe who helped me with the German translations. I wish you all the best with your PhD.

It was a time with many "*vibrations*", exactly like in a Raman spectrum, which I would never have managed to withstand without the support of my family and my good friends. I would like to thank my wonderful parents, who always encouraged me to go on with my studies and showed to me how to become a better person. Also, personal thanks to my brother for helping me improve my English and for his continuous support.

At last I would like to express my gratitude to the three very special friends of mine: Alessandra Bianchi, Smaranda Cota, and Cristiana Mensini. Thank you for listening to me, for being there anytime I needed you, and for the wonderful time spent together.

I came here with "*no luggage*" and I go so "*rich*".

Thank you!

Erklärung

Hiermit erkläre ich an Eides statt, dass ich die Dissertation

„Vibrational spectroscopy and density functional theory calculations, a powerful approach for the characterization of pharmaceuticals and new organometallic complexes.“

selbständig angefertigt und keine anderen als die von mir angegebenen Quellen und Hilfsmittel benutzt habe.

Ich erkläre außerdem, dass diese Dissertation weder in gleicher oder anderer Form bereits in einem anderen Prüfungsverfahren vorgelegen hat.

Ich habe früher außer den mit dem Zulassungsgesuch urkundlich vorgelegten Graden keine weiteren akademischen Grade erworben oder zu erwerben versucht.

Würzburg, den 12. August 2003

.....
(Ioana-Emilia Pavel)